

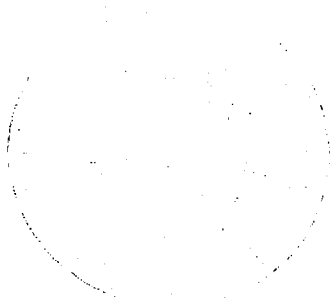
LOAN COPY
ATWL-TECHN
KIRTLAND AF

0062409



TECH LIBRARY KAFB, NM

Additional Flow Field Studies of the GA(W)-1 Airfoil With 30-Percent Chord Fowler Flap Including Slot-Gap Variations and Cove Shape Modifications



W. H. Wentz, Jr., and C. Ostowari

GRANT NGR 17-003-021
MAY 1983

FOR EARLY DOMESTIC DISSEMINATION
Because of its significant early commercial potential, this information, which has been developed under a U.S. Government program, is being disseminated within the United States in advance of general publication. This information may be duplicated and used by the recipient with the express limitation that it not be published. Release of this information to other domestic parties by the recipient shall be made subject to these limitations.
Foreign release may be made only with prior NASA approval and appropriate export licenses. This legend shall be marked on any reproduction of this information in whole or in part.
Review for general release _____ May 31, 1985



NASA Contractor Report 3687

Additional Flow Field Studies of the GA(W)-1 Airfoil With 30-Percent Chord Fowler Flap Including Slot-Gap Variations and Cove Shape Modifications

W. H. Wentz, Jr., and C. Ostowari
Wichita State University
Wichita, Kansas

Prepared for
Langley Research Center
under Grant NGR 17-003-021



National Aeronautics
and Space Administration

Scientific and Technical
Information Branch

1983

SUMMARY

Experimental measurements have been made to determine the effects of slot gap opening and flap cove shape on flap and airfoil flow fields. Test model was the GA(W)-1 airfoil with 0.30c Fowler flap deflected 35°. Tests were conducted with optimum, wide and narrow gaps, and with three cove shapes. Three test angles were selected, corresponding to pre-stall, $c_{\ell_{\max}}$ and post-stall conditions. Reynolds number was 2.2×10^6 and Mach number was 0.13. Force, surface pressure, total pressure, and split-film turbulence measurements were made. Results were compared with theory for those parameters for which theoretical values were available.

The gap study results show that the narrow (.02c) and optimum (.03c) gaps have very similar flow patterns. However, the narrow gap case has a larger region of high turbulence with intermittent reversal at the $c_{\ell_{\max}}$ angle of attack, and post-stall angle of attack. The narrow gap case also has a somewhat lower $c_{\ell_{\max}}$. The wide (.05c) gap has separated regions over the flap at all three angles of attack, and produces substantially lower lift at pre-stall and $c_{\ell_{\max}}$ angles of attack. All three gaps produce lower lift than theory predicts, but the discrepancy is greatest for the large gap case.

Cove shape studies show that both a standard and sharp-lip cove have a region of separation and reattachment ahead of the slot, while a blended cove has no separation. In spite of these differences in cove shape and local flow, all three coves produce very similar velocity profiles at the flap slot exit. While the influence of this separation and reattachment is not modeled by present theory, a separated region of this type does not substantially hinder flow attachment over the flap and attainment of high $c_{\ell_{\max}}$ values. All three cove shapes produce somewhat lower lift than theory predicts.

INTRODUCTION

The application of sophisticated computing machinery to the problem of multiple-element airfoil analysis has resulted in considerable progress in the art of airfoil design. Present theories applied to single-element airfoils make it possible to calculate surface pressures, lift, drag and pitching moment with a high degree of accuracy at least up to the angle of attack at which initial separation occurs (Ref. 1). Progress in slotted flap analysis has not achieved the same degree of success, primarily because of the additional flow complexity associated with the interactions between airfoil and flap boundary layers. For example, Fowler flap $c_{l_{\max}}$ performance for high flap deflection is known from experimental studies to be quite sensitive to flap gap opening, while theoretical calculations do not show strong sensitivity to flap gap. Detailed flow measurements for non-optimum as well as optimum flap positioning are needed to provide a data base for improved theoretical modeling.

Earlier research studies included detailed flow field measurements for a Fowler flap deflection of 40° with optimum gap and overlap (Ref. 2). While 40° flap deflection produced the highest $c_{l_{\max}}$, the configuration was highly sensitive, in that regions of separation or near-separation were present over some portion of the airfoil at every angle of attack. With 35° flap deflection, $c_{l_{\max}}$ is only slightly lower than with 40° flap, and the flow is considerably more stable, as indicated by linearity of c_l vs. α , surface c_p distributions and general observations of model buffeting. For these reasons, 35° flap deflection was selected for the present study.

Most practical-design flap coves result in local regions of flow separation and reattachment ahead of the flap slot on the lower surface. No present computer modeling technique accounts for this effect. Flow studies of practical-design and blended (no separation) coves are needed to provide a data base for refined theoretical modeling.

The purpose of the present research was to provide detailed flow field measurements as well as force and surface pressure measurements for a high $c_{l_{max}}$ Fowler flap configuration with optimum and non-optimum flap gap settings, and to provide similar measurements for two practical-design flap coves and for a blended cove.

SYMBOLS

Dimensional quantities are given in International (SI) Units. Measurements were made in U.S. Customary Units. Conversion factors between the various units may be found in Reference 3. The symbols used in the present report are defined as follows:

c	Airfoil reference chord (flap-nested)
c_d	Airfoil section drag coefficient, section drag/ ($q_\infty * c$)
c_f	Flap chord
c'_f	Local skin friction coefficient, τ/q_∞
c_l	Airfoil section lift coefficient, section lift/ ($q_\infty * c$)
c_m	Airfoil section pitching moment coefficient with respect to the .25c location, section moment/ ($q_\infty * c^2$)
c_{p_s}	Static pressure coefficient, $(p_s - p_\infty)/q_\infty$
c_{p_t}	Total pressure coefficient, $(p_t - p_\infty)/q_\infty$
h	Razor blade half-thickness
p_s	Local static pressure
p_t	Local total pressure
q_∞	Free-stream dynamic pressure
RN	Reynolds number based on wing chord
T	Turbulence, ratio of peak perturbation velocity to local mean, from hot-film trace

U	Velocity at the edge of the boundary layer, non-dimensionalized with respect to free stream velocity
u	Local velocity, non-dimensionalized with respect to free stream velocity
u_x	Component of local velocity in the free stream direction, non-dimensionalized with respect to free stream velocity
u_∞	Free stream velocity
x_a	Coordinate along airfoil chord
x_f	Coordinate along flap chord
x_w	Streamwise coordinate in wake, zero at flap trailing edge
z	Coordinate normal to free stream, zero at local surface, or zero at flap trailing edge in the wake
α	Angle of attack, degrees
α_{wt}	Wind tunnel angle of attack, degrees
α_{fs}	Free stream equivalent angle, degrees
Δp	Pressure difference between the pressure reading with razor blade in position and the true undisturbed static pressure
δ_f	Flap deflection angle, measured from flap chord line in the retracted position, degrees
ρ	Density of air
σ	Standard deviation of velocity (a measure of turbulence intensity)
ν	Kinematic viscosity
τ	Shear stress

MODEL, TEST CONDITIONS, INSTRUMENTATION AND METHODS

Model

The experimental model for the present tests was the GA(W)-1 airfoil section with 30% chord Fowler flap. This model was selected

because of the extensive data available from earlier force, pressure, and flow field studies (Refs. 2, 4 and 5). Airfoil and flap model geometry is shown in Figure 1.

Test Conditions

Tests were conducted in the WSU low speed wind tunnel with 213 cm x 91.4 cm two-dimensional insert. Reynolds number of the tests was 2.2×10^6 based upon model reference chord of 61 cm, and Mach number was 0.13. In earlier tests, transition strips were employed at .05c on upper and lower surface. Experimental pressure distributions from earlier research and theoretical studies show that with high flap deflections, the lower surface stagnation point may be located as far aft as .07c, allowing a laminar boundary layer to develop along the lower surface. For this reason a .10c location was selected for the lower surface transition strip location for the present tests. The upper surface location was retained at .05c. The strips were #80 carborundum grit, 2.5 mm wide. No transition strips were employed on the flap.

Instrumentation and Methods

Forces - Force measurements (lift, pitching moment and drag) were obtained using the wind tunnel main balance system, with linearized wall corrections applied as outlined in Reference 6. Digital data were recorded and processed by an on-line mini-computer. Reference 7 describes the mini-computer data acquisition and processing system.

Pressures - Surface pressures and pressure-type velocity measurements were obtained through a system of pressure selector switches and transducers, with digital data processed on-line. Surface pressure distributions were plotted on-line, and off-line processing was used to obtain integral force coefficients for component loads and moments.

One of the factors applied to correct wind tunnel measurements to free-stream conditions is a term to correct dynamic pressure for wake blockage due to drag (see Ref. 6 for details). This correction has been applied to the force

measurements. However, since drag was not measured simultaneously with pressure measurements, it was not possible to apply this correction directly to the c_p values. When comparisons of experimental surface c_p distributions are to be made with theory, it is essential that the conditions for comparison be as nearly equivalent as possible. To accomplish this purpose in the present study, theoretical calculations for each condition were made at an angle of attack selected to correct for the wake blockage effect. This corrected angle of attack (α_{fs}) is computed according to the method of Reference 6. Both the wind tunnel test angle (α_{wt}) and the equivalent free stream angle (α_{fs}) are labelled on the comparison figures.

Five-Tube Probe - This probe (Fig. 2a) was utilized to obtain most of the flow field data obtained in the present research. Details of calibration and operation of the probe are given in Ref. 8. Through appropriate calibration equations the five pressure measurements are translated into velocity magnitude and direction, static pressure and stagnation pressure. The probe was mounted on a vertical actuator on the test section centerline, with provisions for remote traversing longitudinally and vertically. Position data and pressures were processed by the on-line mini-computer, and velocity vectors were plotted on-line with a digital plotter.

Four-Tube Probe - This probe (Fig. 2b) consists of fore- and aft-facing pitot tubes, flattened for near-wall measurement, and a set of fore- and aft-facing static tubes. This probe permits scans nearer to a surface than is possible with the five-tube probe, and flow reversal detection by observing the larger reading from the two pitot tubes. The probe was mounted on the traversing actuator described in the five-tube probe section. Total pressure, static pressure, velocity, flow direction and position were recorded and processed on-line.

Split-Film Anemometer - Hot-film anemometer surveys were conducted using a 0.15 mm diameter split film probe (Fig. 3) to detect turbulence level, and flow direction and magnitude in regions of high turbulence. For the slot-gap tests, differential output from the split film was displayed on an oscilloscope and observations were recorded manually.

For the cove shape tests, a special computer program was developed to permit direct digital sampling of the turbulent flow signals, and on-line statistical processing. The techniques and calibrations for this instrument are given in References 9 and 10. After preliminary tests with various sampling rates and sample sizes, a sampling rate of 400 hz was selected, with a sample size of 6000. This sampling rate and size provided reasonably repeatable values for mean, standard deviation and intermittency of reversal.

Skin Friction - Skin friction measurements were made from surface pressure readings using the razor blade technique of East (Ref. 11). Geometry of the razor blades is given in Figure 4, and the calibration equation is given in Reference 2. Pressures were recorded and calculated into c_p form with the on-line mini-computer, and skin friction was calculated off-line.

Resolution - Overall resolution capabilities of the various instrumentation systems are given in Table 1:

Table 1 - Instrumentation Resolution

<u>Item</u>	<u>Resolution</u>
lift	$\pm .001 \Delta c_l$
drag	$\pm .0003 \Delta c_d$
pitching moment	$\pm .0003 \Delta c_m$
pressure transducers	$\pm .004 q_\infty$ (test $q_\infty = 1152 \text{ N/M}^2$)
dynamic pressure	$\pm .004 q_\infty$
velocity	$\pm .005 u_\infty$ (5-tube probe)
velocity	$\pm .05 u_\infty$ (split-film anemometer)
flow angle	$\pm 2^\circ$
airfoil angle of attack	$\pm .05^\circ$
flap angle	$\pm .5^\circ$
probe positioning (longitudinal and vertical)	$\pm .0004c$ ($\pm 0.244 \text{ mm}$)

PART I - SLOT GAP STUDIES

Preliminary Experiments

Earlier flow studies with the GA(W)-1 airfoil with 30% flap with 40° deflection showed that some portion of the airfoil or flap was separated at nearly every angle of attack (Ref. 2). At 35° flap deflection, however, more complete flow attachment was achieved, with only a 0.14 lower $c_{l_{max}}$ than 40° flap (Ref. 4). For this reason 35° deflection was selected for the present tests. Preliminary force tests were conducted to establish c_l values for non-optimum flap gaps. Flap gap geometry and flow scanning locations are shown in Figures 5 and 6. The results of the tests are shown in Fig. 7. Comparison of $c_{l_{max}}$ values from the present force tests with data from Reference 4 is shown in Table 2.

Table 2 - Comparison of Present Tests with Previous Tests

		$c_{l_{max}}$		
Gap		Present Tests	Ref. 4	$\Delta c_{l_{max}}$
narrow	0.02c	3.58	3.41	+ .17
optimum	0.03c	3.71	3.68	+ .03
wide	0.05c	3.40	3.52	+ .12

The present tests confirm that the optimum gap is 0.03c, and while the levels are higher than the earlier tests, the agreement is reasonable considering the measurement difficulties at stalling conditions. Based upon these tests, conditions for the present detailed flow studies were selected corresponding to pre- $c_{l_{max}}$, $c_{l_{max}}$, and post- $c_{l_{max}}$ angle conditions for each gap, as shown in Table 3:

Table 3 - Test Conditions for Flow Studies

<u>case</u>	<u>gap</u>	<u>angles of attack</u>
narrow gap	0.02c	5.2°, 10.3°, 12.7°
optimum gap	0.03c	5.2°, 10.3°, 12.7°
wide gap	0.05c	5.2°, 10.3°, 12.7°

Since the end plates had been modified with cutouts and special cover plates to accommodate flow instrumentation for the present tests, a difference in end plate drag was expected relative to earlier tests. The present end plate tare was determined by comparing drag measurements for the optimum gap with the results of Reference 4. The end plate tare correction was adjusted to provide the same airfoil-flap drag level at $c_\ell = 2.0$ as the earlier tests. This technique is justified on the basis that direct incremental effects of gap changes were measured. Pitching moment data for the optimum gap compare very favorably with Reference 4 data.

Theoretical Studies

Theoretical computer studies using the method of Reference 1 were conducted for the nine test conditions. Results from the theoretical analysis are compared with appropriate experimental data in the various figures, as noted in the section which follows.

Presentation of Slot Gap Flow Studies

Flow field studies are presented in figures as listed in Table 4. In each case data are shown for narrow, optimum, and wide gap.

Table 4 - Presentation of Slot Gap Data

<u>Type of Data</u>	<u>Instrument</u>	<u>Remarks</u>	<u>Figures</u>
Model geometry	---	---	1
Instrument details	---	---	2,3,4
Gap settings	---	---	5
Scanning locations	---	---	6
Forces	Balance	Theory and experiment	7
Surface pressures	Surface holes	Theory and experiment	8,9,10,11
Velocity field maps	4-tube/5-tube/ split film	Experiment	12,13,14
Static pressure contours	4-tube/5-tube	Experiment	15,16,17
Total pressure contours	4-tube/5-tube	Experiment	18,19,20
Boundary layer profiles	4-tube/5-tube	Experiment	21 - 29
Velocity and pressures in wake	4-tube/5-tube	Experiment	30 - 38
Skin friction	Razor blade	Theory and experiment	39
Turbulence and flow reversal maps	Split film	Experiment	40,41

Discussion of Slot Gap Studies

Force Measurements (Figure 7)

These data show that the 0.03c gap provides the highest $c_{l_{max}}$. For all three gaps, the angle for $c_{l_{max}}$ is about 10.4° .

The narrow and optimum gaps provide essentially equal lift performance for angles up to 5° . Above 5° the lift with narrow gap falls slightly below the optimum gap case. For the wide gap the lift is substantially lower than with optimum gap for all angles up to stall. At post-stall angles of attack the wide gap provides slightly more lift than either of the other settings.

Drag data show that the narrow gap configuration has slightly higher drag than the optimum gap, and that the wide gap configuration has substantially higher drag. The pitching moment data show that the narrow and optimum gap configurations have nearly the same moment. The wide gap configuration has a reduction in (negative) pitching moment, indicating separation over the rear portion of the airfoil-flap combination.

Surface Pressure Measurements (Figures 8 through 11)

At the lower angles of attack, surface pressures indicate attached flow over the airfoil and flap for narrow and optimum gaps, and separation at about mid-flap chord for the wide gap. (Separation is indicated by a constant pressure region and failure to recover to free stream pressure at the flap trailing edge.) When separation occurs over the trailing edge of the forward element, a low pressure wake appears above the flap. This wake evidently reduces the amount of fluid which must be turned by the flap. Consequently, a thin layer of slot flow turns and remains attached over the flap upper surface. The pressure plateau characteristic of flap separation vanishes from the flap under these conditions, and is replaced by a pressure distribution which shows continuous recovery from the minimum pressure point of the trailing edge. The low pressure wake from the forward element changes the boundary condition for the flap, requiring trailing edge pressure to recover not to free stream pressure, but rather to the lower wake pressure. Thus of the two pressure distribution characteristics trends usually associated with trailing edge separation on single element airfoils: (1) lack of trailing edge pressure recovery and (2) constant pressure region (pressure plateau); only the pressure plateau criteria can be applied to studies of slotted flap separation.

A reduction of forward element lift due to loss of flap circulation is also shown in the wide gap data. At the post-stall angle of attack (12.7° or $\alpha_{fs} = 15.1^\circ$) separation is indicated from about $0.6c$ aft on the main element for all three gaps, and flap flow appears fully attached. Comparisons of experimental pressures with theory show generally good agreement except where either forward element or flap separation is present.

Velocity Plots (Figures 12 through 14)

Earlier studies (ref.2) for the same GA(w)-1 airfoil and flap with 40° flap deflection revealed that with the optimum slot gap, an unsheared potential flow ($c_{p_t} = 1.0$) core was present in the flap slot, with sheared flow (wing and flap boundary layers) above and below the core. Further, it was found that the core flow continued beyond the slot exit, but did not always persist as far aft as the flap trailing edge.

Velocity plots from the present test for narrow and optimum gap indicate fully attached flow over airfoil and flap at the pre-stall (5.2°) angle and the angle for $c_{l_{max}}$, with a substantial core flow in each case. Careful examination reveals that the velocity profile at the flap trailing edge at the angle for $c_{l_{max}}$ is slightly fuller (slightly wider core flow, less prone to separation) for the optimum gap than for the narrow gap. At the post-stall angle (12.7°) a large region of separation appears on the airfoil forward section (from about $0.3c$ aft) for both narrow and optimum gaps, and the flap flow remains fully attached with core flow extending to the flap trailing edge in both cases.

The velocity plots for the wide gap show separation at the flap trailing edge even at the pre-stall angle. A wide core flow is present at the slot exit, but the core is displaced upward at the flap trailing edge by the reversed flow region. At $c_{l_{max}}$ the separation is forward of mid-flap chord. At post-stall, a major portion of the flap is separated as well as the aft station on the airfoil. Wakes from the airfoil trailing edge and flap merge ahead of the flap mid-chord location at the $c_{l_{max}}$ and post-stall angles, rapidly dissipating the core flow.

The slot exit flow profiles indicate non-reversed flow with relatively thin slot sidewall viscous layers for all three gaps and all three angles tested.

Static Pressure Contours (Figures 15 through 17)

The data at the pre-stall and $c_{l_{max}}$ angles of attack indicate attached flow (isobars perpendicular to the local surface) over the flap for narrow and optimum gaps, but separated flow (isobars parallel to the local surface) over the flap for the wide gap. At the post-stall angle of attack, regions of local separation are indicated at the trailing edge of the forward

element for the narrow gap, just aft of the slot exit for the optimum gap and over nearly the entire flap for the wide gap.

Total Pressure Contours (Figures 18 through 20)

The total pressure contours are of particular interest, since the $c_{p_t} = 1.0$ contour defines the extremity of the viscous flow region. The narrow and optimum gaps exhibit quite similar characteristics. At 5.2° and 10.3° , separate definable wakes appear from the forward element trailing edge and the flap. At the post-stall angle of attack, evidence of forward element separation appears as indicated by a relatively large region of reduced total pressure. The flap wake remains relatively thin.

With the wide gap, a wide wake is present behind the flap at all angles of attack, indicating substantial flap separation.

Boundary Layer Profiles (Figures 21 through 29)

The near-wall velocity profiles, c_{p_s} profiles and c_{p_t} profiles are quite similar for narrow and optimum gaps. The data indicate non-reversed flow at all stations for the two lower angles of attack, and reversed flow at $.80c$ and $1.005c$ on the forward element at the post-stall angle of attack. The flow through the slot is non-reversed even at the post-stall angle.

The measurements with the wide gap are quite different. With this gap, reversed flow is observed at the flap trailing edge station even at the pre-stall angle of attack condition. At the $c_{l_{max}}$ angle, reversed flow is observed at all flap stations and at the forward element trailing edge, even though a positive slot flow exists. At the airfoil trailing edge station, no data were obtained for positions just above the surface ($z/c = .003$ to $.006$), due to the highly unsteady character of the flow.

At the post-stall angle, the measurements with the wide gap show reversal of flow at all flap stations even though a thin layer of positive flow exists at the slot. On the forward element, a thin ($.0005c$) region of reversed flow was measured as far forward as the $.80x/c$ station. Unsteadiness again prohibited measurements at the forward element trailing edge for positions just above the airfoil surface ($x/c = 1.005$, $.0025 < z/c < .0040$).

Wake Characteristics (Figures 30 through 38)

Wake measurements for narrow and optimum gaps are quite similar, showing no reversal of flow at pre-stall and $c_{l_{\max}}$ angles of attack, and substantial reversal at post-stall.

The wide gap measurements show reversed flow at the $x_w/c = .075$ and $.15$ stations at the angle of attack for $c_{l_{\max}}$ and at the $x_w/c = .15$ and $.30$ stations at the post-stall angle of attack. The apparent absence of reversed flow at the $x_w/c = .075$ location with post-stall angle of attack is questionable, since high turbulence prohibited measurement at a number of points at this station.

Skin Friction (Figure 39)

At the pre-stall and $c_{l_{\max}}$ angles of attack, skin friction measurements on the forward element follow the trend predicted by theory, but measured levels are consistently below theory. On the flap upper surface, data for narrow and optimum gaps agree well with theory. Measurements with the wide gap show levels near theory over the forward portion of the flap, but levels far below theory over the aft portion of the flap upper surface at the pre-stall angle of attack. At the $c_{l_{\max}}$ angle of attack, skin friction with the wide gap is far below theory over the entire flap upper surface.

At the post-stall angle of attack, skin friction measurements on the forward element have substantial scatter, showing nearly constant friction at average levels which are about half of the theoretical predictions. Flap skin friction measurements for all gap settings show strong variation with position as indicated by theory, but at somewhat higher levels than theory. These observations for narrow and optimum gaps are consistent with the basic surface pressure distributions, velocity field maps and split film turbulence surveys which indicate attached flow over the flap even at the post-stall angle of attack. The wide gap measurements are not so consistent. The velocity field maps and split film surveys indicate flap separation, while the surface pressure measurements and skin friction measurements indicate attached flap flow. It must be remembered, of course, that the razor blade skin friction measurements are obtained in part from surface pressure measurements; therefore surface pressure and skin friction data are not completely independent parameters. Furthermore,

total pressure measurements (such as with a razor blade) tend to read higher than true mean value in regions of high turbulence.

Turbulence and Flow Reversal Maps (Figures 40 and 41)

Regions of steady flow and regions with various degrees of turbulence, i.e., moderate intermittency (1% time < reversal < 50% time) of reversal and high intermittency (reversed > 50% of time) of reversal are shown. Measurements were made only for the $c_{l_{max}}$ angle and post-stall angle. In interpreting these results, and comparing them with other data, only the high intermittency regions are considered to be regions of "flow reversal."

For the $c_{l_{max}}$ angle of attack, the narrow gap configuration has a region of heavy turbulence over the aft region of the flap, but no region on the surface where intermittency of reversal greater than 50% was measured. With the optimum gap no airfoil or flap separation is present, but a small region of moderate intermittency of reversal extends from the flap trailing edge aft, a distance of about $0.20c$. With the wide gap, substantial flap separation is again present.

At the post-stall angle of attack, the narrow gap configuration has separation from about $0.70c$ aft on the main section and moderate intermittency of reversal over the entire flap. With the optimum gap, the airfoil has a major region of separation, but a thin layer of attached flow remains over the flap. With the wide gap, flow reversal is diminished over the airfoil forward element, but flap separation is substantially increased.

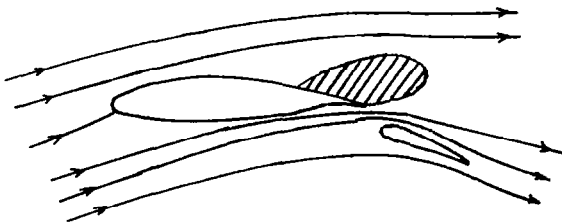
CONCLUSIONS FROM GAP STUDIES

1. For the optimum gap, separation was minimized and lift was maximum. Initial separation occurred at the airfoil trailing edge, and the flap remained fully attached through the stall.

2. With a narrower than optimum gap, surface flow separation characteristics are nearly identical to those for the optimum gap. On the other hand, substantially larger regions of high turbulence with moderate intermittency of reversal were observed over the flap at the $c_{l_{max}}$ angle and the post-stall angle.

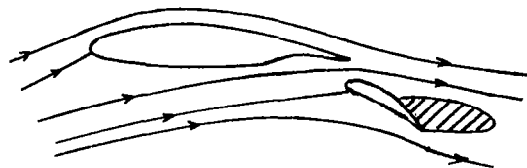
3. With a wider than optimum gap, flow measurements indicate that the flap was partially separated at all angles of attack. In this case, the efflux from the slot exit does not follow the flap contour, but rather flows nearly streamwise, merging with the airfoil forward element wake. All measurements except the surface pressure data at the post-stall angle of attack substantiate this general picture of the flow. These conflicting results present a dilemma as to the actual flow situation.

Observation from other tests on multiple-element configurations indicate that when separation appears at the trailing edge of the element forward of the flap, the flap flow becomes more stable. Thus two post-stall separation patterns may appear: the first is predominantly separation on the forward element, with a layer of fluid entering the slot and remaining attached over the flap (Sketch A); the second pattern or mode is separation over the flap with attached flow on the forward element (Sketch B). It is believed that separation was predominantly over the flap for all runs except the surface c_p measurements at the post-stall angle in the present tests, and that when surface c_p measurements were being made the separation shifted to the forward element.



Sketch A

MODE I - AIRFOIL SEPARATION



Sketch B

MODE II - FLAP SEPARATION

PART II - FLAP COVE SHAPE STUDIES

Geometric Considerations

Effects of cove shape on Fowler flap performance have not been previously studied in detail. Most designs utilize either a smooth entry lip (Figure 42) or a sharp-edge entry lip. The smooth lip would appear to be designed to promote attached flow from the airfoil lower surface to the flap slot, although both theory and experiment show that separation occurs even for a fairly generous lip radius. Disadvantages of this design are undercutting the aft spar cap area (if a generous radius is used), and possible drag penalty at cruise due to the local surface dip (or "notch") which remains with flap nested. Unpublished WSU wind tunnel studies have shown that the drag penalty due to the surface notch is quite small at low Reynolds number and low Mach number. On the other hand, the notch and rounded entry cove tend to promote leakage through the flap slot, and leakage flow can cause severe drag penalties. (See Ref. 5 for details.)

The sharp lip cove maximizes structural volume, provides a smoother contour at cruise, and is easier to fit with a seal to minimize leakage problems. Flap optimization studies with various cove shapes (Ref. 4) indicate that little $c_{l,max}$ penalty is associated with the sharp lip cove.

Sharp-lip cove entry shapes cannot be analyzed by current computational models. Theoretical studies with rounded entry lip predict separation on the lip at all angles of attack with flap extended. Experiments confirm the separation, but show that reattachment occurs ahead of the flap slot for optimum gap and overlap. Since computer models do not account for post-separated flows, or separated flows with reattachment, theoretical results for geometry which results in separation must be viewed with skepticism.

In order to study the effects of flap cove separation and reattachment, experiments were conducted for three flap cove shapes (Figure 42):

- 1) a round entry lip cove (standard cove)
- 2) a "blended" cove
- 3) a sharp-lip cove

The blended cove was designed to provide for fully attached flow in the cove region. A contour of this type could be provided on an operational aircraft only by means of a rather complicated variable-geometry cove. The objective of studying this geometry in the present research was not to suggest the blended cove as a practical design, but rather to investigate the effects of fully attached flow versus separated and reattaching flow on flap performance and flap cove and slot flow characteristics.

Preliminary Experiments

Preliminary Force Tests:

For these tests the flap deflection was 35° and overlap was $0.012c$. Force runs were conducted to determine the optimum gap (for highest $c_{l_{\max}}$) for each cove shape. The tests showed that the optimum gap was the same ($0.030c$) for all three cove shapes, even though $c_{l_{\max}}$ levels varied somewhat.

Flow Visualization:

Tuft and oil dot flow studies were conducted to determine separation and reattachment locations for each cove configuration. While these preliminary studies were not documented with photographs, these studies showed that the standard cove separates at the radius of the cove entrance, and the sharp-lip cove separates at the cove lip. In both cases, reattachment occurs at about the $0.90c$ station. The blended cove showed no indication of separation.

Flow Measurements in Cove Region:

Because of the restrictive geometric constraints of the cove shapes, only limited measurements were possible with the 5-tube probe and 4-tube probes.

The small size of the split-film anemometer makes it suitable for scanning the flap cove regions. Equally important, this device is capable of making measurements in regions of high turbulence, including turbulent flows with intermittent reversal.

Presentation of Cove Shape Studies

Results of these studies are presented in Figures as listed in Table 5. Except where noted, data are presented for standard, blended, and sharp-lip cove.

Table 5 - Presentation of Cove Shape Data

<u>Type data</u>	<u>Instrument</u>	<u>Remarks</u>	<u>Figures</u>
Cove geometry	---	---	42
Forces	Balance	Theory for standard & blended coves only	43
Surface pressures	Transducers	Theory for standard & blended coves only	44,45,46
Surface flow	Tufts	---	47
Velocity field maps	5-tube, 2-tube, split-film	---	48,49,50
Near-wall velocity profiles	5-tube, 4-tube, split-film	$x/c = .60$ and $.975$	51,54
Turbulence and flow reversal maps	Split-film	For standard and sharp lip only	52,53
Wake velocity profiles	Split-film	$x_w/c = .02$	55
Static pressure contours	4-tube, 5-tube	---	56,57,58

Discussion of Cove Shape Studies

Force Measurements (Figure 43)

The data for the standard cove show reasonable agreement with earlier (Ref. 2) wind tunnel data and other test data with the same geometry (Fig. 7). The drag data have been corrected for end plate tare differences as noted on page 8.

The present data show that at low angles of attack, the lift is the same for all three cove shapes. Near $c_{l_{max}}$ the blended and sharp-lip coves exhibit less lift and a lower stalling angle than the standard case, indicating early flap or airfoil upper surface separation. The differences between the blended and sharp-lip cove results are quite

small. At post-stall angles of attack, all three cove shapes produce essentially the same lift.

Surface Pressures (Figures 44 through 46)

The experimental pressure distributions for all three cove shapes are nearly identical for angles up to 7.7° . At 10.3° the data for the standard cove show higher lift and a smoother distribution over the airfoil forward element than the sharp-lip and blended coves which have separation on the forward element. At 12.7° , pressure measurements for all three cove shapes are again essentially the same. These trends correlate well with the observations from the force measurements.

As discussed earlier, theoretical predictions using the method of Reference 1 are not possible for sharp-lip coves. Comparisons with theory for the standard cove case show fairly good agreement at angles prior to separation, and poor agreement when substantial separation is present ($\alpha_{fs} = 14.8^\circ$). Even at the pre-separation angles, both upper and lower surface experimental pressures show smoother distributions than the theory predicts in the vicinity of the cove.

The blended cove theoretical results show smooth distributions, and therefore slightly better agreement with experiment than the standard cove case. At 11.7° (α_{fs}) the experimental data show some inconsistency which is believed to be an indication of instability of the separation point location, and consequent unsteadiness of the entire pressure field. (A slow-scan method for pressure data recording was used, with pressure locations being sampled in groups of four.) The flap pressures for this angle indicate attached flow but substantially lower peak (negative) pressures than theory. The 14.8° data indicate a substantial region of stable separation on the forward element, and a flap pressure distribution similar to the 11.7° case.

Surface Flow (Figure 47)

Lower surface tuft photos with standard cove show separated flow in the cove at all angles of attack, with reattachment taking place ahead of the slot lip. Flap lower surface flow is attached in all cases. The blended cove photos show completely attached lower surface flow. The sharp-lip cove was fabricated from plexiglas to permit flow visualization within the cove. These photos show separation and reattachment ahead of the slot lip, generally similar to the standard cove.

Velocity Field Maps (Figures 48 through 50)

These maps show composite data obtained from the 5-tube pressure probe and from the split film anemometer. The pressure probe is the preferred instrument in regions of steady flow, since it gives flow angularity information and static and total pressures, and is not prone to calibration shifts. On the other hand the split-film anemometer is capable of measurement in highly turbulent, reversing flows, and its small size enabled scans to be conducted at a station just forward of the slot exit ($x/c = .975$).

Study of all these figures reveals that agreement between the 5-tube probe and split-film anemometer is quite good at the outer edges of the boundary layers. At the wake survey stations, however some inconsistencies are present. These occur in regions of relatively high turbulence, where pitot-type probes are known to produce readings higher than the true mean. Only the mean values from the split-film anemometer data are shown on these figures.

The cove region surveys confirm the presence of separation with reattachment ahead of the slot exit for the standard cove and sharp-lip coves, and fully attached flow for the blended cove. The data for the sharp-lip cove reveal an unexpected result. The flow in the cove near the entrance lip ($x/c = .775$) does not show substantial reversal. In fact, the profiles at this station for pre-stall and post-stall angles show nearly zero mean velocity for the region from the wall to about $.05 z/c$, and the profile at the $c_{\ell_{\max}}$ angle shows a positive mean flow. This result was so surprising that scans were repeated with the probe reversed, and re-calibration of the probe was performed to confirm the findings.

Near-Wall Velocity Profiles at Cove Entry (Figure 51)

Near-wall scans were conducted at $0.60 x/c$ to determine whether the cove shape variations would have a significant influence on the approaching boundary layers. These data show that the boundary layers at this station are quite thin for all cases. In fact, at the $c_{\ell_{\max}}$ angle, the profiles are virtually unaffected by cove geometry.

Cove Turbulence Surveys (Figures 52 and 53)

These measurements were conducted only for the standard and sharp-lip coves, since no separation was observed with the blended cove. With the standard cove, the flow shows some reduction of turbulence between the pre-stall and $c_{l_{\max}}$ angles of attack. Data for both cove shapes show that the flow entering the flap slot was not reversing, and had moderate or less turbulence at the $c_{l_{\max}}$ angle. The sharp-lip cove seems to promote a slightly more stable flow entering the flap slot and a somewhat thinner region of influence of the reversed flow.

Flap Slot and Wake Velocity Profiles (Figures 54 and 55)

Split-film anemometer scans near the flap slot ($x/c = .975$) show similar trends for all three coves. In this figure, bandwidths of ± 3 standard deviations (σ) are shown as well as mean values. The data for mean velocity are quite similar for all three cove shapes. The standard cove shows slightly higher turbulence level (larger bandwidth for 3σ) at the maximum velocity point and the sharp-lip cove shows higher turbulence near the wall, including reversal with the $\pm 3\sigma$ bandwidth.

Wake profiles measured just downstream from the flap trailing edge ($x_w/c = 0.02$) show reversal of the mean flow for the blended and sharp-lip coves, but no reversal of the mean flow for the standard cove. (Intermittent reversal is present in all cases.) The standard cove flow data also show that the region of high turbulence is located well above the flap trailing edge, indicating that the separation originates primarily from the forward element rather than from the flap.

Static Pressure Contours (Figures 56 through 58)

These data indicate fairly regular contours for the blended cove with fully attached flow. For the standard and sharp-lip coves, regions of separation are indicated by plateaus of constant pressure near the airfoil surface. Since the pressure tends to become constant in regions of separation, isobars will

tend to become parallel to the surface when separation is present. For unseparated flows, isobars tend to be orthogonal to the surface. Careful comparison of these figures with split-film velocity profiles in figures 48 through 50 indicates some discrepancies in the extent of the reversed flow regions. These discrepancies are attributed to pressure measurement inaccuracies associated with the highly turbulent nature of the flow in these regions.

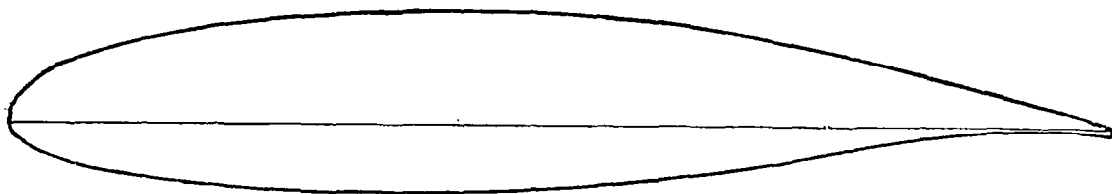
CONCLUSIONS FROM FLAP COVE SHAPE STUDIES

1. Local flow separation within a flap cove region does not seem to be a hindrance to attainment of high maximum c_ℓ values, so long as the flow reattaches ahead of the flap slot. In fact in the present tests, a completely blended cove which did not have flow separation actually produced a slightly lower $c_{\ell_{\max}}$ than a more conventional ("standard") cove with flow separation and reattachment.

2. Detailed measurements within three cove regions show that while the details of the flow within the cove differ, all three coves produced very similar flap slot velocity profiles.

REFERENCES

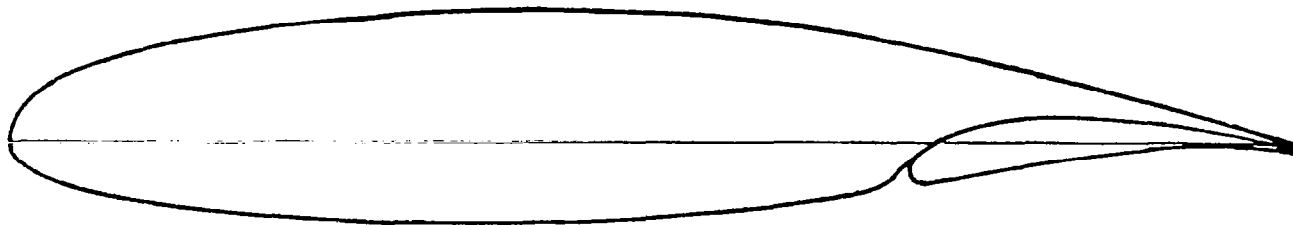
1. Stevens, W.A., Goradia, S.H., and Braden, J.A.: Mathematical Model for Two-Dimensional Multi-Component Airfoils in Viscous Flow. NASA CR-1843, 1971.
2. Wentz, W.H., Jr., and Seetharam, H.C.: A Low-Speed Two-Dimensional Study of Flow Separation on the GA(W)-1 Airfoil with 30-Percent Chord Fowler Flap. NASA CR-2844, 1977.
3. Mechtly, E.A.: The International System of Units - Physical Constants and Conversion Factors (Revised). NASA SP-7012, 1969.
4. Wentz, W.H., Jr., and Seetharam, H.C.: Development of a Fowler Flap System for a High Performance General Aviation Airfoil. NASA CR-2443, 1974.
5. Wentz, W.H., Jr., and Volk, C.G., Jr.: Reflection-Plane Tests of Spoilers on an Advanced Technology Wing With a Large Fowler Flap. NASA CR-2696, 1976.
6. Pope, A. and Harper, J.J.: Low Speed Wind Tunnel Testing. John Wiley, 1966.
7. Fisco, K.A. and Howe, D.: Minicomputer Utilization as a Method of Data Reduction in a Low Speed Wind Tunnel. AIAA Paper 78-313, 1978.
8. Seetharam, H.C., Wentz, W.H., Jr., and Walker, J.K.: Measurement of Post-Separated Flow Fields on Airfoils, Tech. Note, AIAA J. of Aircraft, Vol. 14, No. 1, January 1977.
9. Rodgers, E.J., Wentz, W.H., Jr., and Seetharam, H.C.: Instrumentation, Techniques and Data Reduction Associated with Airfoil Testing Programs at Wichita State University. Advanced Technology Airfoil Research - Volume I, NASA CP-2045, Part 2, 1979, pp. 539-558.
10. Wentz, W.H., Jr. and Seetharam, H.C.: Split-Film Anemometer Measurements on an Airfoil with Turbulent Separated Flow. Fifth Biennial Symposium on Turbulence, University of Missouri--Rolla, October 1977.
11. East, L.F.: Measurement of Skin Friction at Low Subsonic Speeds by the Razor-Blade Technique. British R & M No. 3525, 1968.



Upper Surface		Lower Surface	
x/c	z/c	x/c	z/c
0.00000	0.00000	0.00000	0.00000
.00200	.01300	.00200	-.00930
.00500	.02040	.00500	-.01380
.01250	.03070	.01250	-.02050
.02500	.04170	.02500	-.02690
.03750	.04965	.03750	-.03190
.05000	.05589	.05000	-.03580
.07500	.06551	.07500	-.04210
.10000	.07300	.10000	-.04700
.12500	.07900	.12500	-.05100
.15000	.08400	.15000	-.05430
.17500	.08840	.17500	-.05700
.20000	.09200	.20000	-.05930
.25000	.09770	.25000	-.06270
.30000	.10160	.30000	-.06450
.35000	.10400	.35000	-.06520
.40000	.10491	.40000	-.06490
.45000	.10445	.45000	-.06350
.50000	.10258	.50000	-.06100
.55000	.09910	.55000	-.05700
.57500	.09668	.57500	-.05400
.60000	.09371	.60000	-.05080
.62500	.09006	.62500	-.04690
.65000	.08599	.65000	-.04280
.67500	.08136	.67500	-.03840
.70000	.07634	.70000	-.03400
.72500	.07092	.72500	-.02940
.75000	.06513	.75000	-.02490
.77500	.05907	.77500	-.02040
.80000	.05286	.80000	-.01600
.82500	.04646	.82500	-.01200
.85000	.03988	.85000	-.00860
.87500	.03315	.87500	-.00580
.90000	.02639	.90000	-.00360
.92500	.01961	.92500	-.00250
.95000	.01287	.95000	-.00260
.97500	.00609	.97500	-.00400
1.00000	-.00070	1.00000	-.00800

(a) GA(W)-1 Airfoil Coordinates.

Figure 1 - Model Geometry.



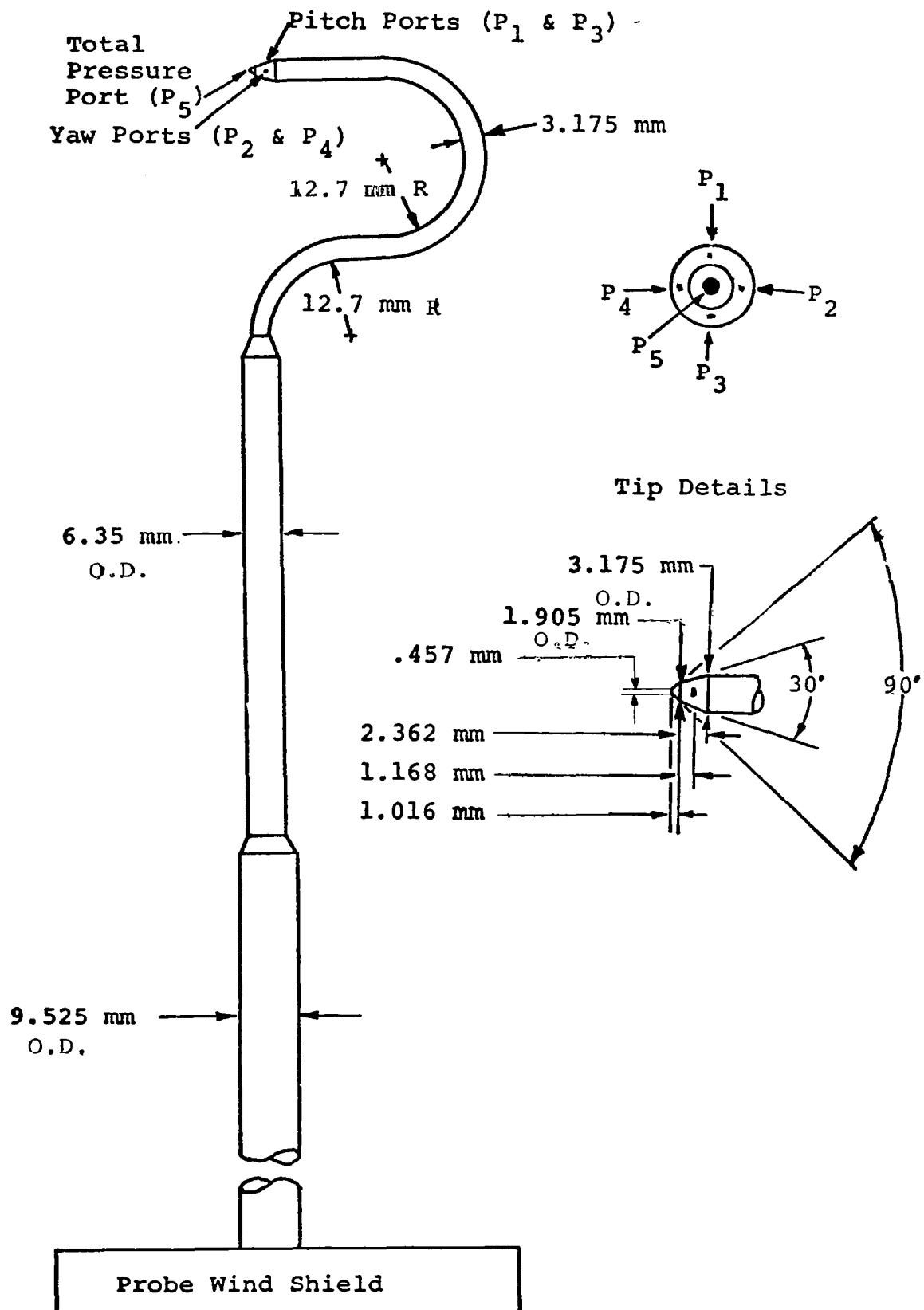
30% c Fowler Flap Coordinates

Upper Surface		Lower Surface	
x_f/c	z_f/c	x_f/c	z_f/c
.000	-.01920	.000	-.01920
.025	.00250	.025	-.02940
.050	.01100	.050	-.02490
.075	.01630	.075	-.02040
.100	.01900	.100	-.01600
.125	.01950	.125	-.01200
.150	.01820	.150	-.00860
.175	.01670	.175	-.00580
.200	.01330	.200	-.00360
.225	.00950	.225	-.00250
.250	.00530	.250	-.00260
.275	.00100	.275	-.00400
.300	-.00435	.300	-.00800

L.E. Radius = 0.0122c

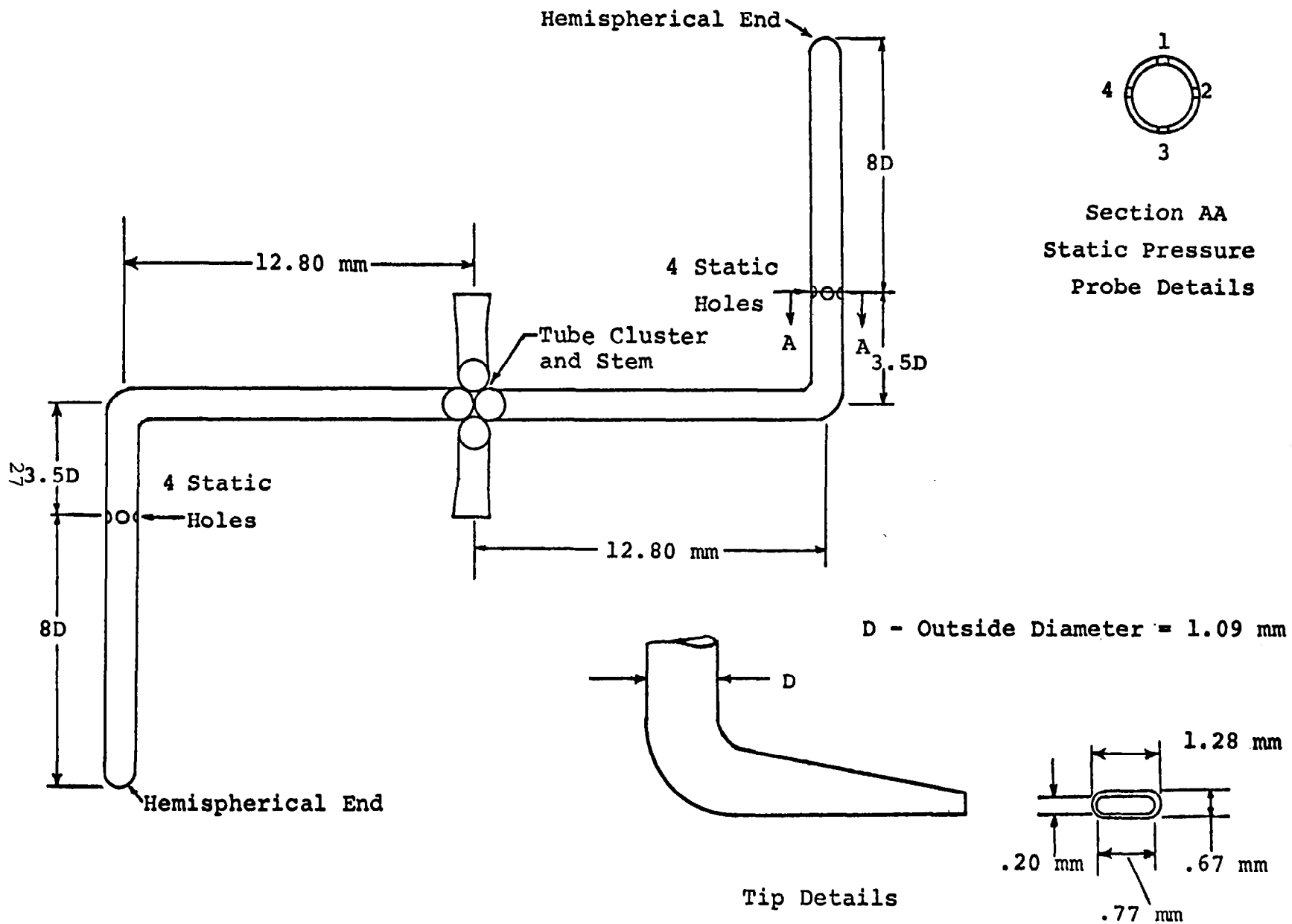
(b) Flap Coordinates.

Figure 1 - Continued.

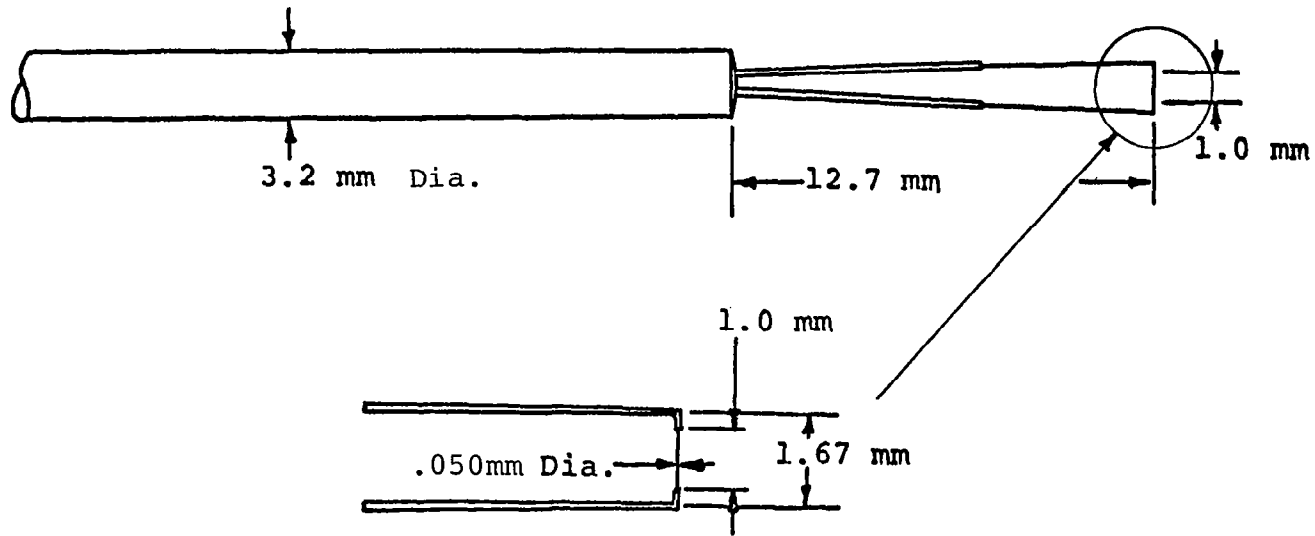


(a) Five Tube Probe.

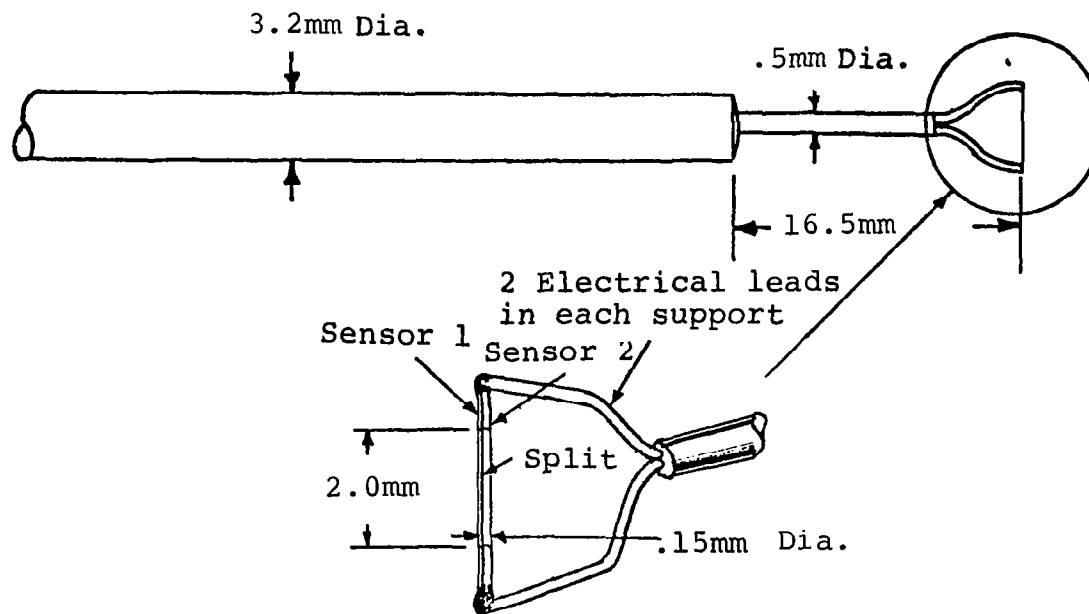
Figure 2 - Pressure Probes.



(b) Four Tube Probe.
Figure 2 - Concluded.

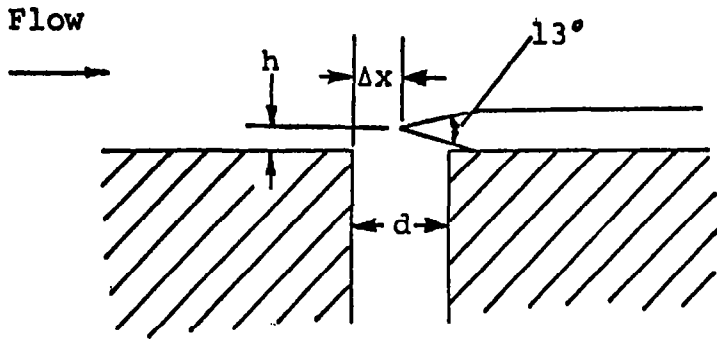


a) Single Sensor



(b) Split-Film Sensor

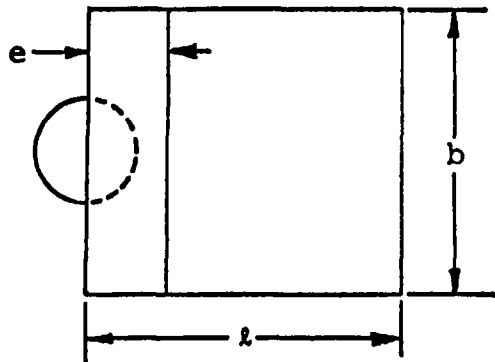
Figure 3 - Hot Film Anemometry.



Surface Static Pressure Tap

Dimensions

d	1.07 mm
e	.46 mm
h	.052 mm
l	6.35 mm
b	6.35 mm
d/h	20.5
b/h	122.
l/b	1.0
Δx	0.0



Criteria from Ref. 11;

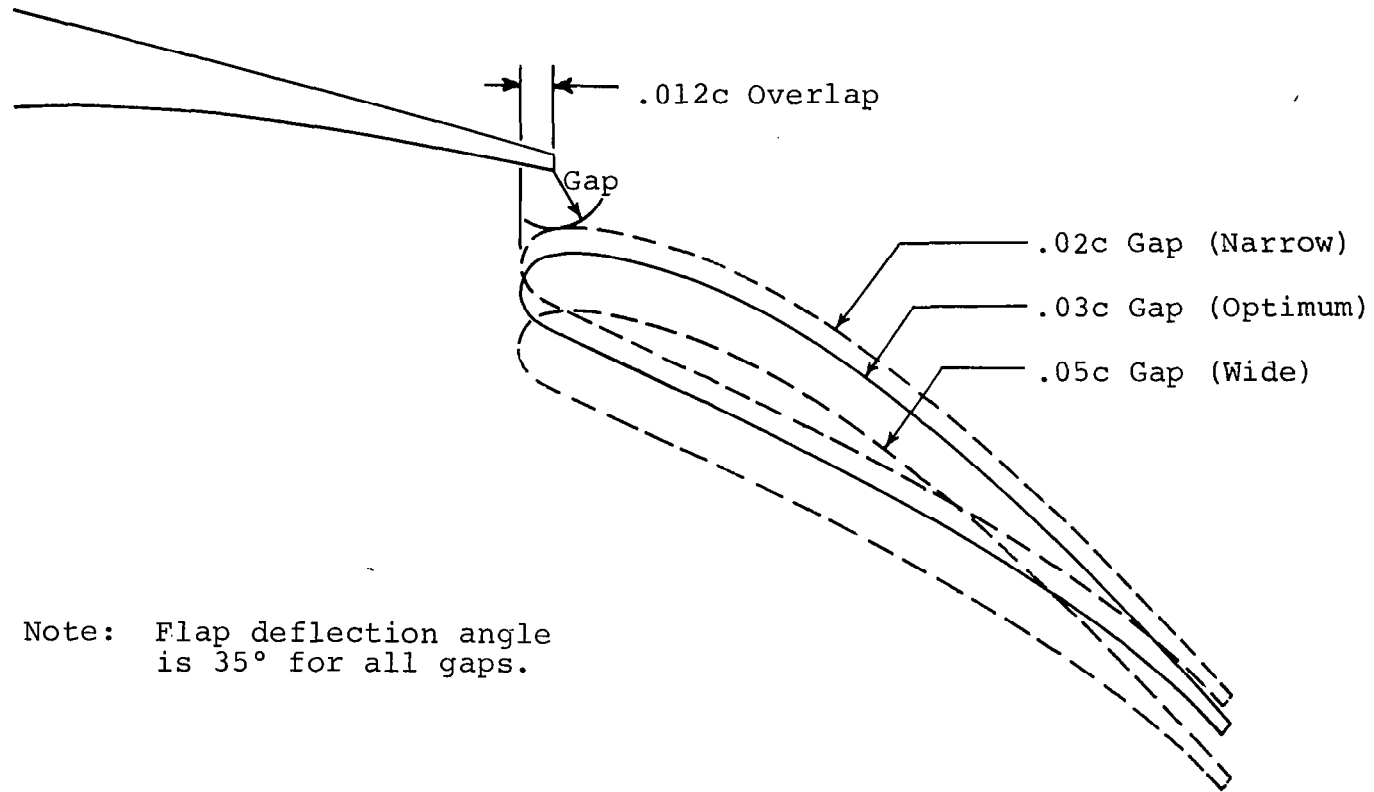
$$\frac{d}{h} > 6$$

$$\frac{b}{h} > 36$$

$$\frac{l}{b} = 1$$

$$\Delta x = 0$$

Figure 4 - Razor Blade Technique: Details of Dimensions and Positioning.



Note: Flap deflection angle is 35° for all gaps.

Figure 5 - Flap Settings For Gap Study.

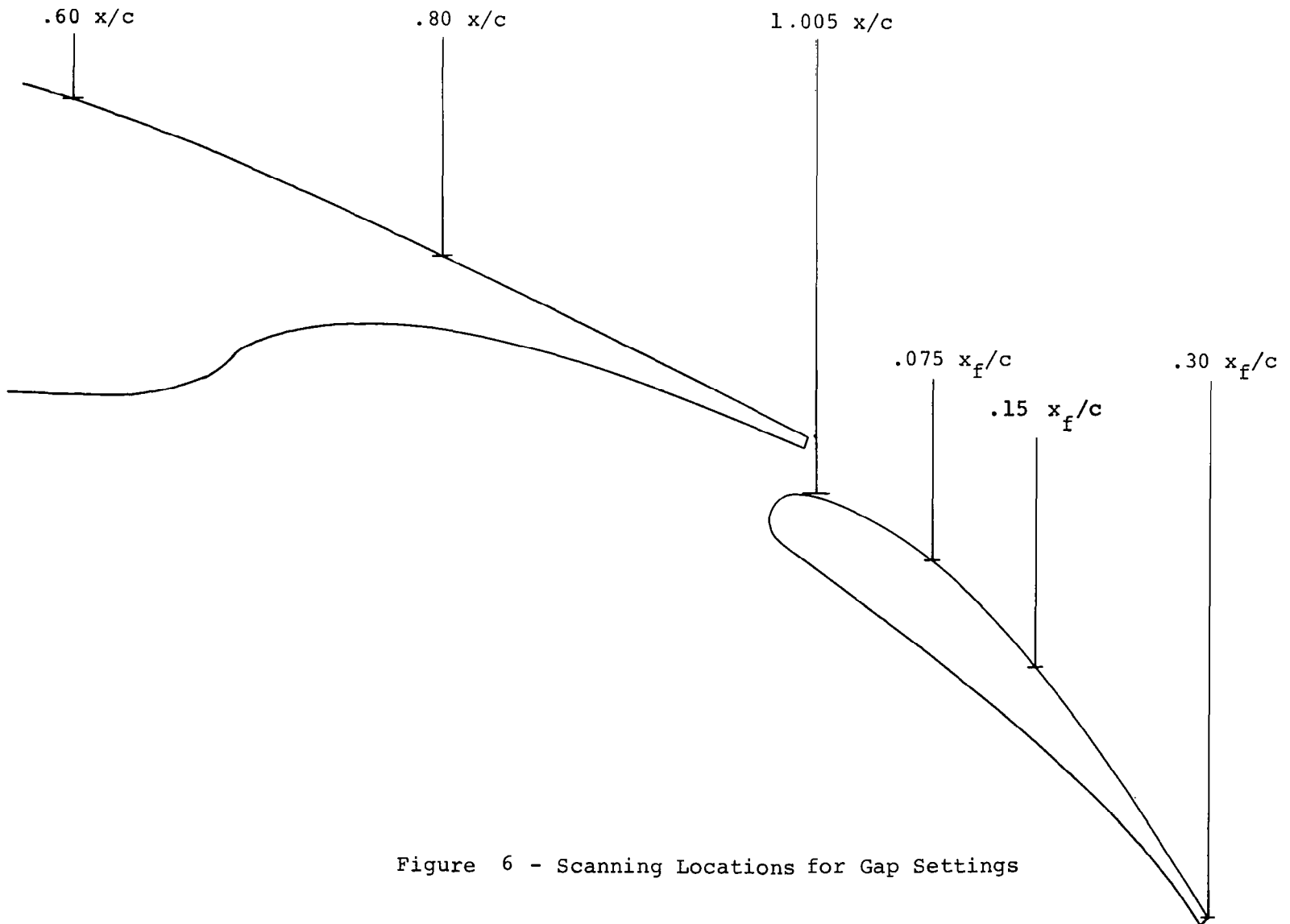
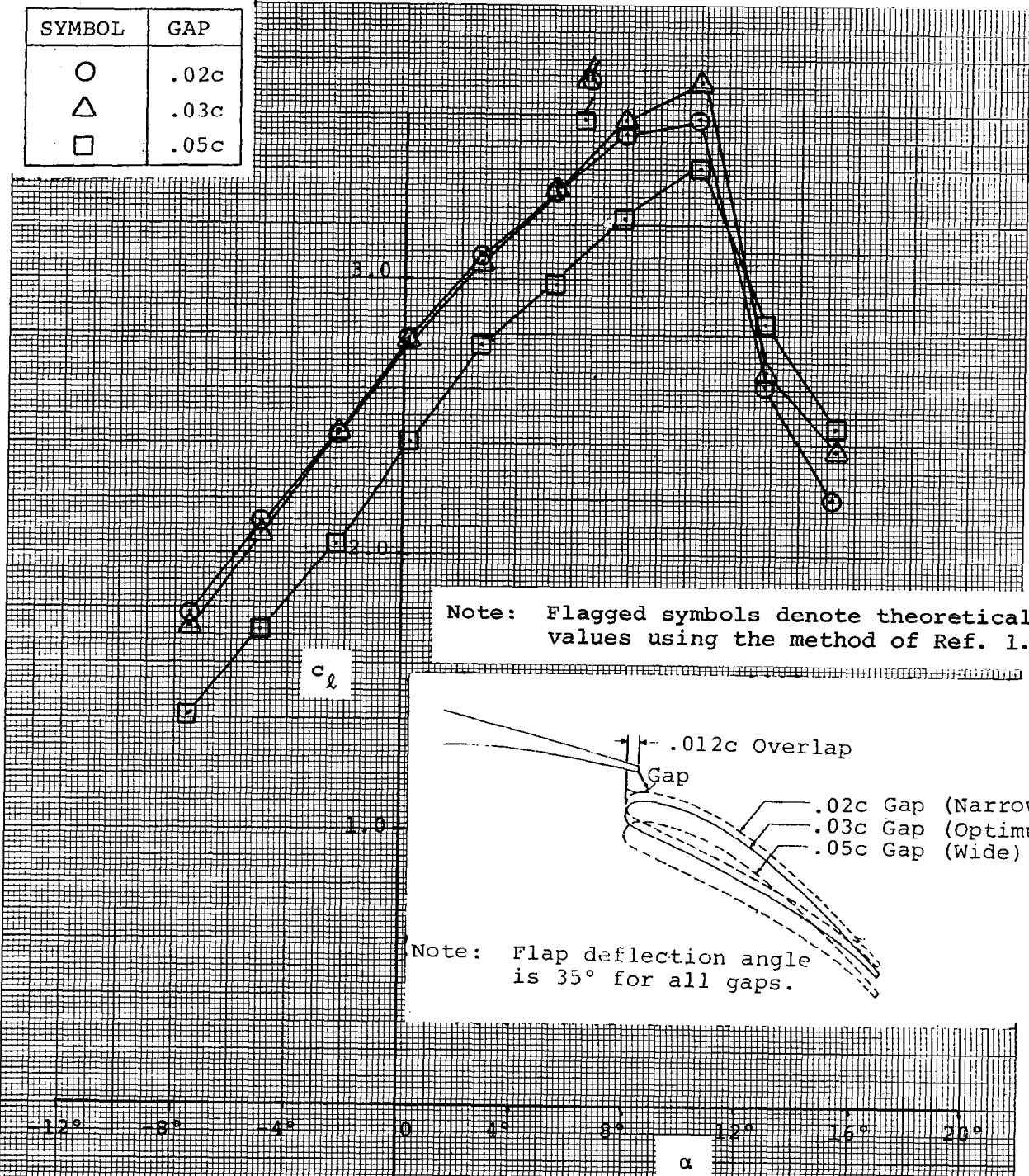


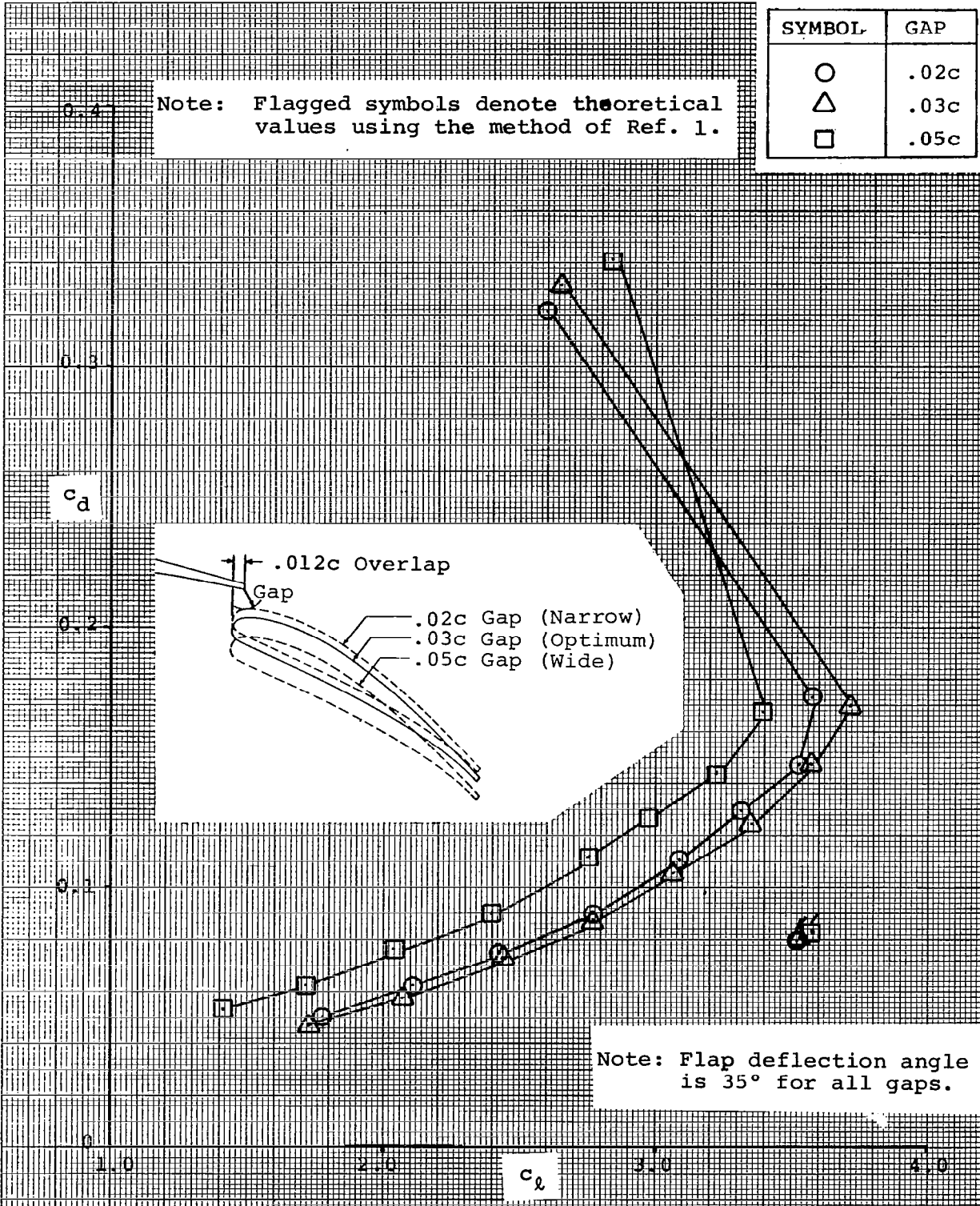
Figure 6 - Scanning Locations for Gap Settings

SYMBOL	GAP
○	.02c
△	.03c
□	.05c



(a) Lift

Figure 7- Effects of Slot Gap on Forces.

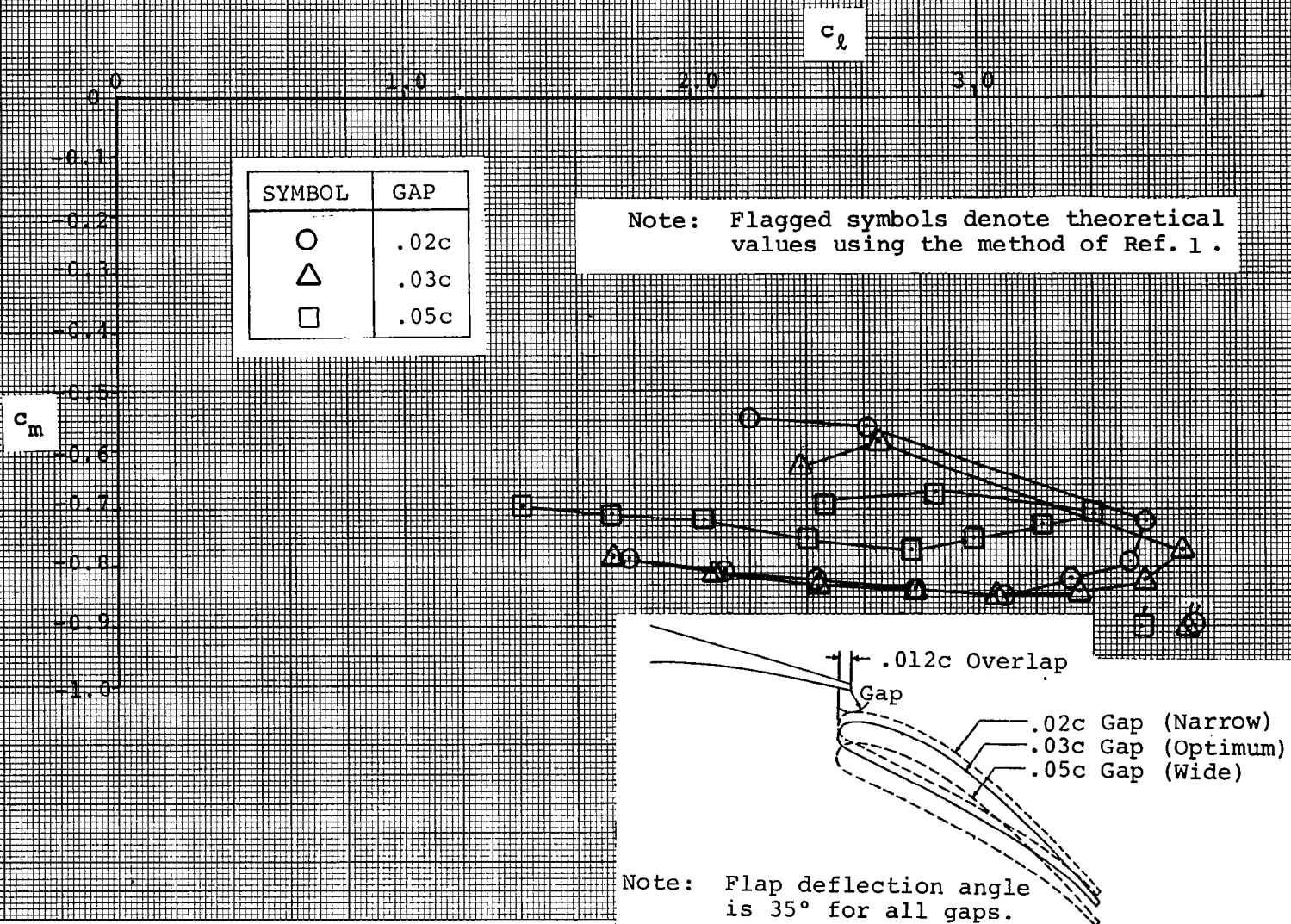


(b) Drag

Figure 7 - Continued.

Figure 7 - Concluded.

(c) Moment



(a) ANGLE-OF-ATTACK = 0.1°
 Flap Deflection = 35.0°
 Mach Number = 0.13
 Reynolds Number = $2.2 \text{ E } 06$
 Overlap = $0.012c$

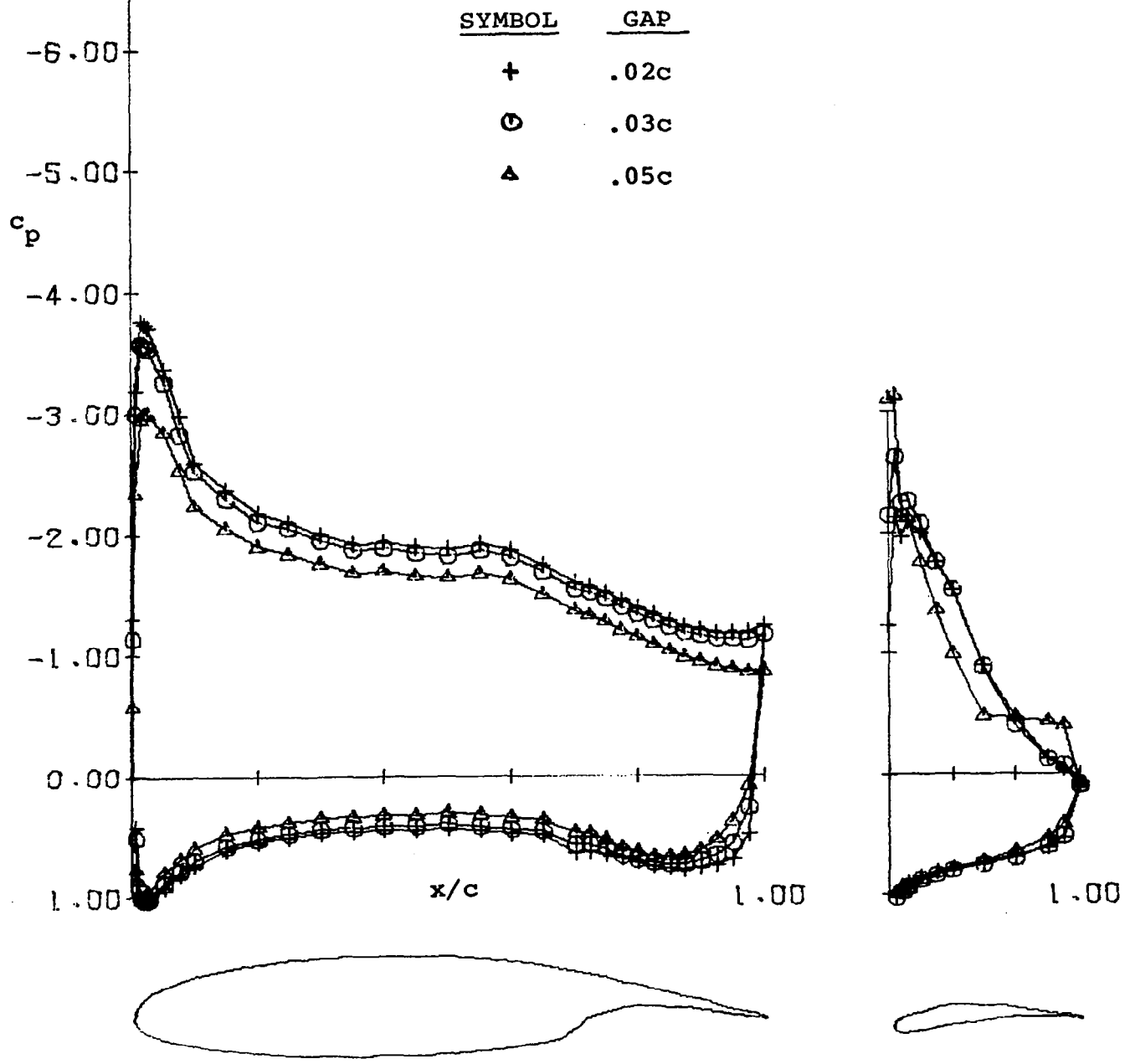
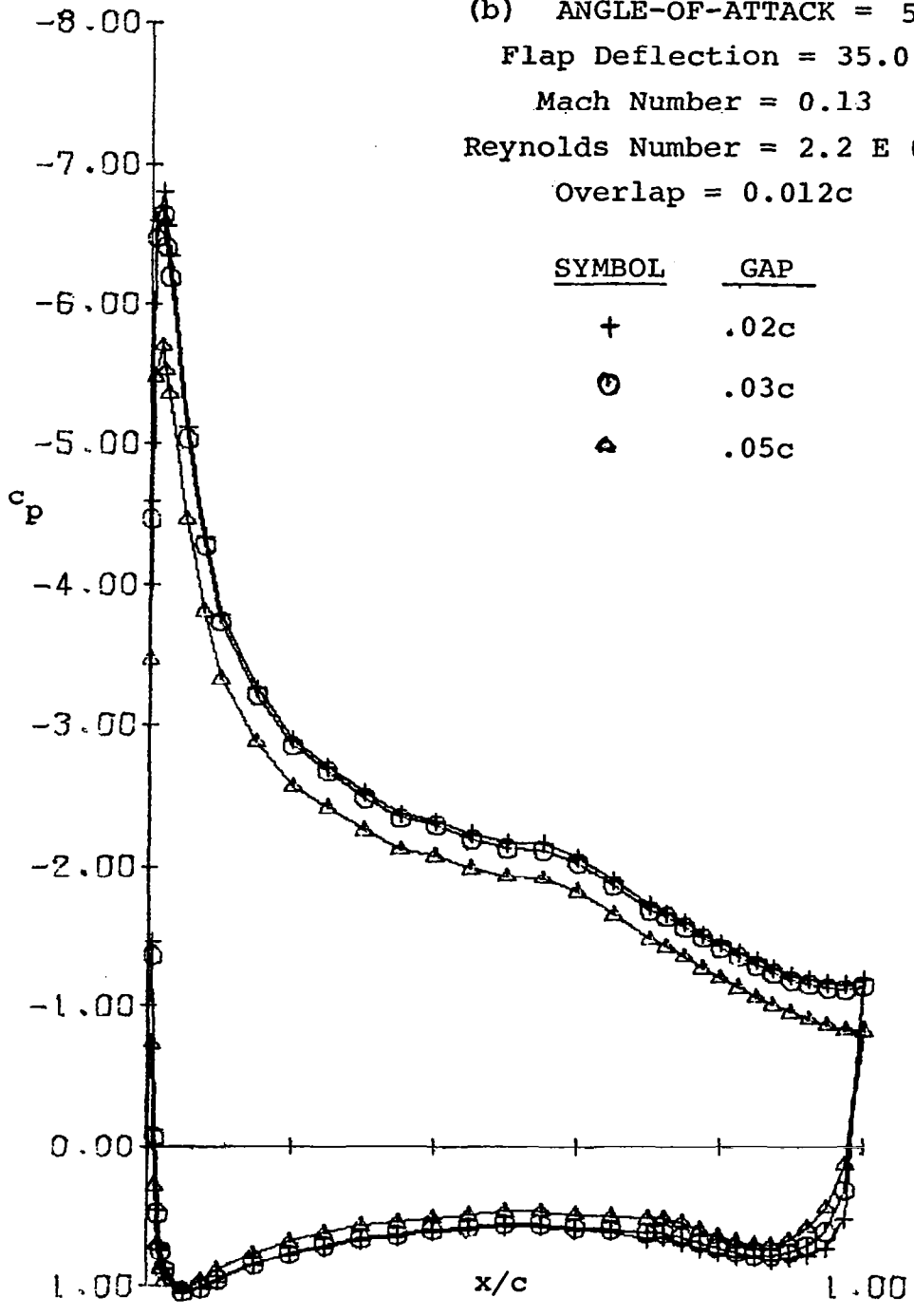


Figure 8 - Effects of Gap on Pressures.

(b) ANGLE-OF-ATTACK = 5.2°
 Flap Deflection = 35.0°
 Mach Number = 0.13
 Reynolds Number = $2.2 \text{ E } 06$
 Overlap = $0.012c$



<u>SYMBOL</u>	<u>GAP</u>
+	.02c
O	.03c
Δ	.05c

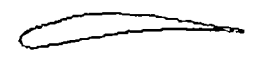
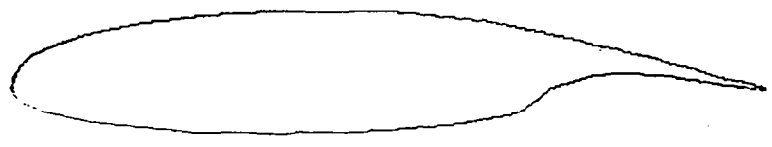
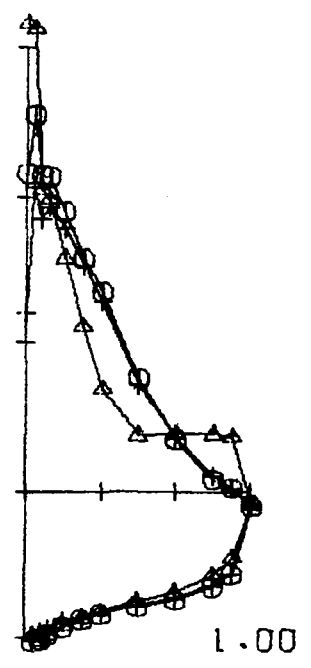


Figure 8- Continued.

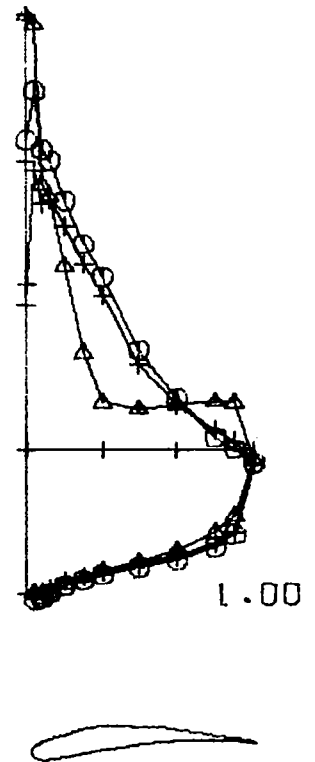
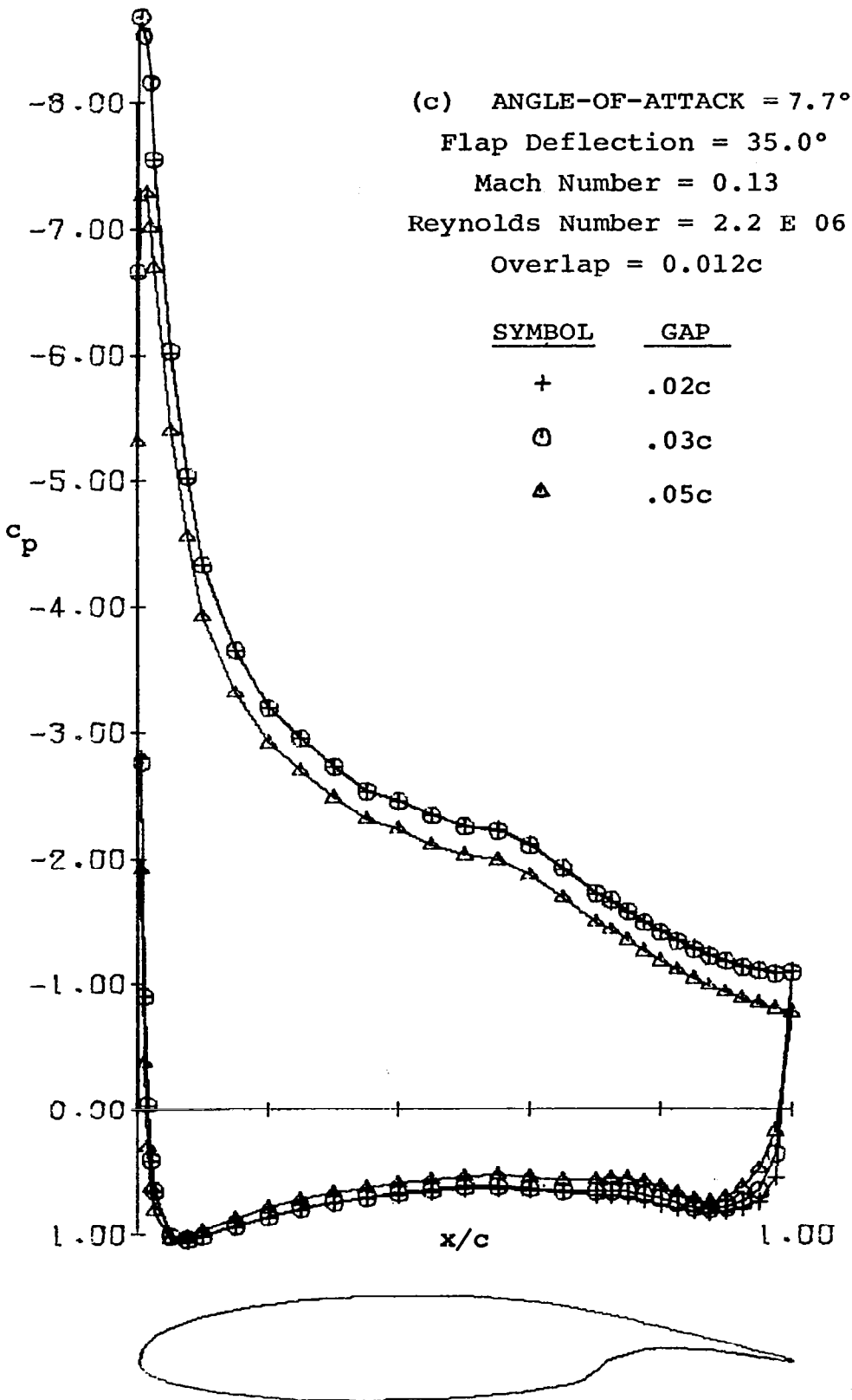


Figure 8 - Continued.

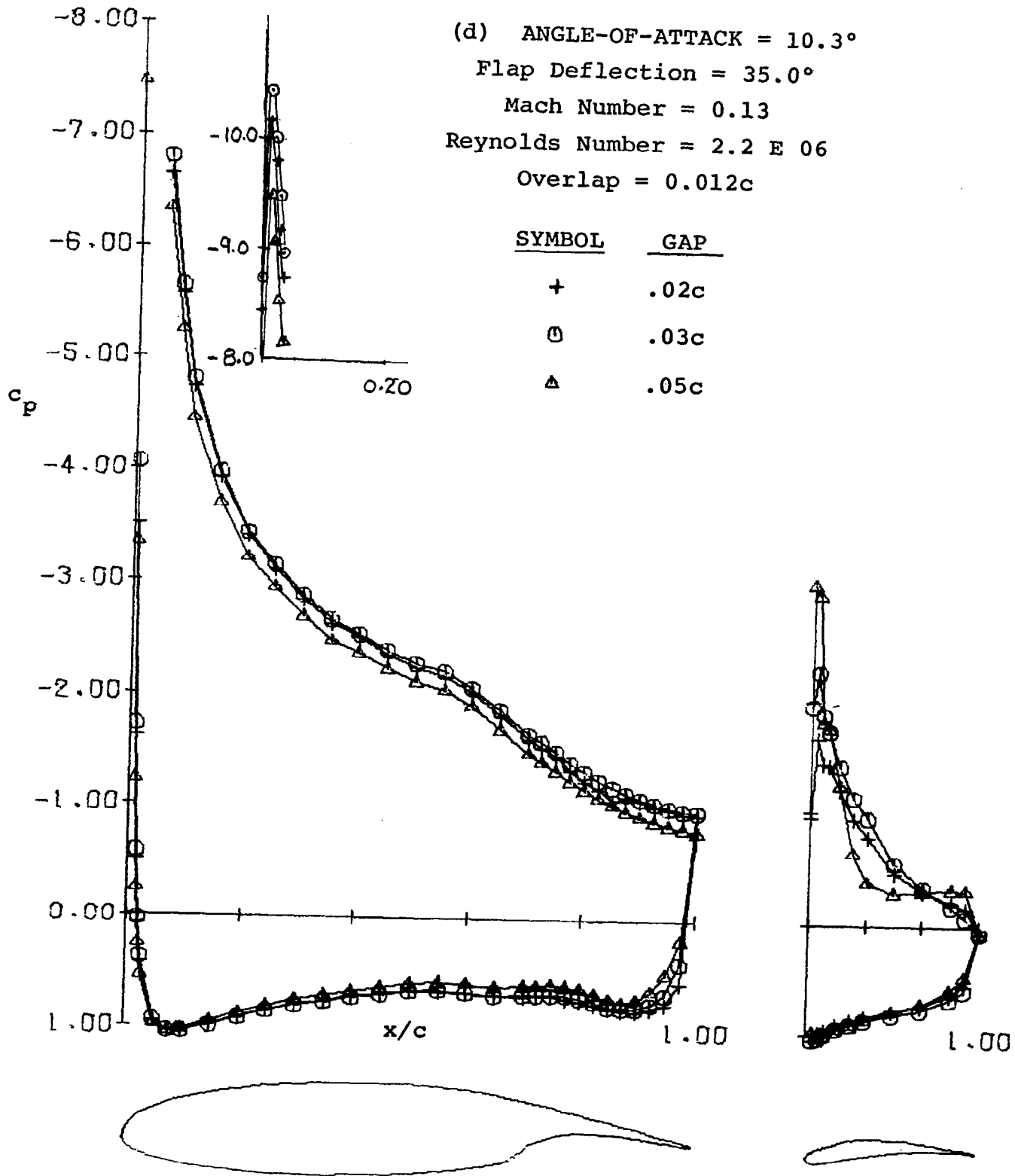


Figure 8 - Continued.

(e) ANGLE-OF-ATTACK = 12.7°
 Flap Deflection = 35.0°
 Mach Number = 0.13
 Reynolds Number = 2.2 E 06
 Overlap = 0.012c

<u>SYMBOL</u>	<u>GAP</u>
+	.02c
○	.03c
△	.05c

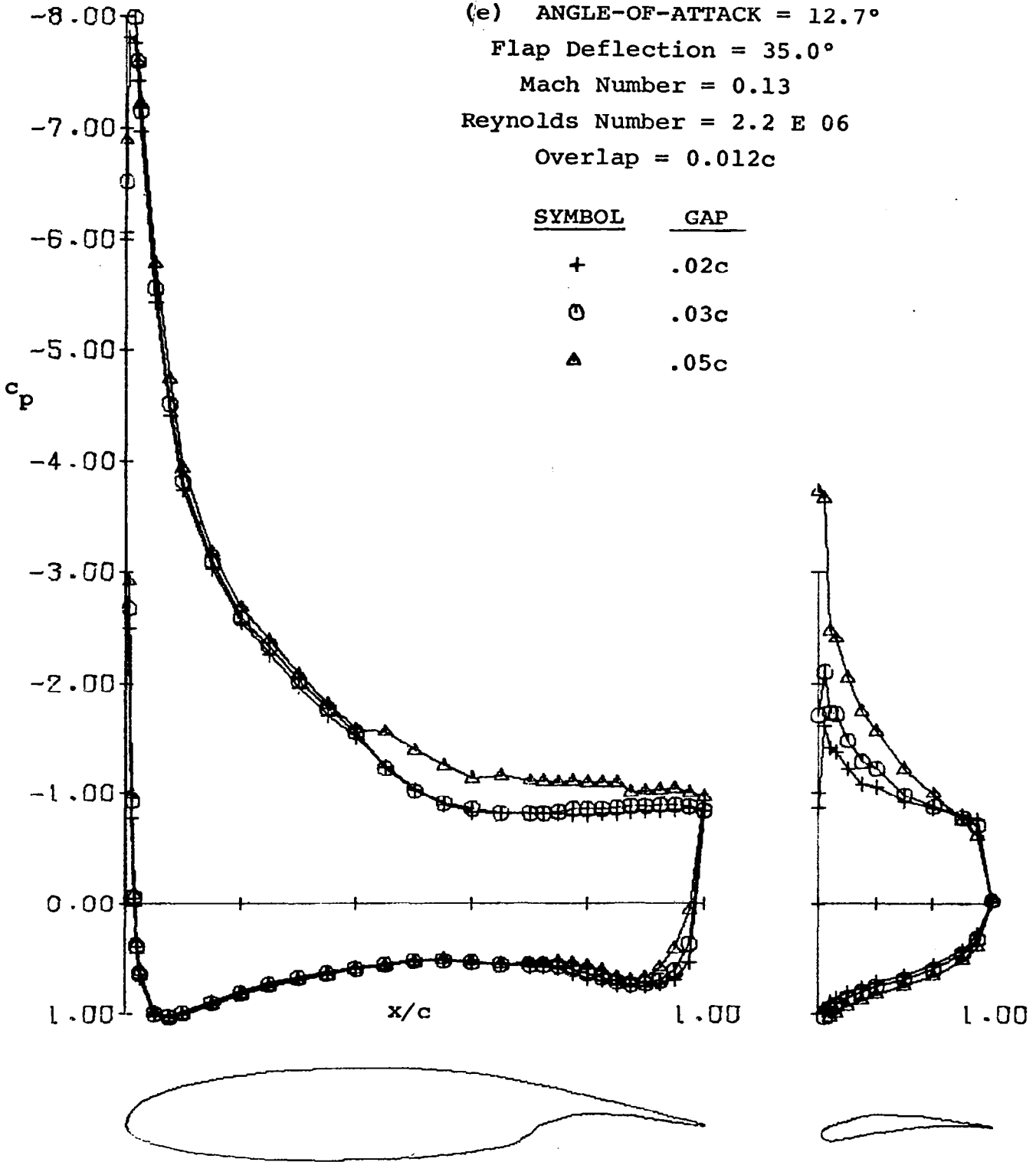


Figure 8- Concluded.

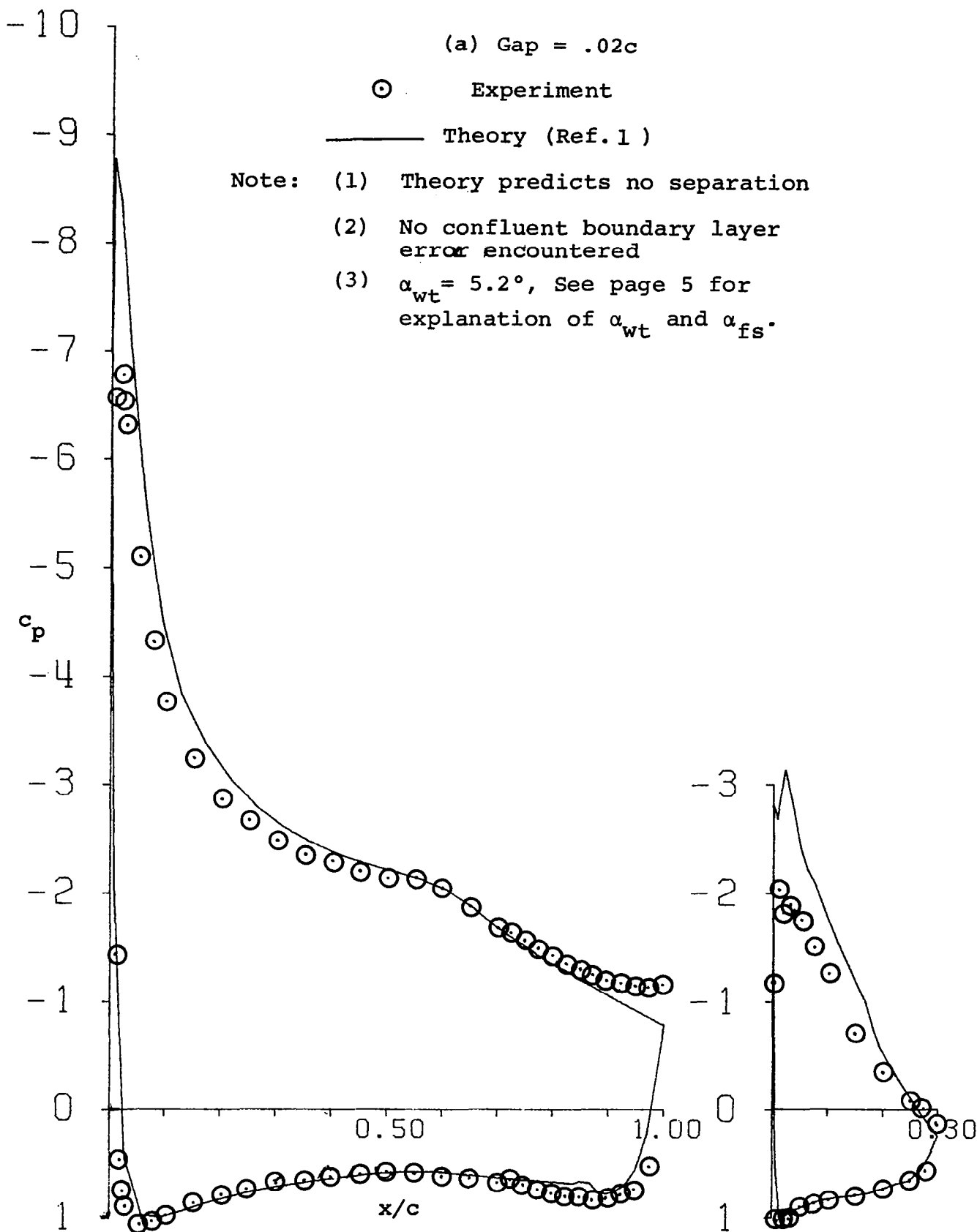


Figure 9 - Theoretical and Experimental Pressures, $\alpha_{fs} = 6.4^\circ$.

(b) Gap = .03c

⊙ Experiment

— Theory (Ref. 1)

- Note: (1) Theory predicts no separation.
(2) No confluent boundary layer error encountered
(3) $\alpha_{wt} = 5.2^\circ$, See page 5 for explanation of α_{wt} and α_{fs} .

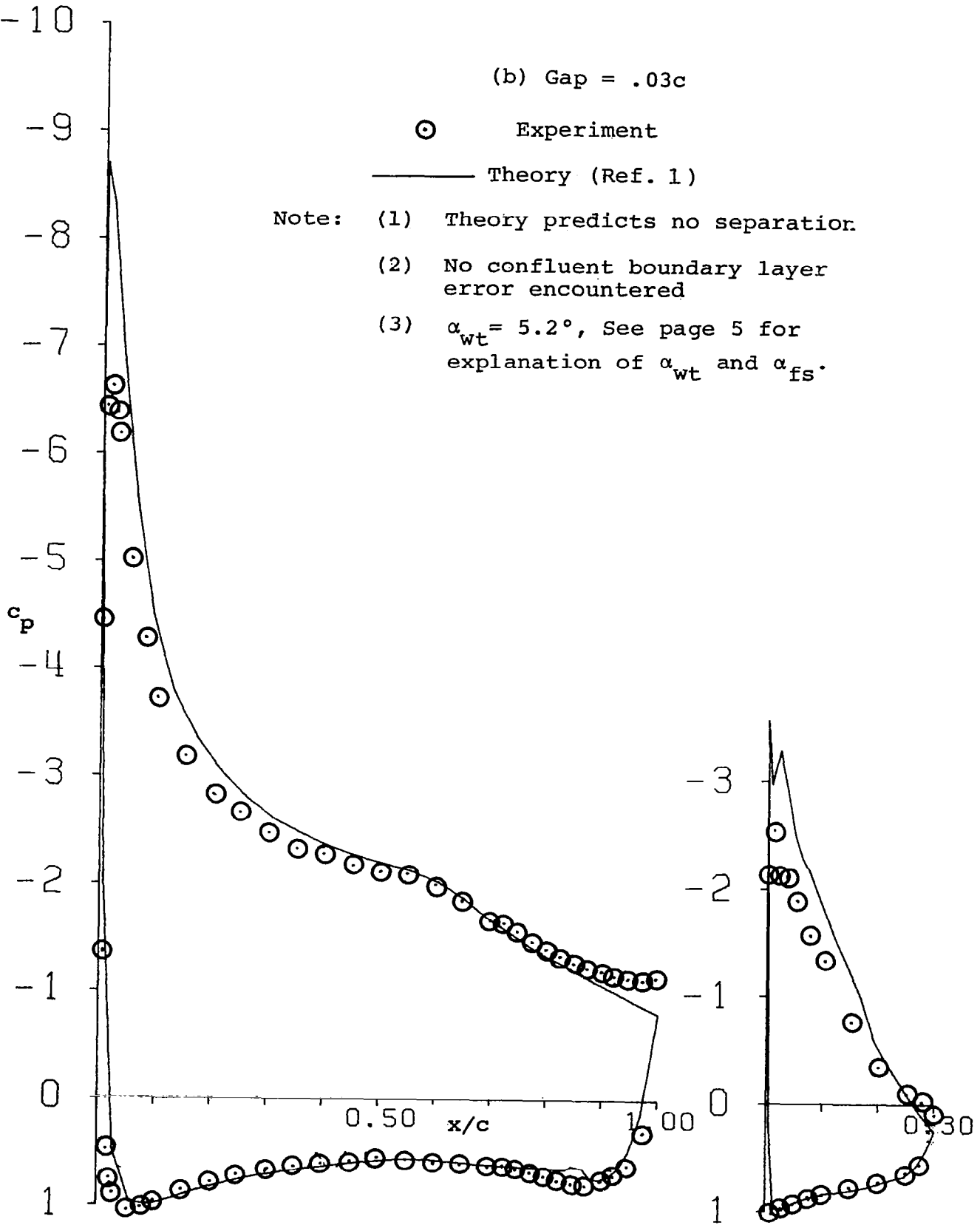


Figure 9 - Continued.

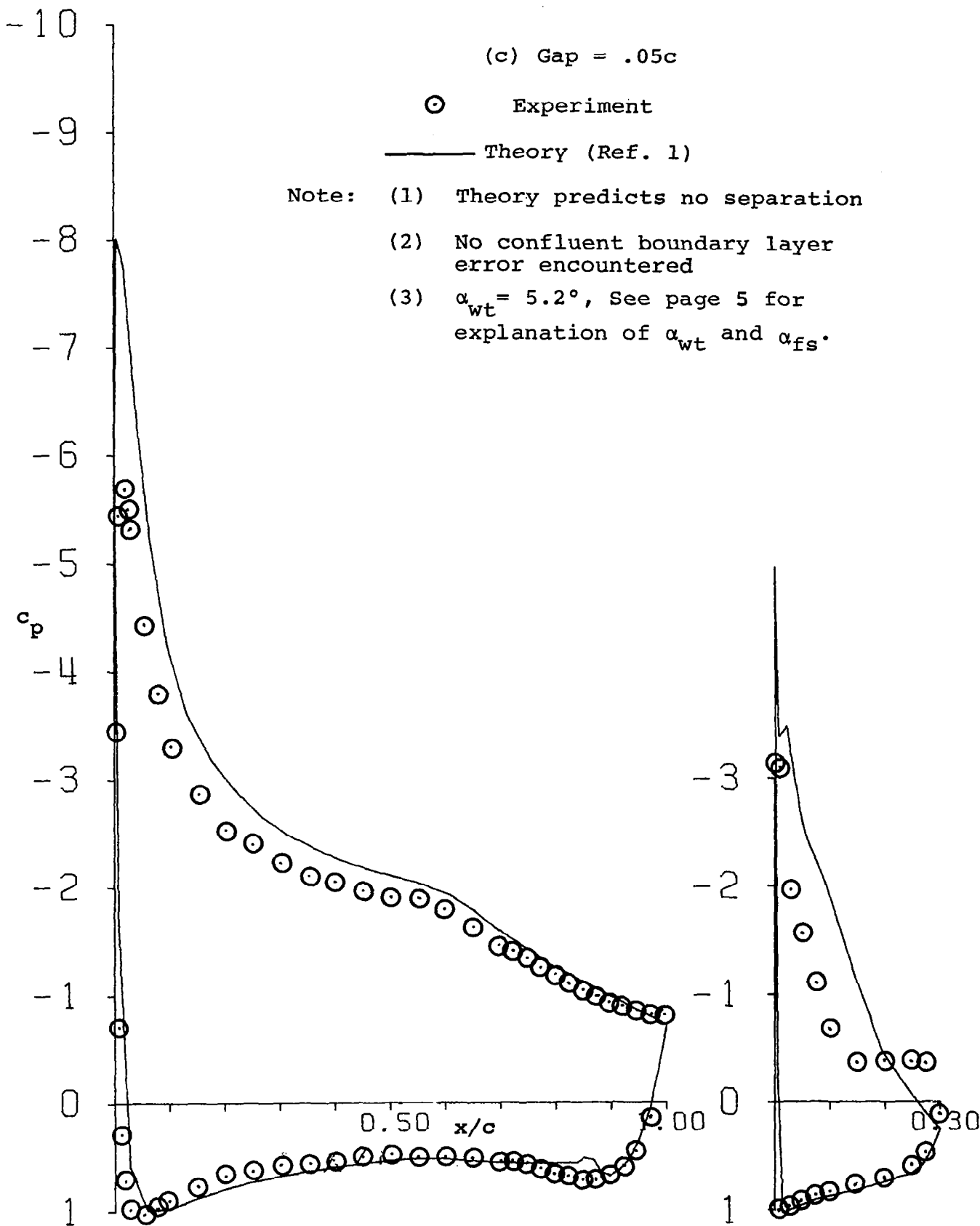


Figure 9 - Concluded.

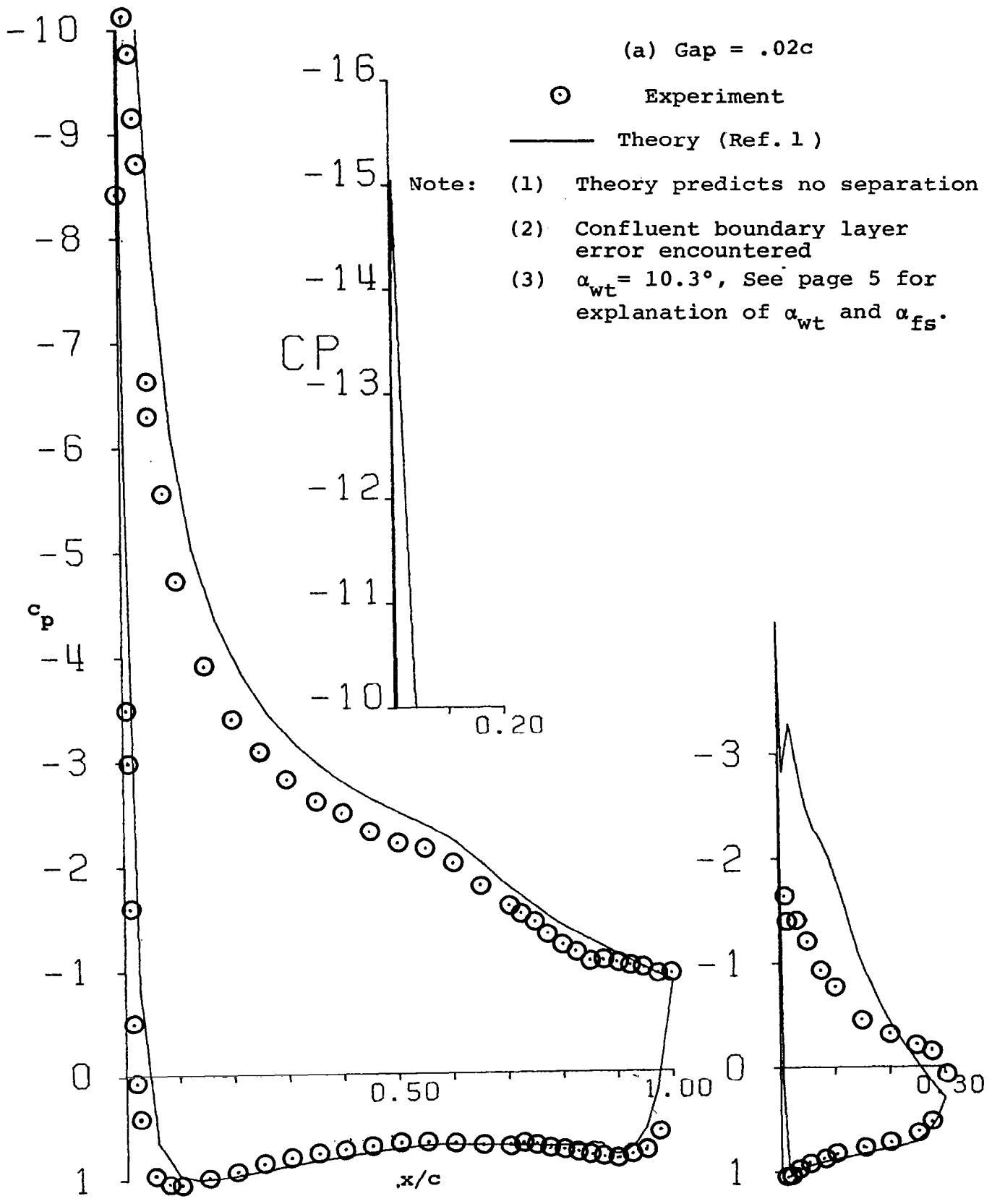


Figure 10- Theoretical and Experimental Pressures, $\alpha_{fs} = 12.1^\circ$.

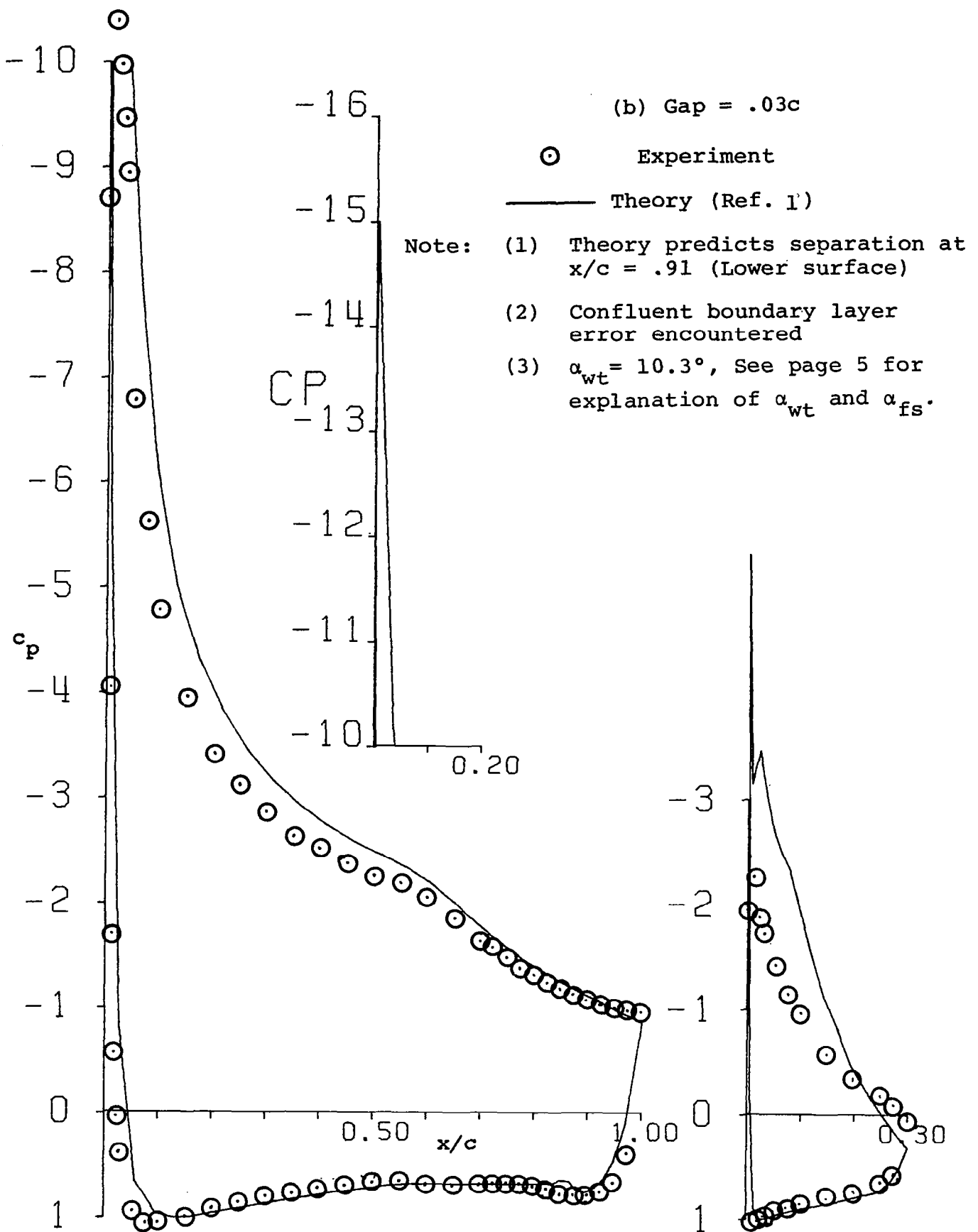


Figure 10- Continued.

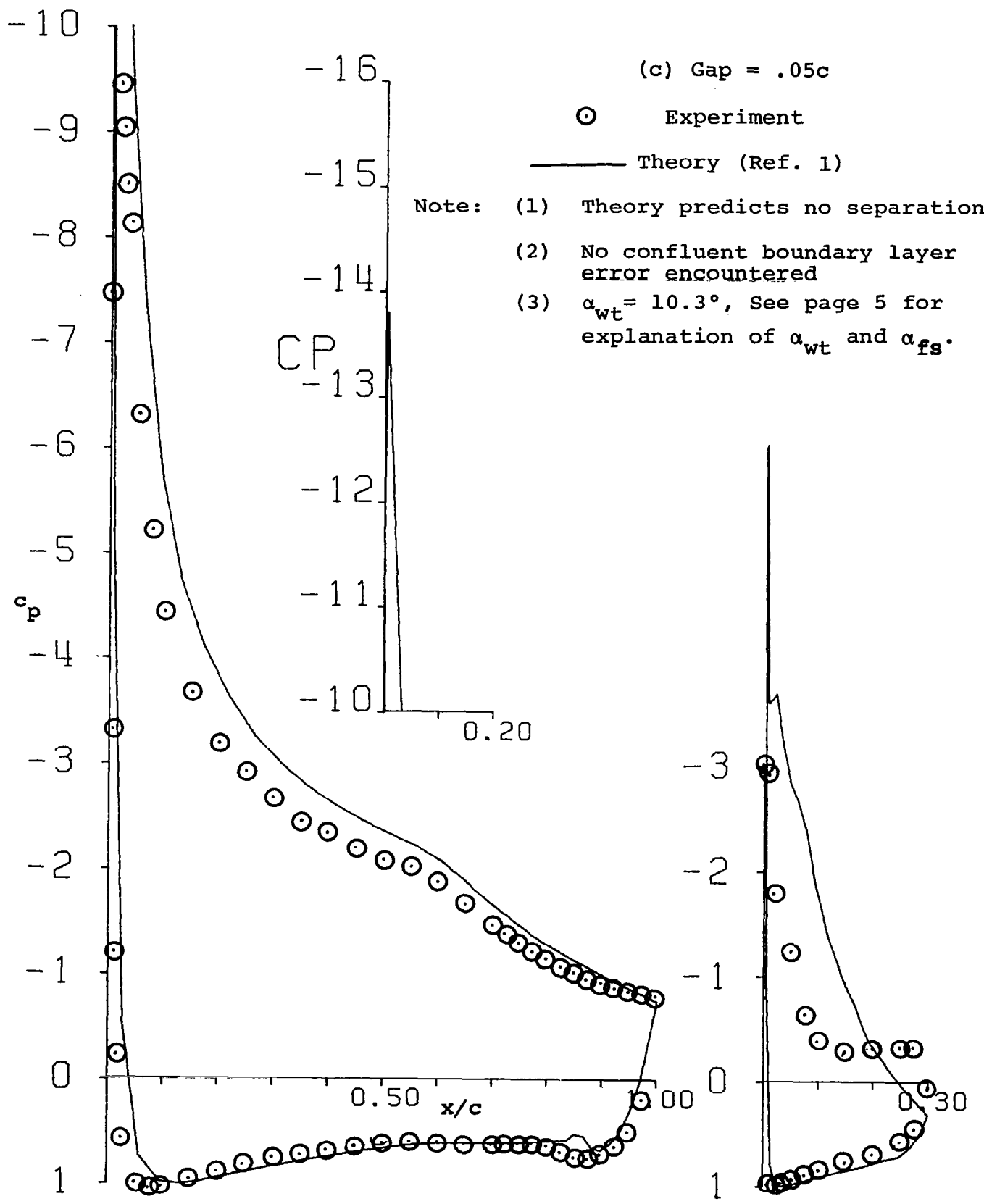


Figure 10- Concluded.

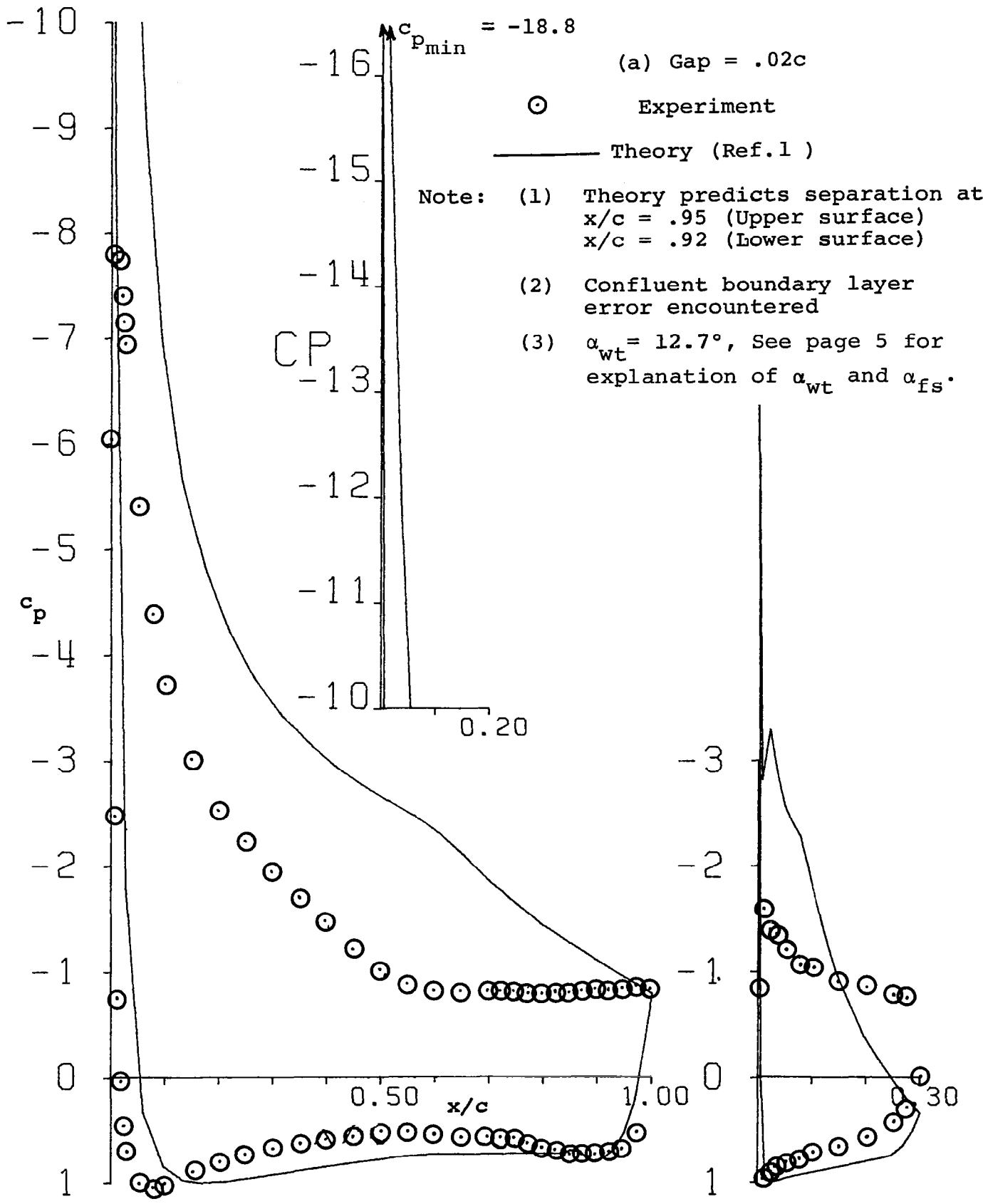


Figure 11- Theoretical and Experimental Pressures, $\alpha_{fs} = 15.1^\circ$.

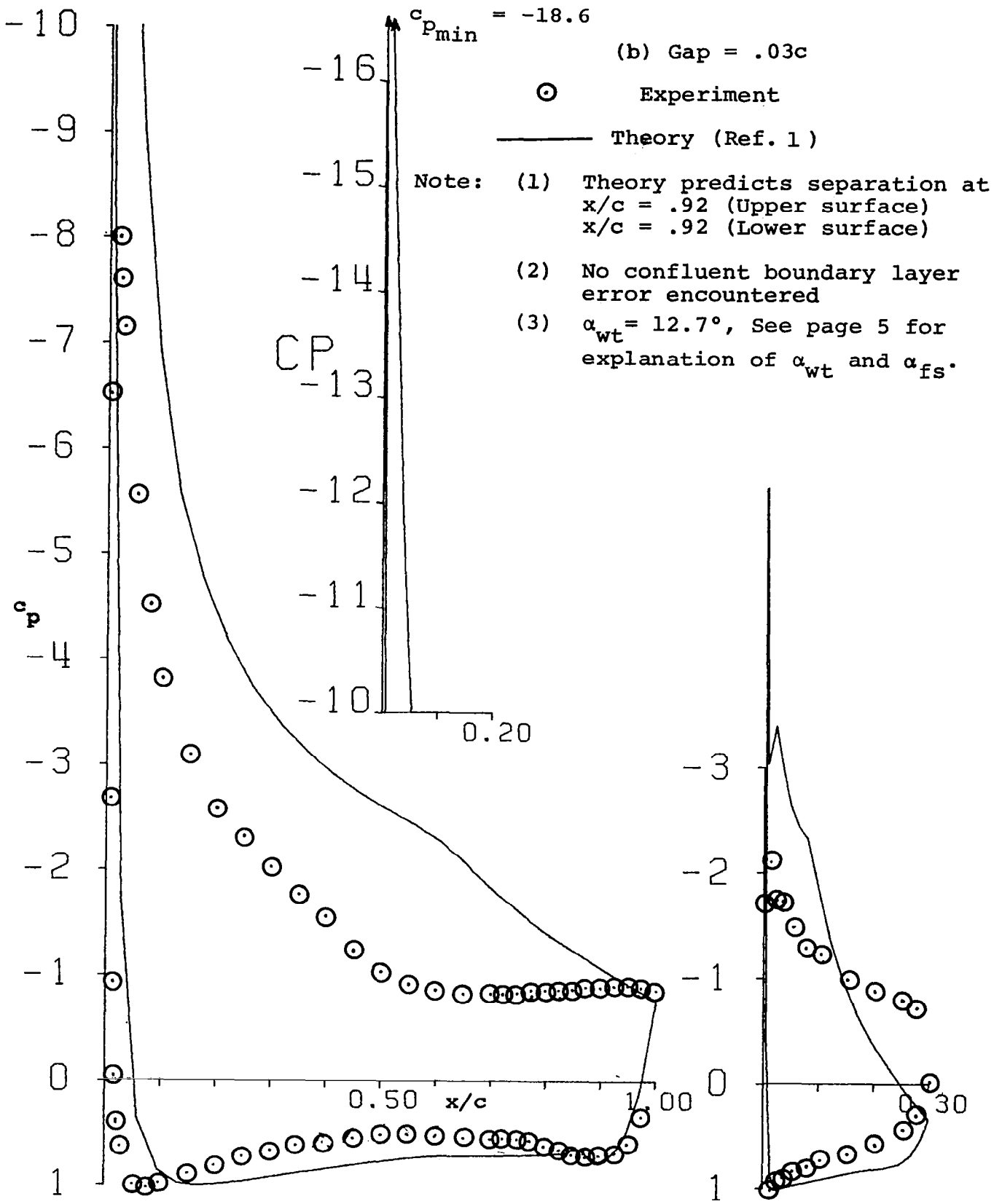


Figure 11 - Continued.

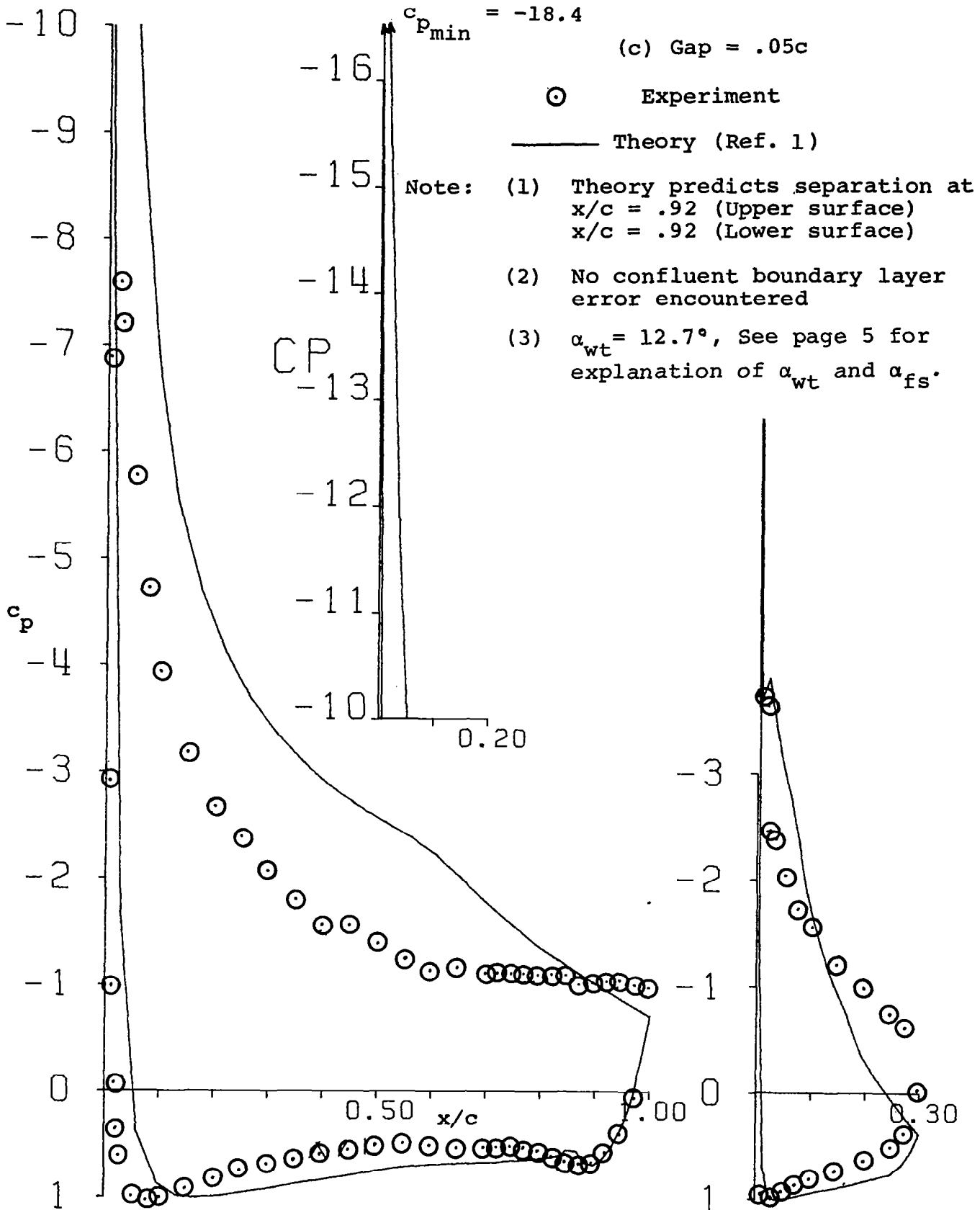
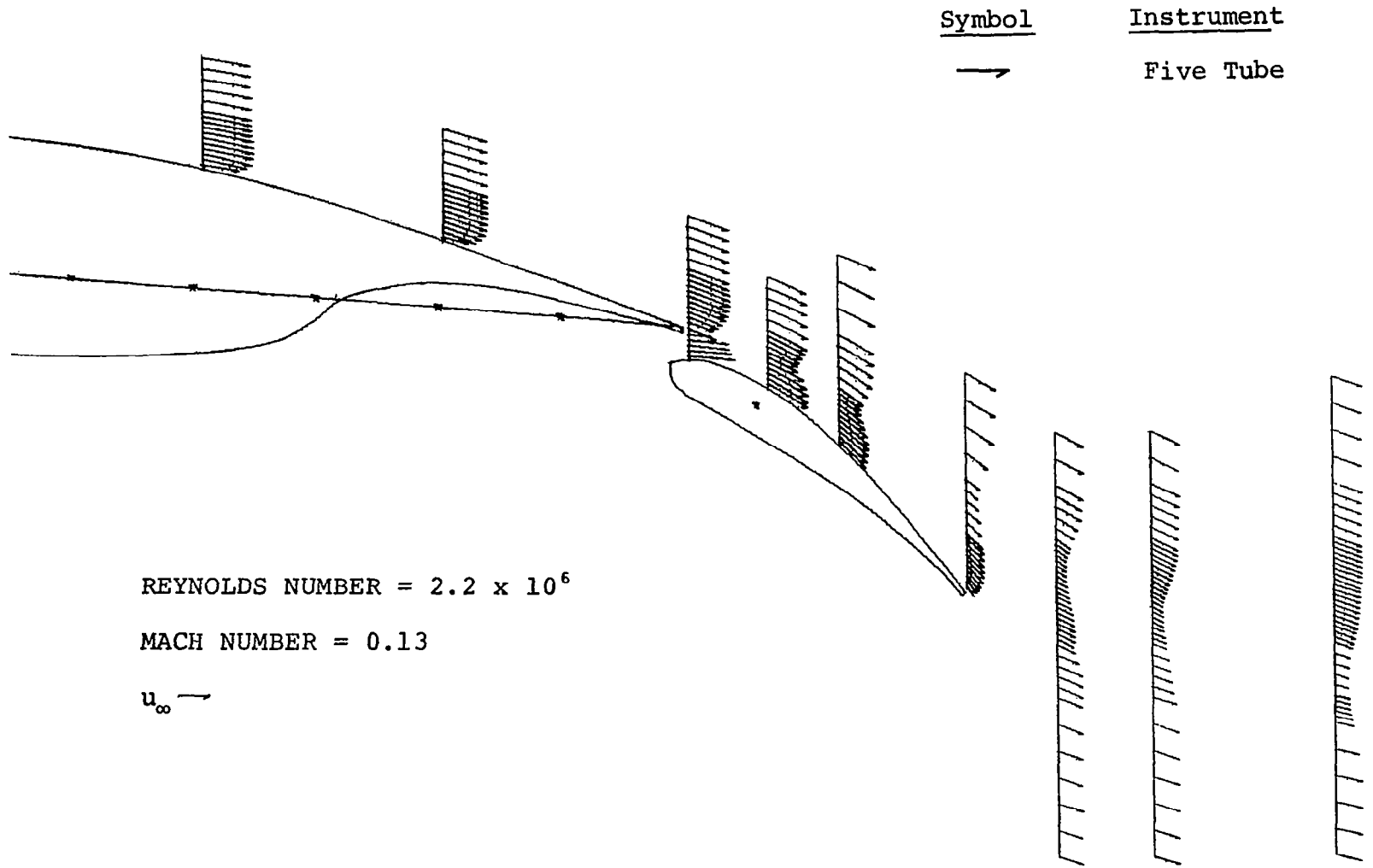
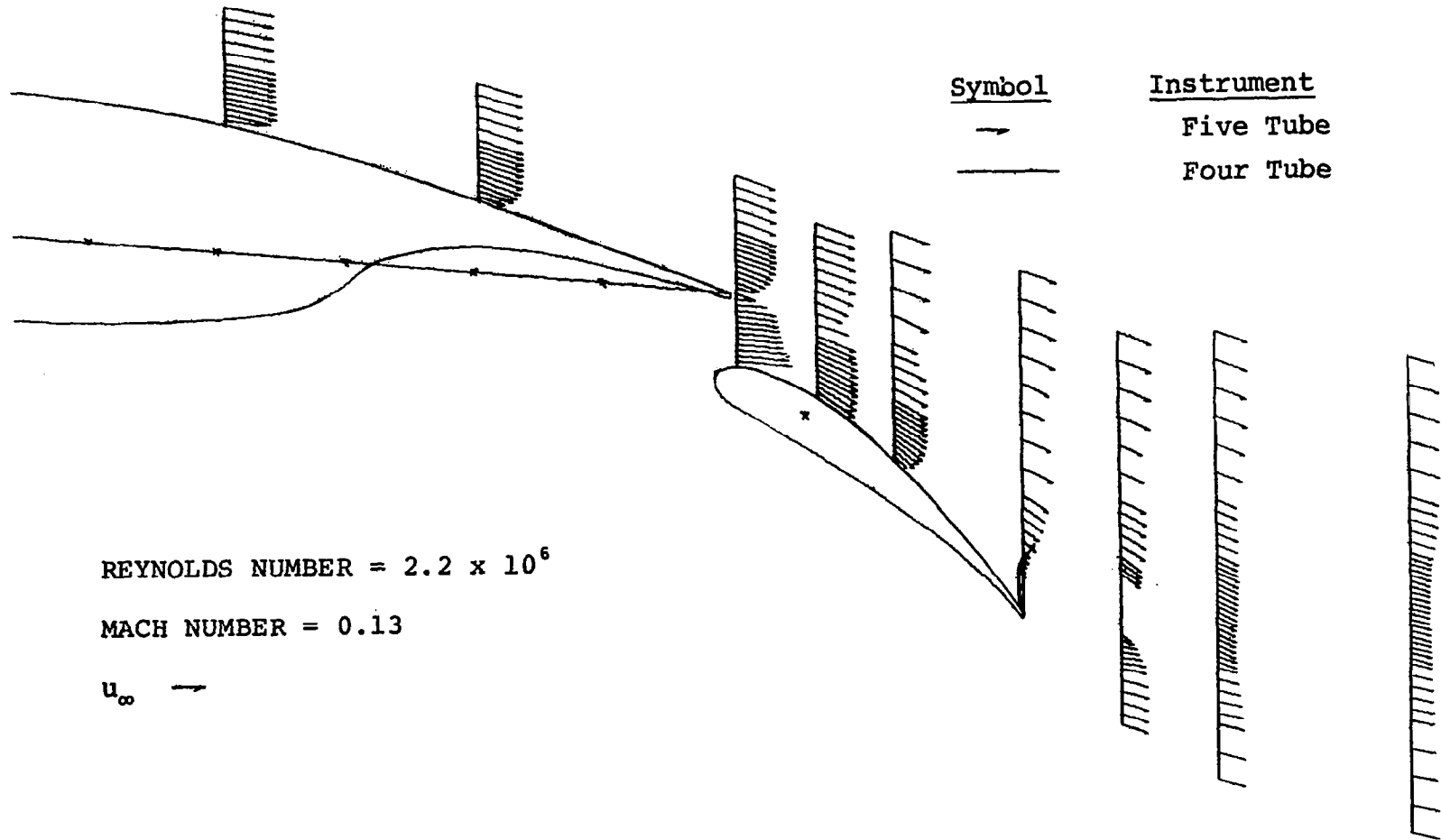


Figure 11 - Concluded.



a) Gap = .02 c

Figure 12- Experimental Velocity Profiles, $\alpha = 5.2^\circ$



c) Gap = .05 c

Figure 12 - Concluded.

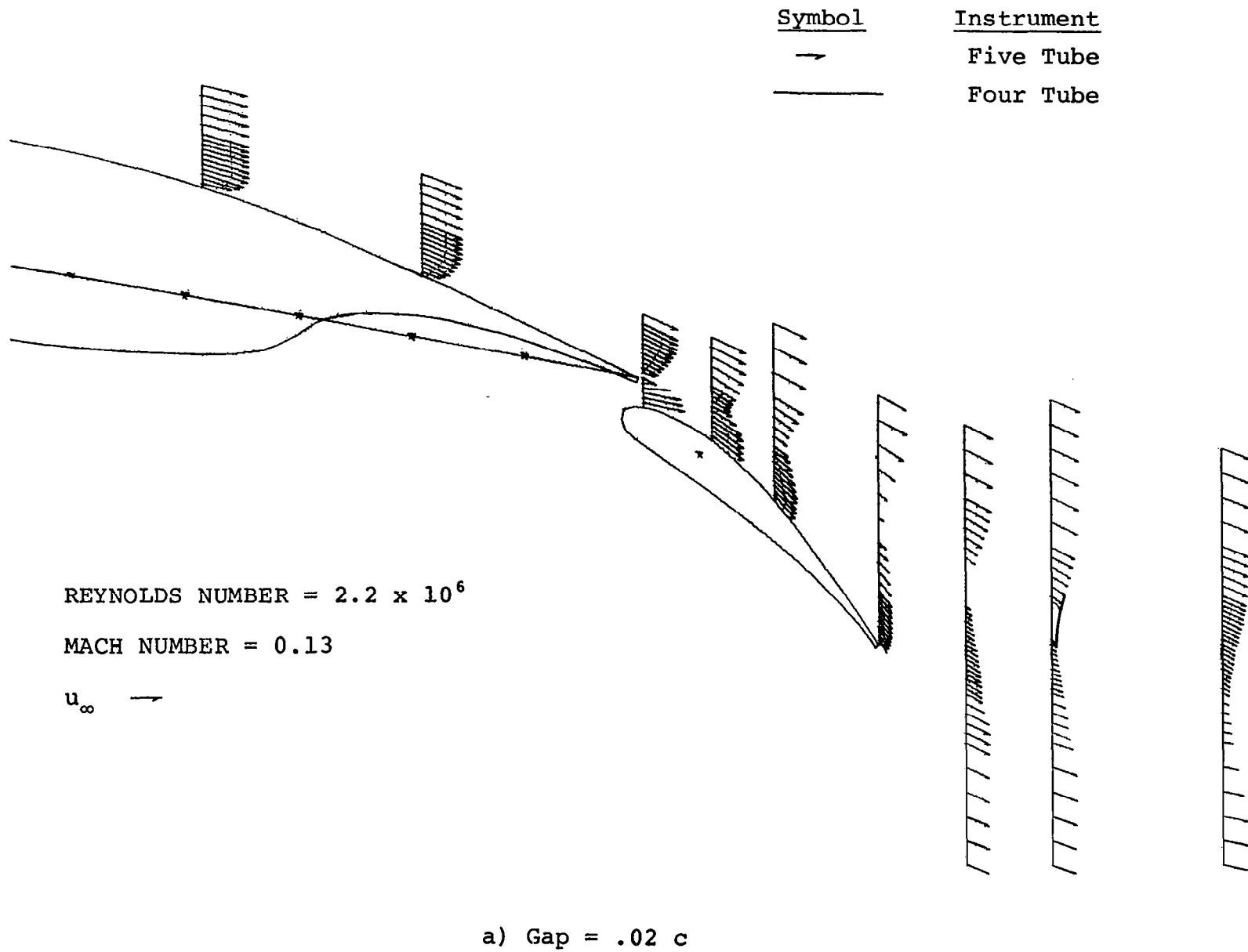


Figure 13- Experimental Velocity Profiles, $\alpha = 10.3^\circ$

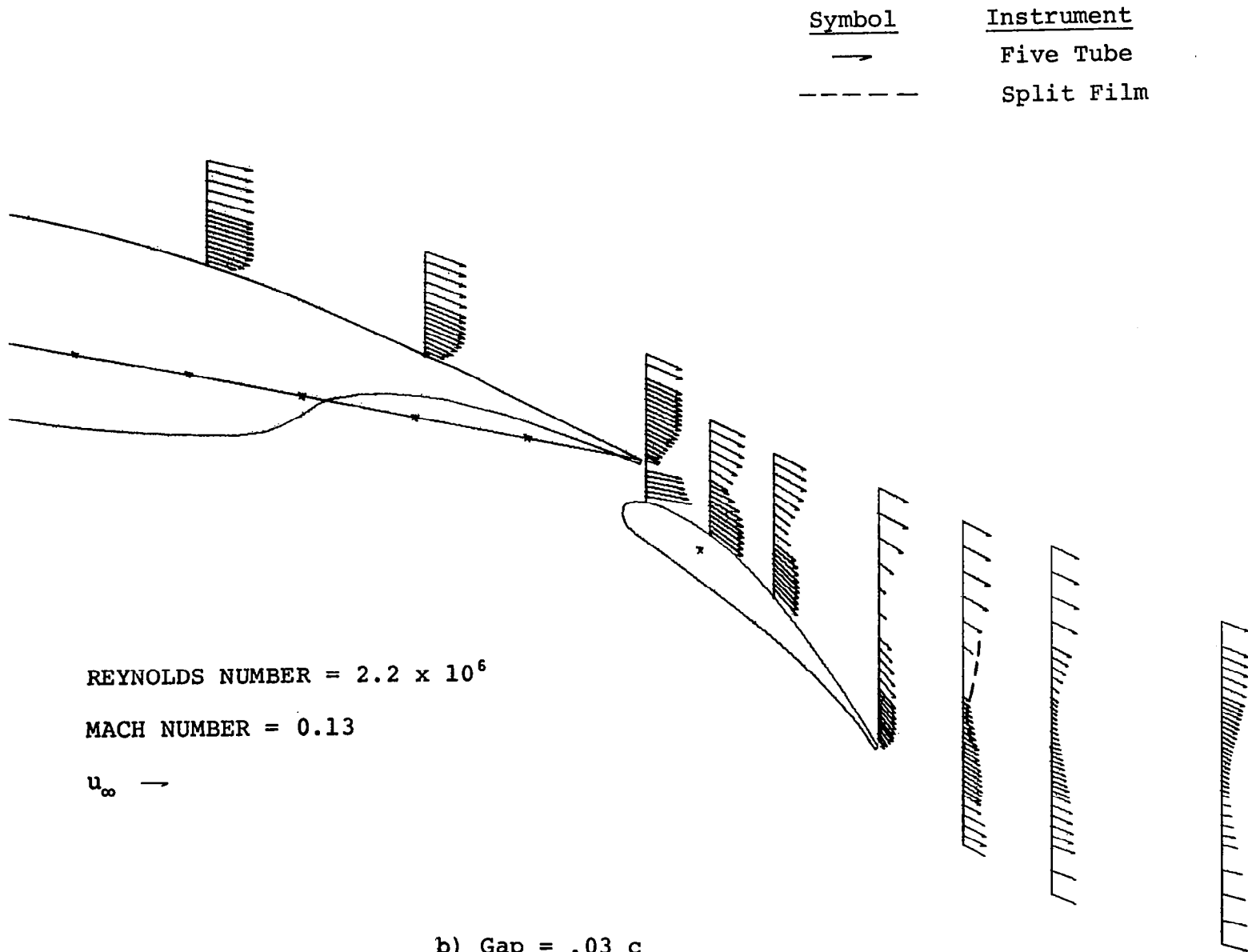
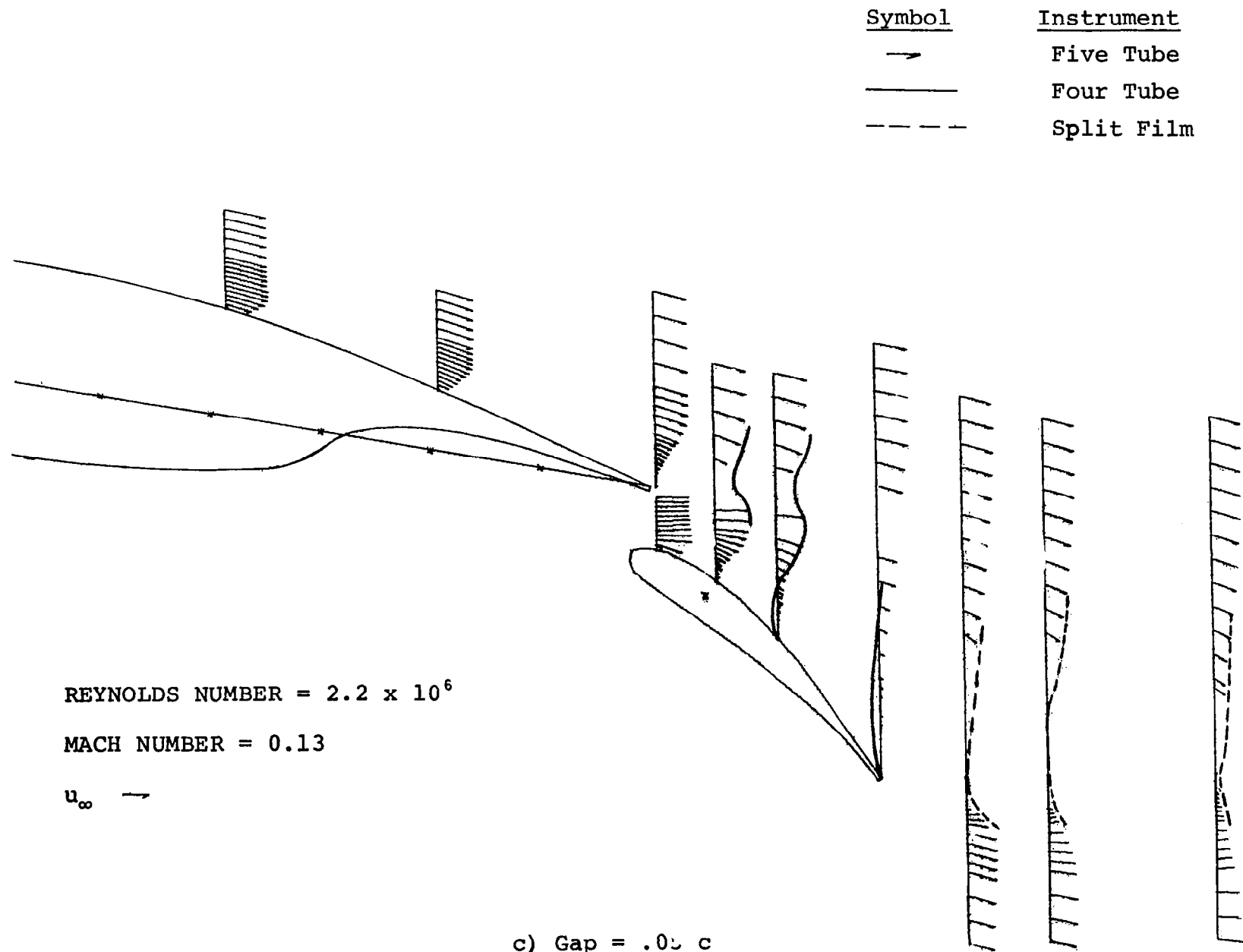


Figure 13 - Continued.



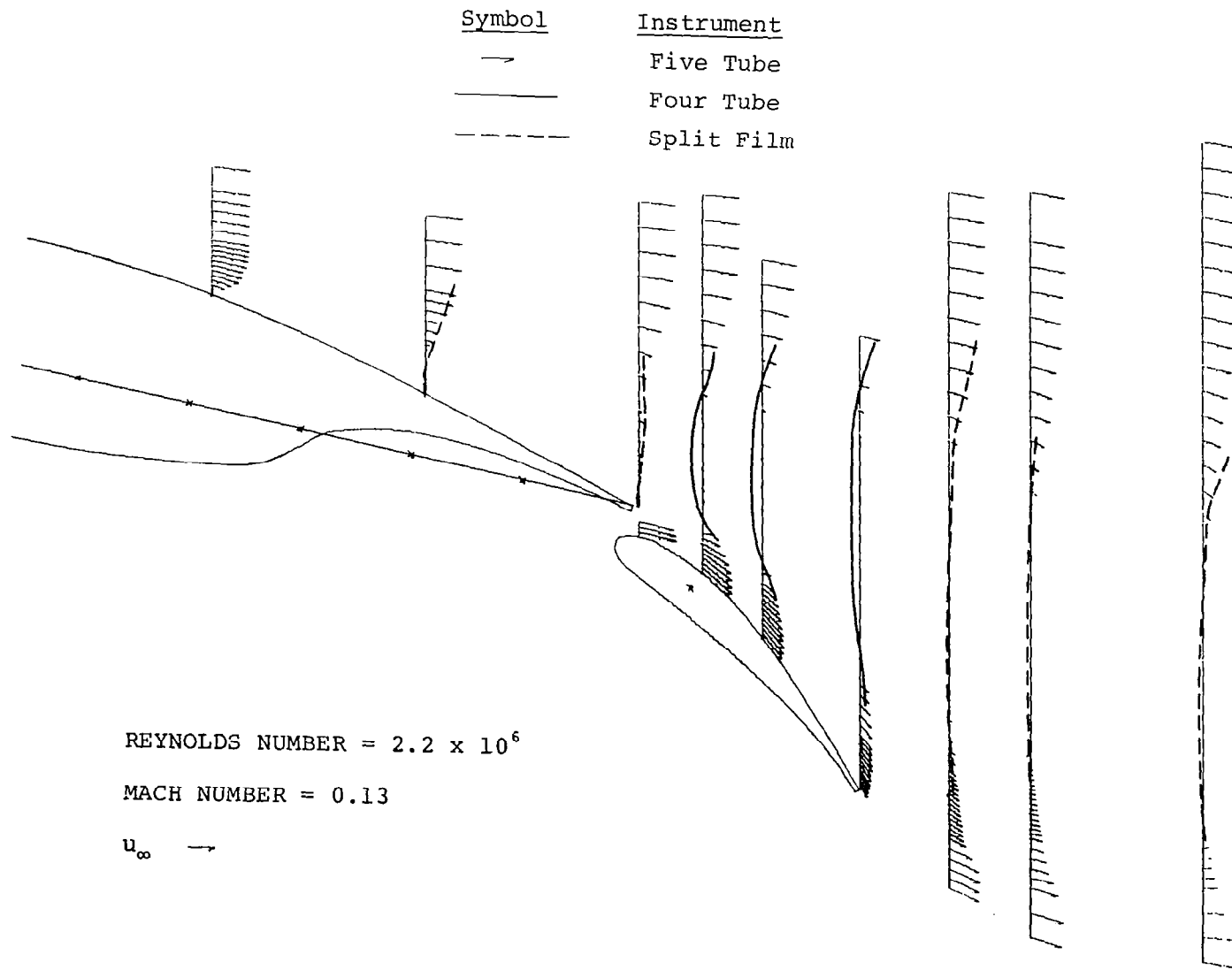
REYNOLDS NUMBER = 2.2×10^6

MACH NUMBER = 0.13

u_∞ →

c) Gap = .05 c

Figure 13 - Concluded.



a) Gap = .02 c

Figure 14- Experimental Velocity Profiles, $\alpha = 12.7^\circ$.

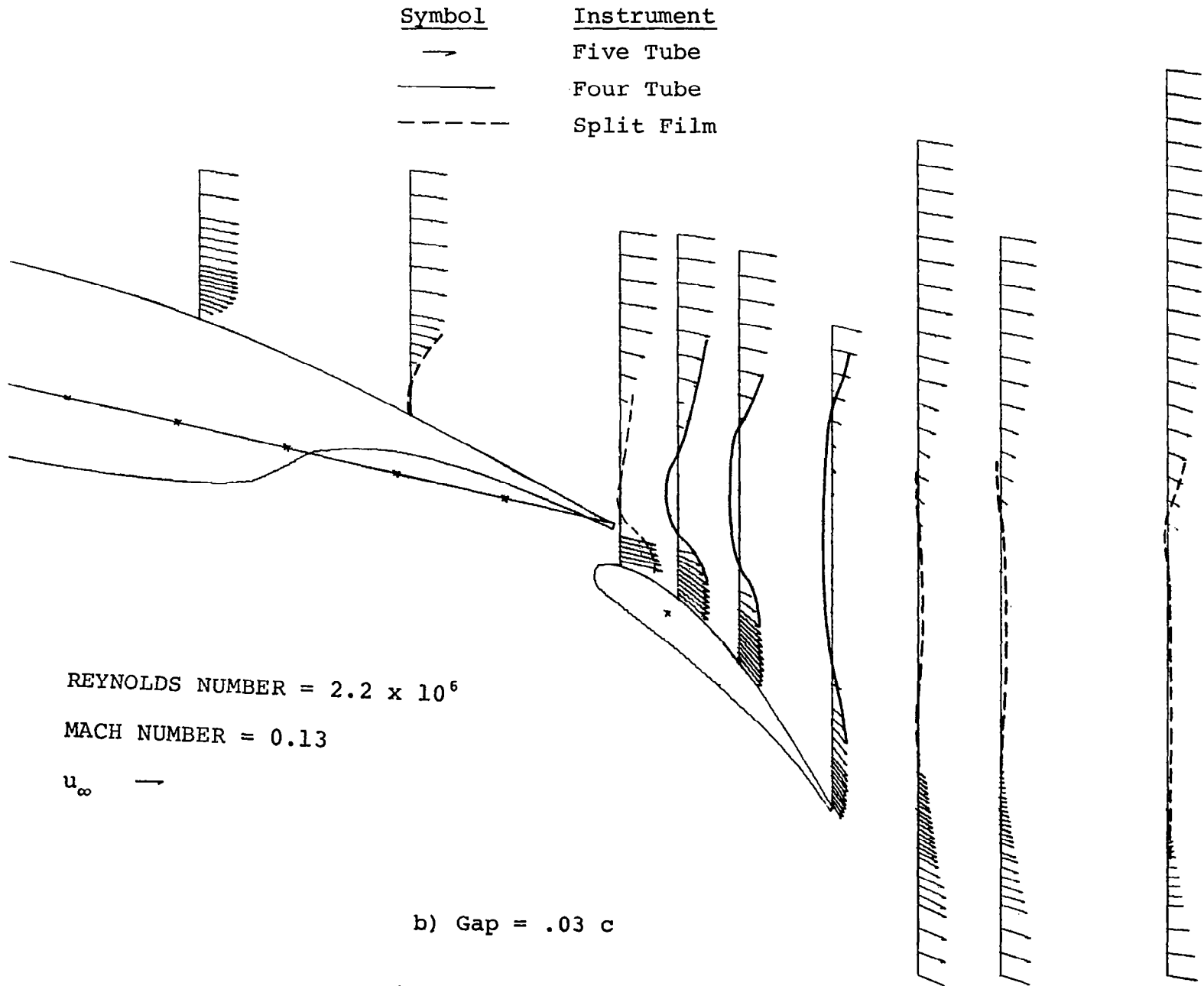


Figure 14- Continued.

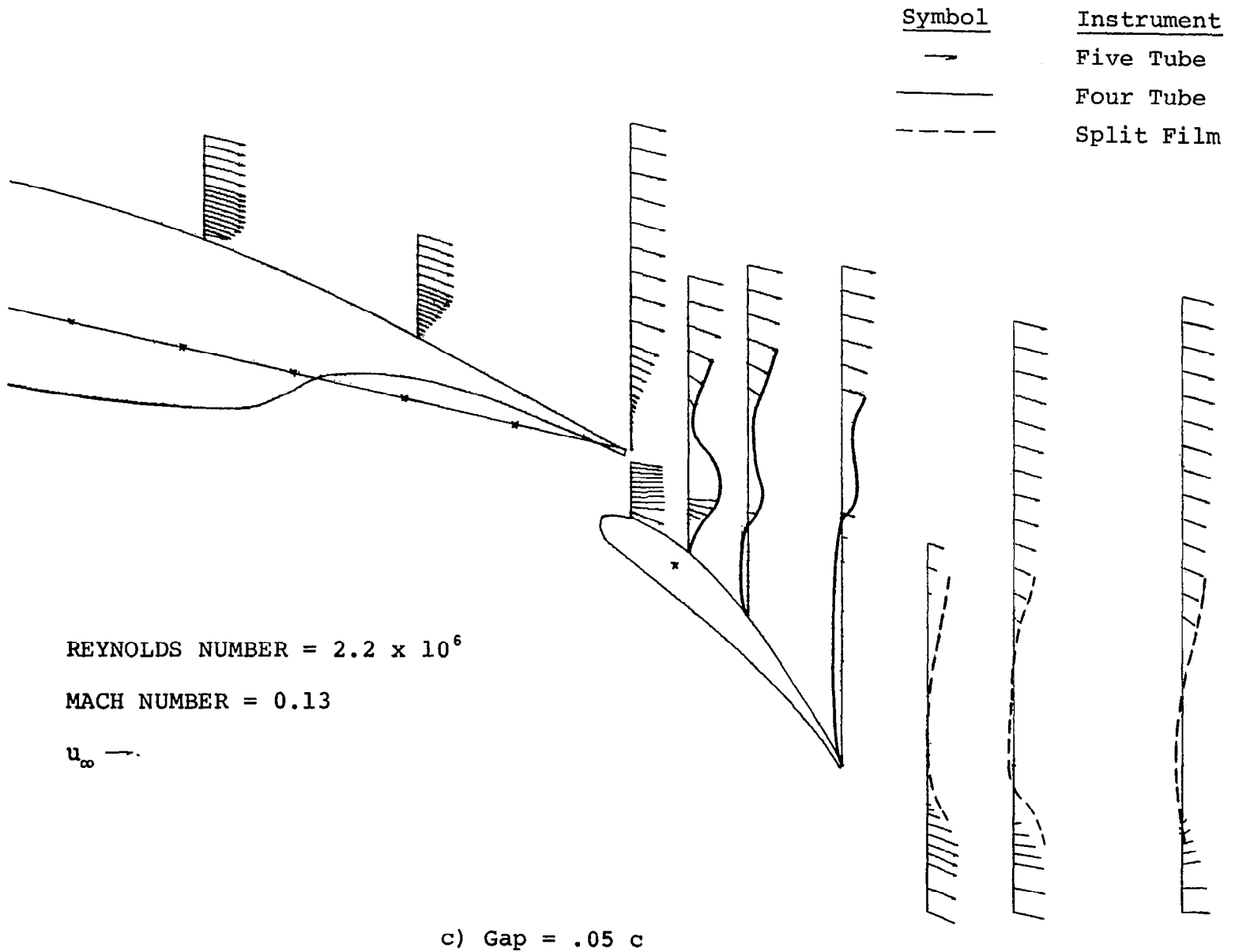
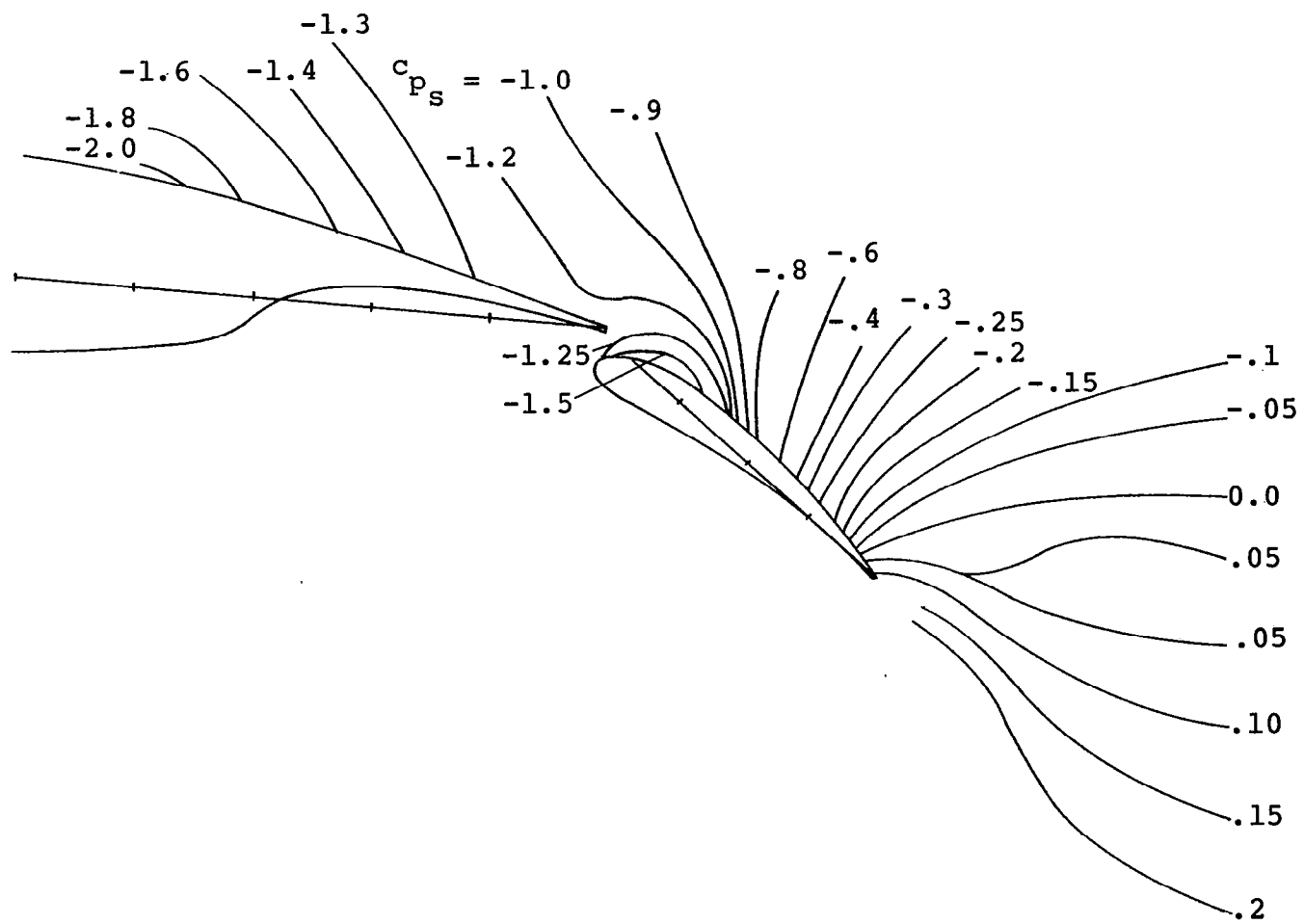
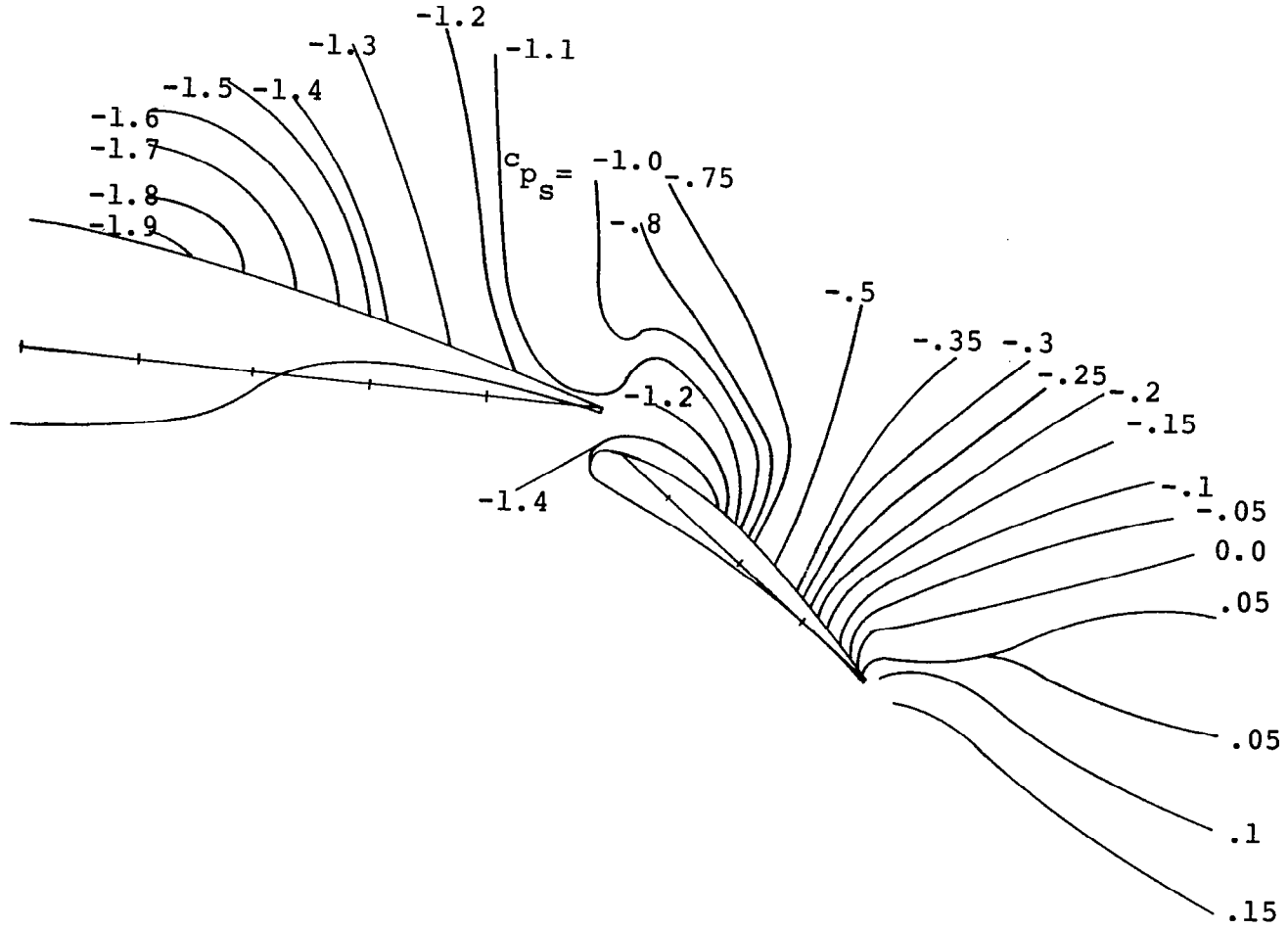


Figure 14 - Concluded.



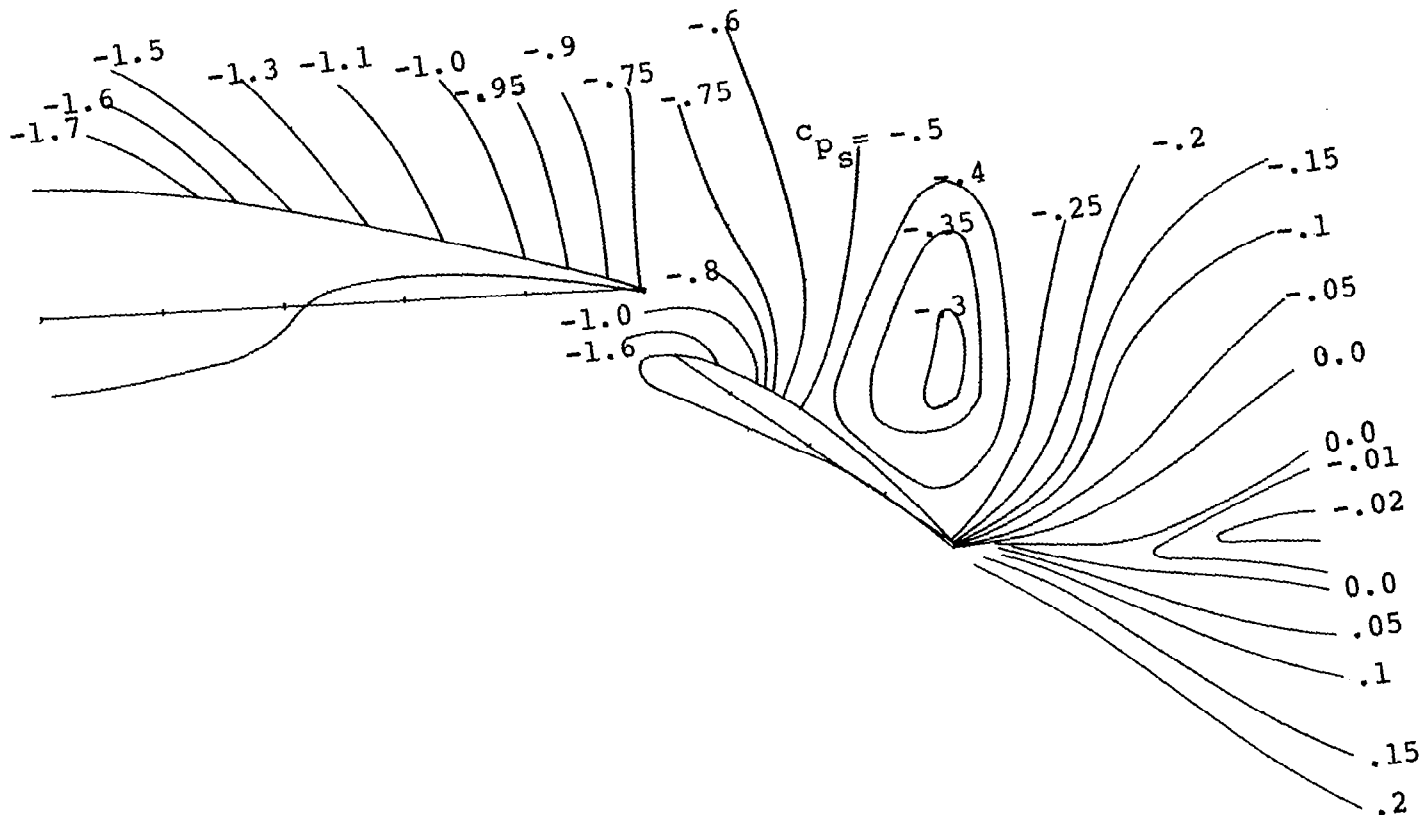
a) Gap = .02 c

Figure 15 - Static Pressure Contours, $\alpha = 5.2^\circ$

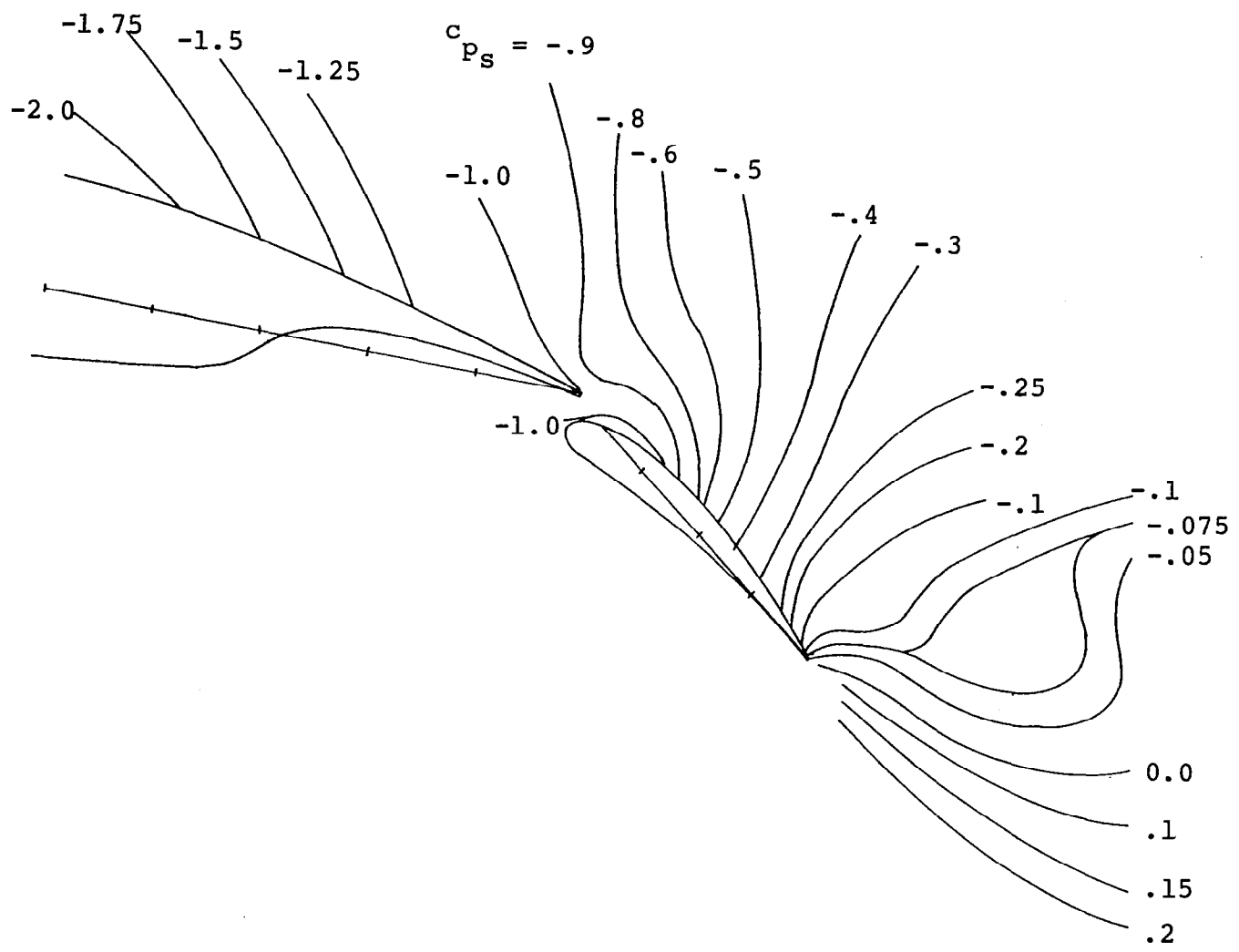


b) Gap = .03 c

Figure 15- Continued.

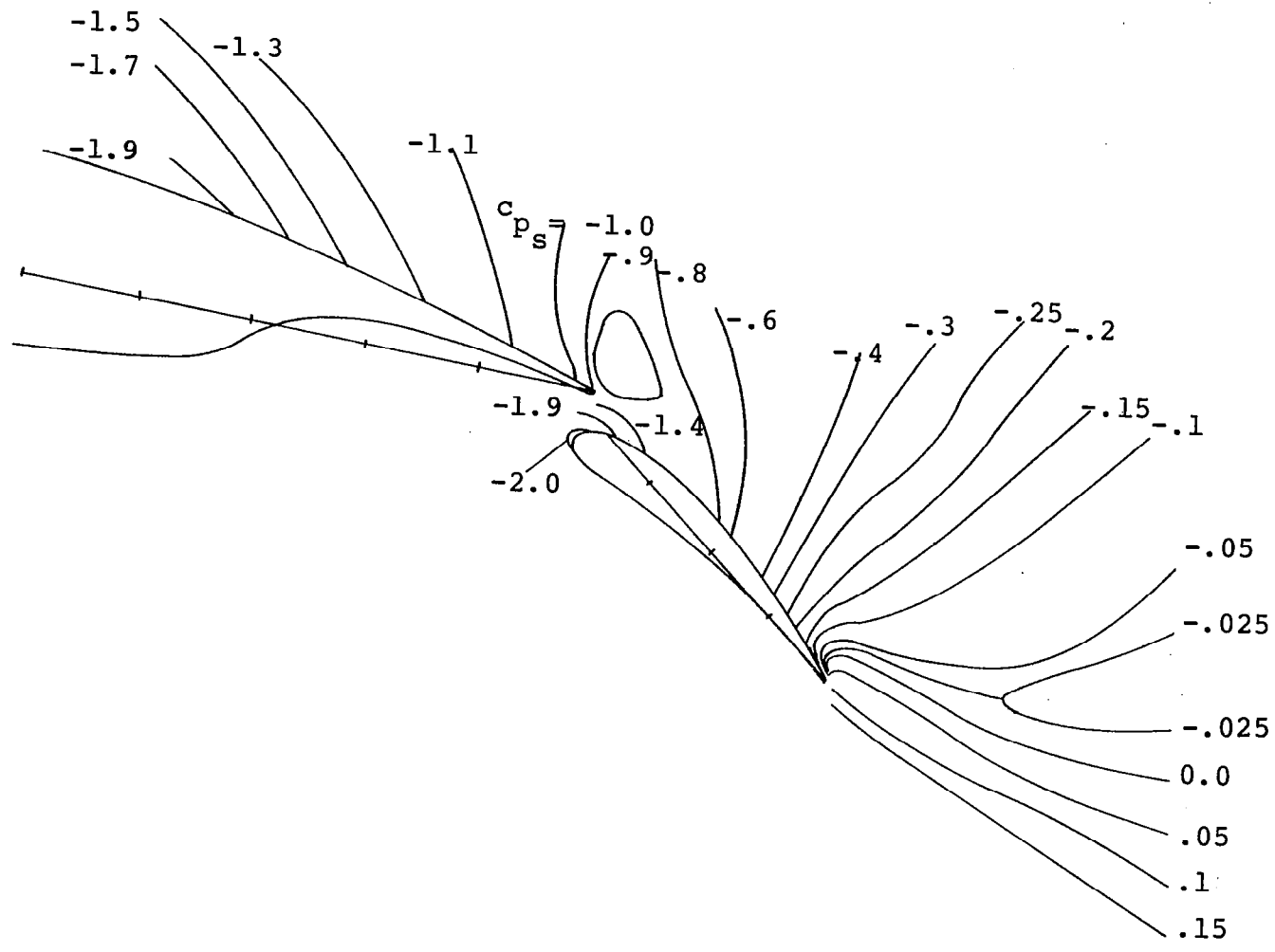


c) Gap = .05 c



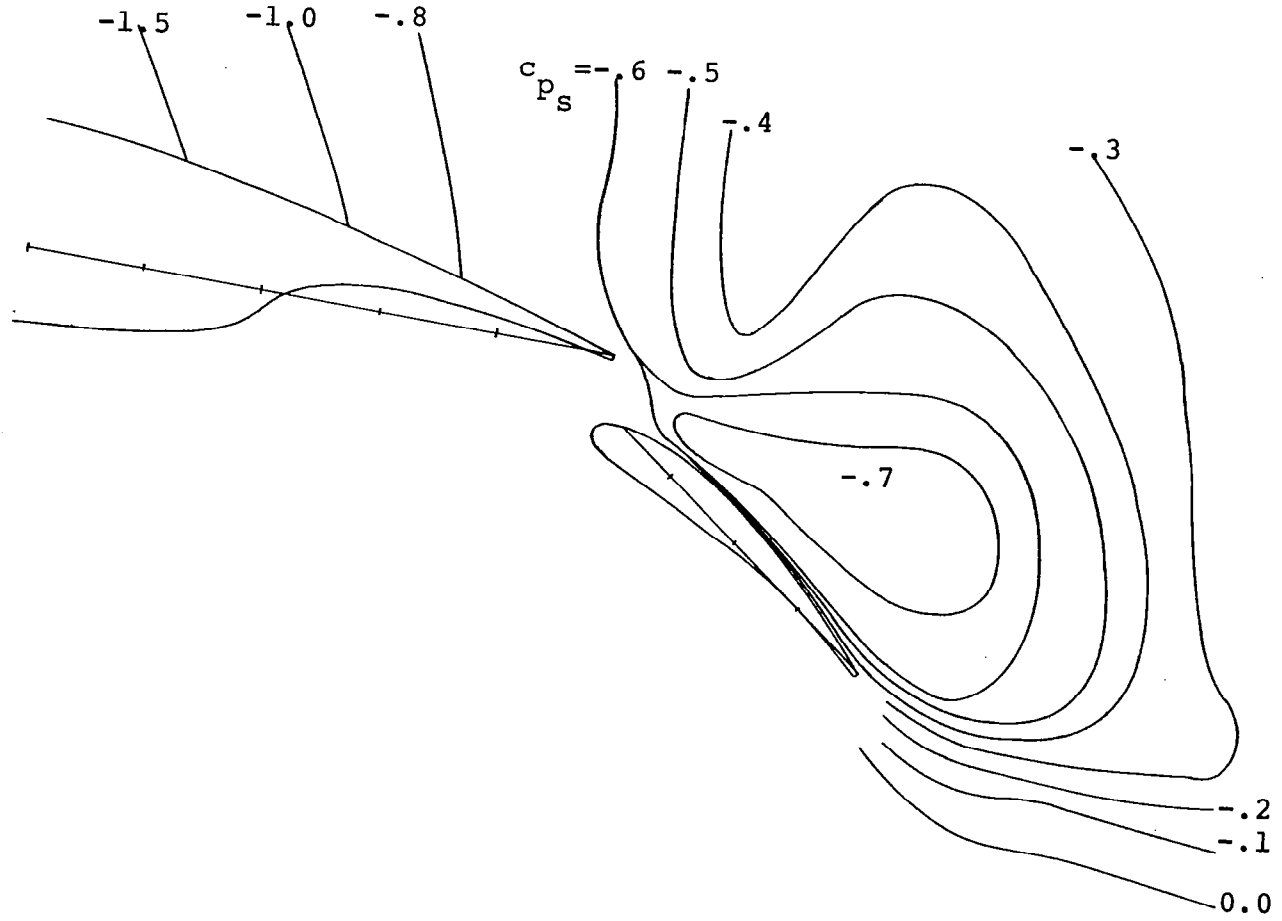
a) Gap = .02 c

Figure 16- Static Pressure Contours, $\alpha = 10.3^\circ$.



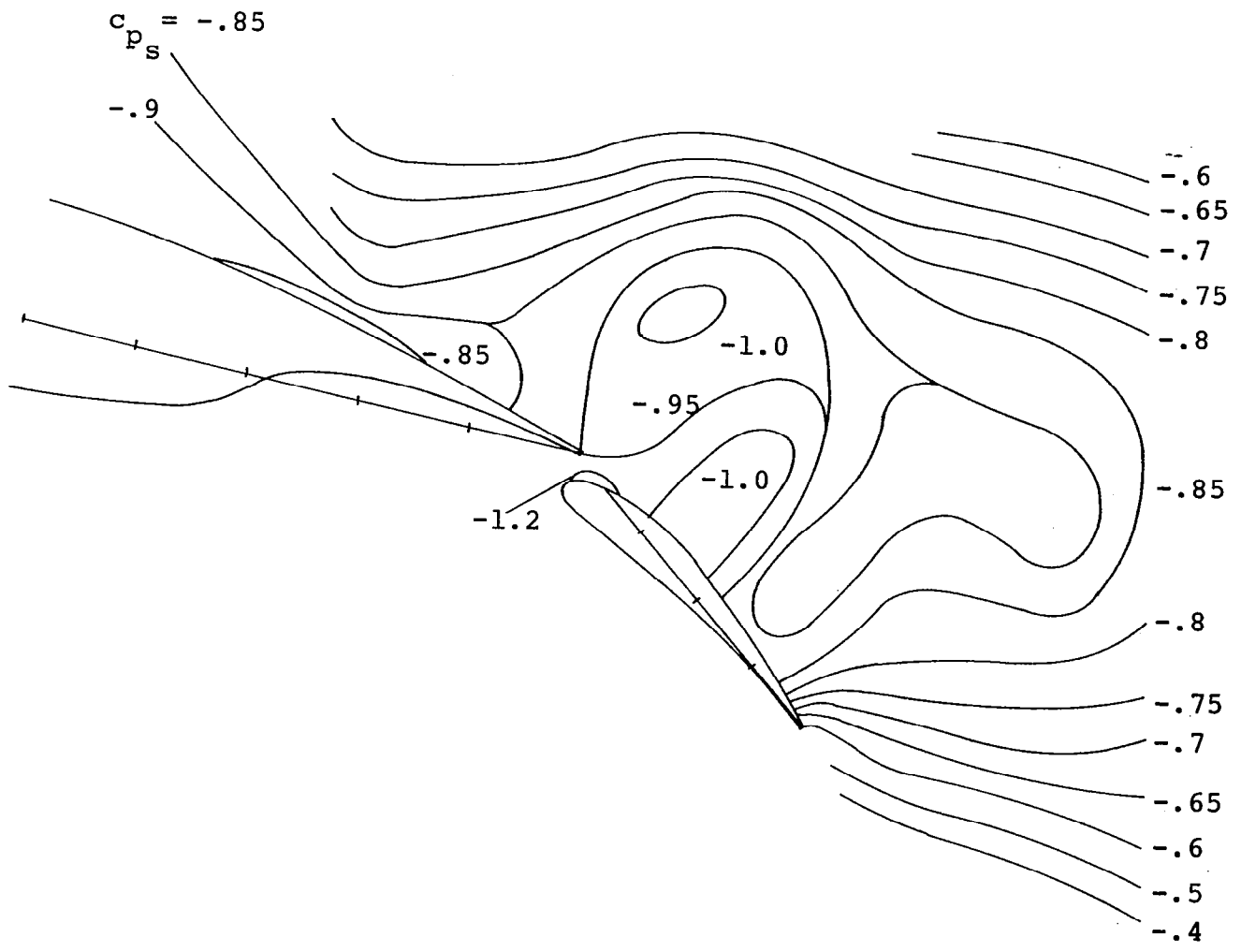
b) Gap = .03 c

Figure 16 - Continued.



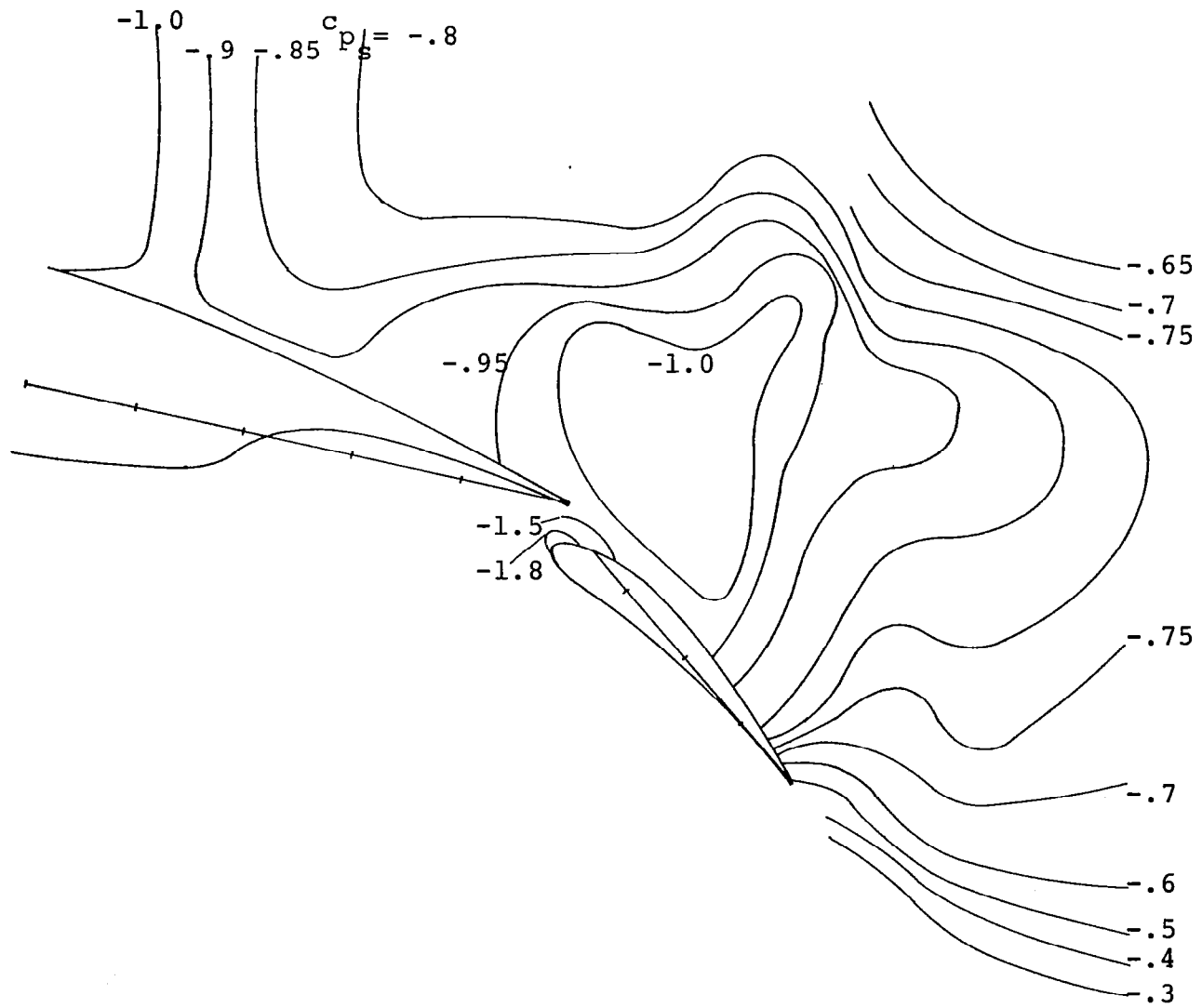
c) Gap = .05 c

Figure 16- Concluded.



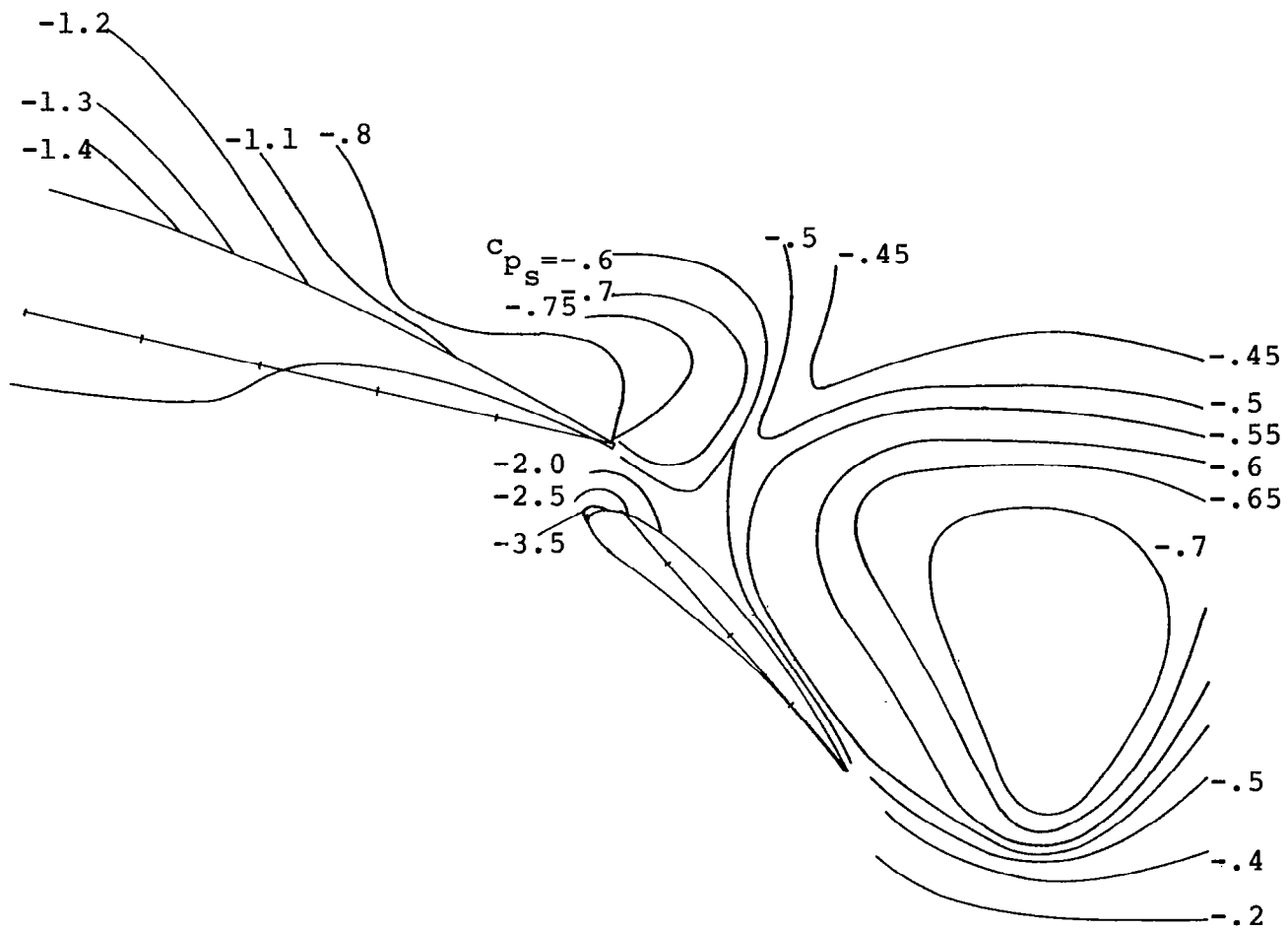
a) Gap = .02' c

Figure 17- Static Pressure Contours, $\alpha = 12.7^\circ$



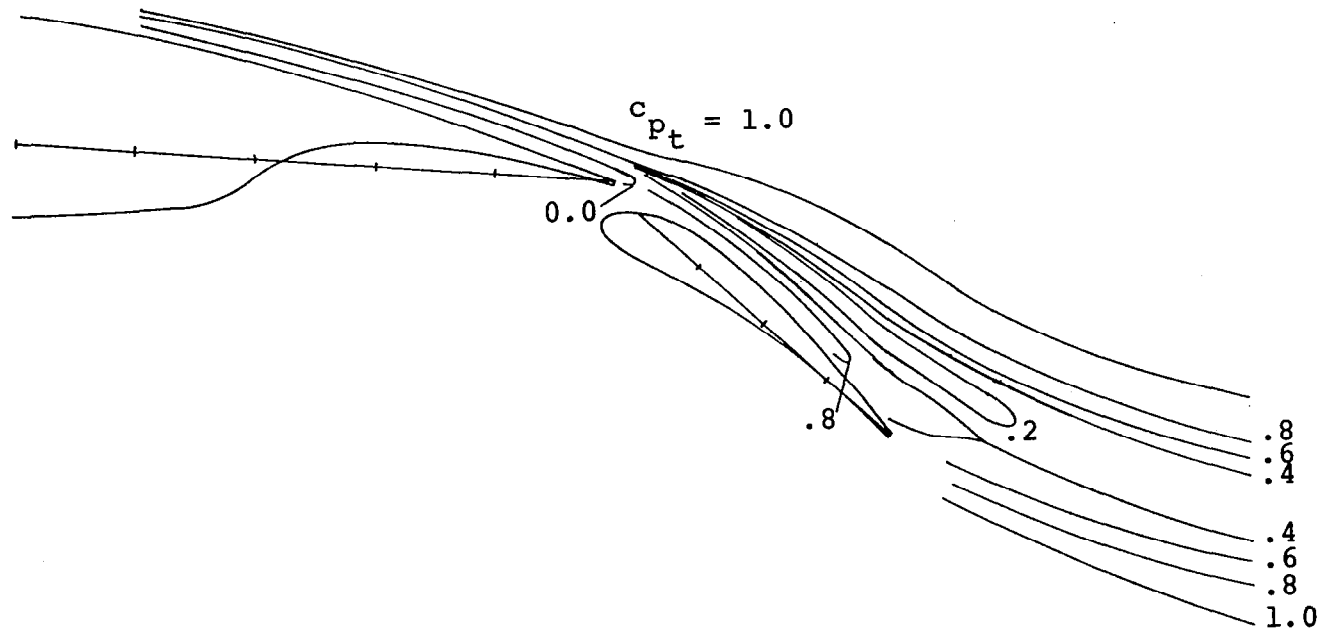
b) Gap = .03 c

Figure 17- Continued.



c) Gap = .05 c

Figure 17- Concluded.



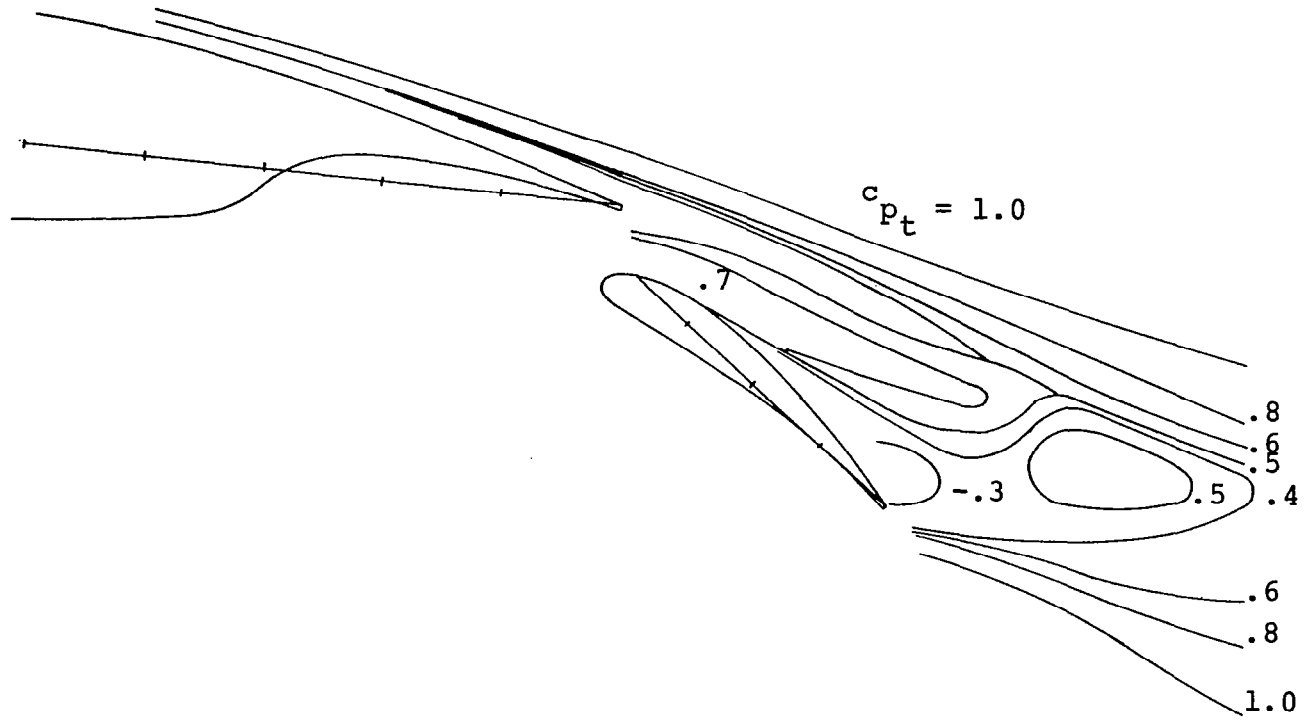
a) Gap = .02 c

Figure 18 - Total Pressure Contours, $\alpha = 5.2^\circ$



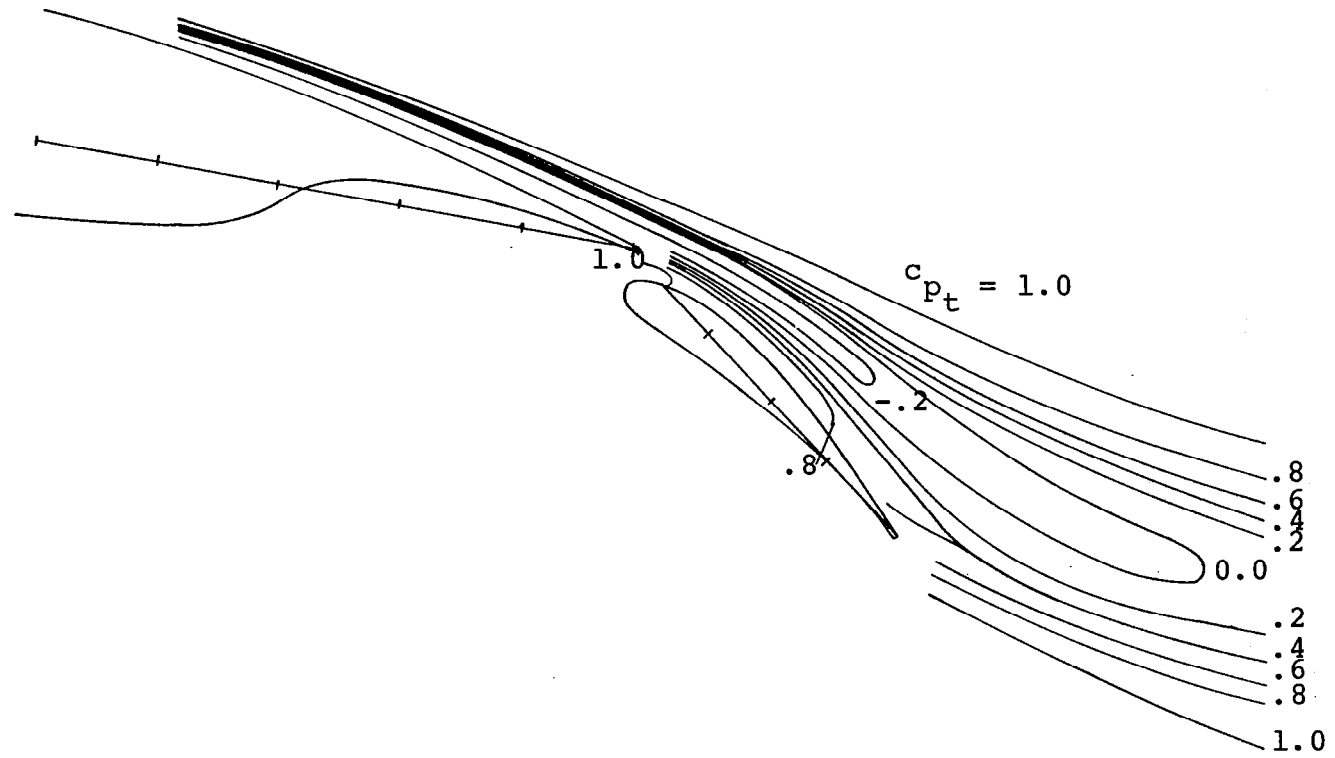
b) Gap = .03 c

Figure 18- Continued.



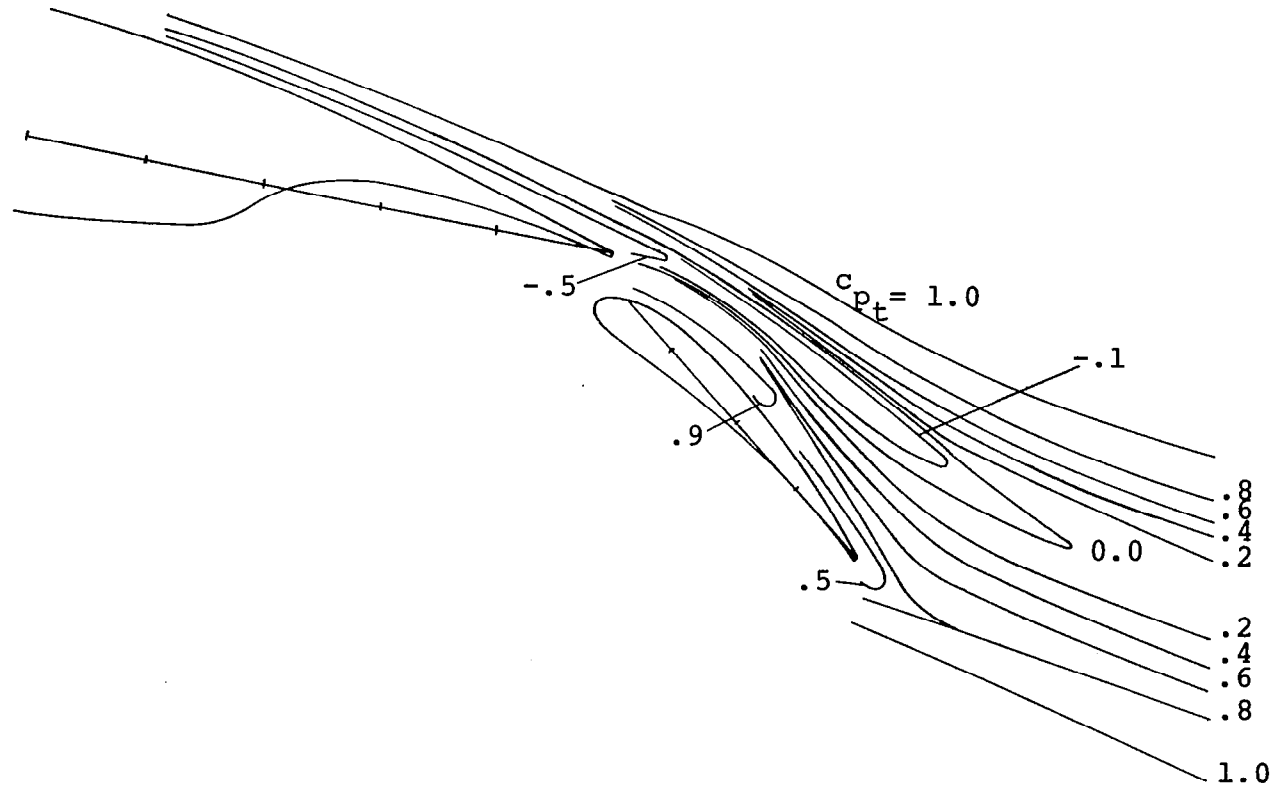
c) Gap = .05 c

Figure 18 - Concluded.



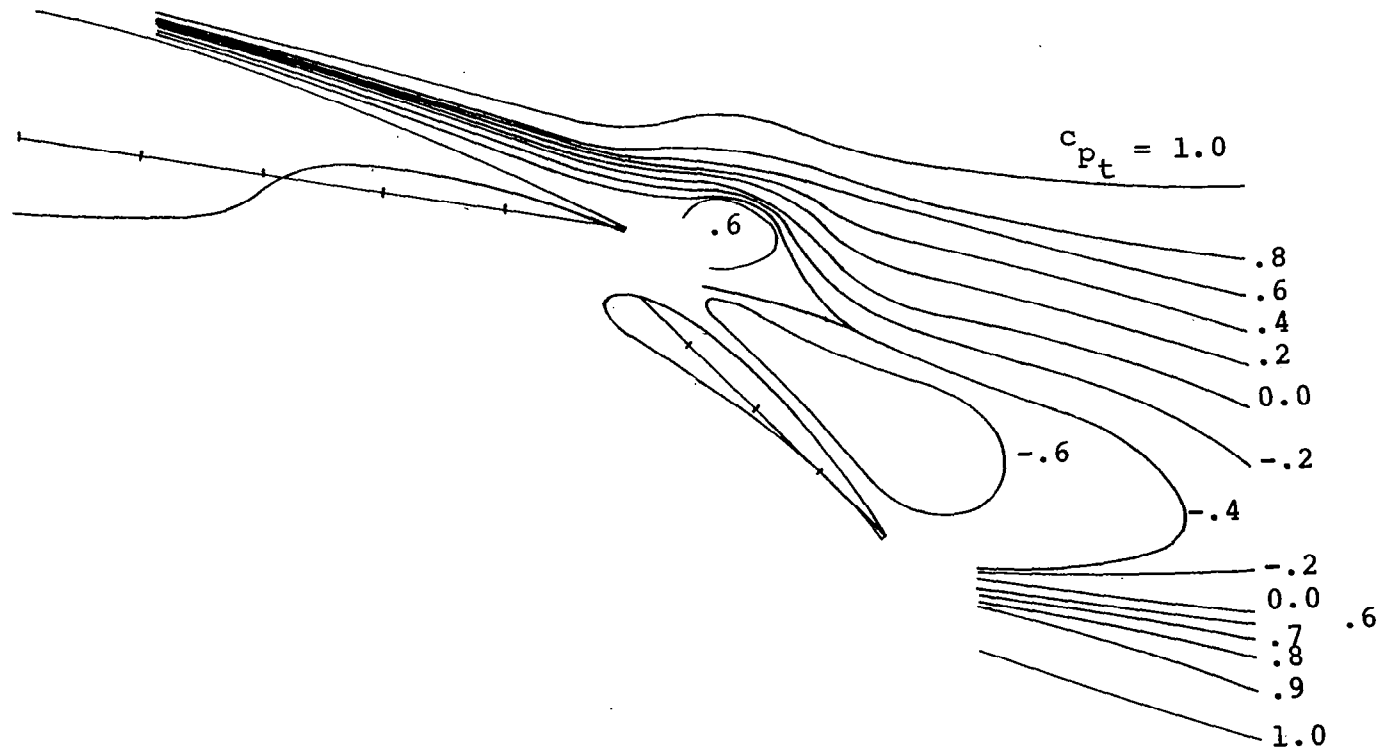
a) Gap = .02 c

Figure 19- Total Pressure Contours, $\alpha = 10.3^\circ$



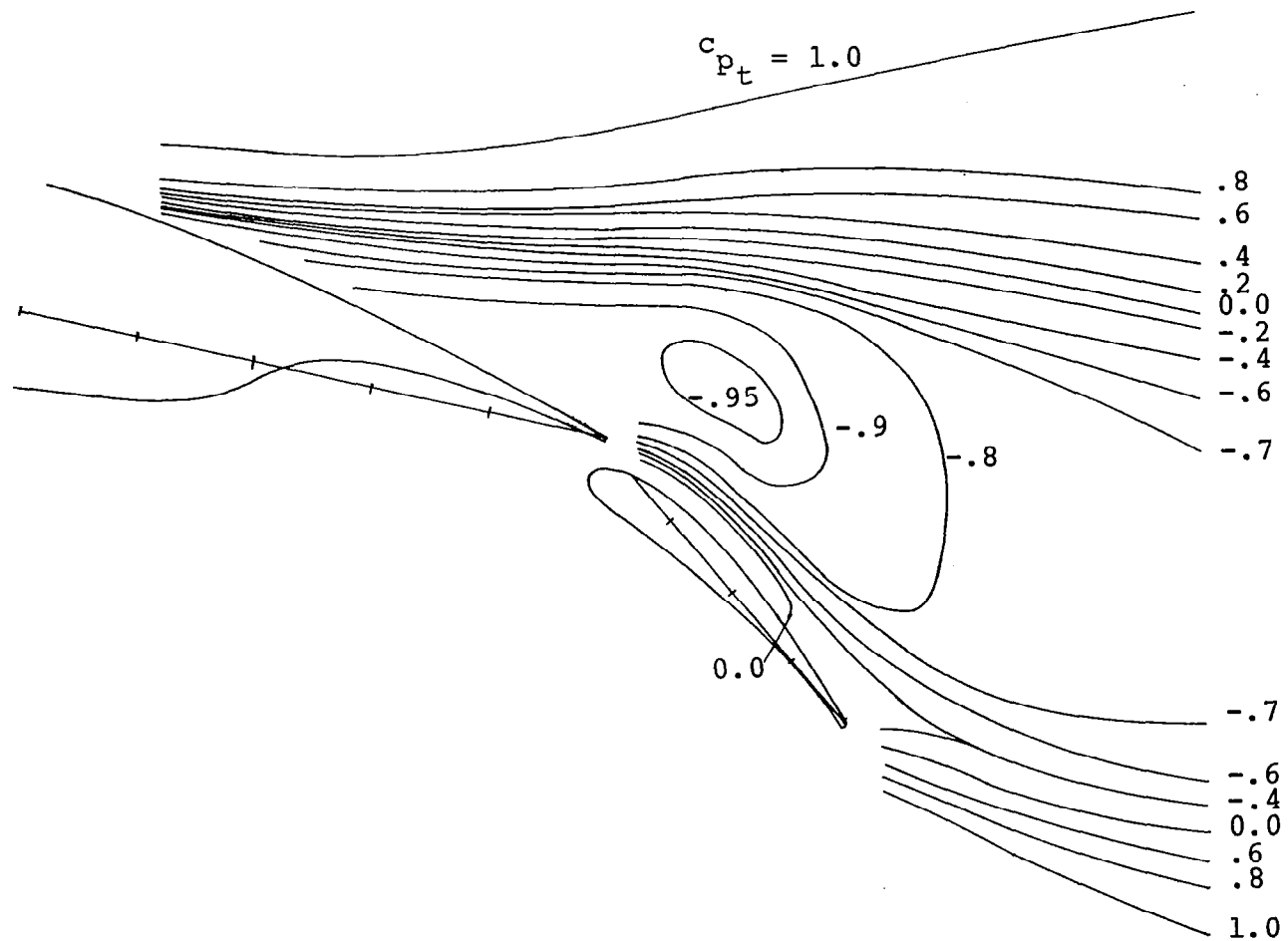
b) Gap = .03 c

Figure 19 - Continued.



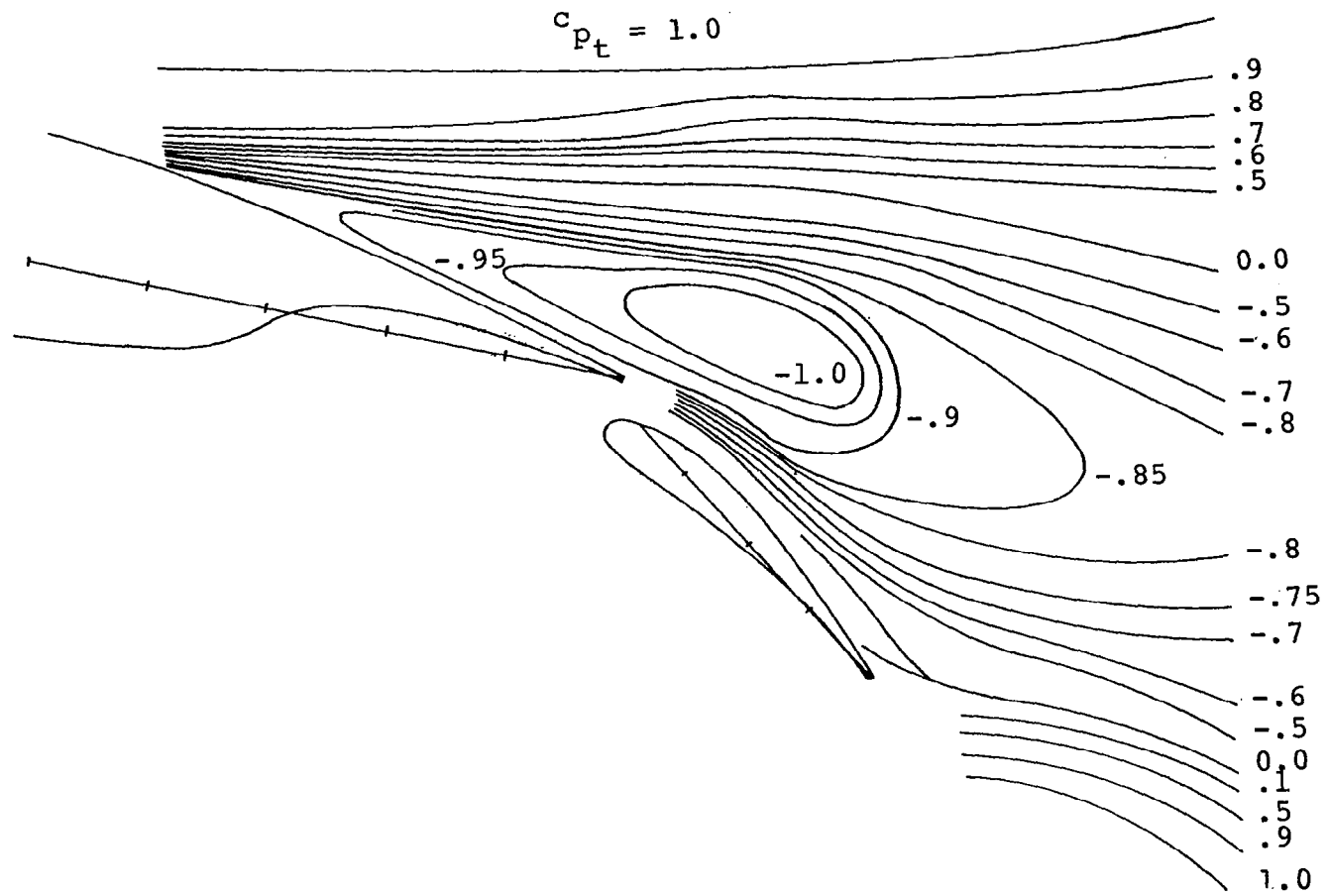
c) Gap = .05 c

Figure 19- Concluded.



a) Gap = .02 c

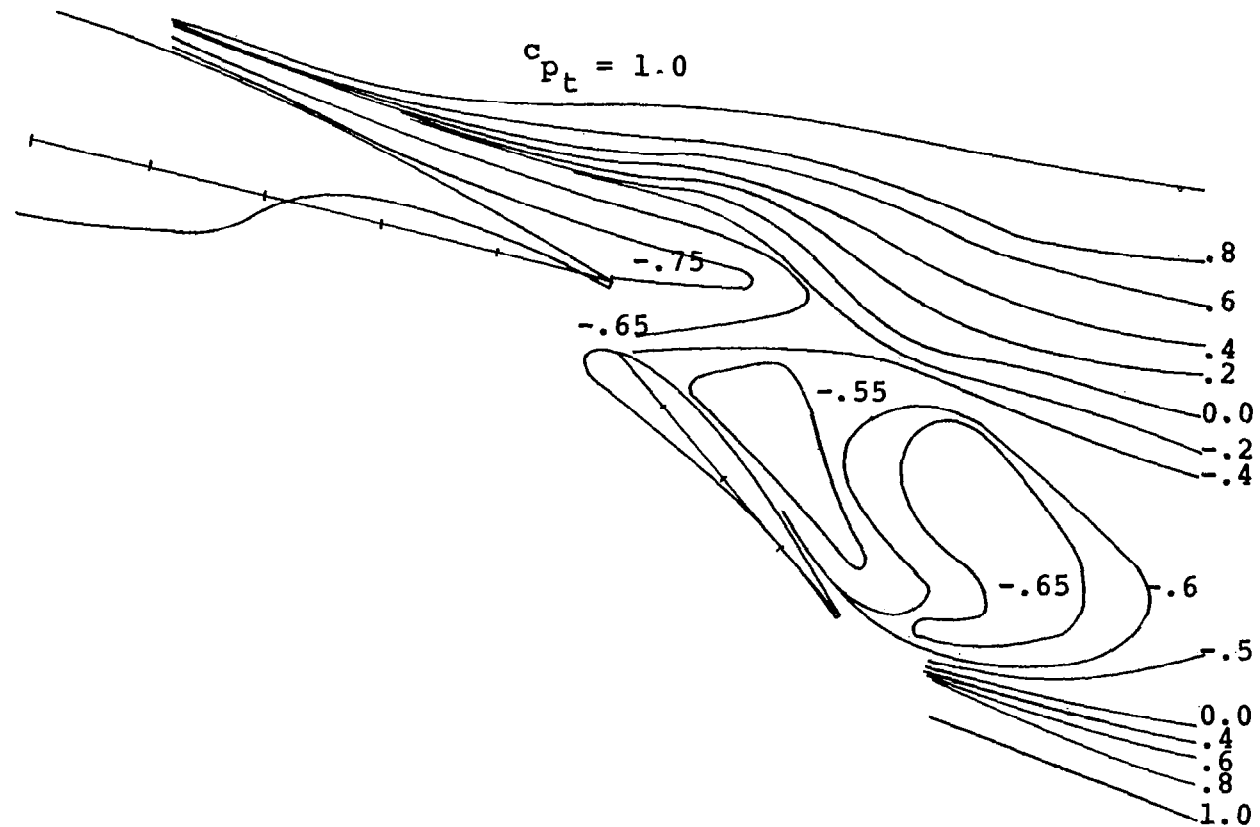
Figure 20- Total Pressure Contours, $\alpha = 12.7^\circ$



74

b) Gap = .03 c

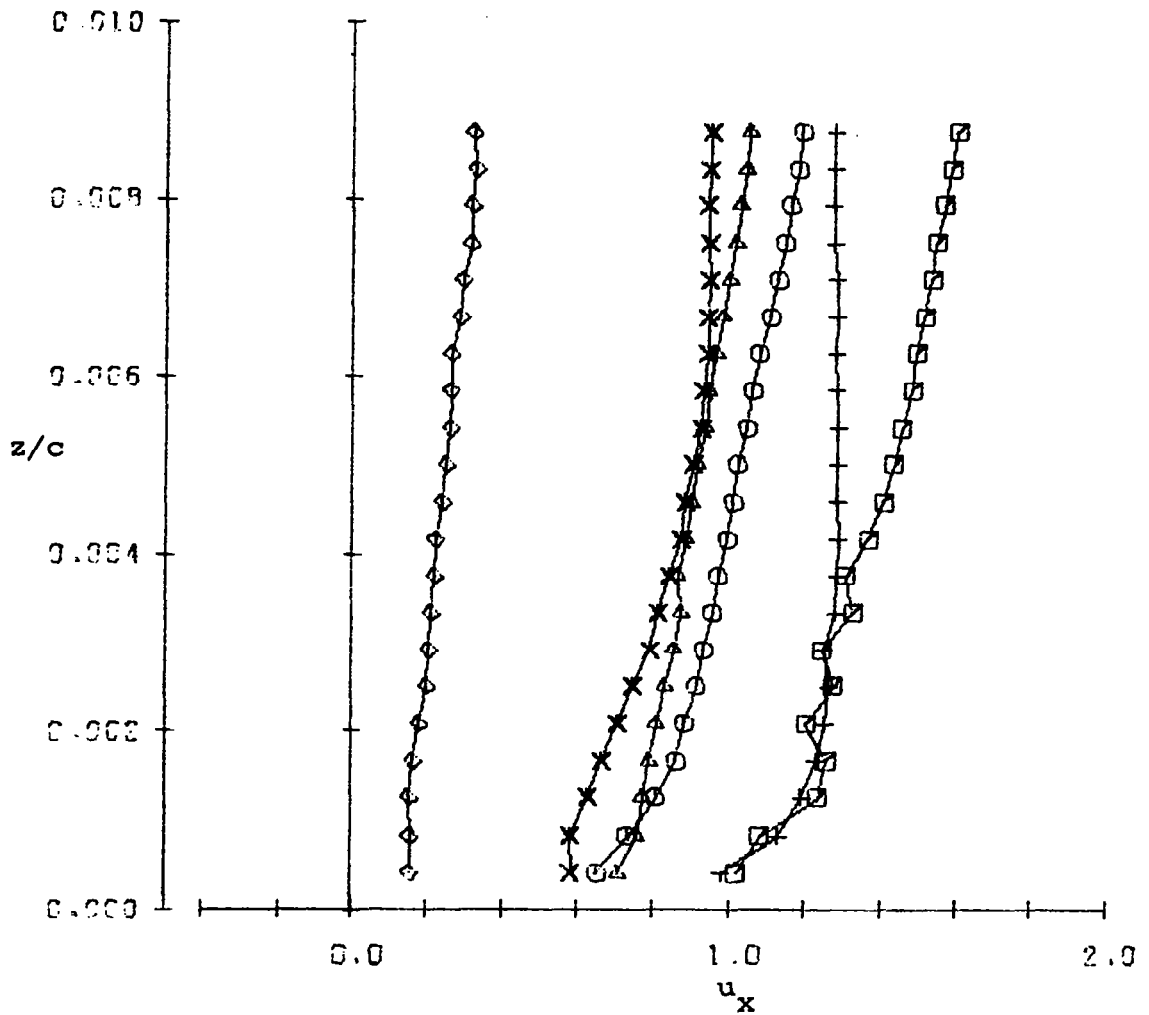
Figure 20 - Continued.



c) Gap = .05 c

Figure 20- Concluded.

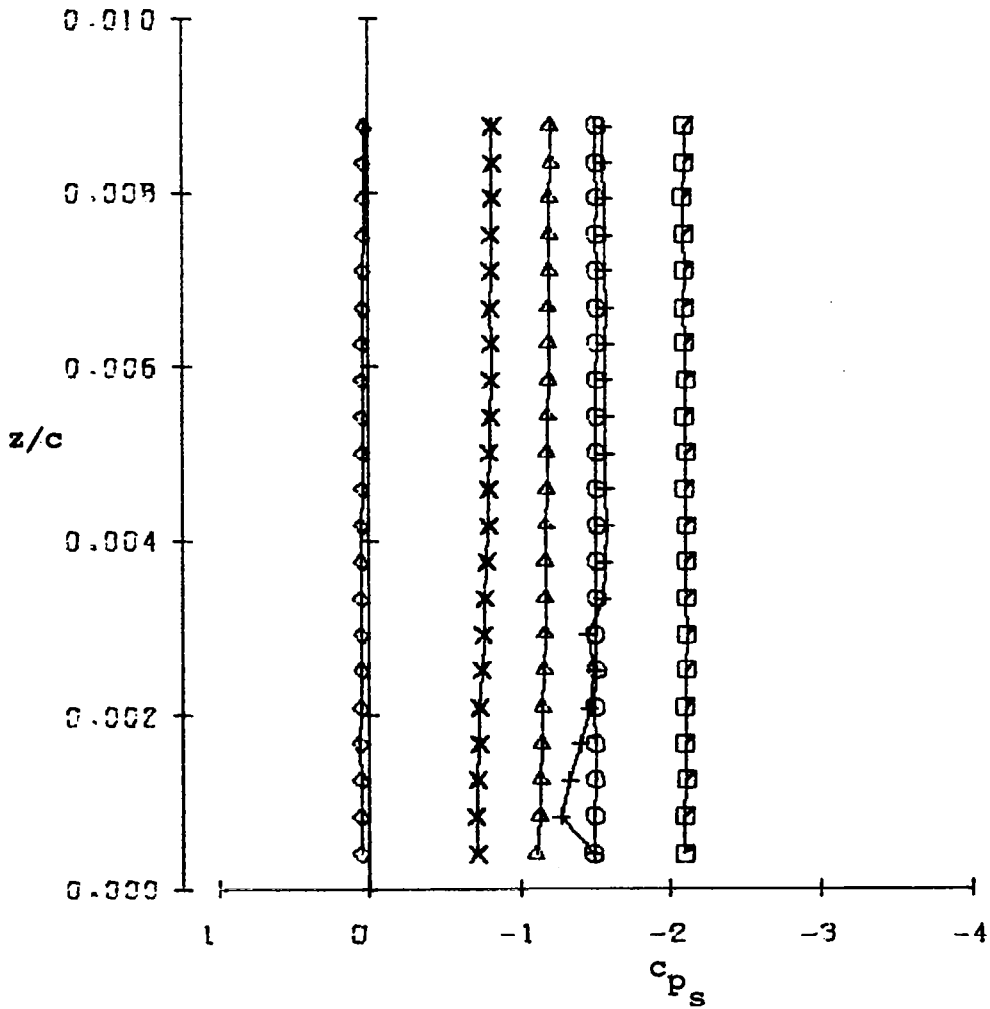
SYMBOL	LOCATION
◻	0.600 x/c
○	0.800 x/c
△	1.005 x/c
+	0.075 x _f /c
×	0.150 x _f /c
◇	0.300 x _f /c



(a) Velocity.

Figure 21 - Boundary Layer Characteristics, gap = .02c, $\alpha = 5.2^\circ$

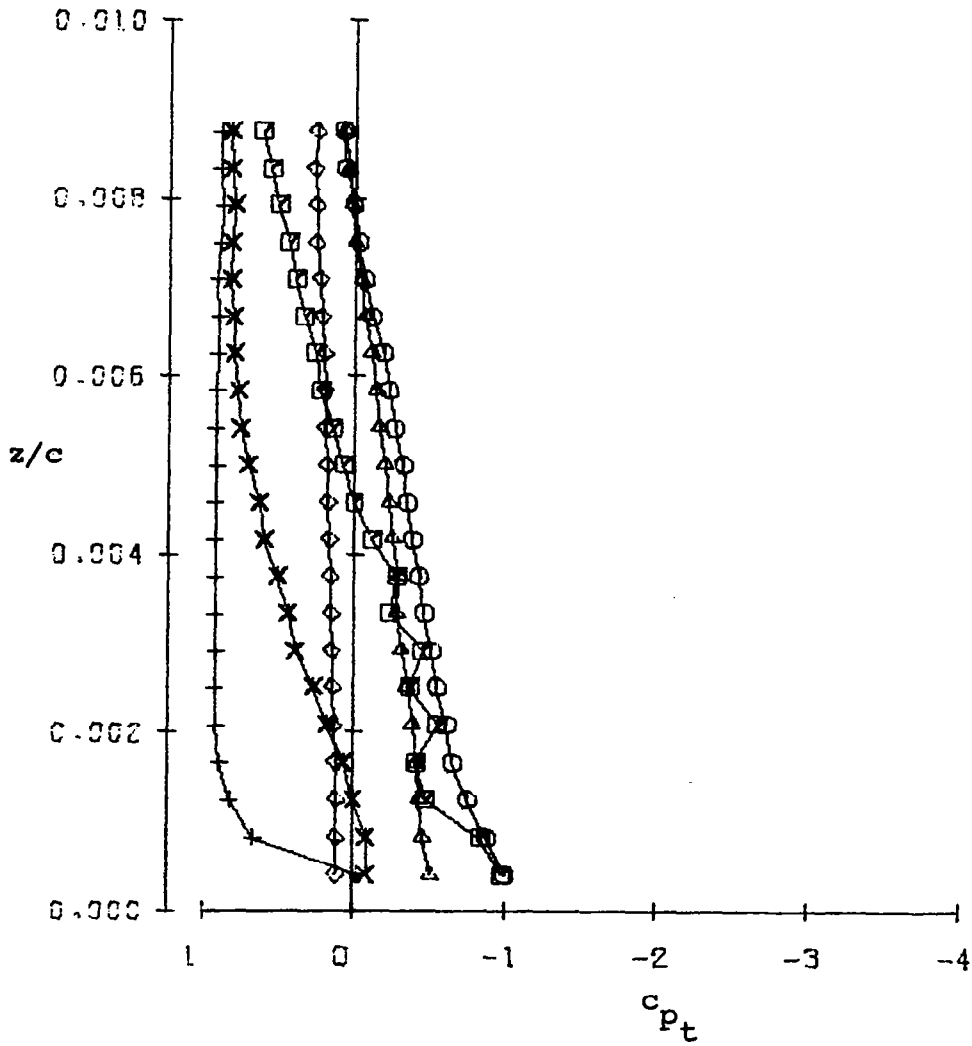
SYMBOL	LOCATION
□	0.600 x/c
○	0.800 x/c
△	1.005 x/c
+	0.075 x _f /c
×	0.150 x _f /c
◇	0.300 x _f /c



(b) Static Pressure.

Figure 21- Continued.

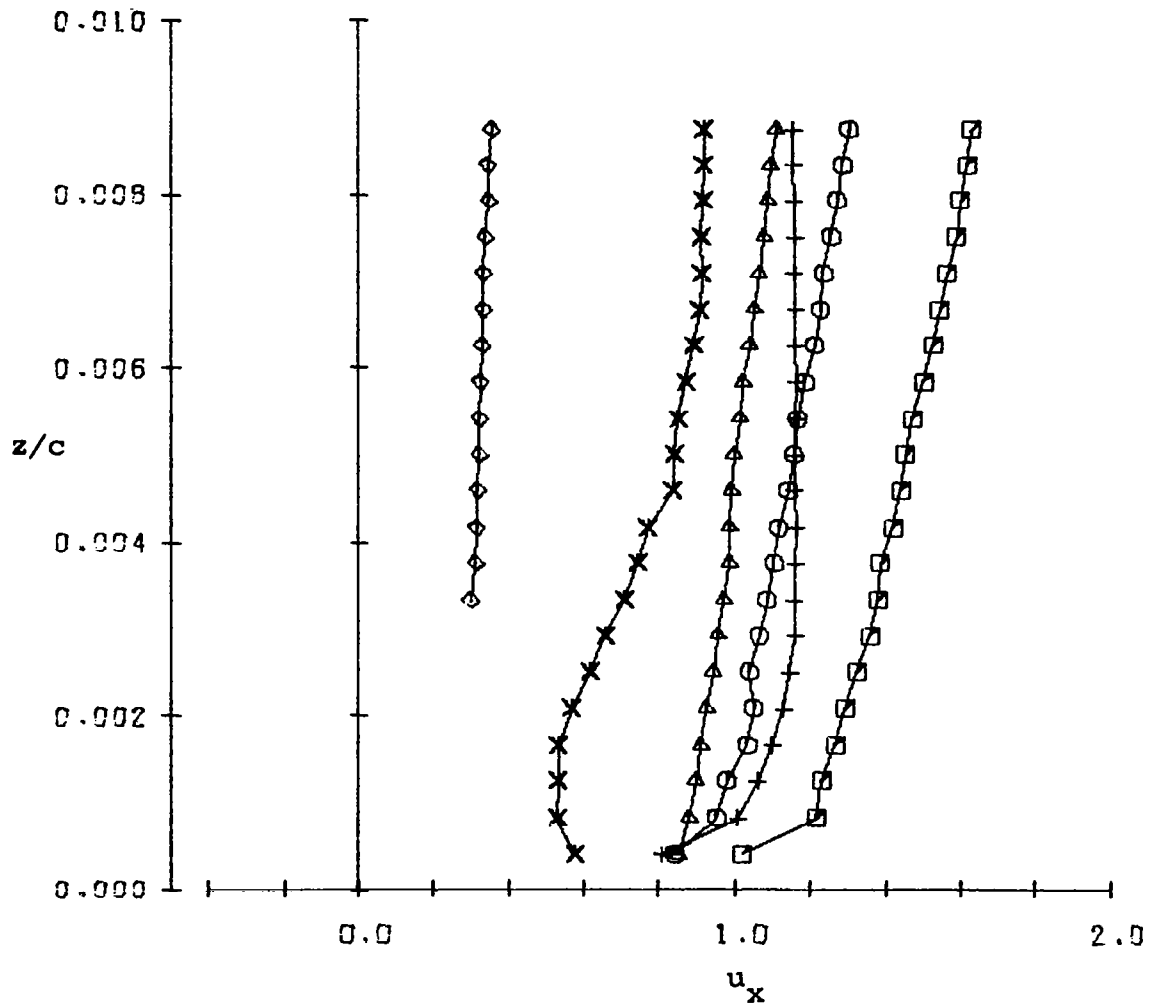
SYMBOL	LOCATION
□	0.600 x/c
○	0.800 x/c
△	1.005 x/c
+	0.075 x _f /c
×	0.150 x _f /c
◇	0.300 x _f /c



(c) Total Pressure.

Figure 21 - Concluded.

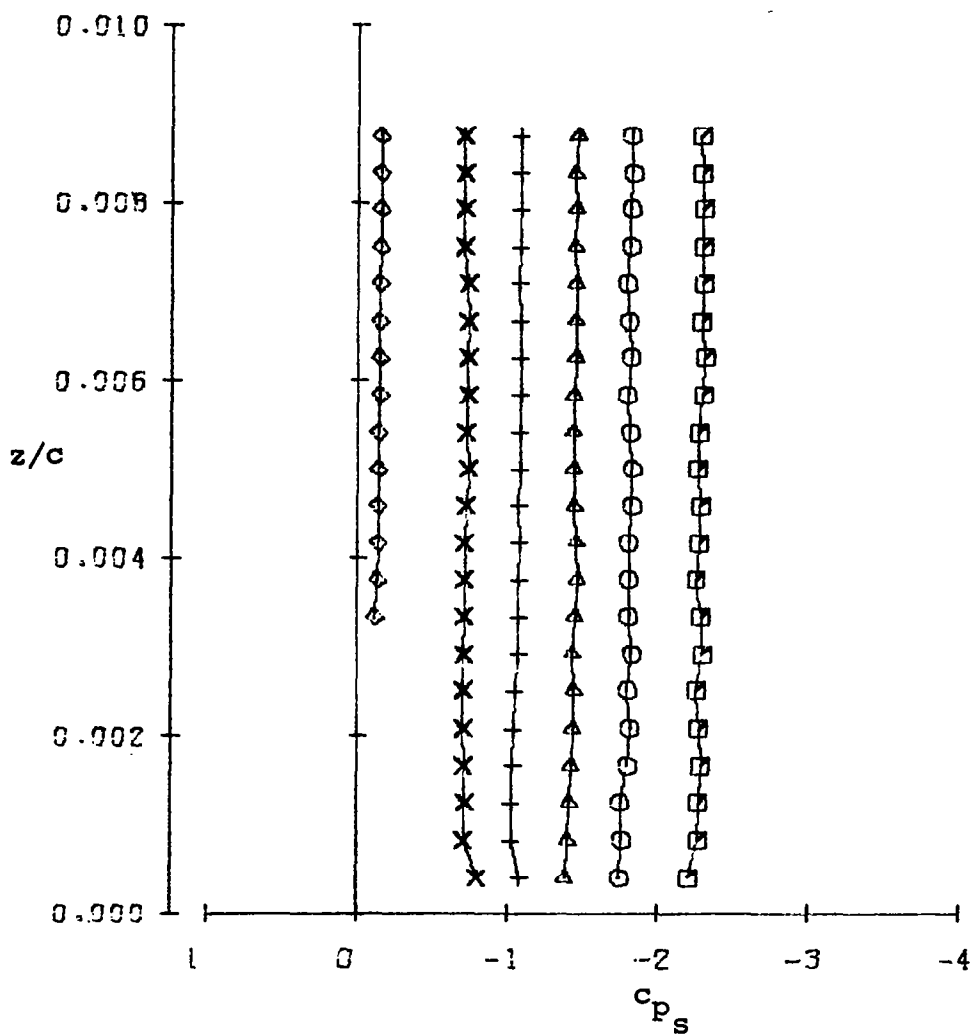
SYMBOL	LOCATION
◻	0.600 x/c
○	0.800 x/c
▲	1.005 x/c
+	0.075 x_f/c
×	0.150 x_f/c
◇	0.300 x_f/c



(a) Velocity.

Figure 22 - Boundary Layer Characteristics, gap = .03c, $\alpha = 5.2^\circ$

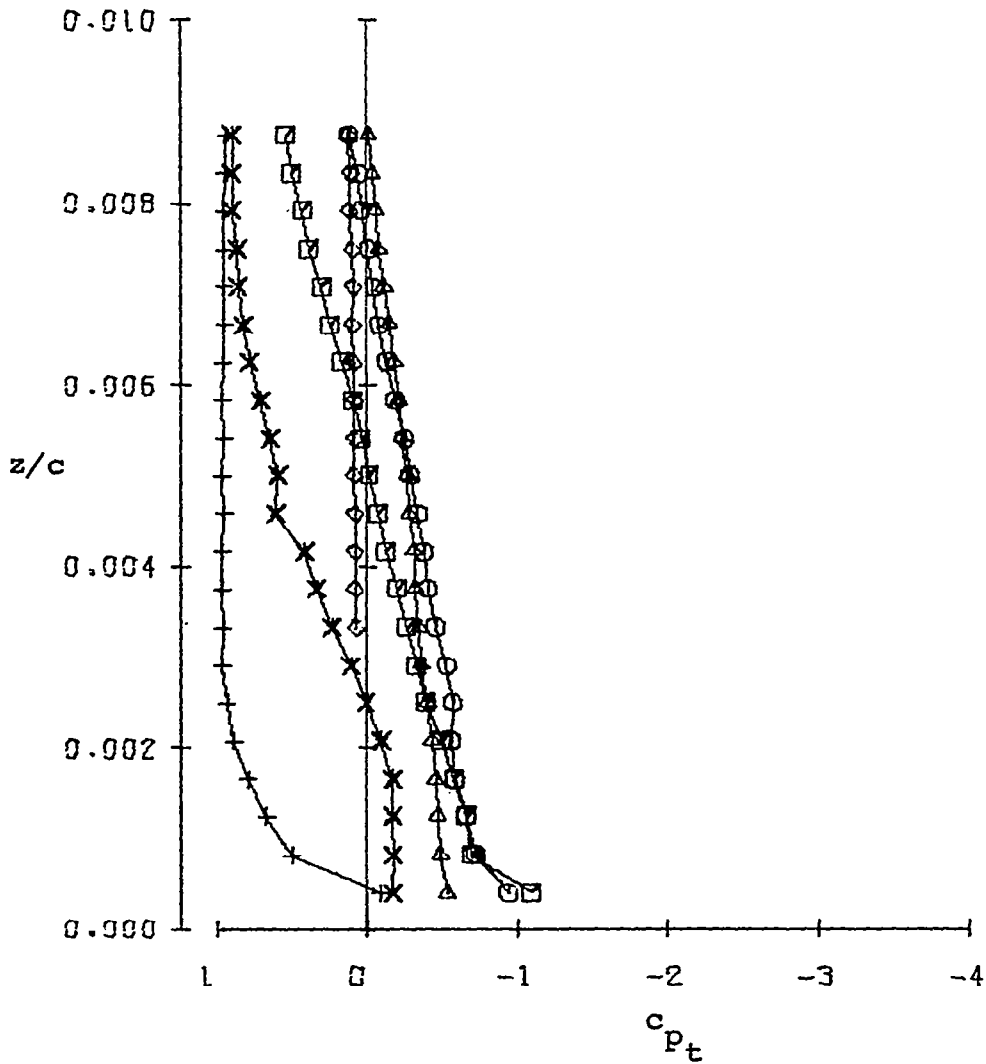
SYMBOL	LOCATION
◻	0.600 x/c
⊙	0.800 x/c
△	1.005 x/c
+	0.075 x _f /c
×	0.150 x _f /c
◇	0.300 x _f /c



(b) Static Pressure.

Figure 22 - Continued.

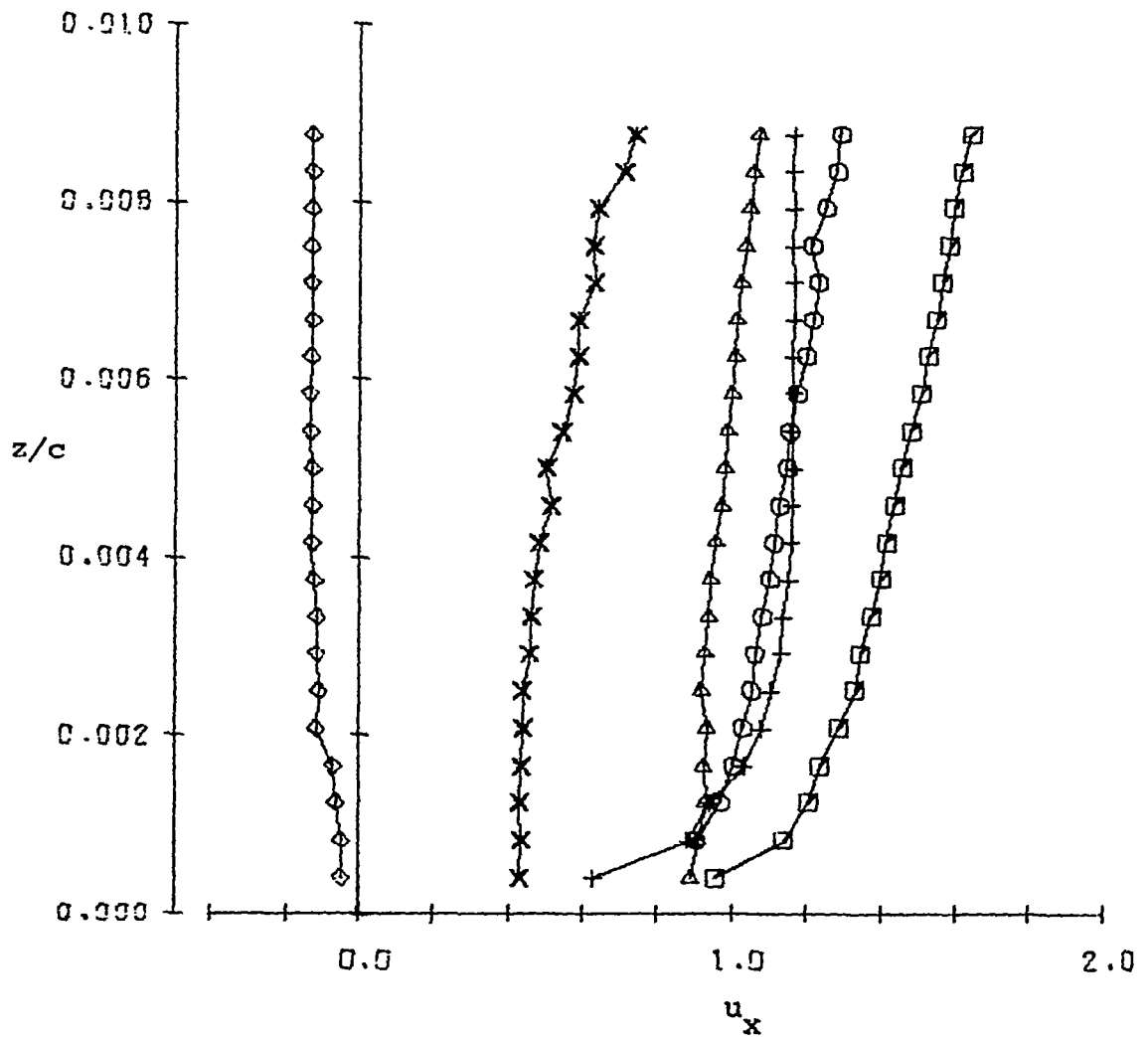
SYMBOL	LOCATION
◻	.600 x/c
⊙	0.800 x/c
△	1.005 x/c
+	0.075 x_f/c
×	0.150 x_f/c
◇	0.300 x_f/c



(c) Total Pressure.

Figure 22 - Concluded.

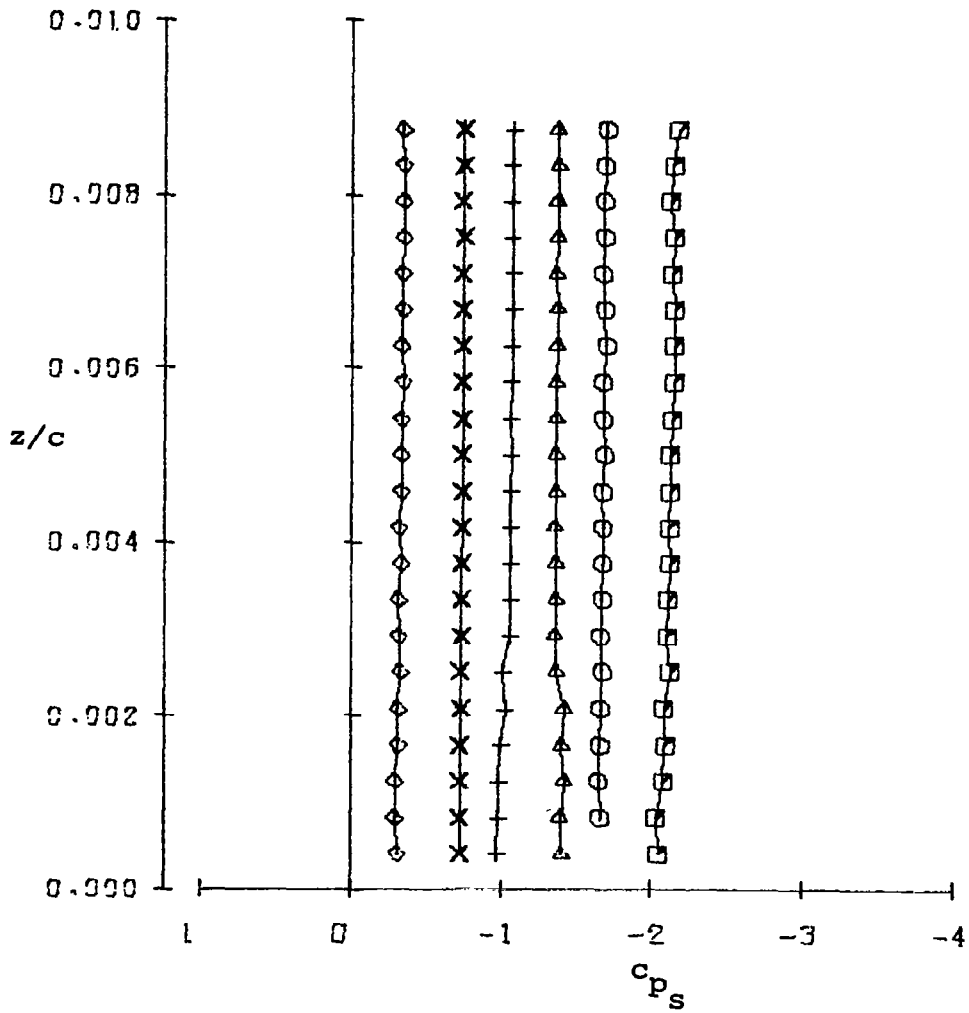
SYMBOL	LOCATION
□	0.600 x/c
○	0.800 x/c
△	1.005 x/c
+	0.075 x _f /c
×	0.150 x _f /c
◇	0.300 x _f /c



(a) Velocity.

Figure 23 - Boundary Layer Characteristics, gap = .05c, $\alpha = 5.2^\circ$

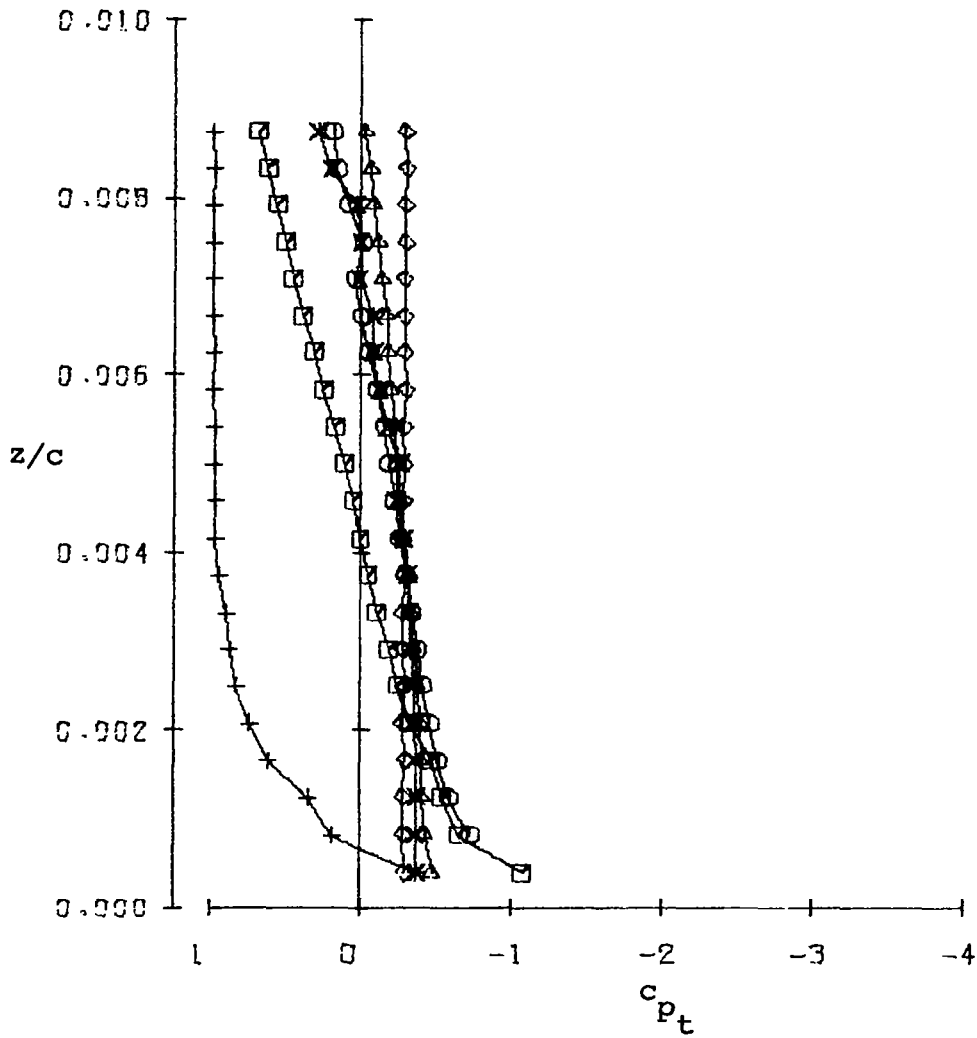
SYMBOL	LOCATION
◻	0.600 x/c
⊙	0.800 x/c
△	1.005 x/c
+	0.075 x _f /c
×	0.150 x _f /c
◇	0.300 x _f /c



(b) Static Pressure.

Figure 23 - Continued.

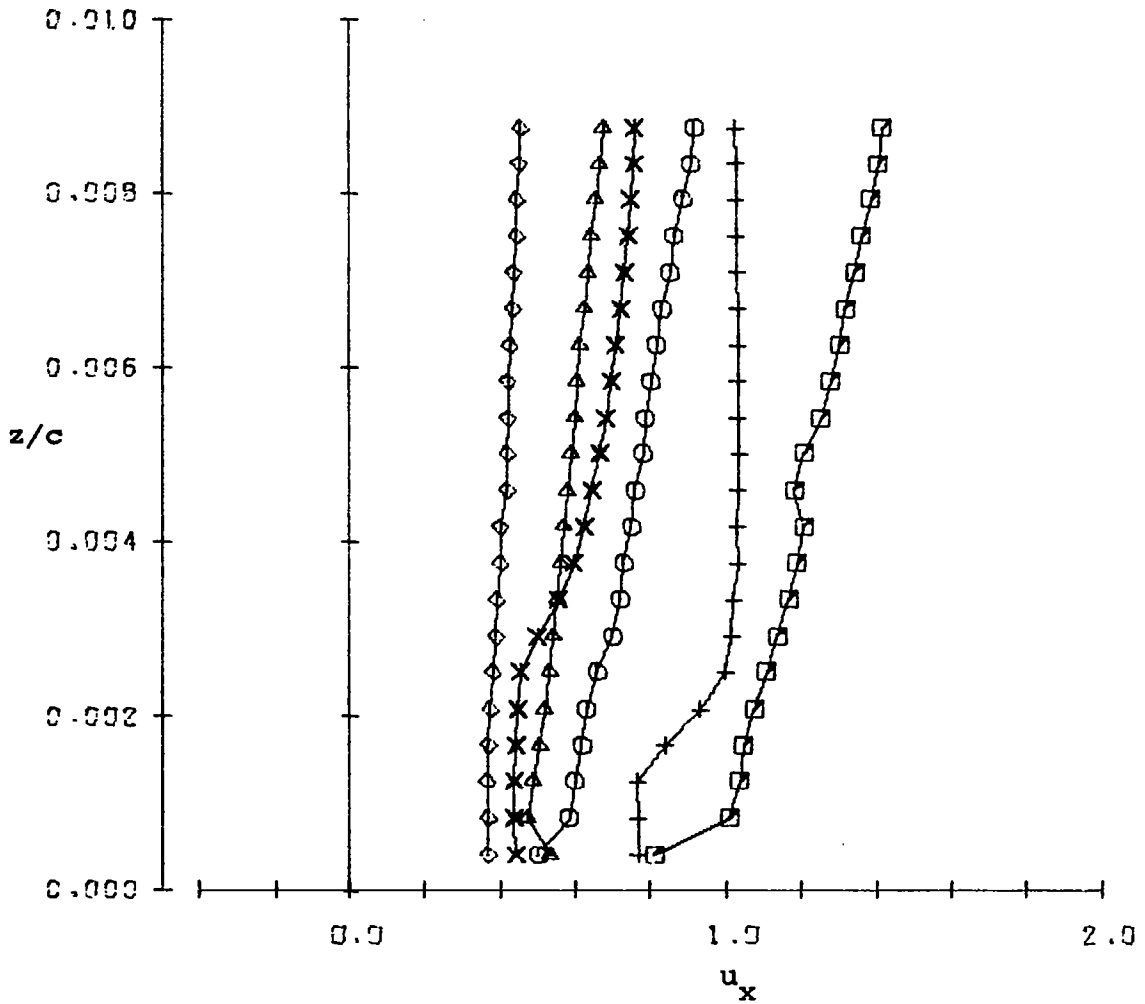
SYMBOL	LOCATION
◻	0.600 x/c
○	0.800 x/c
△	1.005 x/c
+	0.075 x _f /c
×	0.150 x _f /c
◇	0.300 x _f /c



(c) Total Pressure.

Figure 23 - Concluded.

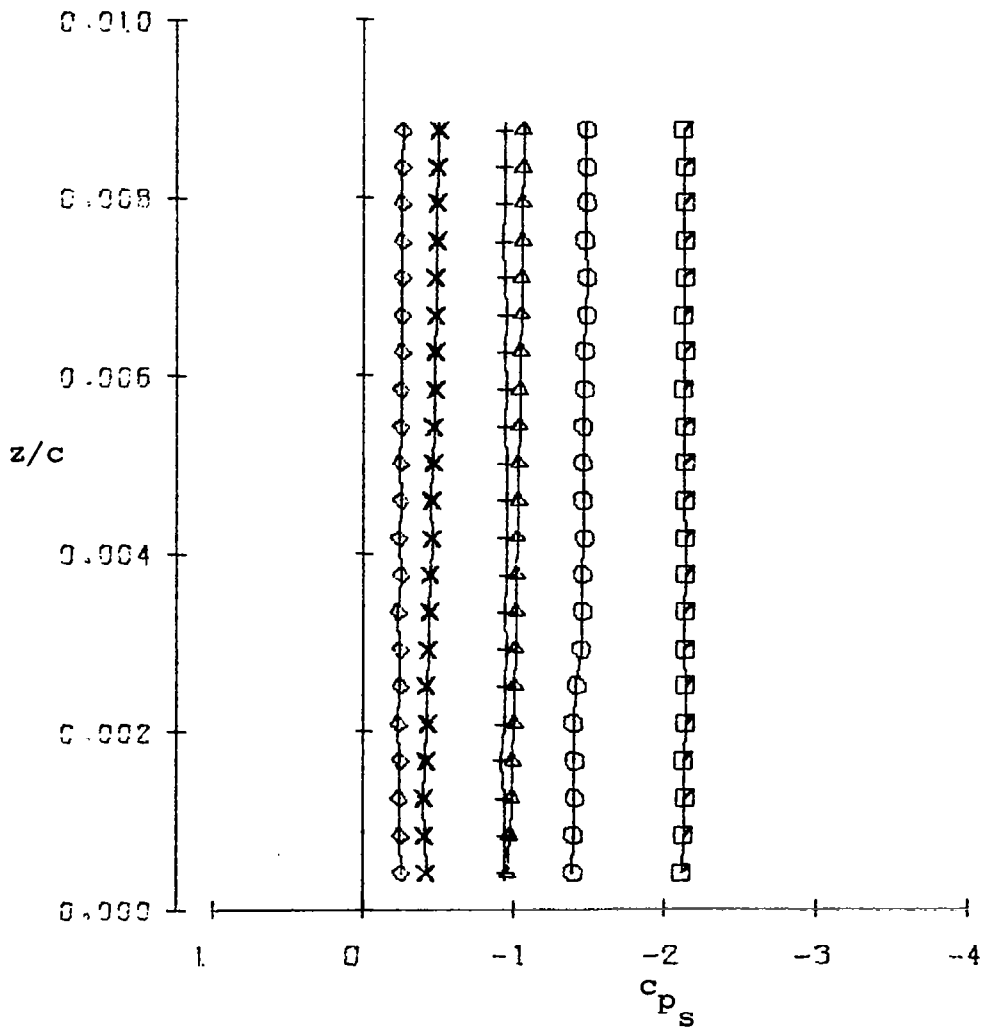
SYMBOL	LOCATION
◻	0.600 x/c
○	0.800 x/c
△	1.005 x/c
+	0.075 x_f/c
×	0.150 x_f/c
◇	0.300 x_f/c



(a) Velocity.

Figure 24 - Boundary Layer Characteristics, gap = .02c, $\alpha = 10.3^\circ$

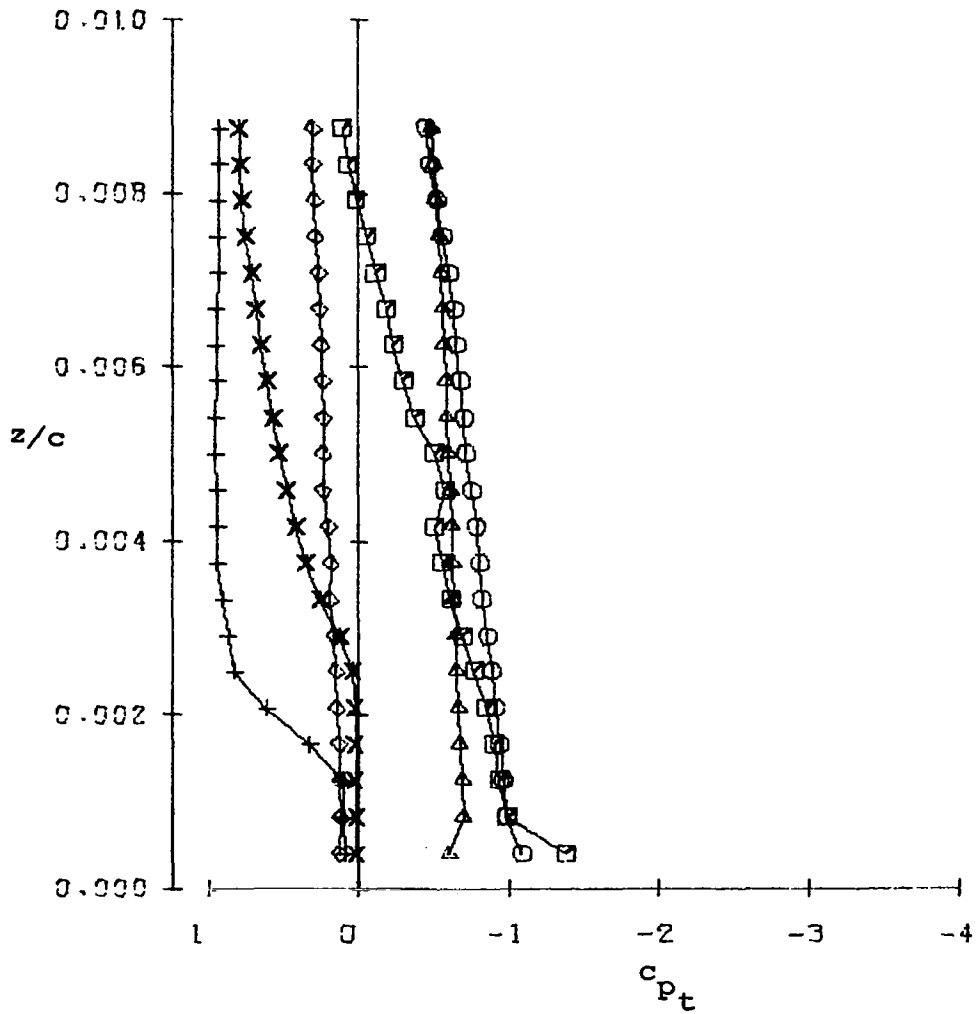
SYMBOL	LOCATION
◻	.600 x/c
○	0.800 x/c
△	1.005 x/c
+	0.075 x_f/c
×	0.150 x_f/c
◇	0.300 x_f/c



(b) Static Pressure.

Figure 24 - Continued.

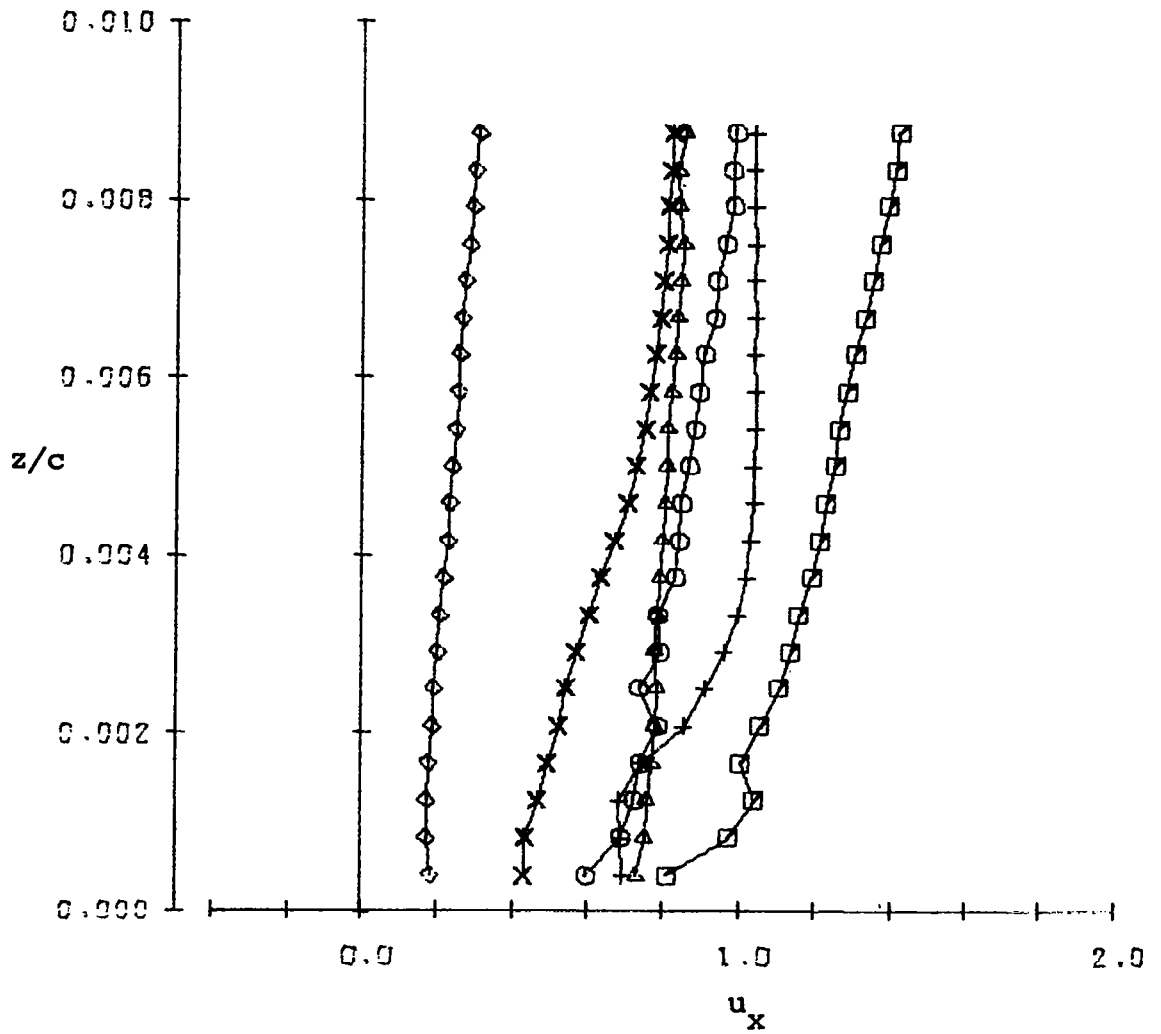
SYMBOL	LOCATION
◻	0.600 x/c
⊙	0.800 x/c
△	1.005 x/c
+	0.075 x _f /c
×	0.150 x _f /c
⊕	0.300 x _f /c



(c) Total Pressure.

Figure 24 - Concluded.

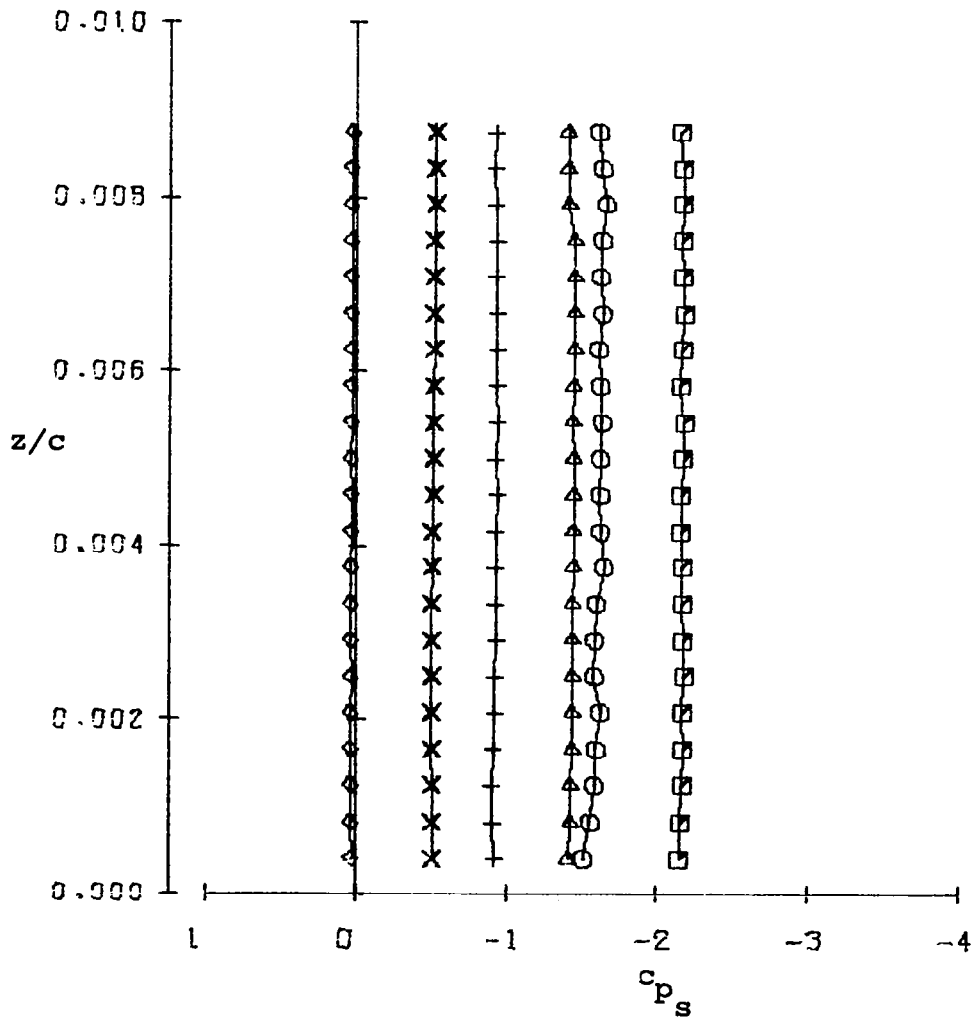
SYMBOL	LOCATION
◻	0.600 x/c
○	0.800 x/c
△	1.005 x/c
+	0.075 x_f/c
×	0.150 x_f/c
◇	0.300 x_f/c



(a) Velocity.

Figure 25 - Boundary Layer Characteristics, gap = .03c, $\alpha = 10.3^\circ$

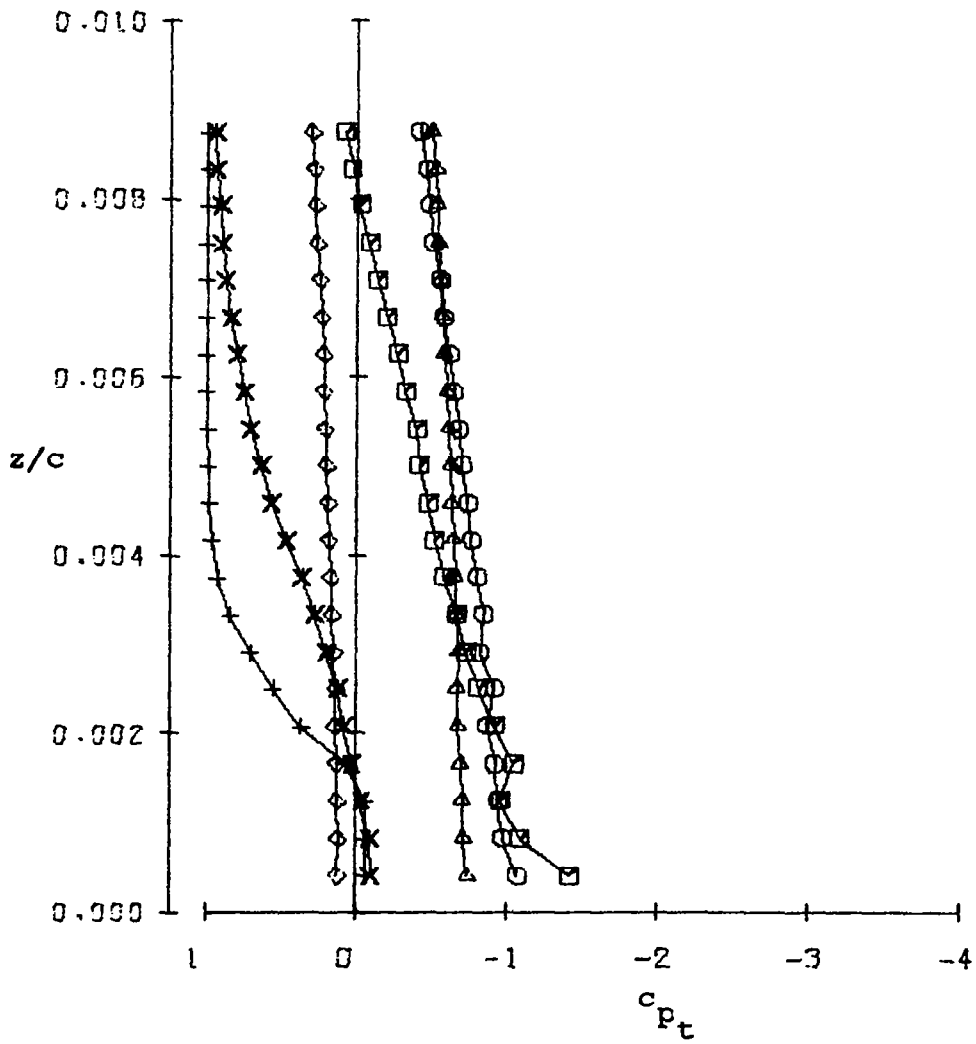
SYMBOL	LOCATION
□	0.600 x/c
○	0.800 x/c
△	1.005 x/c
+	0.075 x _f /c
×	0.150 x _f /c
◇	0.300 x _f /c



(b) Static Pressure.

Figure 25 - Continued.

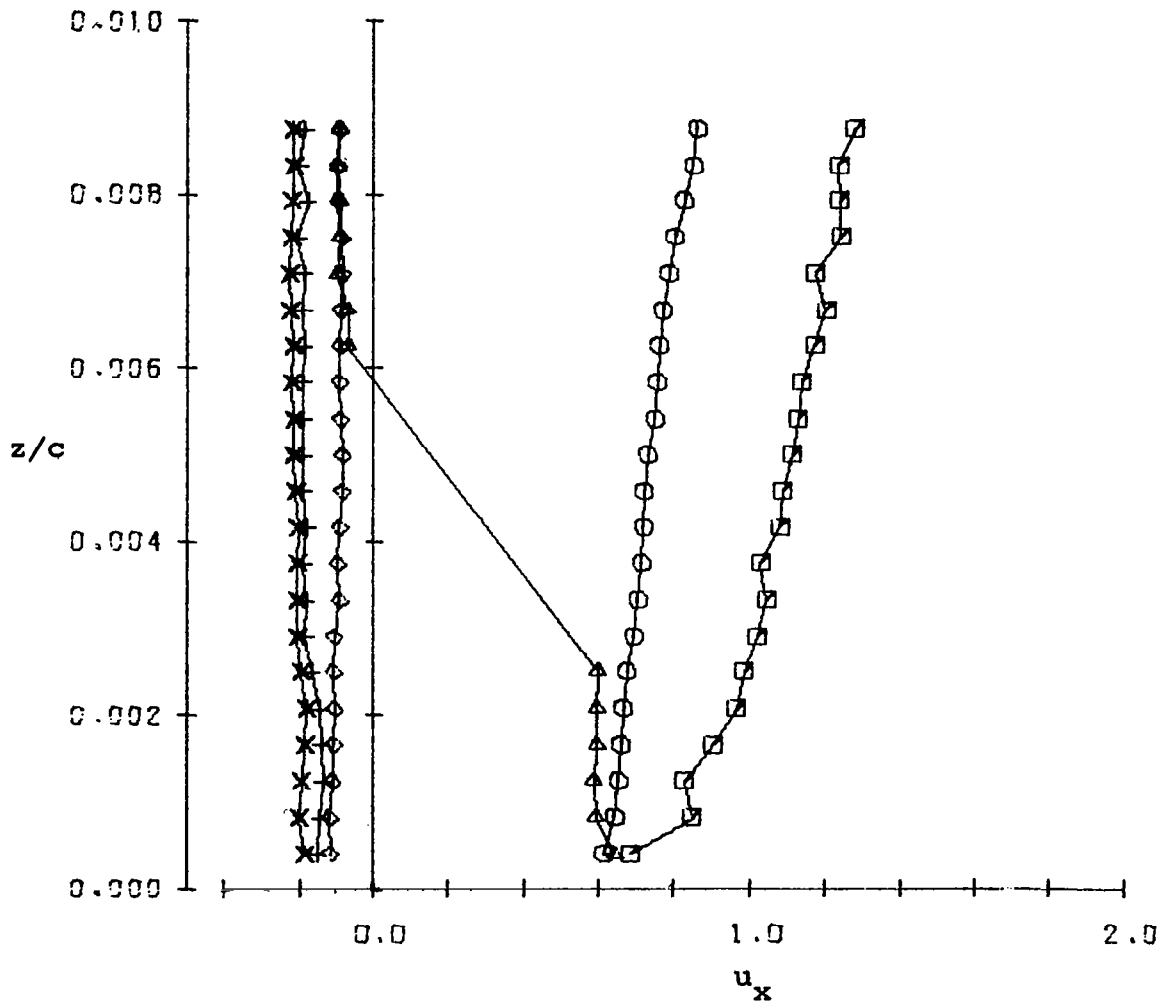
SYMBOL	LOCATION
◻	0.600 x/c
⊙	0.800 x/c
△	1.005 x/c
+	0.075 x _f /c
×	0.150 x _f /c
◇	0.300 x _f /c



(c) Total Pressure.

Figure 25 - Concluded.

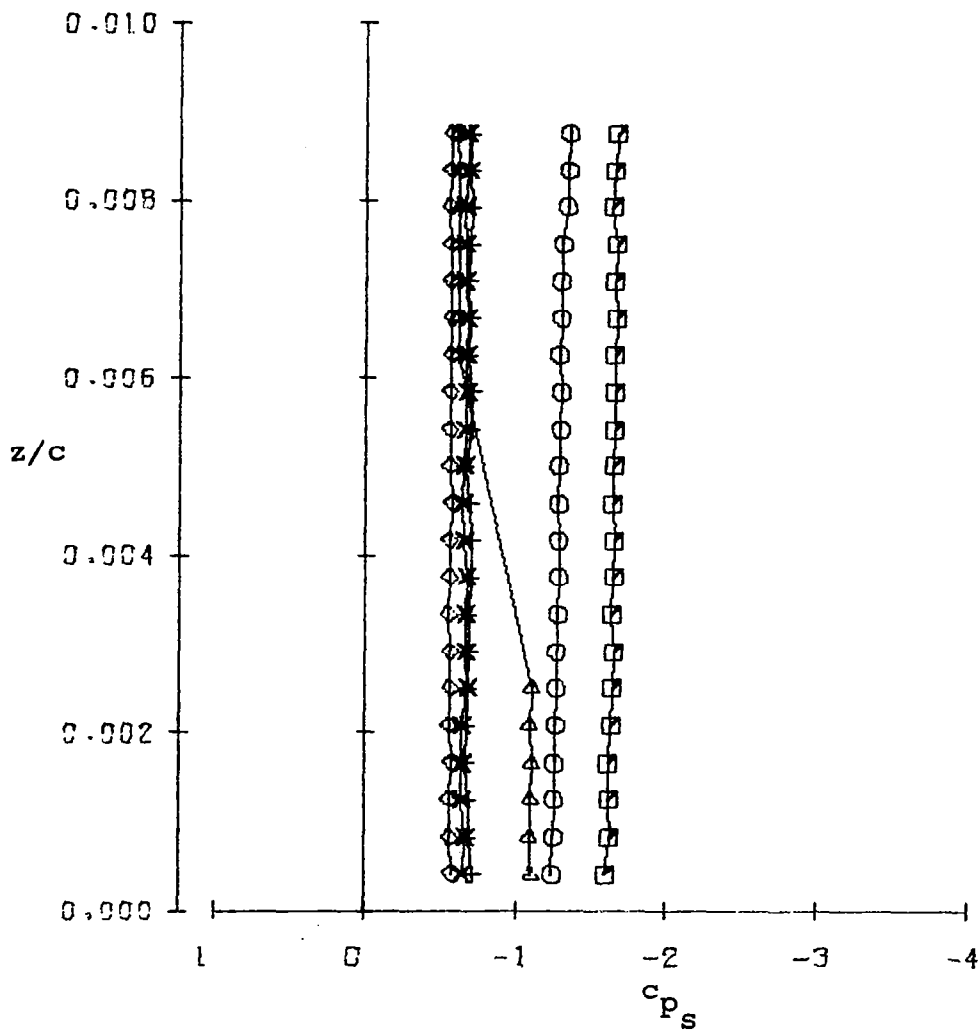
SYMBOL	LOCATION
◻	0.600 x/c
○	0.800 x/c
△	1.005 x/c
+	0.075 x _f /c
×	0.150 x _f /c
◇	0.300 x _f /c



(a) Velocity.

Figure 26 - Boundary Layer Characteristics, gap = .05c, $\alpha = 10.3^\circ$

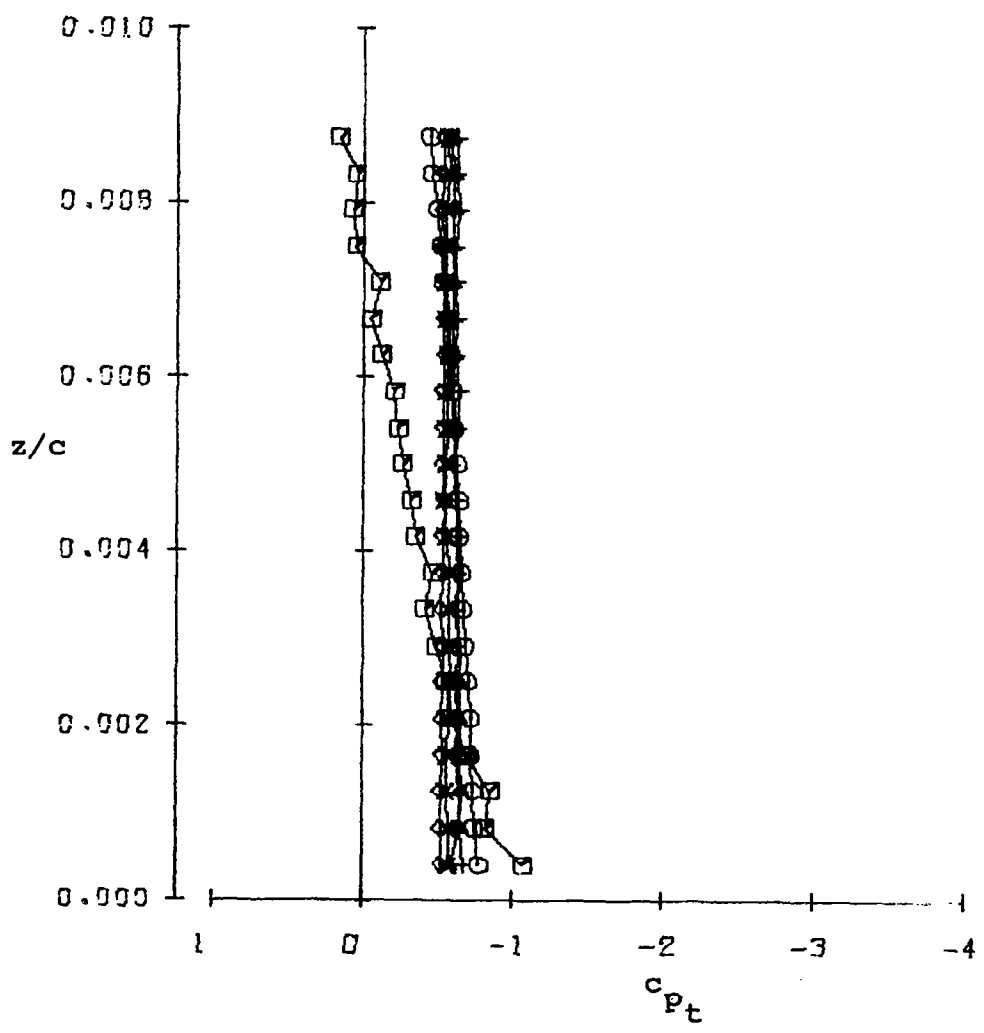
SYMBOL	LOCATION
◻	0.600 x/c
⊙	0.800 x/c
△	1.005 x/c
+	0.075 x_f/c
×	0.150 x_f/c
◇	0.300 x_f/c



(b) Static Pressure.

Figure 26 - Continued.

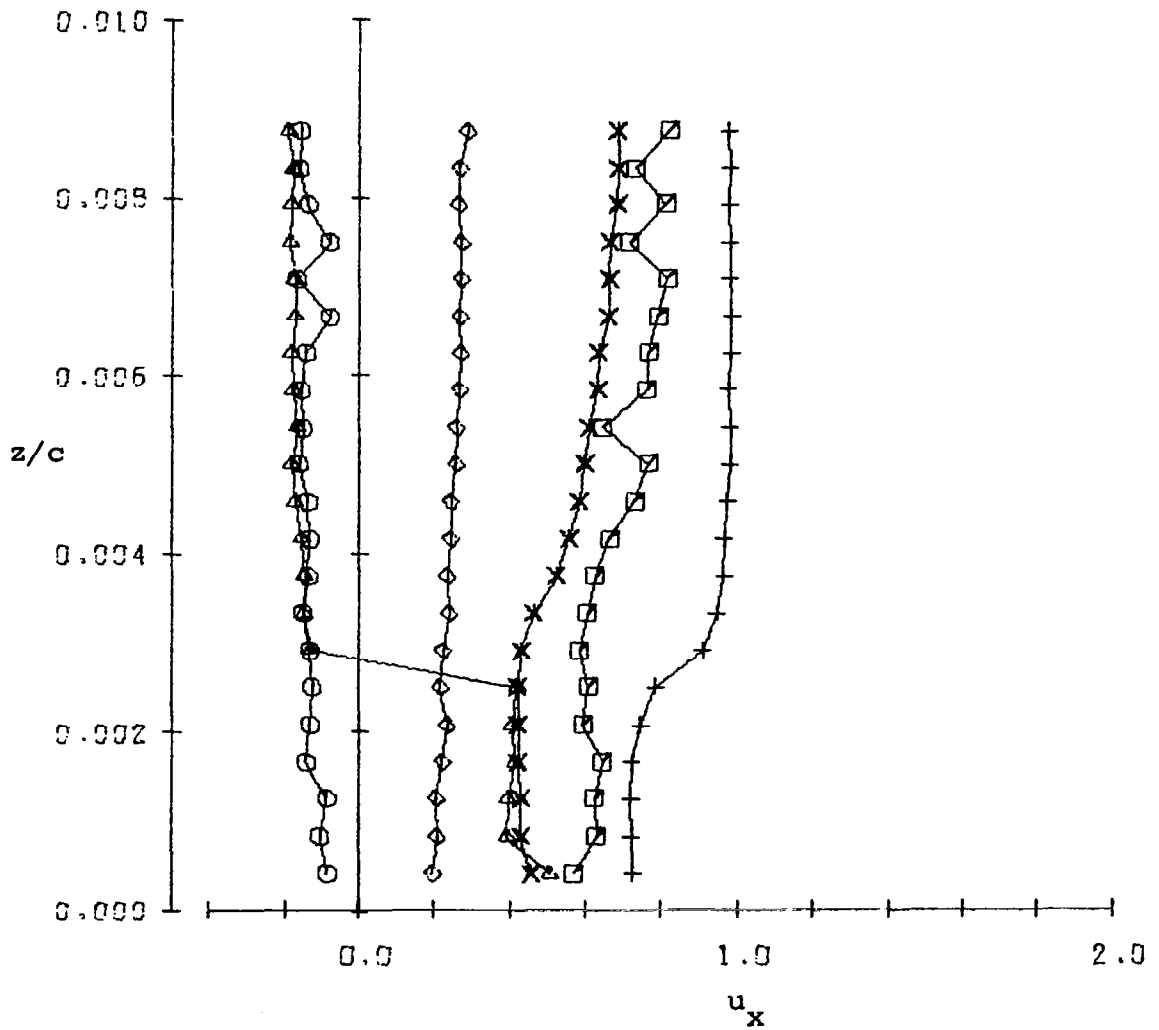
SYMBOL	LOCATION
□	0.600 x/c
⊙	0.800 x/c
△	1.005 x/c
+	0.075 x _f /c
×	0.150 x _f /c
◇	0.300 x _f /c



(c) Total Pressure.

Figure 26 - Concluded.

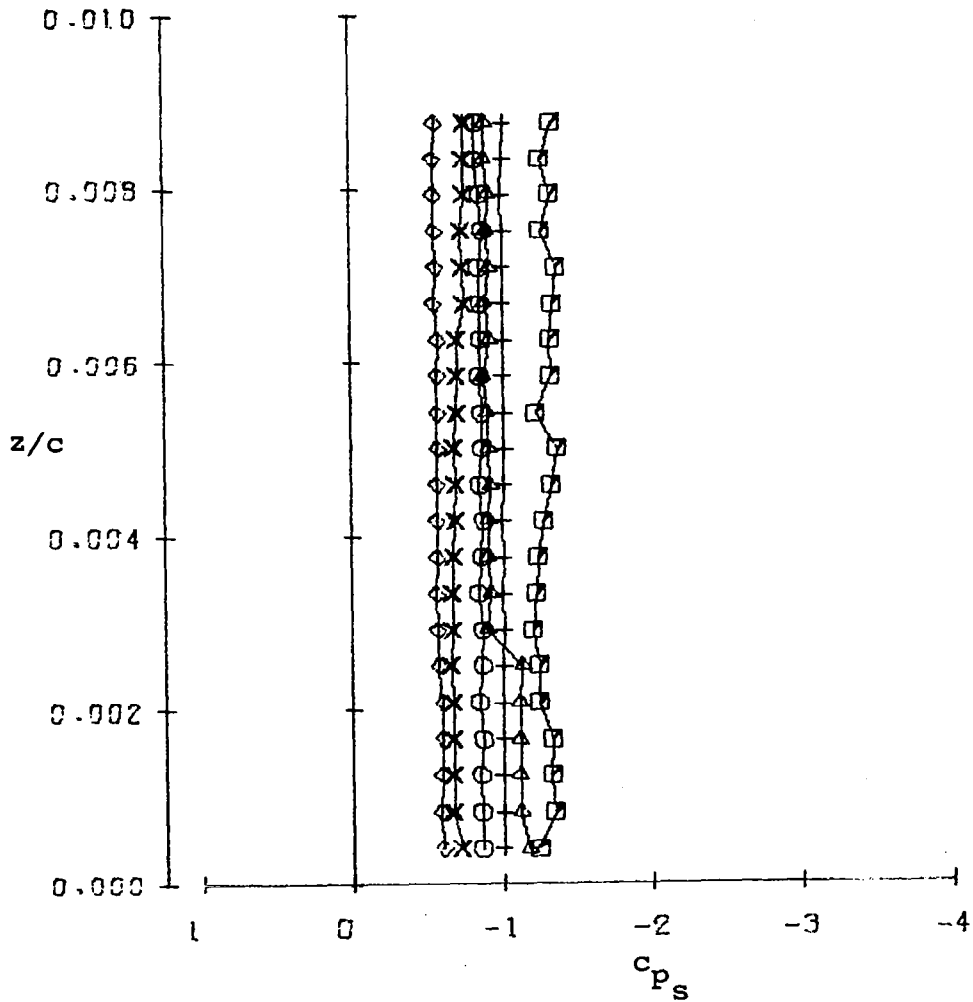
SYMBOL	LOCATION
◻	0.600 x/c
○	0.800 x/c
△	1.005 x/c
+	0.075 x _f /c
×	0.150 x _f /c
◇	0.300 x _f /c



(a) Velocity.

Figure 27- Boundary Layer Characteristics, gap = .02c, $\alpha = 12.7^\circ$

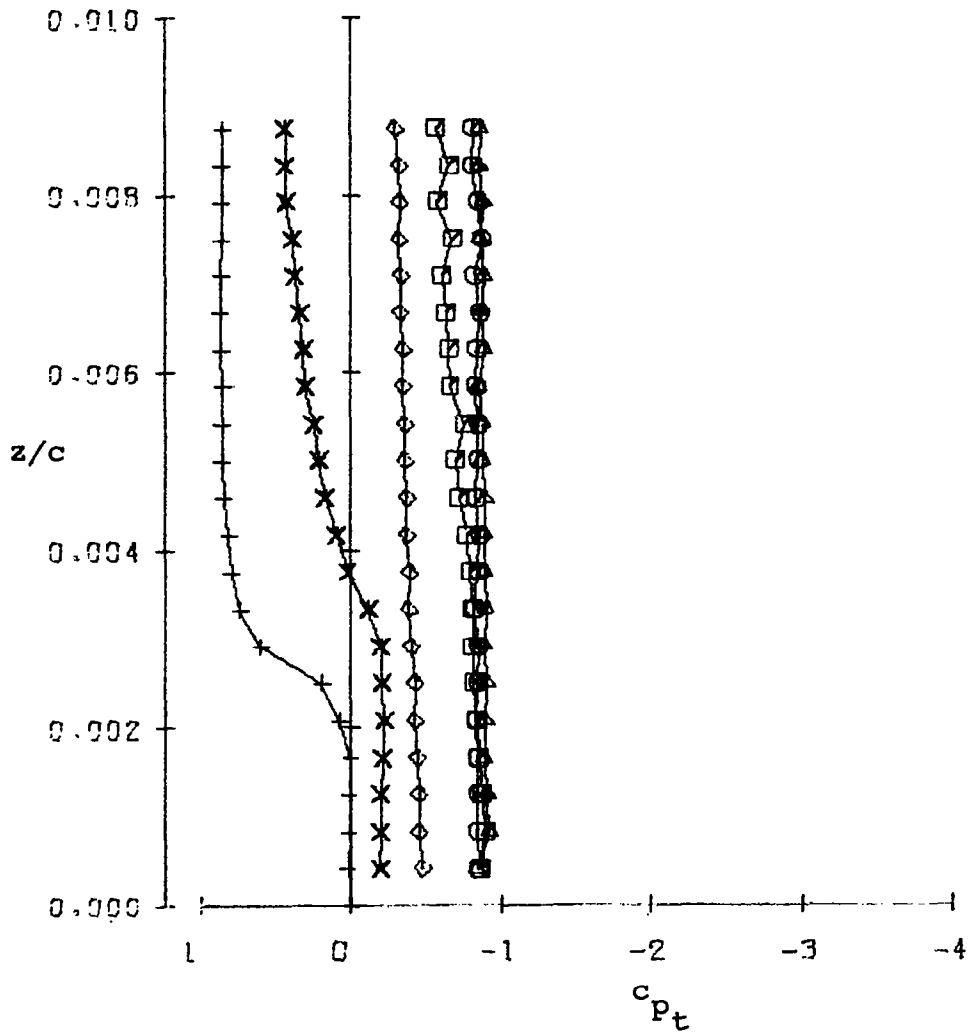
SYMBOL	LOCATION
□	0.600 x/c
⊙	0.800 x/c
△	1.005 x/c
+	0.075 x _f /c
×	0.150 x _f /c
◇	0.300 x _f /c



(b) Static Pressure.

Figure 27 - Continued.

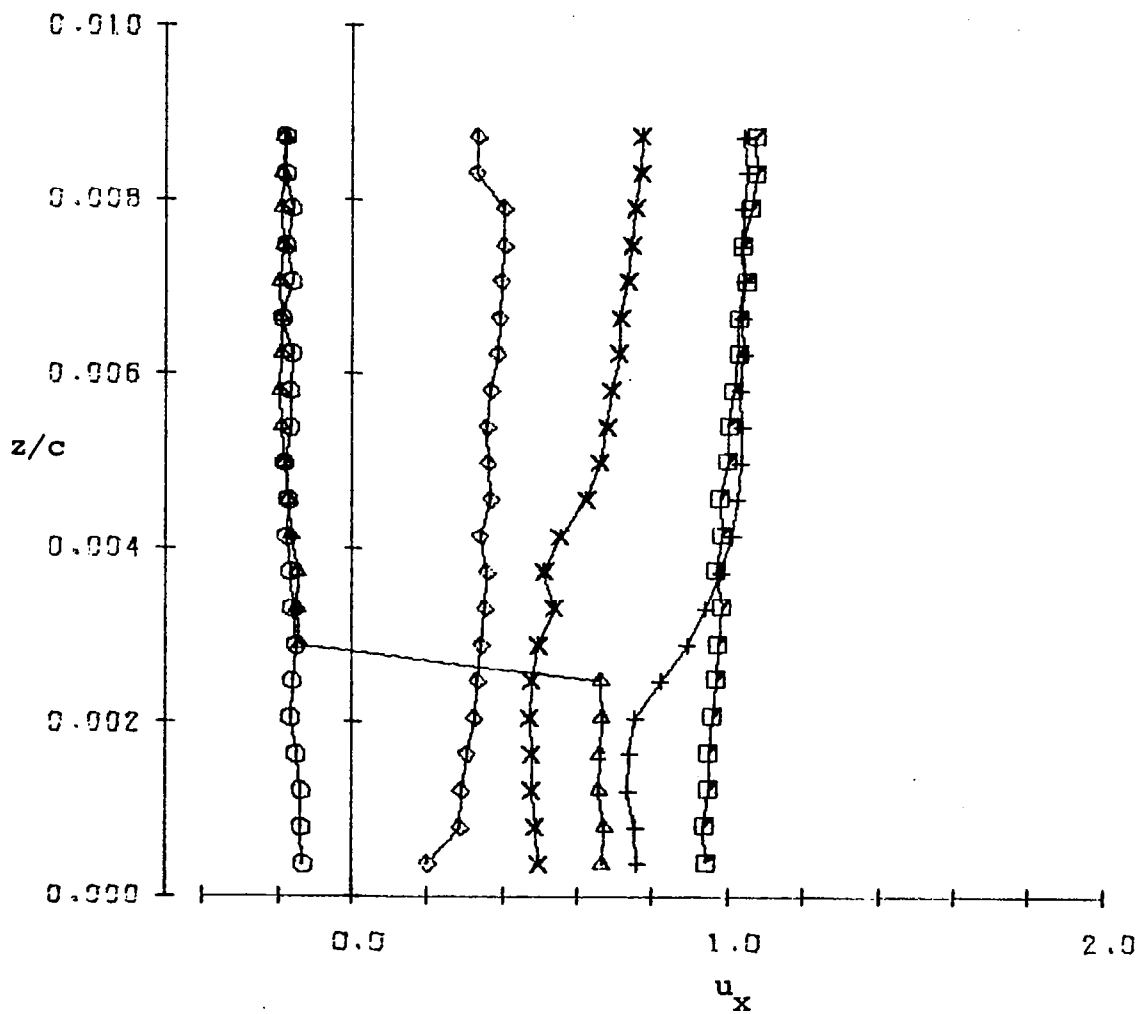
SYMBOL	LOCATION
□	0.600 x/c
○	0.800 x/c
△	1.005 x/c
+	0.075 x _f /c
×	0.150 x _f /c
◇	0.300 x _f /c



(c) Total Pressure.

Figure 27 - Concluded.

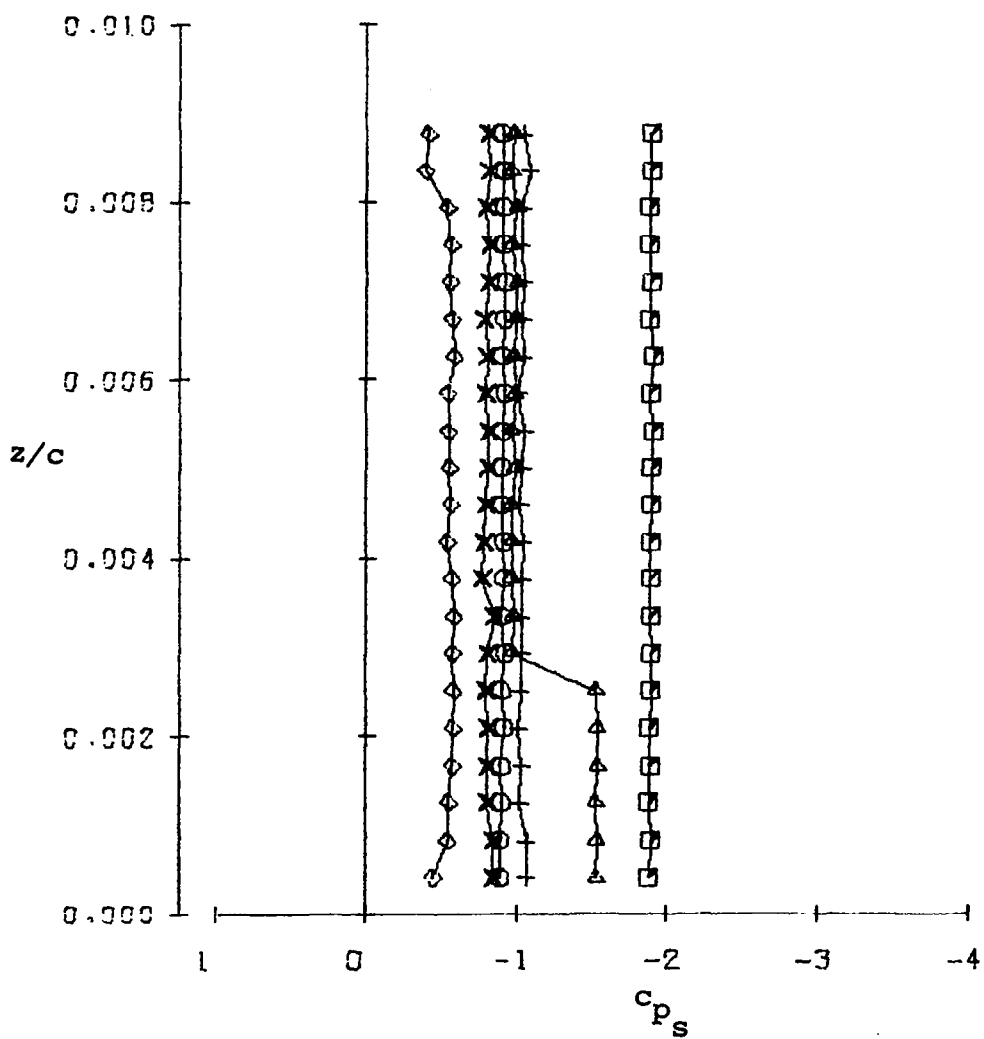
SYMBOL	LOCATION
◻	0.600 x/c
○	0.800 x/c
△	1.005 x/c
+	0.075 x_f/c
×	0.150 x_f/c
◇	0.300 x_f/c



(a) Velocity.

Figure 28 - Boundary Layer Characteristics, gap = .03c, $\alpha = 12.7^\circ$

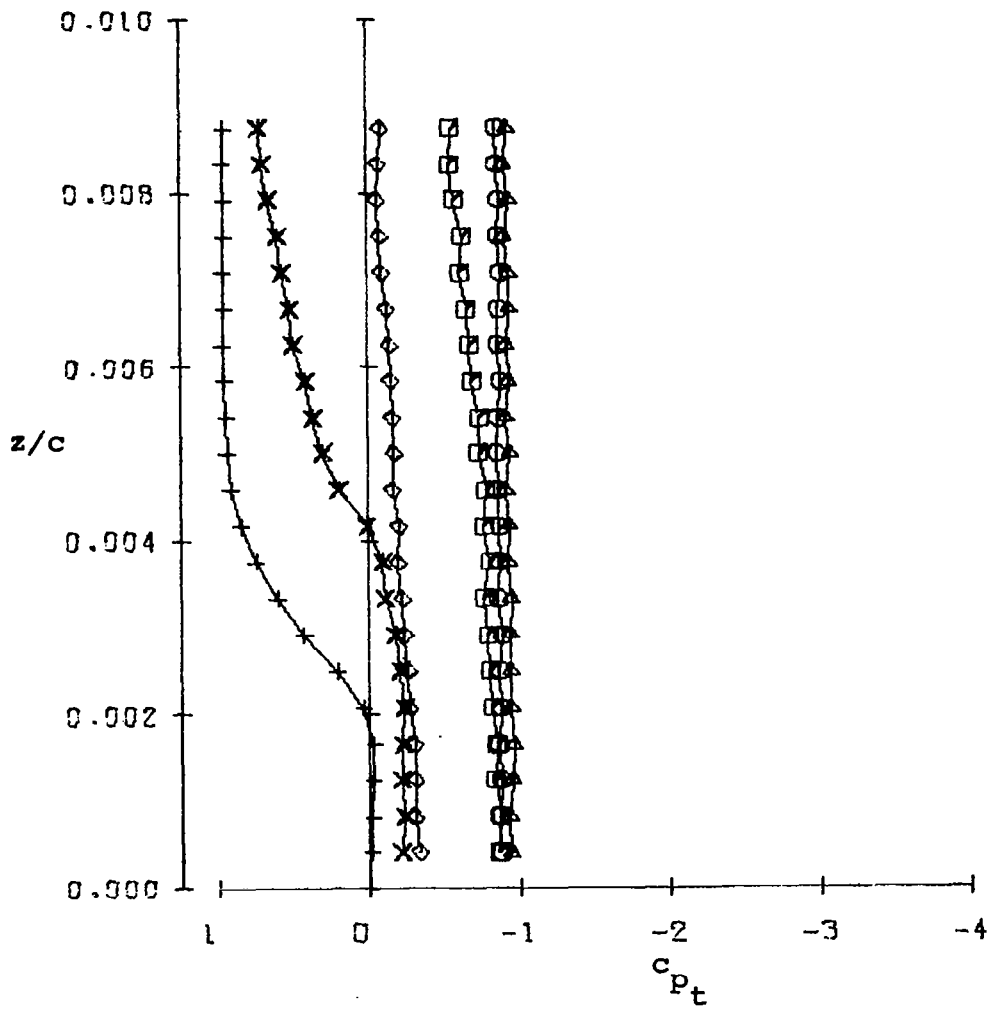
SYMBOL	LOCATION
◻	0.600 x/c
⊙	0.800 x/c
△	1.005 x/c
+	0.075 x _f /c
×	0.150 x _f /c
◇	0.300 x _f /c



(b) Static Pressure.

Figure 28 - Continued.

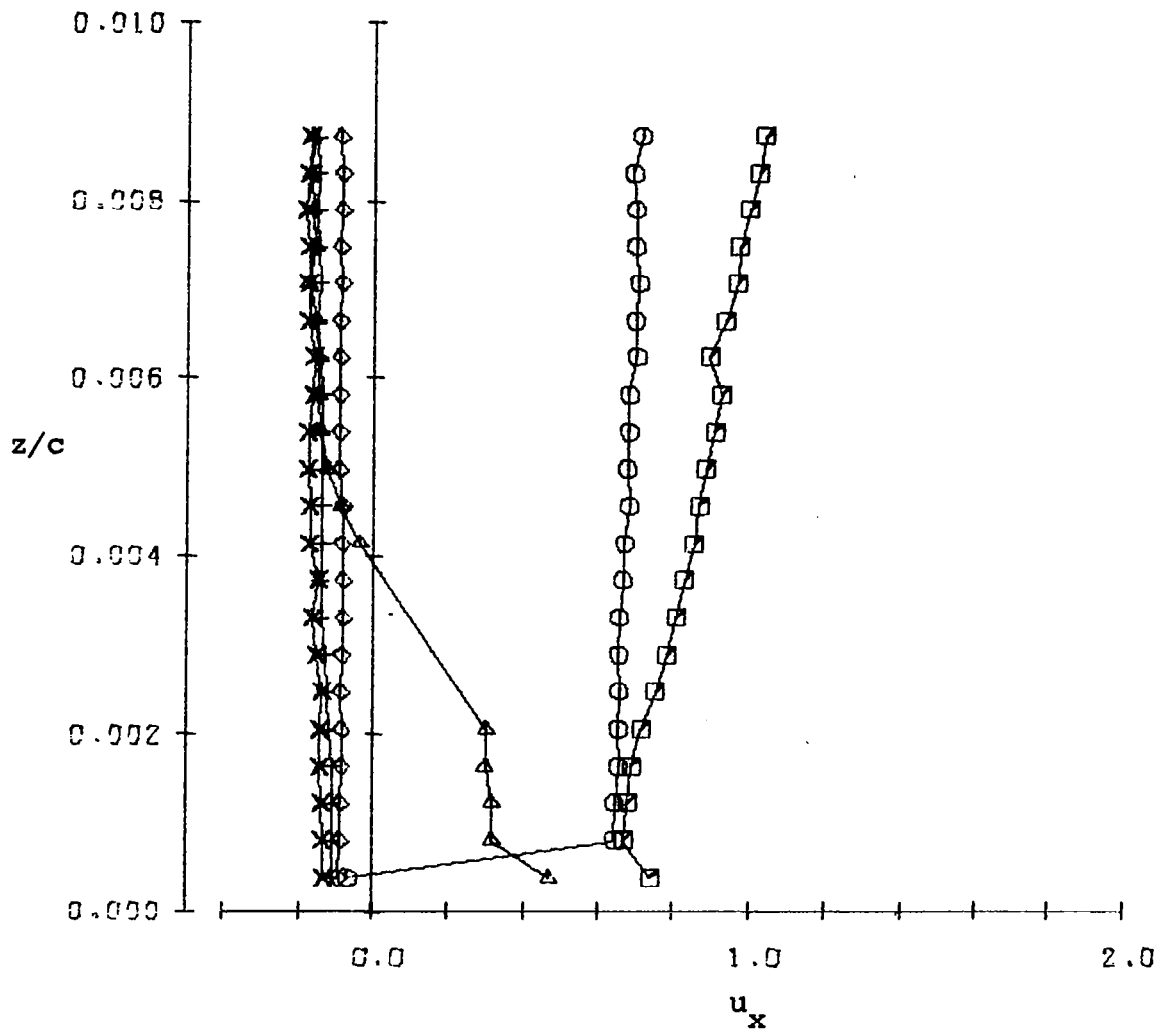
SYMBOL	LOCATION
□	0.600 x/c
○	0.800 x/c
△	1.005 x/c
+	0.075 x _f /c
×	0.150 x _f /c
◇	0.300 x _f /c



(c) Total Pressure.

Figure 28- Concluded.

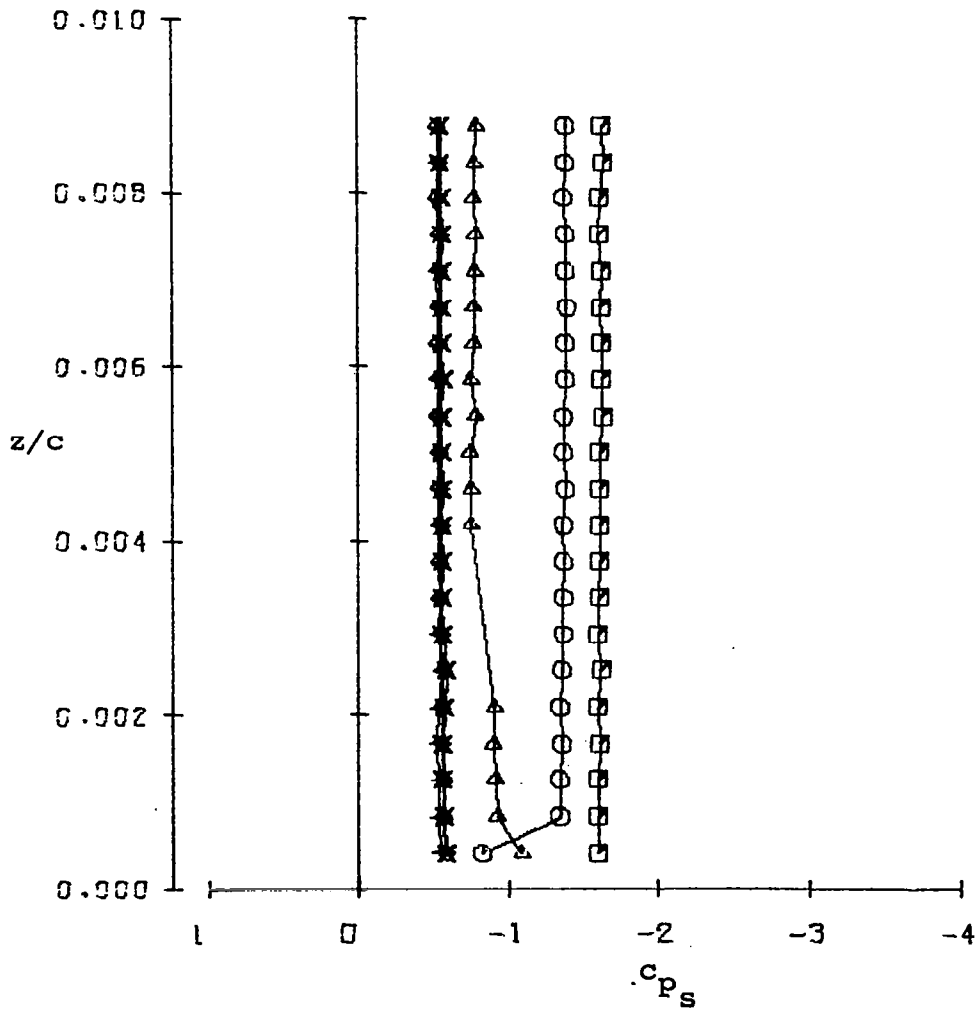
SYMBOL	LOCATION
◻	0.600 x/c
○	0.800 x/c
△	1.005 x/c
+	0.075 x _f /c
×	0.150 x _f /c
◇	0.300 x _f /c



(a) Velocity.

Figure 29- Boundary Layer Characteristics, gap = .05c, $\alpha = 12.7^\circ$

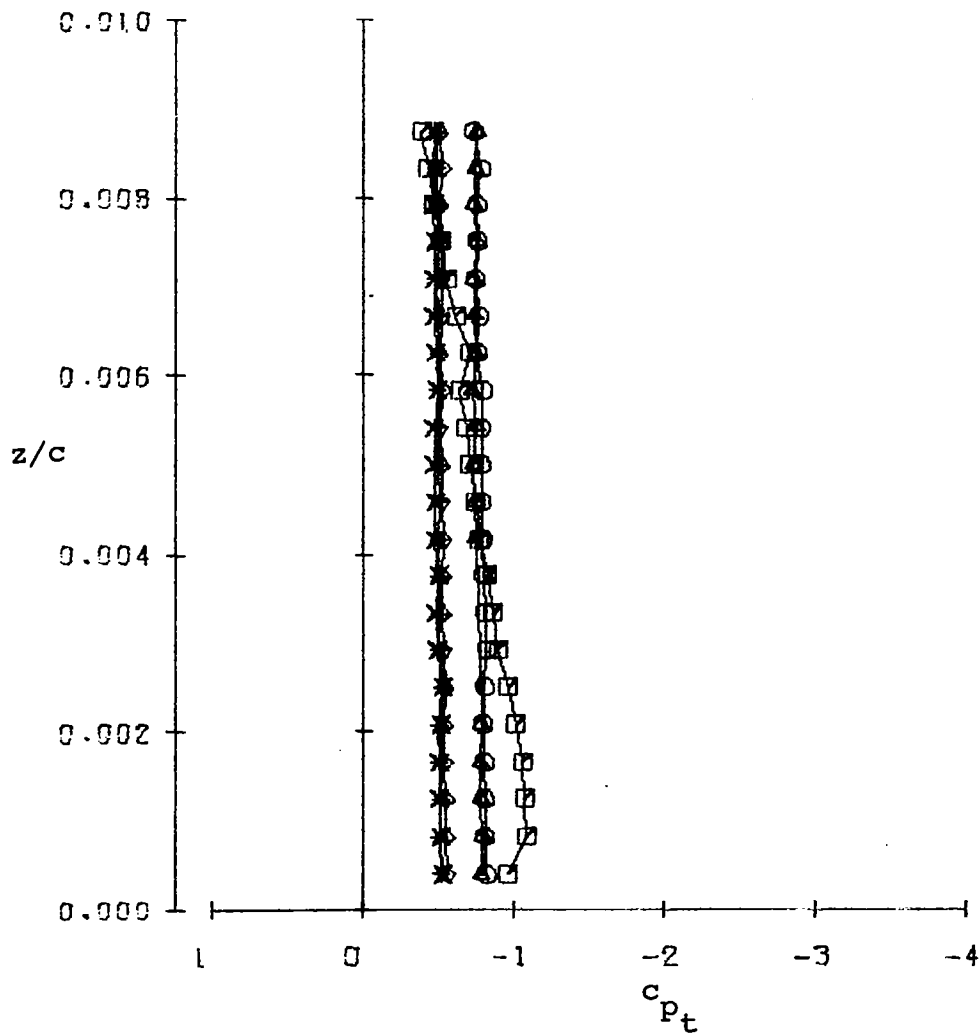
SYMBOL	LOCATION
◻	0.600 x/c
○	0.800 x/c
△	1.005 x/c
+	0.075 x _f /c
×	0.150 x _f /c
◇	0.300 x _f /c



(b) Static Pressure.

Figure 29 - Continued.

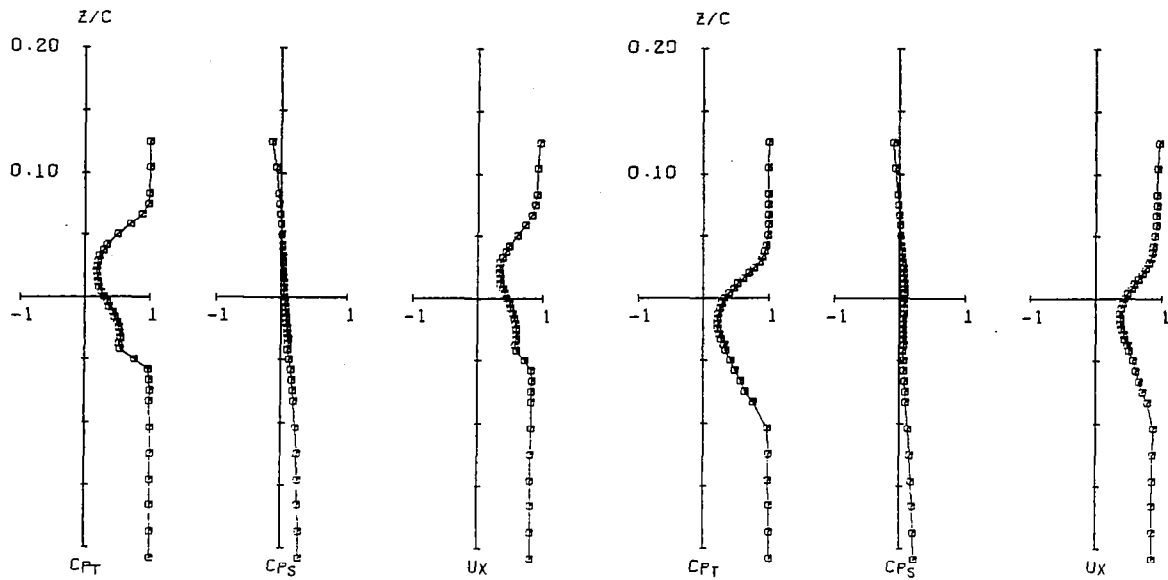
SYMBOL	LOCATION
◻	0.600 x/c
⊙	0.800 x/c
△	1.005 x/c
+	0.075 x _f /c
×	0.150 x _f /c
◇	0.300 x _f /c



(c) Total Pressure.

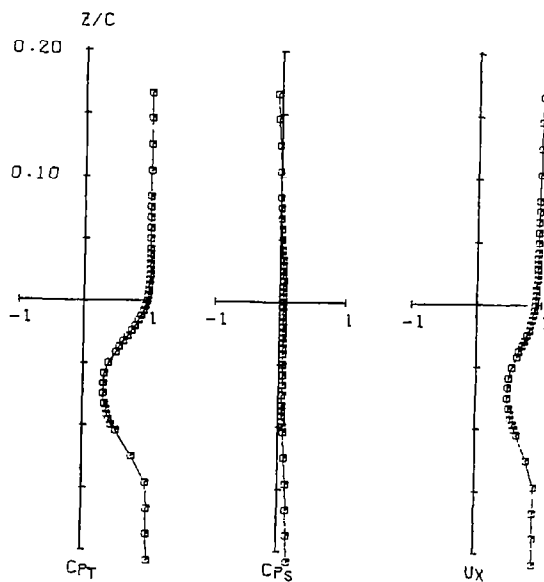
Figure 29 - Concluded.

□ - Five Tube



(a) $x_w/c = .075$

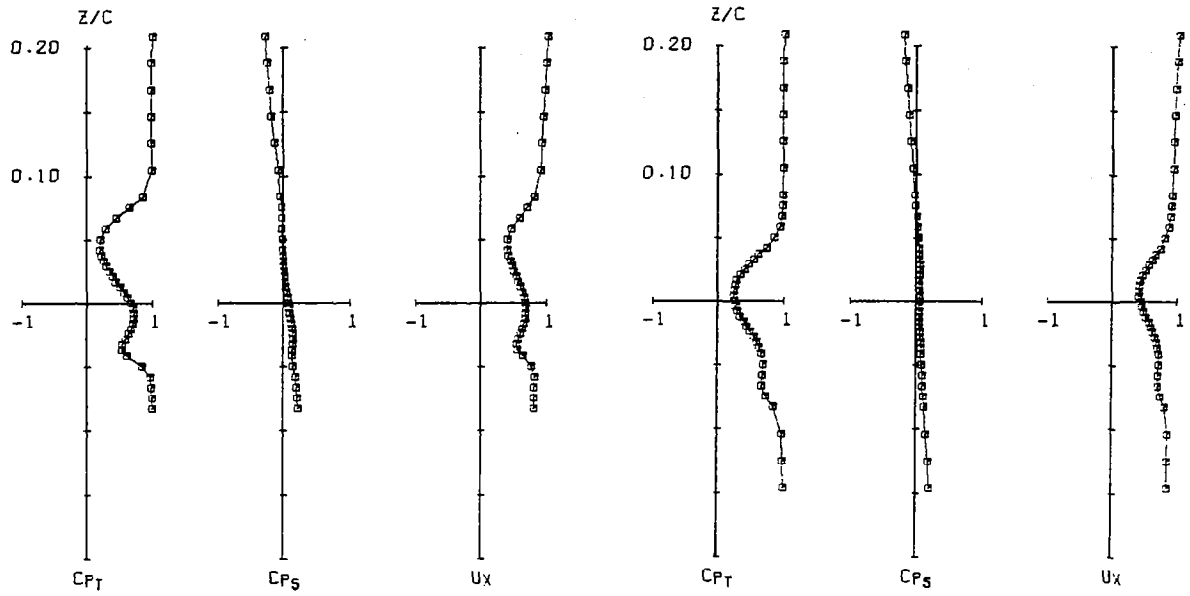
(b) $x_w/c = .150$



(c) $x_w/c = .300$

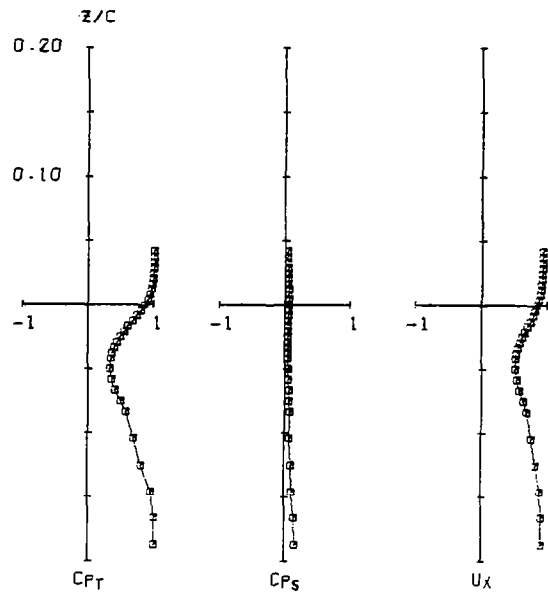
Figure 30 - Wake Characteristics, gap = $.02c$, $\alpha = 5.2^\circ$

□ - Five Tube



(a) $x_w/c = .075$

(b) $x_w/c = .150$



(c) $x_w/c = .300$

Figure 31 - Wake Characteristics, $gap = .03c$, $\alpha = 5.2^\circ$.

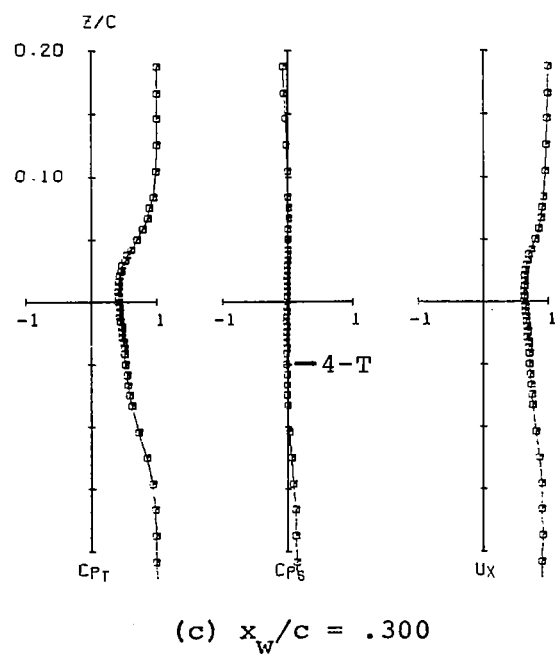
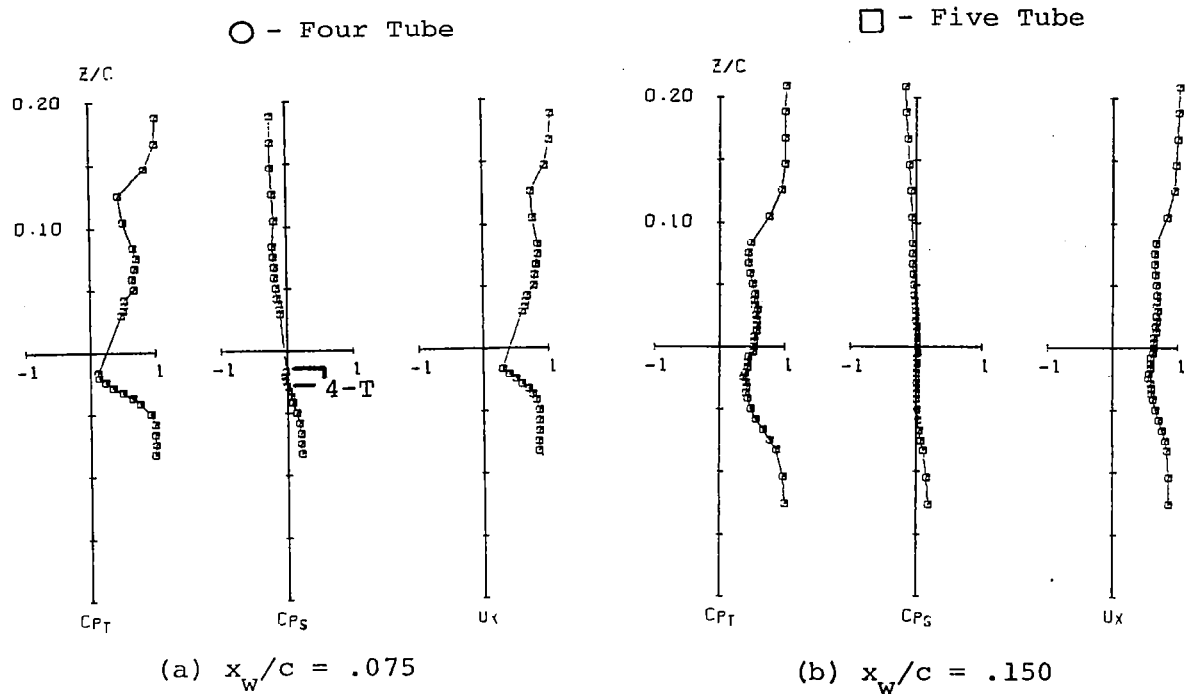
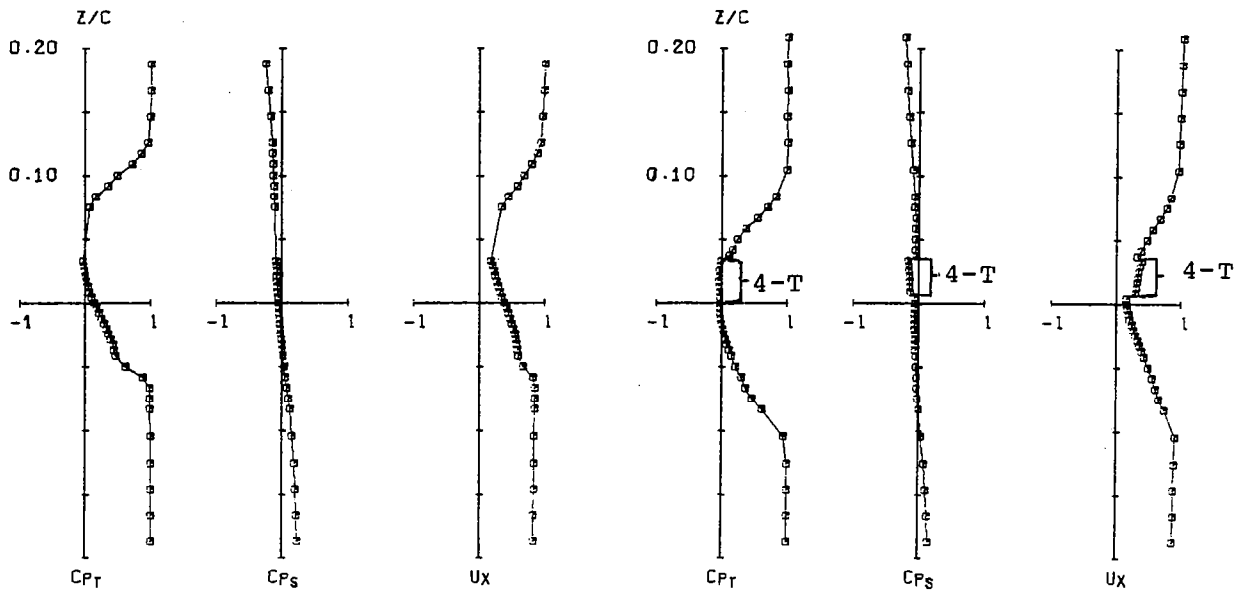


Figure 32 - Wake Characteristics, $gap = .05c$, $\alpha = 5.2^\circ$.

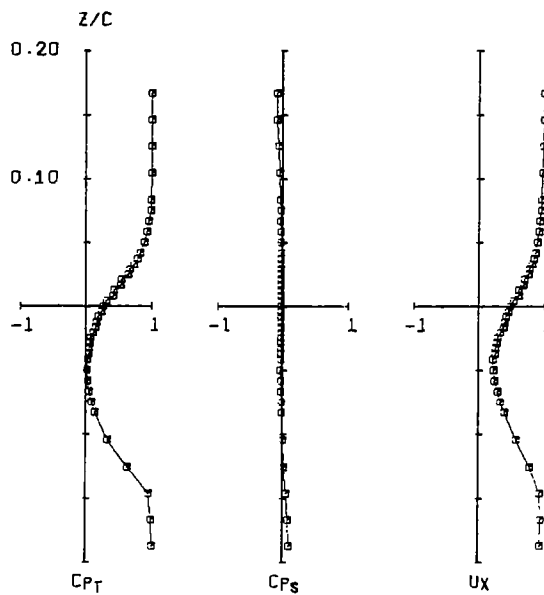
○ - Four Tube

□ - Five Tube



(a) $x_w/c = .075$

(b) $x_w/c = .150$



(c) $x_w/c = .300$

Figure 33 - Wake Characteristics, gap = .02c, $\alpha = 10.3^\circ$

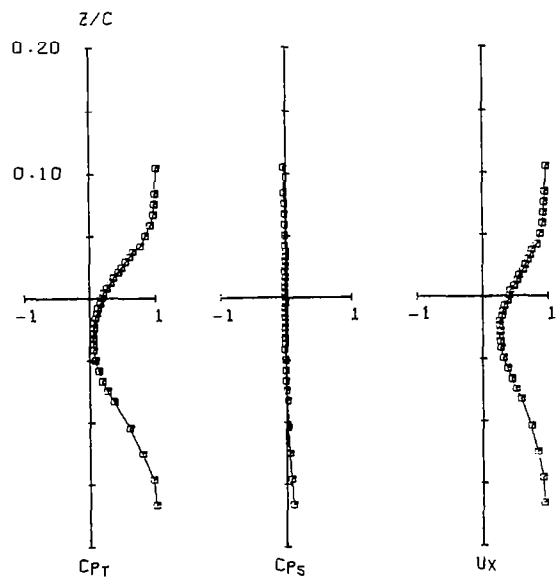
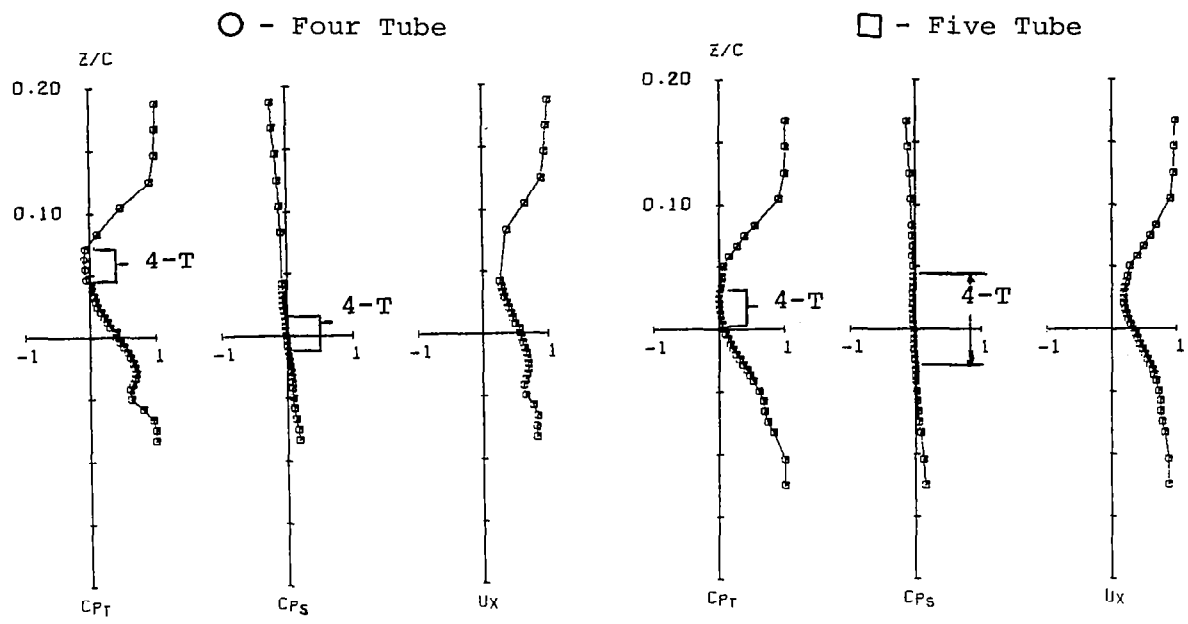
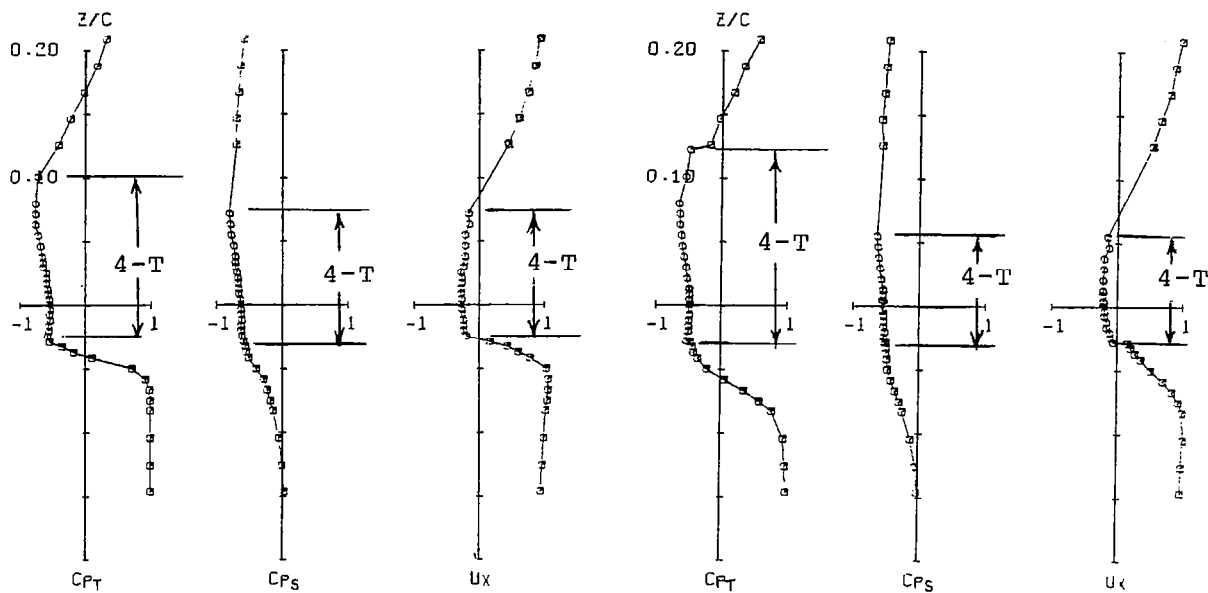


Figure 34 - Wake Characteristics, gap = .03c, $\alpha = 10.3^\circ$

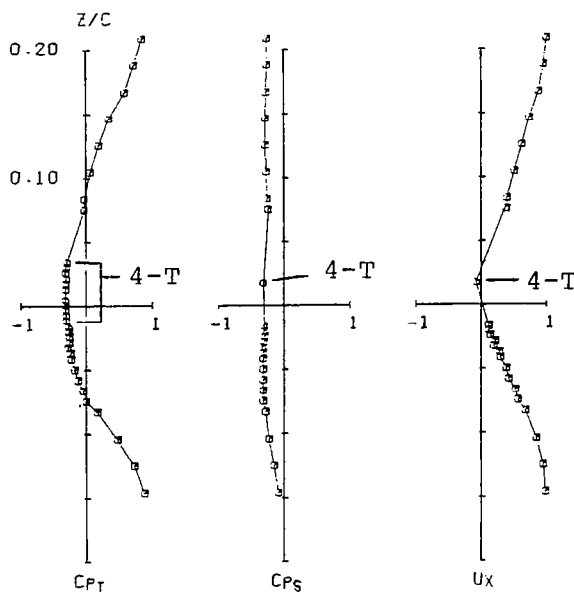
○ - Four Tube

□ - Five Tube



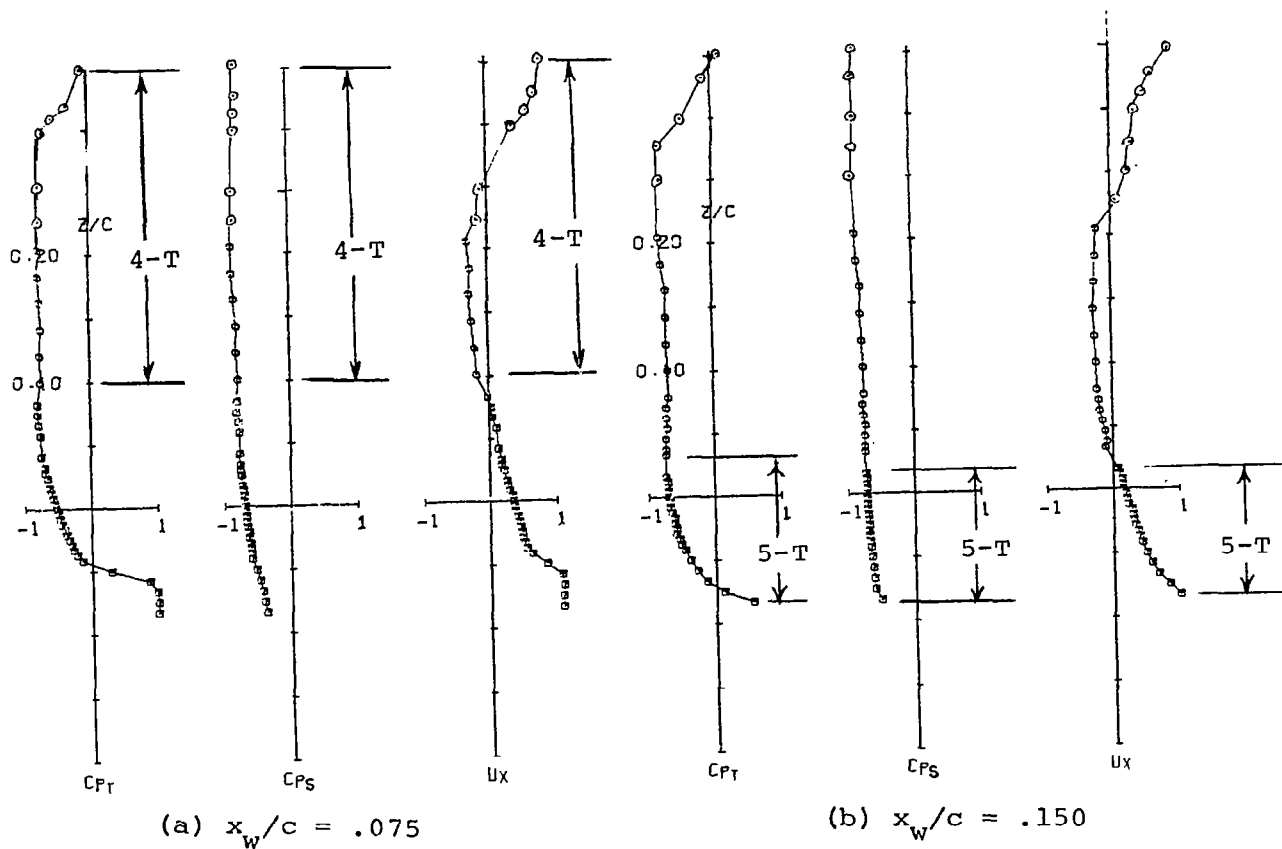
(a) $x_w/c = .075$

(b) $x_w/c = .150$



(c) $x_w/c = .300$

Figure 35 - Wake Characteristics, gap = .05c, $\alpha = 10.3^\circ$



○ - Four Tube
 □ - Five Tube

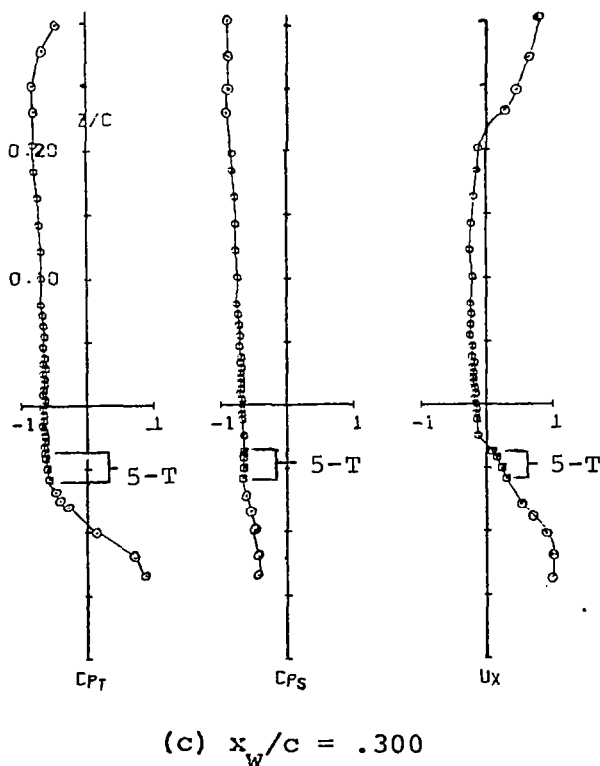


Figure 36 - Wake Characteristics, gap = $.02c$, $\alpha = 12.7^\circ$

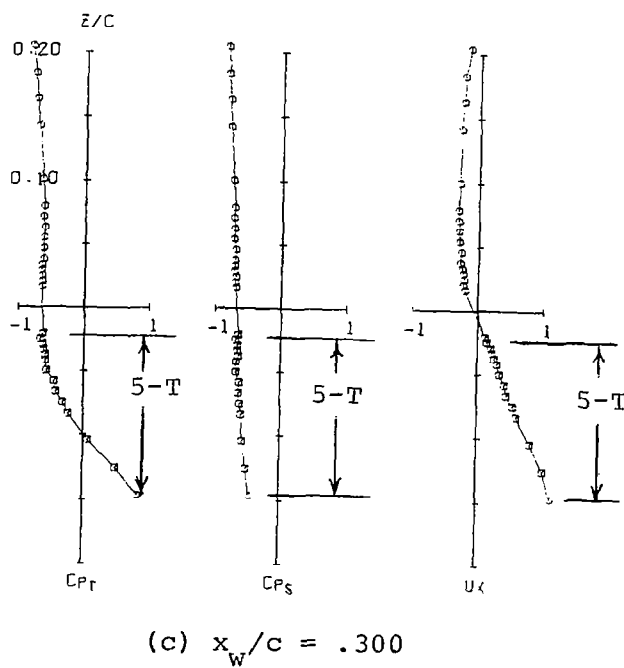
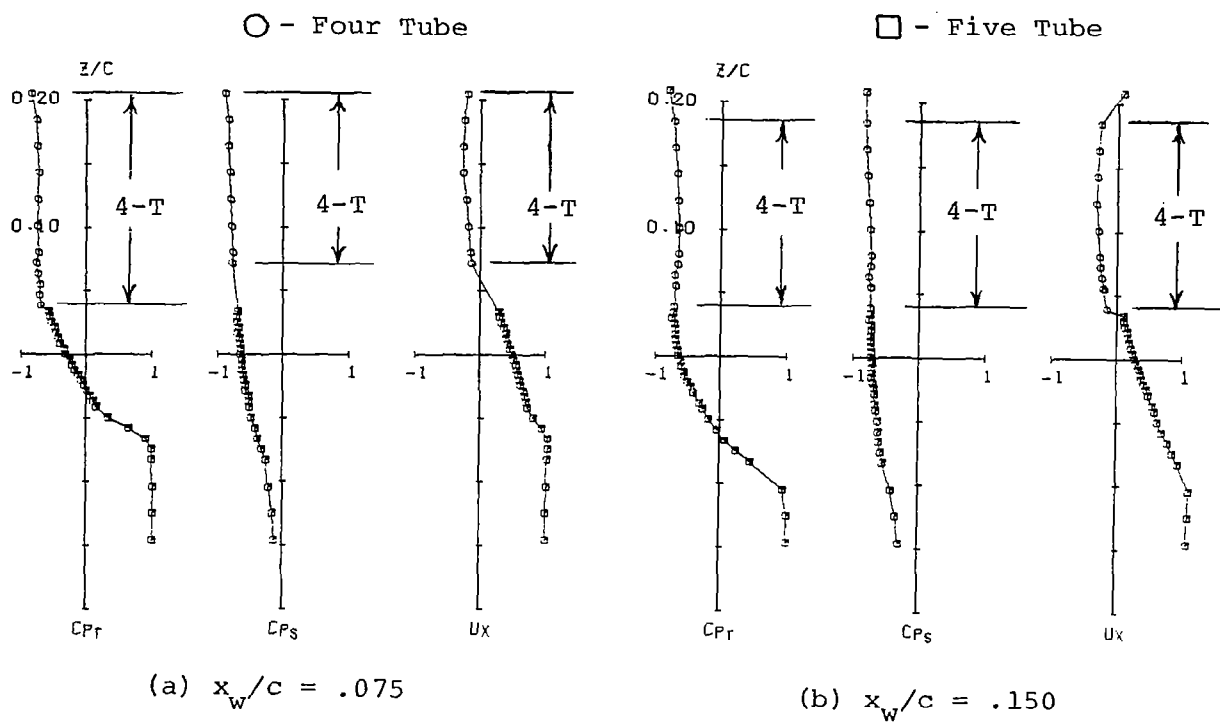
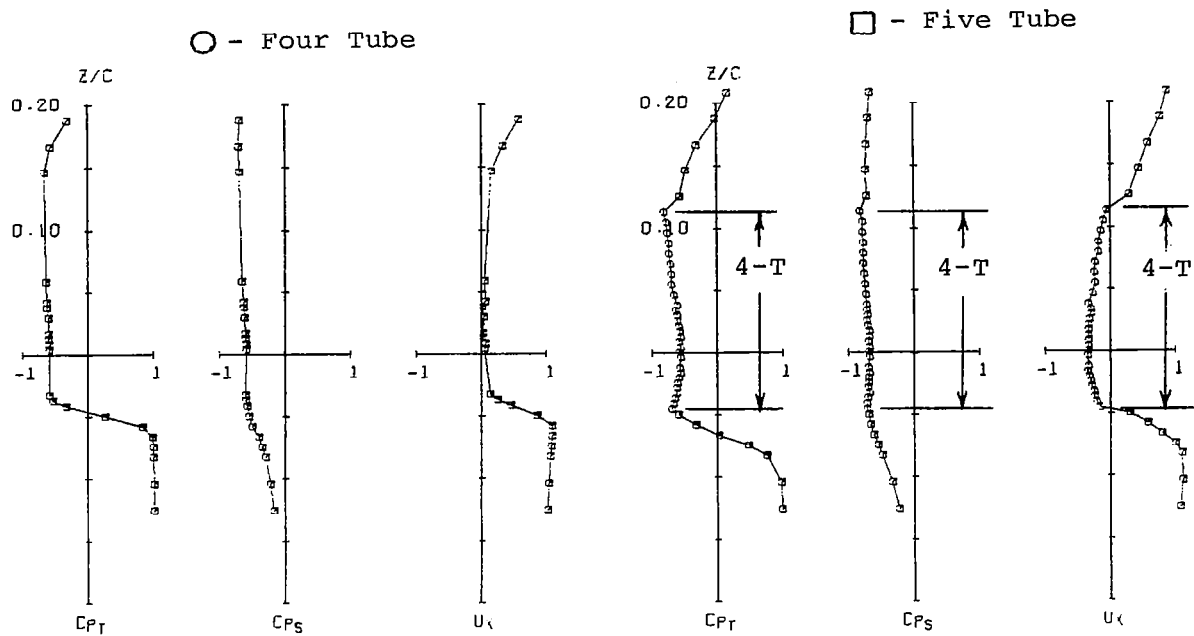
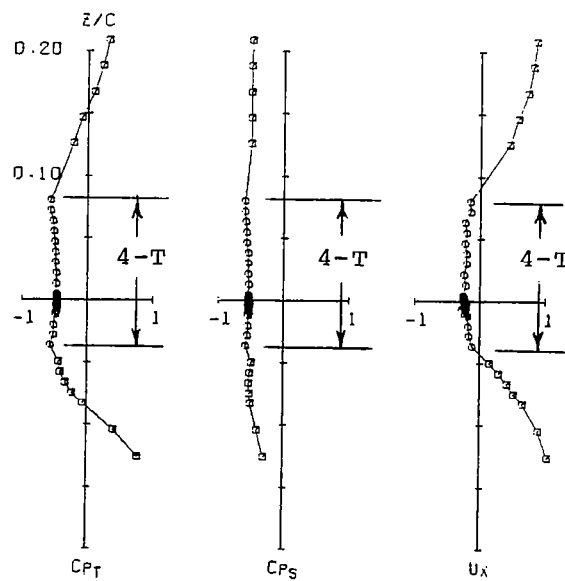


Figure 37 - Wake Characteristics, gap = .03c, $\alpha = 12.7^\circ$



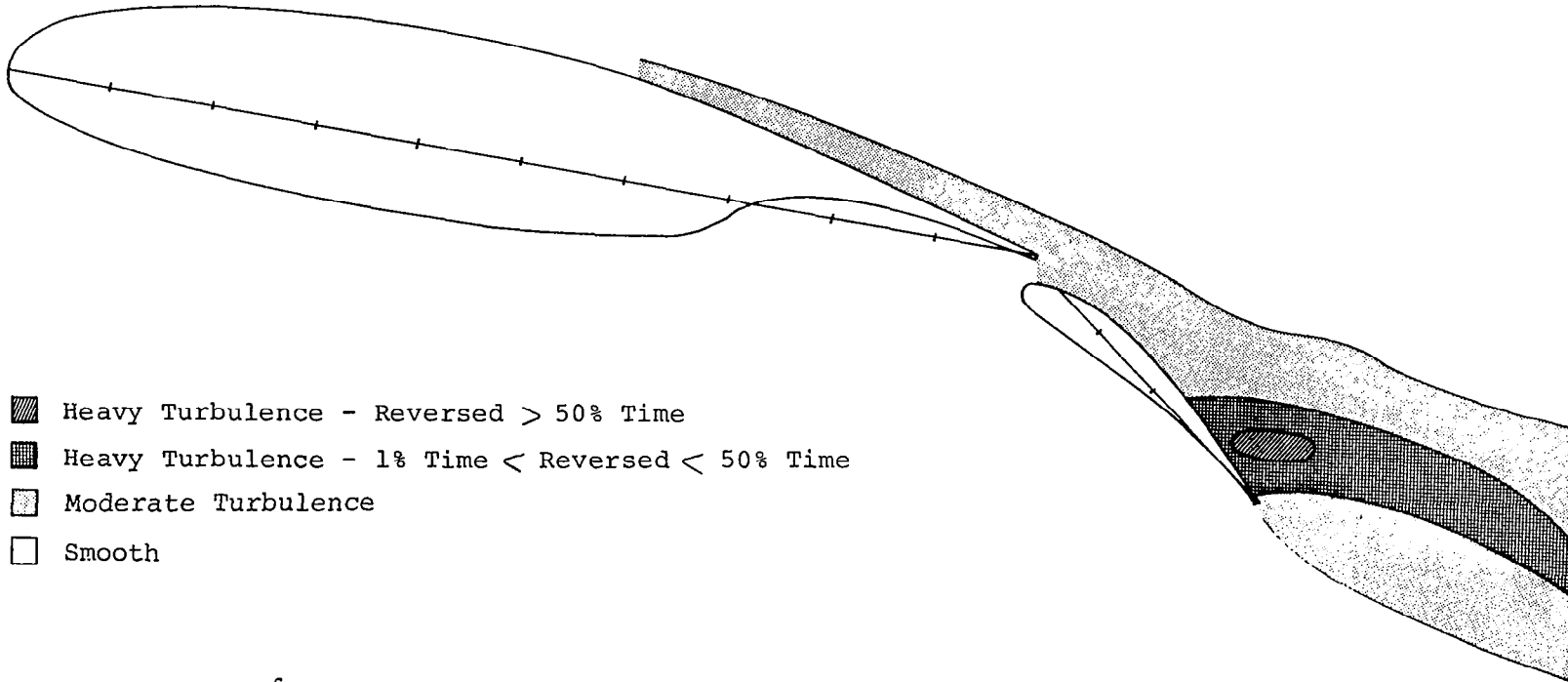
(a) $x_w/c = .075$

(b) $x_w/c = .150$



(c) $x_w/c = .300$

Figure 38 - Wake Characteristics, gap = $.05c$, $\alpha = 12.7^\circ$



$RN = 2.2 \times 10^6$
 Mach No. = 0.13

(a) Gap = $.02c$

Figure 40-Split Film Velocity Field Surveys, $\alpha = 10.3^\circ$

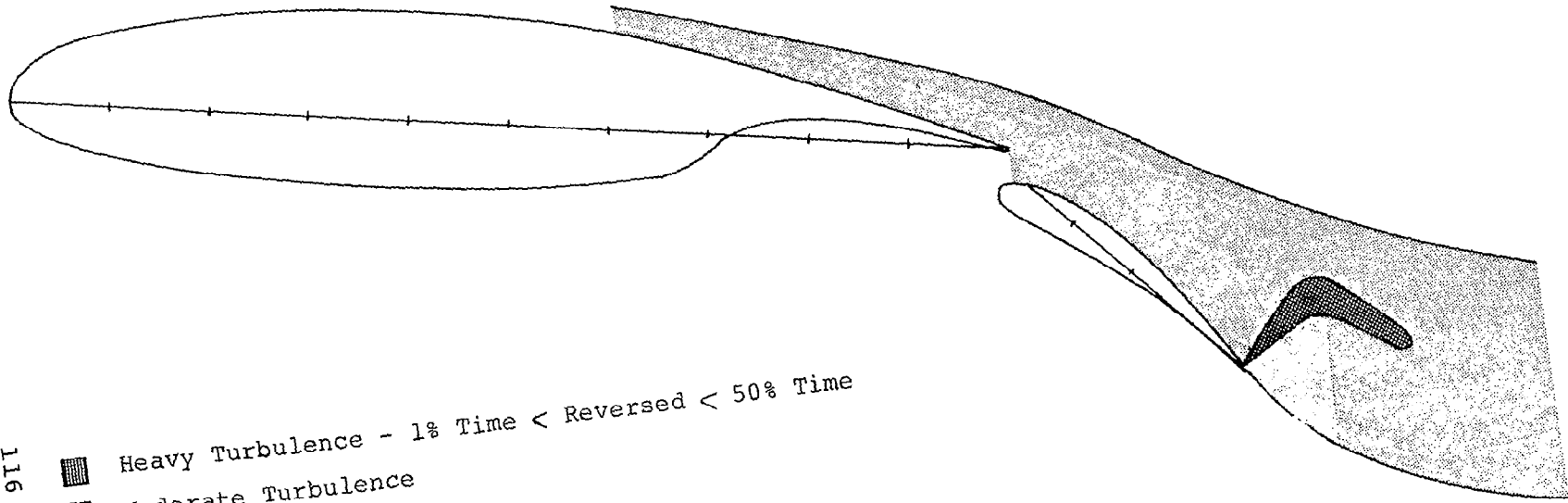
116

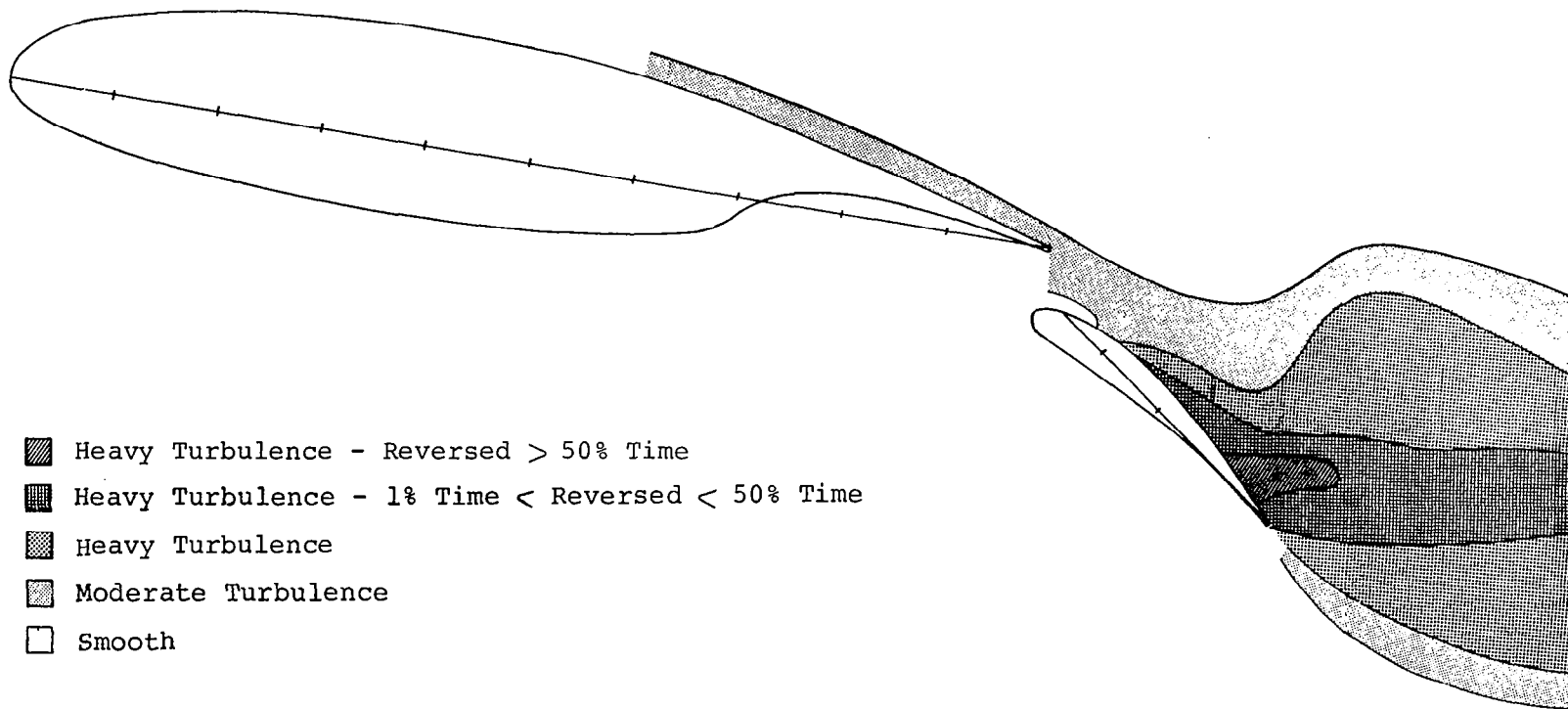
- Heavy Turbulence - 1% Time < Reversed < 50% Time
- ▒ Moderate Turbulence
- Smooth

$RN = 2.2 \times 10^6$
Mach No. = 0.13

(b) Gap = .03 c

Figure 40 - Continued

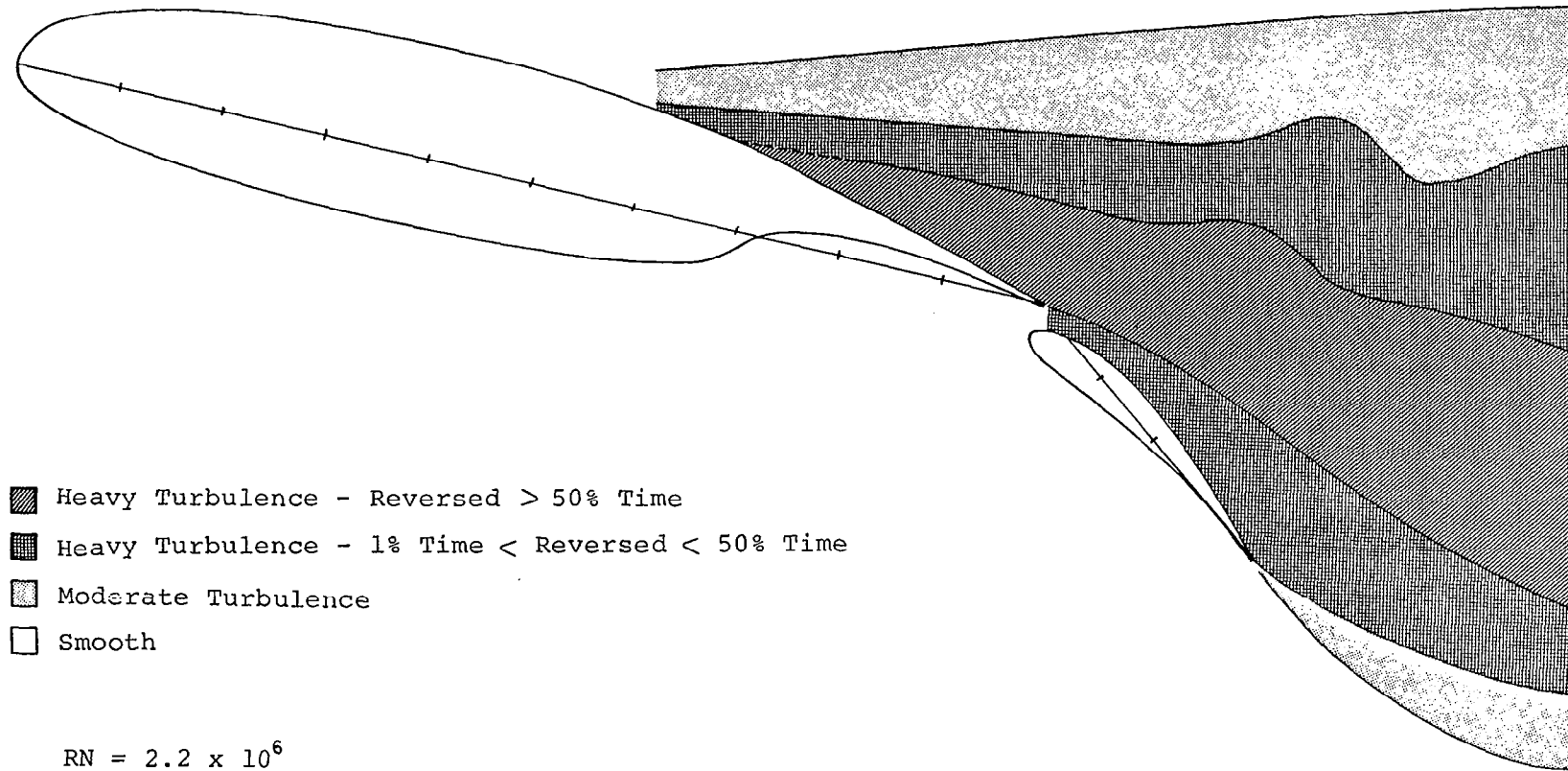




$RN = 2.2 \times 10^6$
Mach No. = 0.13

(c) Gap = .05 c

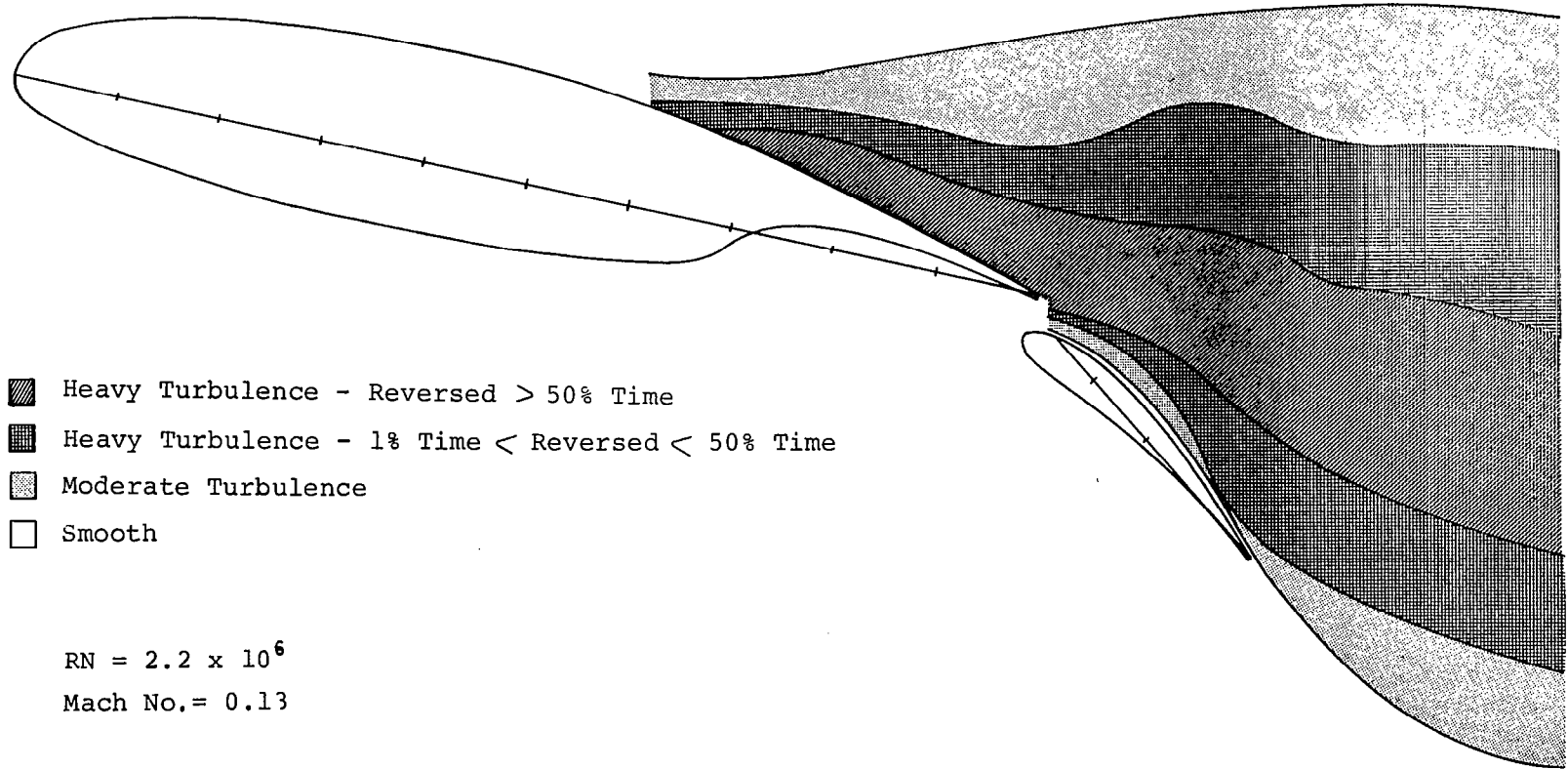
Figure 40 - Concluded



$RN = 2.2 \times 10^6$
 Mach No. = 0.13

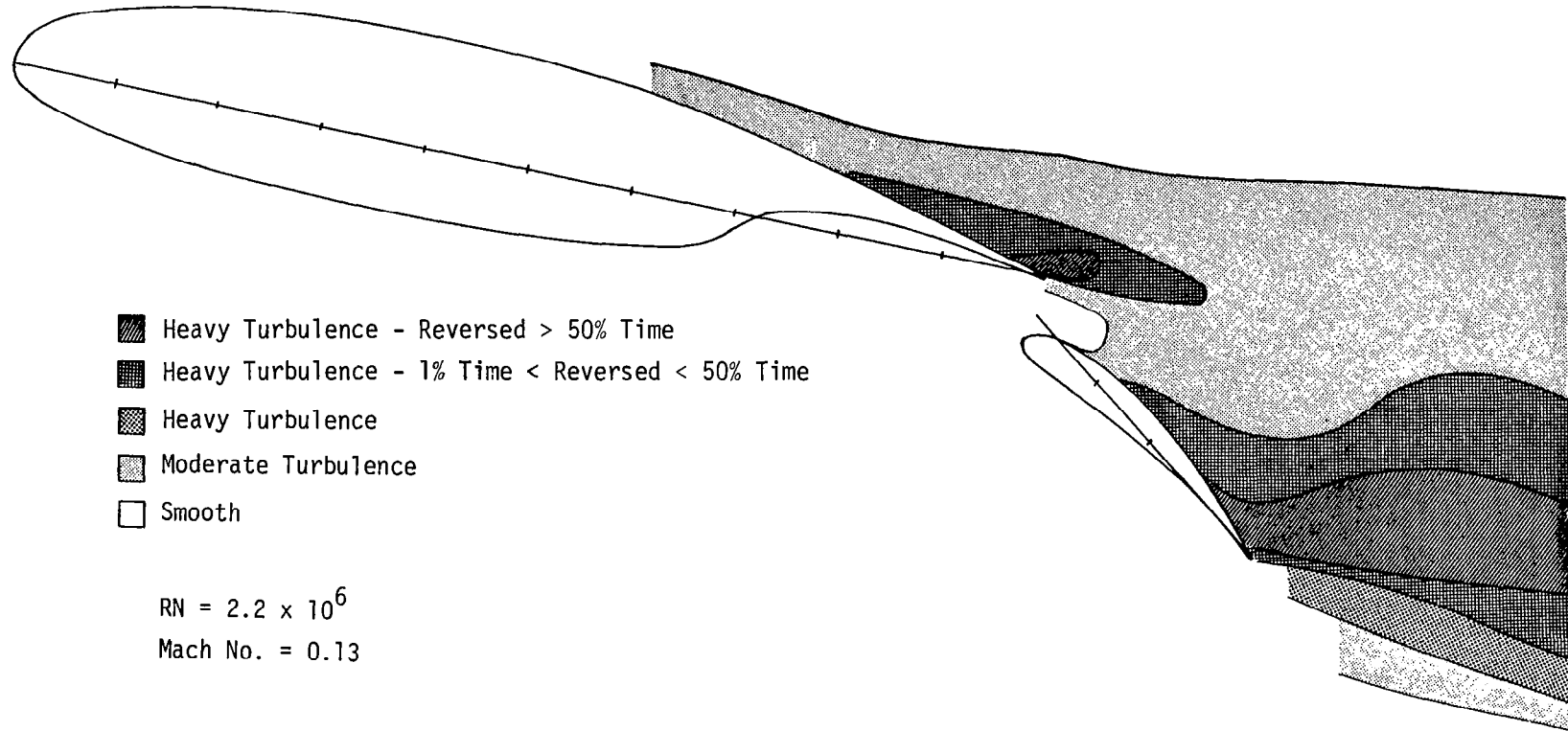
(a) Gap = .02 c

Figure 41-Split Film Velocity Field Surveys, $\alpha = 12.7^\circ$



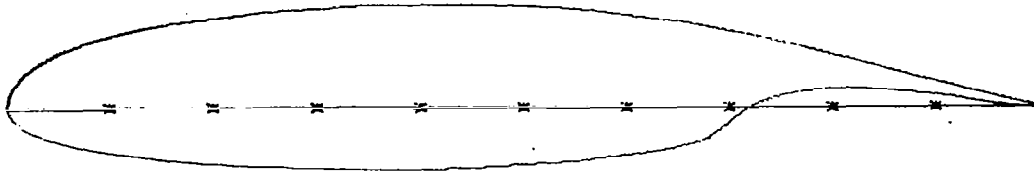
(b) Gap = .03 c

Figure 41 - Continued



(c) Gap = .05

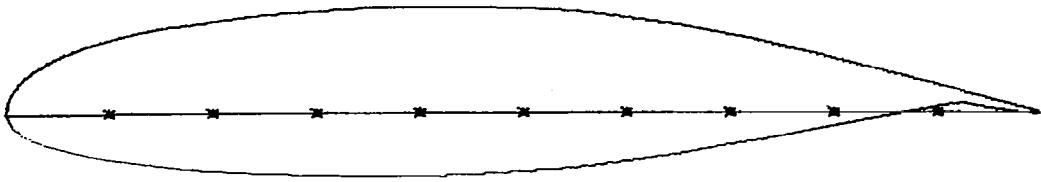
Figure 41 - Concluded



<u>UPPER SURFACE</u>		<u>LOWER SURFACE</u>	
x/c	z/c	x/c	z/c
0.0000	0.0000	0.0000	0.0000
.0020	.0130	.0020	-.0093
.0050	.0204	.0050	-.0138
.0125	.0307	.0125	-.0205
.0250	.0417	.0250	-.0269
.0375	.0497	.0375	-.0319
.0500	.0559	.0500	-.0358
.0750	.0655	.0750	-.0421
.1000	.0730	.1000	-.0470
.1250	.0790	.1250	-.0510
.1500	.0840	.1500	-.0543
.1750	.0884	.1750	-.0570
.2000	.0920	.2000	-.0593
.2500	.0977	.2500	-.0627
.3000	.1016	.3000	-.0645
.3500	.1040	.3500	-.0652
.4000	.1049	.4000	-.0649
.4500	.1045	.4500	-.0635
.5000	.1026	.5000	-.0610
.5500	.0991	.5500	-.0570
.5750	.0967	.5750	-.0540
.6000	.0937	.6000	-.0508
.6250	.0901	.6250	-.0469
.6500	.0860	.6500	-.0428
.6750	.0814	.6750	-.0348
.7000	.0763	.7000	-.0289
.7250	.0709	.7150	-.0035
.7500	.0651	.7250	.0025
.7750	.0591	.7500	.0110
.8000	.0529	.7750	.0163
.8250	.0465	.8000	.0190
.8500	.0399	.8250	.0195
.8750	.0332	.8750	.0167
.9000	.0264	.9000	.0133
.9250	.0196	.9250	.0095
.9500	.0129	.9500	.0053
1.0000	-.0007	.9750	.0010
		1.0000	-.0044

(a) GA(W)-1 Standard Cove Airfoil

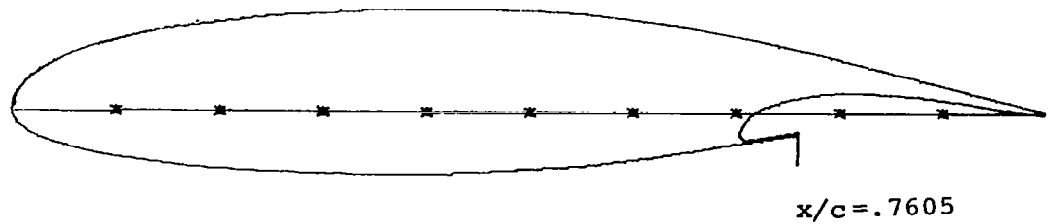
Figure 42- Geometry For Coves.



<u>UPPER SURFACE</u>		<u>LOWER SURFACE</u>	
x/c	z/c	x/c	z/c
0.0000	0.0000	0.0000	0.0000
.0020	.0130	.0020	-.0093
.0050	.0204	.0050	-.0138
.0125	.0307	.0125	-.0205
.0250	.0417	.0250	-.0269
.0375	.0497	.0375	-.0319
.0500	.0559	.0500	-.0358
.0750	.0655	.0750	-.0421
.1000	.0730	.1000	-.0470
.1250	.0790	.1250	-.0510
.1500	.0840	.1500	-.0543
.1750	.0884	.1750	-.0570
.2000	.0920	.2000	-.0593
.2500	.0977	.2500	-.0627
.3000	.1016	.3000	-.0645
.3500	.1040	.3500	-.0652
.4000	.1049	.4000	-.0649
.4500	.1045	.4500	-.0635
.5000	.1026	.5000	-.0610
.5500	.0991	.5500	-.0570
.5750	.0967	.5750	-.0540
.6000	.0937	.6000	-.0508
.6250	.0901	.6250	-.0469
.6500	.0860	.6583	-.0412
.6750	.0814	.7000	-.0333
.7000	.0763	.7500	-.0246
.7250	.0709	.8000	-.0146
.7500	.0651	.8500	-.0050
.7750	.0591	.9250	.0096
.8000	.0529	.9500	.0053
.8250	.0465	.9700	.0019
.8500	.0399	.9750	.0010
.8750	.0332	.9800	-.0001
.9000	.0264	.9850	-.0012
.9250	.0196	.9900	-.0022
.9500	.0129	.9950	-.0033
1.0000	-.0007	1.0000	-.0044

(b) GA(W)-1 Blended Cove Airfoil

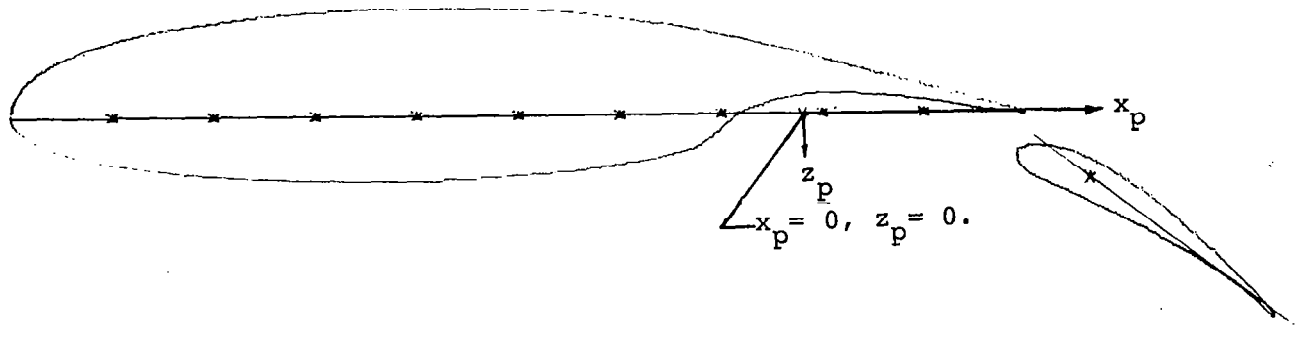
Figure 42 - continued



<u>UPPER SURFACE</u>		<u>LOWER SURFACE</u>	
x/c	z/c	x/c	z/c
0.0000	0.0000	0.0000	0.0000
.0020	.0130	.0020	-.0093
.0050	.0204	.0050	-.0138
.0125	.0307	.0125	-.0205
.0250	.0417	.0250	-.0269
.0375	.0497	.0375	-.0319
.0500	.0559	.0500	-.0358
.0750	.0655	.0750	-.0421
.1000	.0730	.1000	-.0470
.1250	.0790	.1250	-.0510
.1500	.0840	.1500	-.0543
.1750	.0884	.1750	-.0570
.2000	.0920	.2000	-.0593
.2500	.0977	.2500	-.0627
.3000	.1016	.3000	-.0645
.3500	.1040	.3500	-.0652
.4000	.1049	.4000	-.0649
.4500	.1045	.4500	-.0635
.5000	.1026	.5000	-.0610
.5500	.0991	.5500	-.0570
.5750	.0967	.5750	-.0540
.6000	.0937	.6000	-.0508
.6250	.0901	.6250	-.0469
.6500	.0860	.6500	-.0428
.6750	.0814	.6550	-.0420
.7000	.0763	.7000	-.0339
.7250	.0709	.7605	-.0235
.7500	.0651	.7600	-.0205
.7750	.0591	.7075	-.0297
.8000	.0529	.7035	-.0260
.8250	.0465	.7049	-.0178
.8500	.0399	.7150	-.0035
.8750	.0332	.7250	.0025
.9000	.0264	.7500	.0110
.9250	.0196	.7750	.0163
.9500	.0129	.8000	.0190
1.0000	-.0007	.8250	.0195
		.8500	.0182
		.8750	.0167
		.9000	.0133
		.9250	.0095
		.9500	.0053
		.9750	.0010
		1.0000	-.0044

(c) GA(W)-1 Sharp-Lip Cove Airfoil

Figure 42 - continued



30% Fowler Flap Coordinates

Upper Surface		Lower Surface	
x_f/c	z_f/c	x_f/c	z_f/c
.000	-.01920	.000	-.01920
.025	.00250	.025	-.02940
.050	.01100	.050	-.02490
.075	.01630	.075	-.02040
.100	.01900	.100	-.01600
.125	.01950	.125	-.01200
.150	.01820	.150	-.00860
.175	.01670	.175	-.00580
.200	.01330	.200	-.00360
.225	.00950	.225	-.00250
.250	.00530	.250	-.00260
.275	.00100	.275	-.00400
.300	-.00435	.300	-.00800

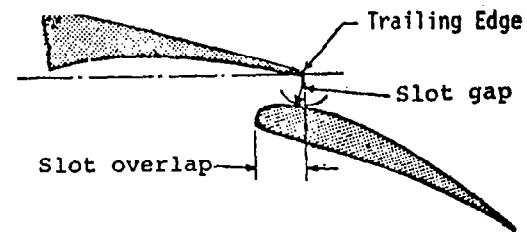
L.E. Radius = 0.0122c

Flap Pivot Point Locations

type	cove	δ_f	x_p/c	z_p/c
standard		35°	.2844	.0646
blended		35°	.2844	.0646
sharp-lip		35°	.2844	.0646

gap/c = .030 overlap/c = .012

Note: Pivot point origin is at $0.25c_f$ (or $0.775x/c$) on the wing chord line.



Definitions of gap and overlap.

(d) 30% Fowler Flap.

Figure 42 - concluded.

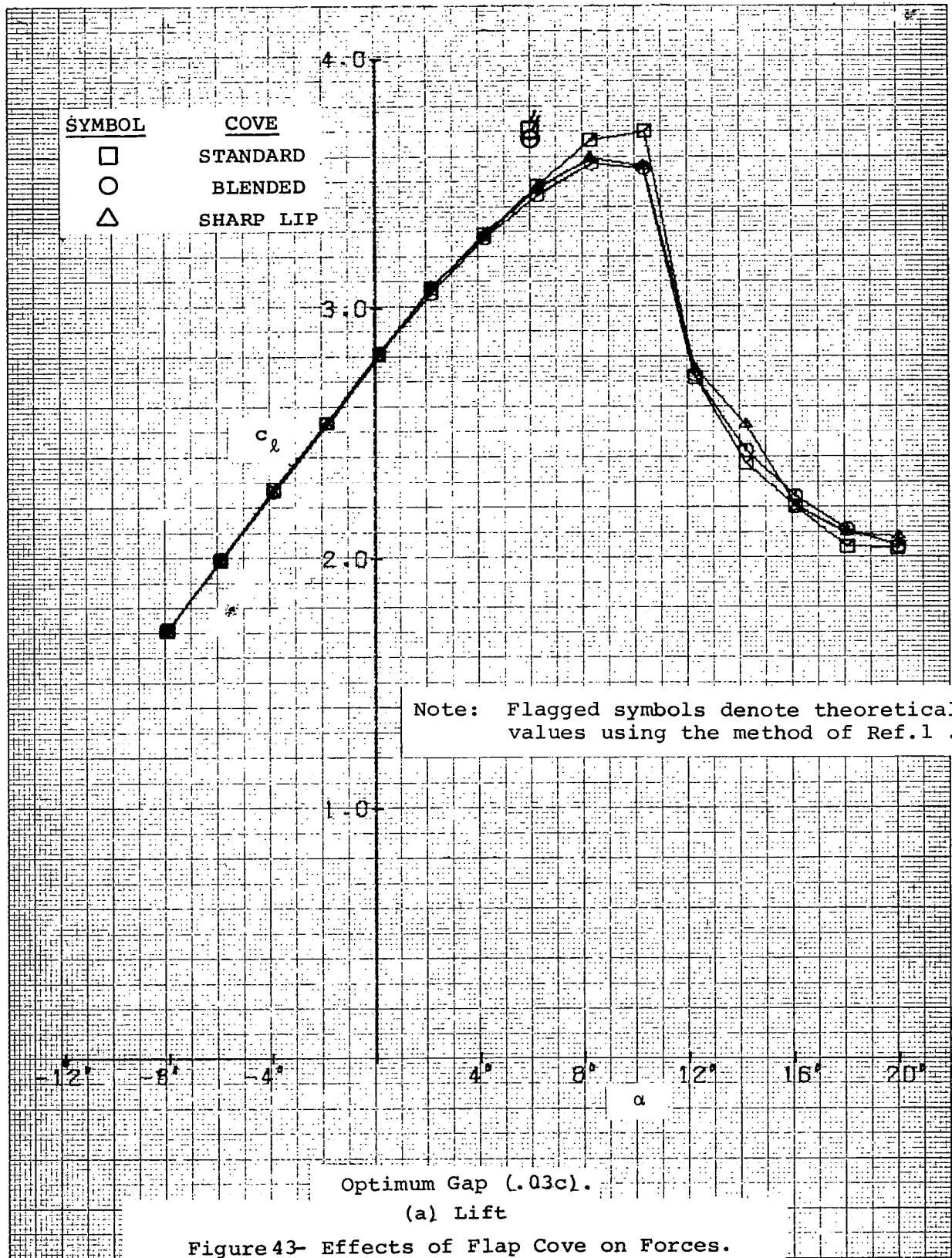
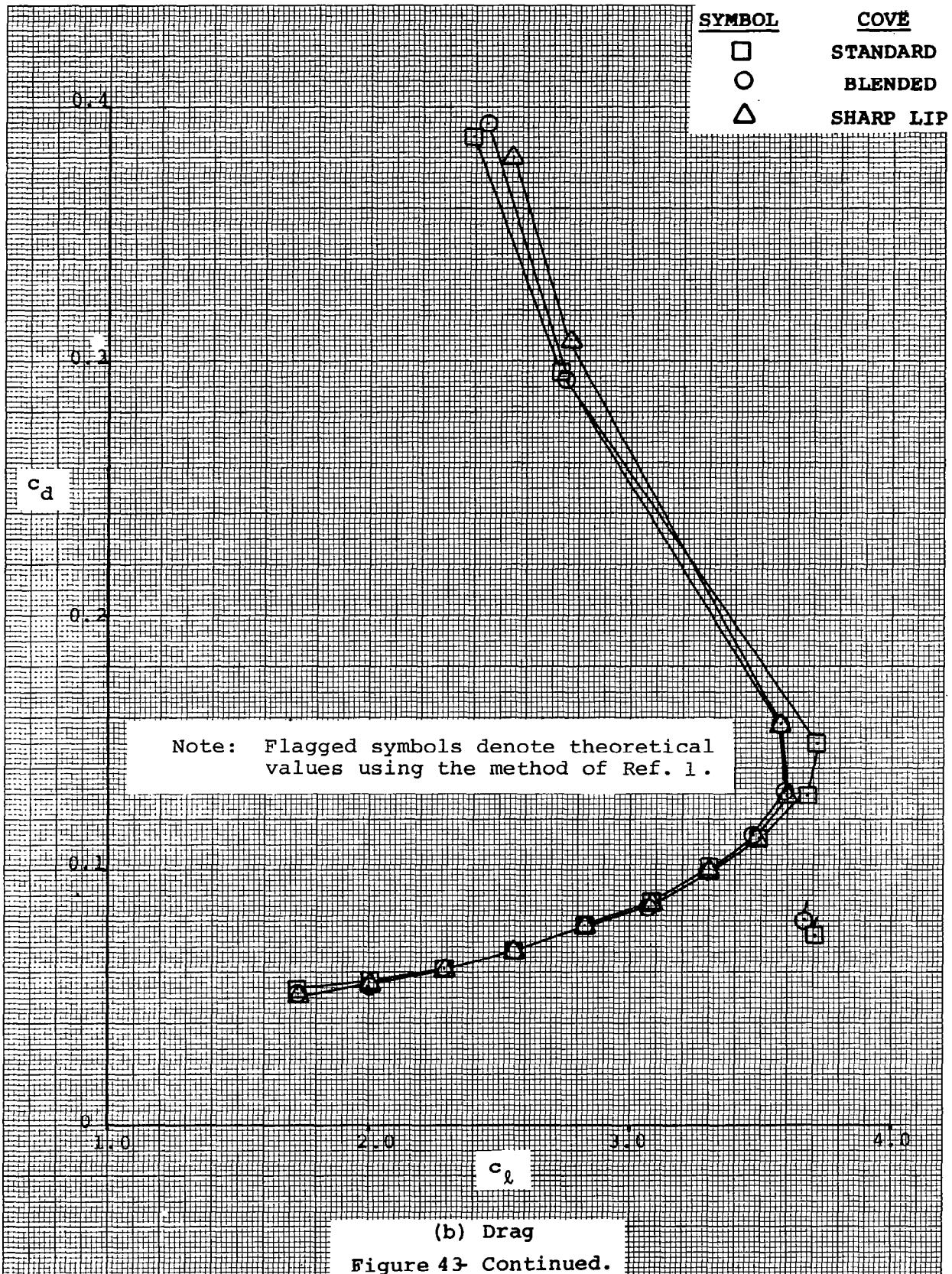
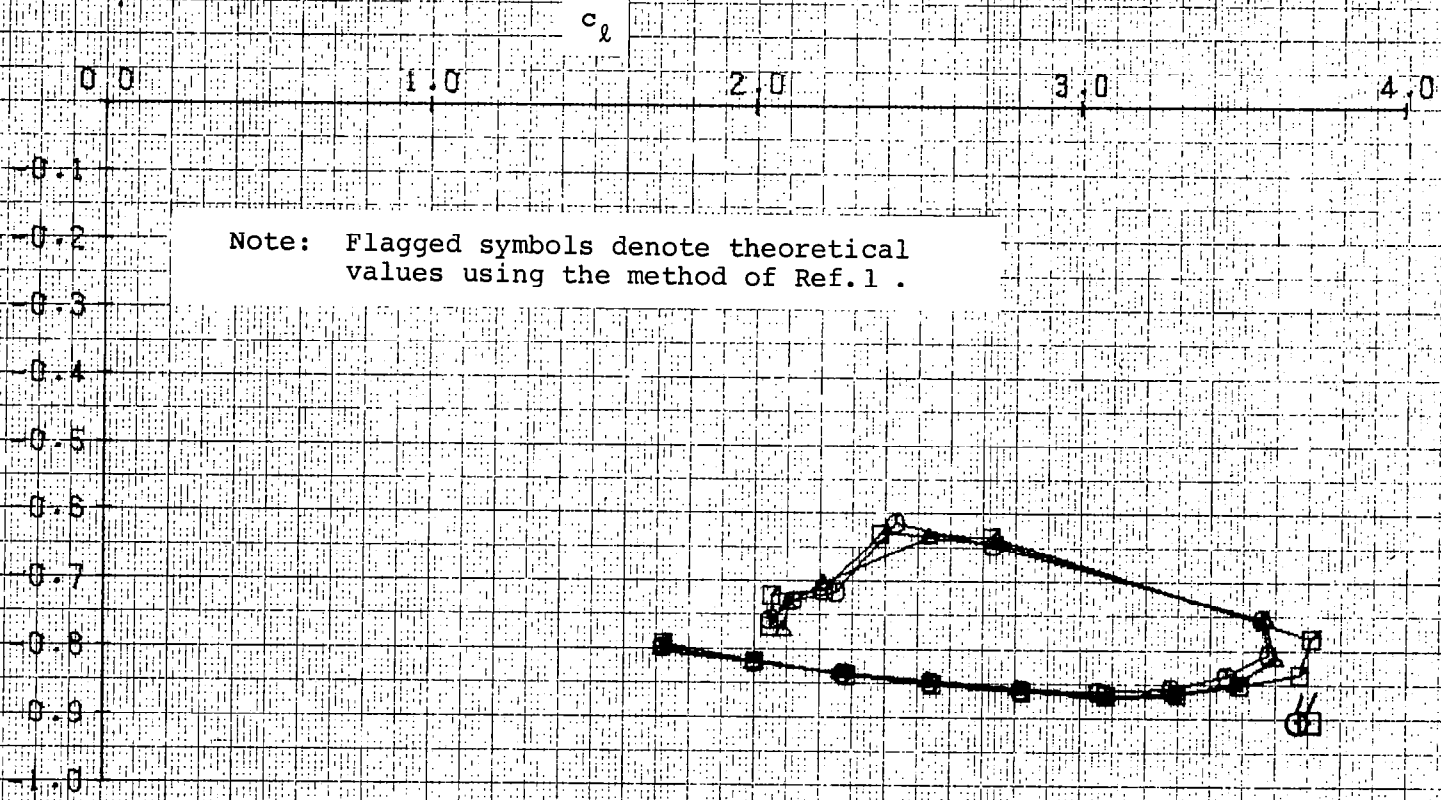


Figure 43- Effects of Flap Cove on Forces.



SYMBOL	COVE
□	STANDARD
○	BLENDED
△	SHARP LIP



(c) Moment
 Figure 43- Concluded.

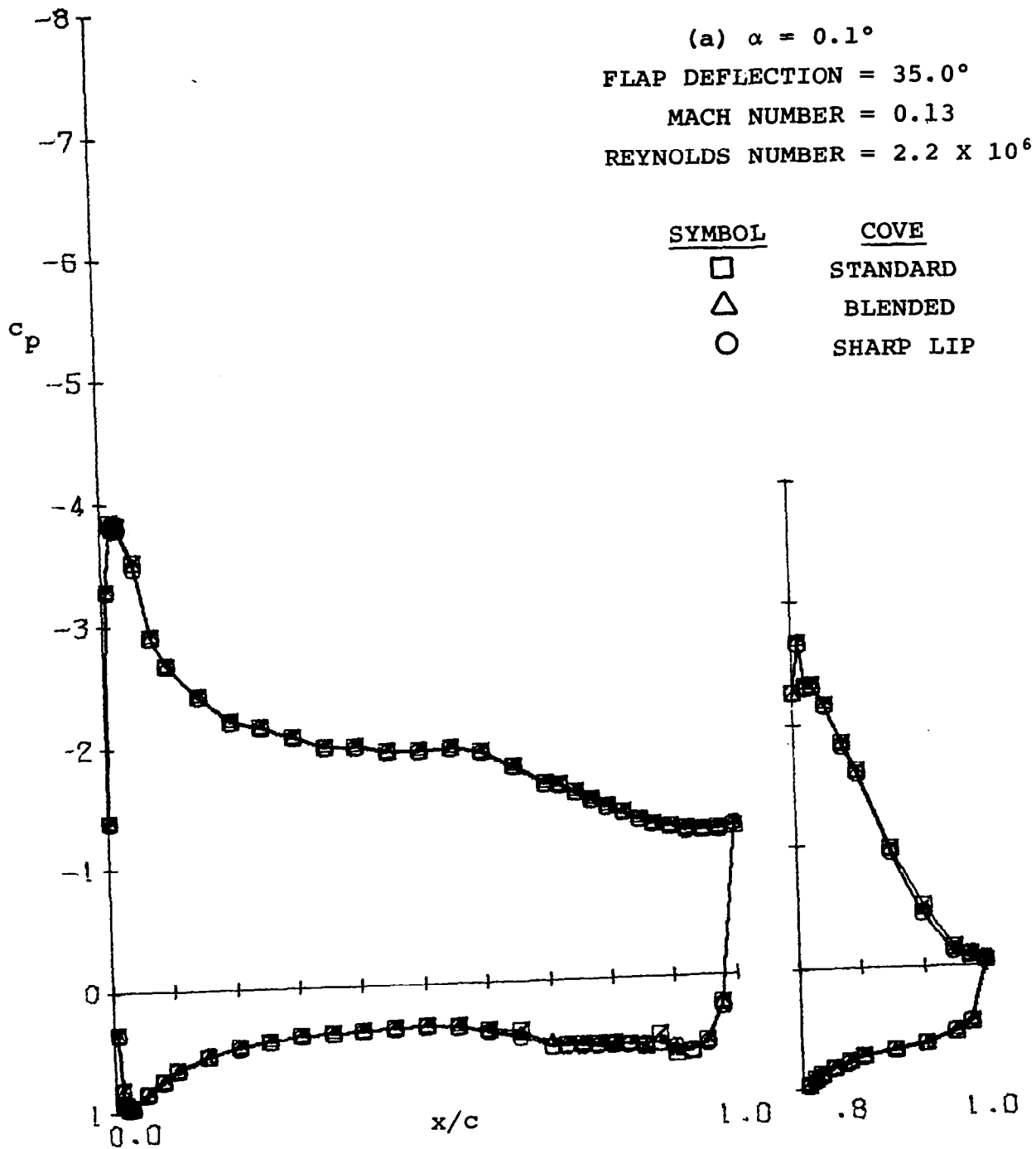


Figure 44- Effects of Flap Cove on Pressures.

(b) $\alpha = 5.2^\circ$

FLAP DEFLECTION = 35.0°

MACH NUMBER = 0.13

REYNOLDS NUMBER = 2.2×10^6

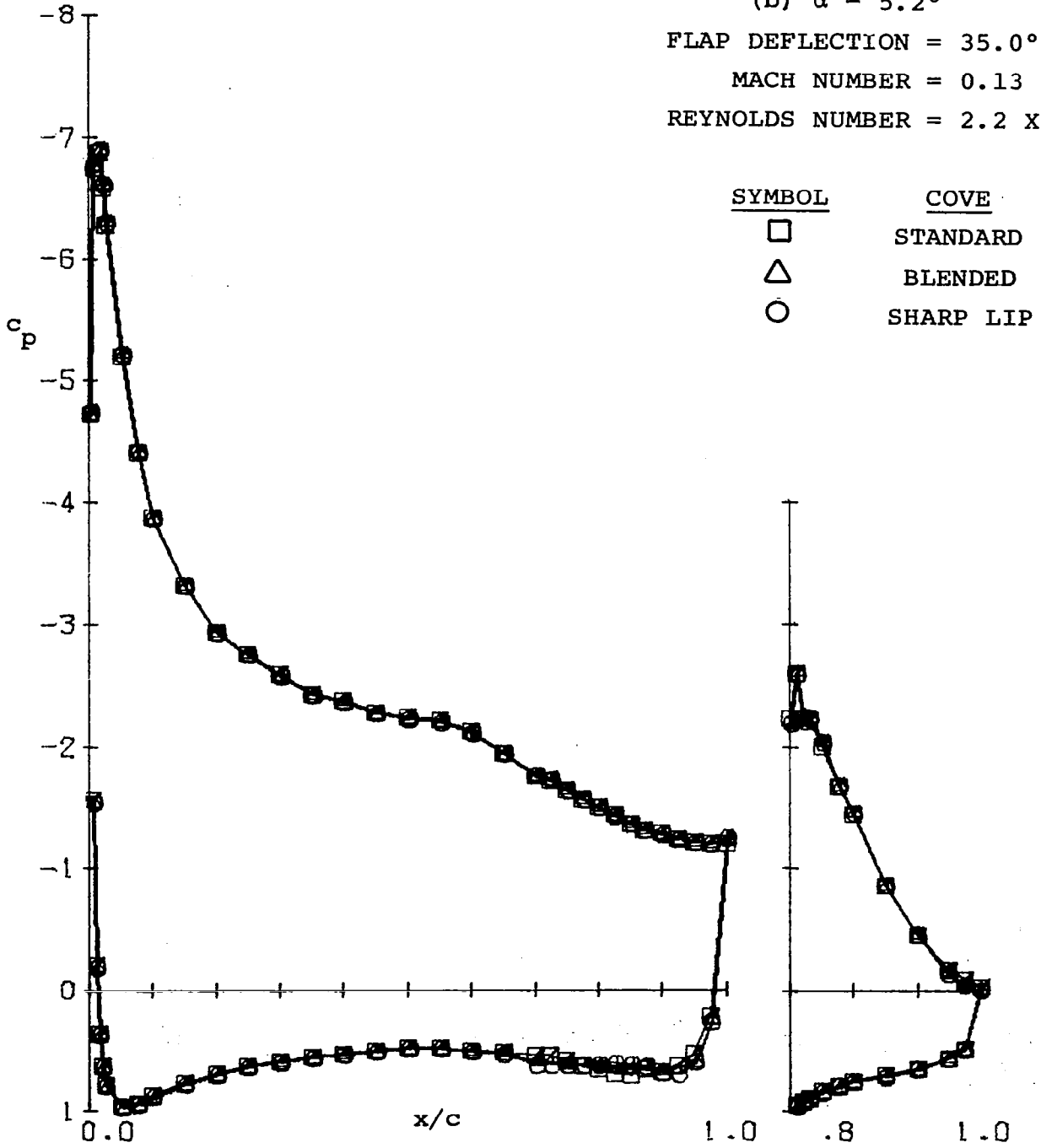


Figure44- Continued.

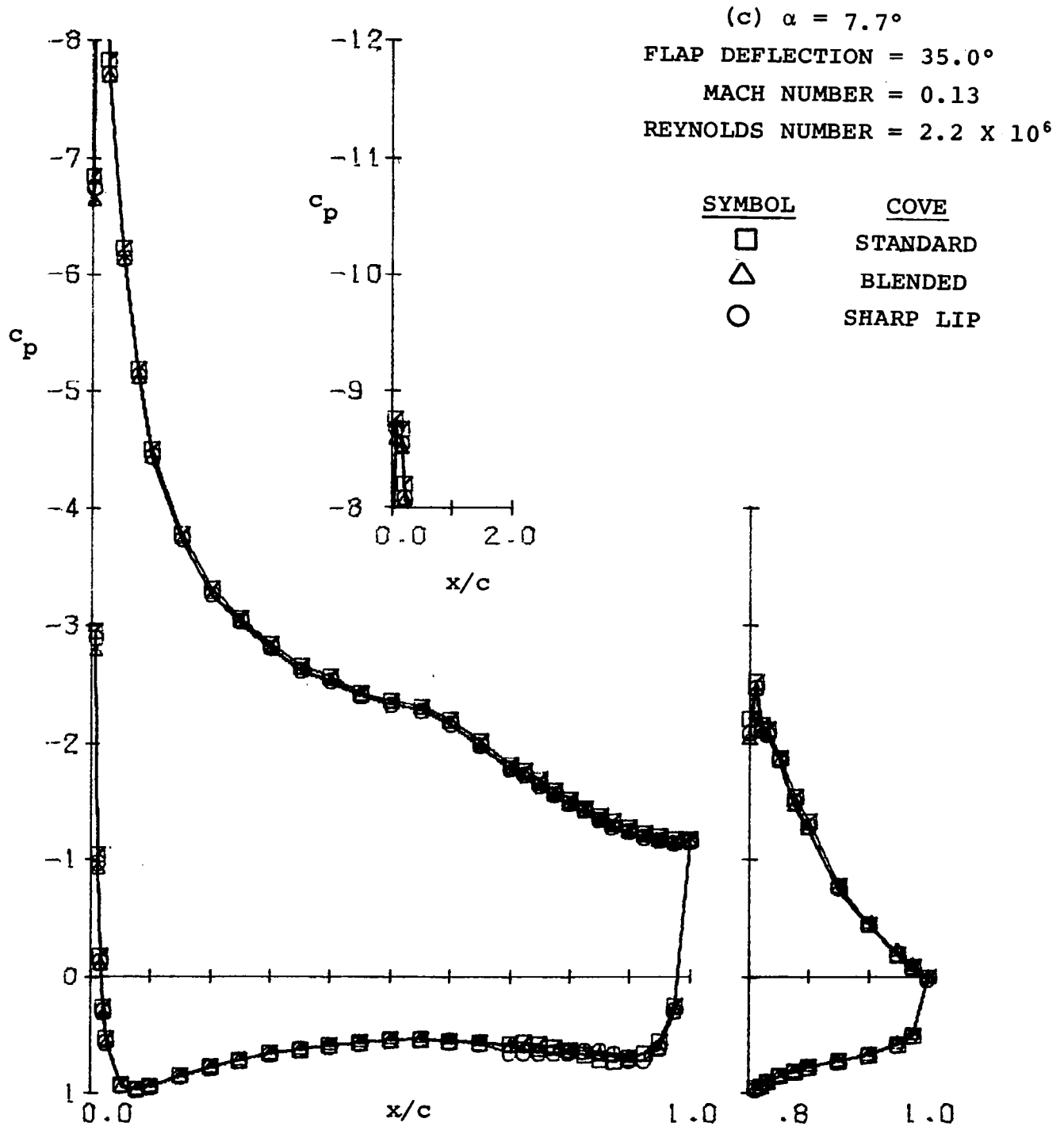


Figure 44- Continued.

(d) $\alpha = 10.3^\circ$

FLAP DEFLECTION = 35.0°

MACH NUMBER = 0.13

REYNOLDS NUMBER = 2.2×10^6

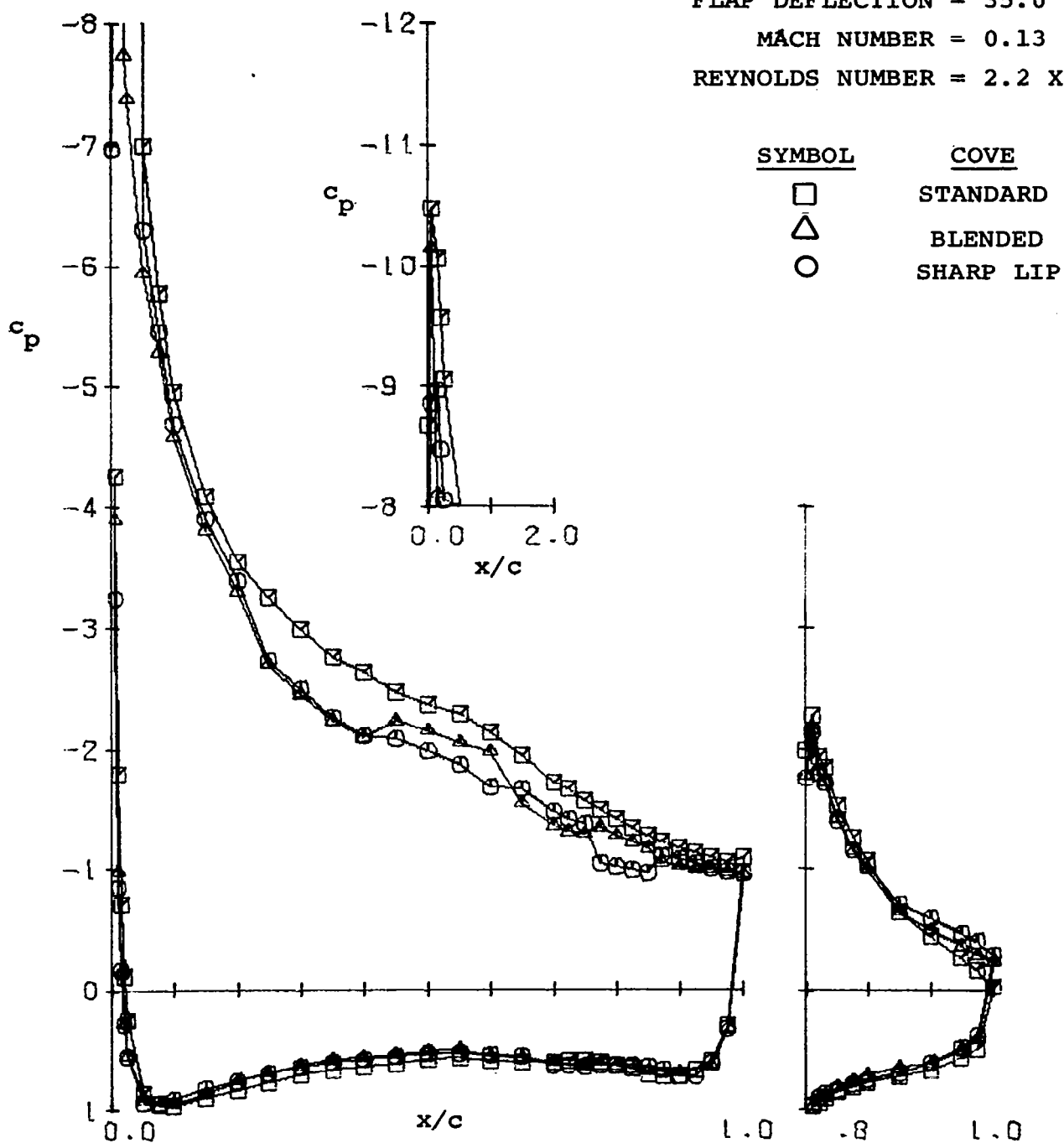


Figure44- Continued.

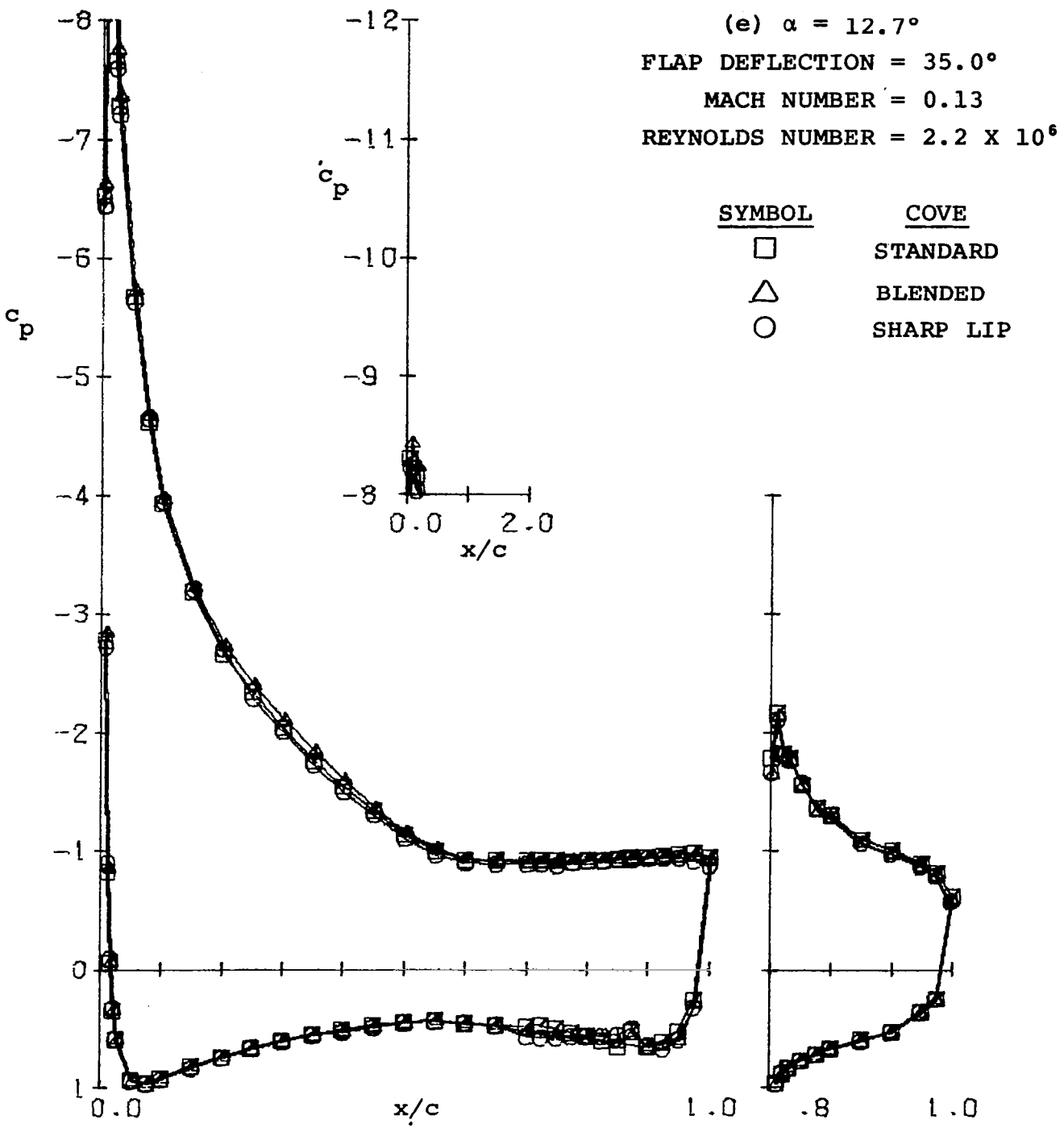


Figure44- Concluded.

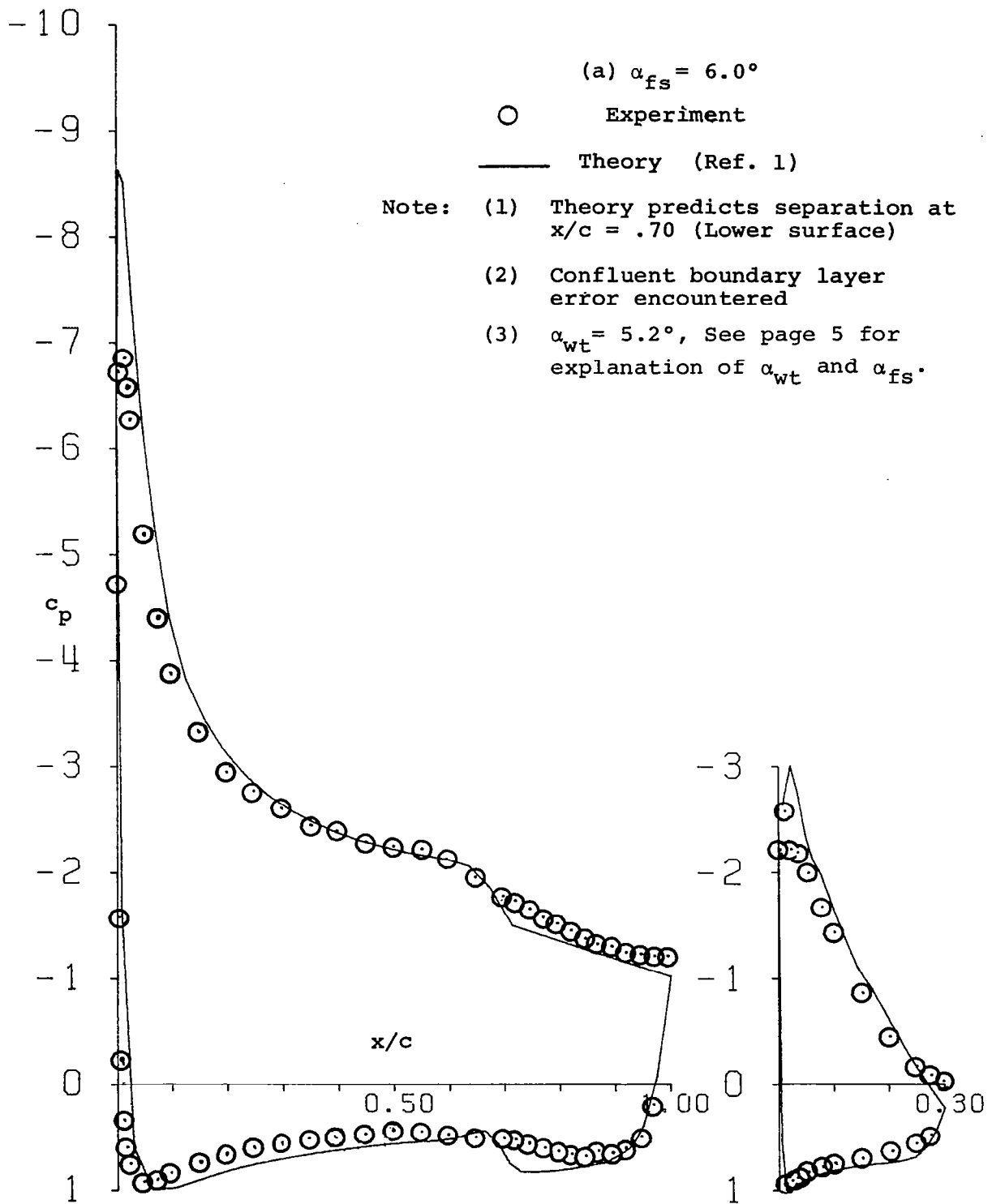


Figure 45 - Theoretical and Experimental Pressures, Standard Cove.

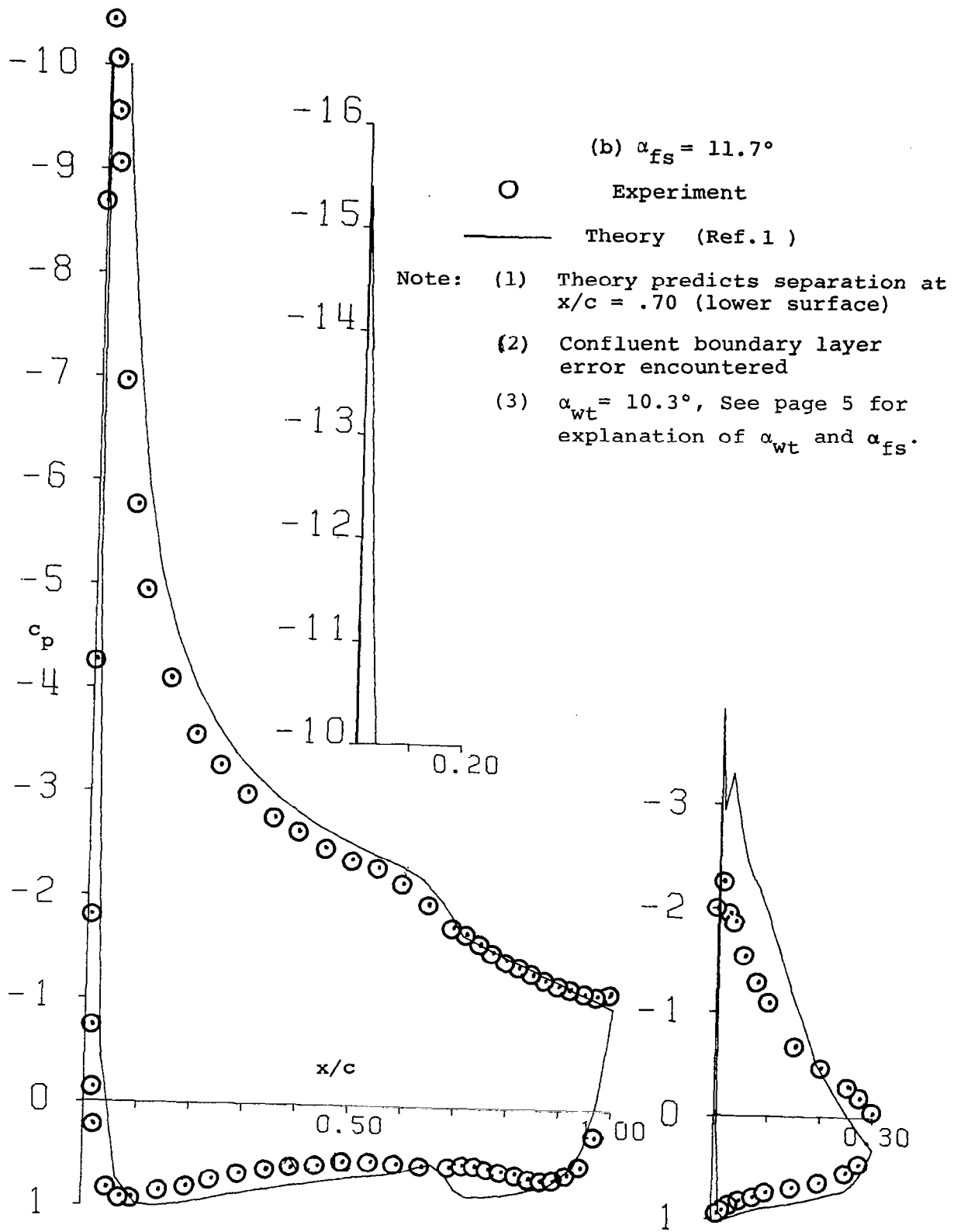


Figure 45 - Continued.

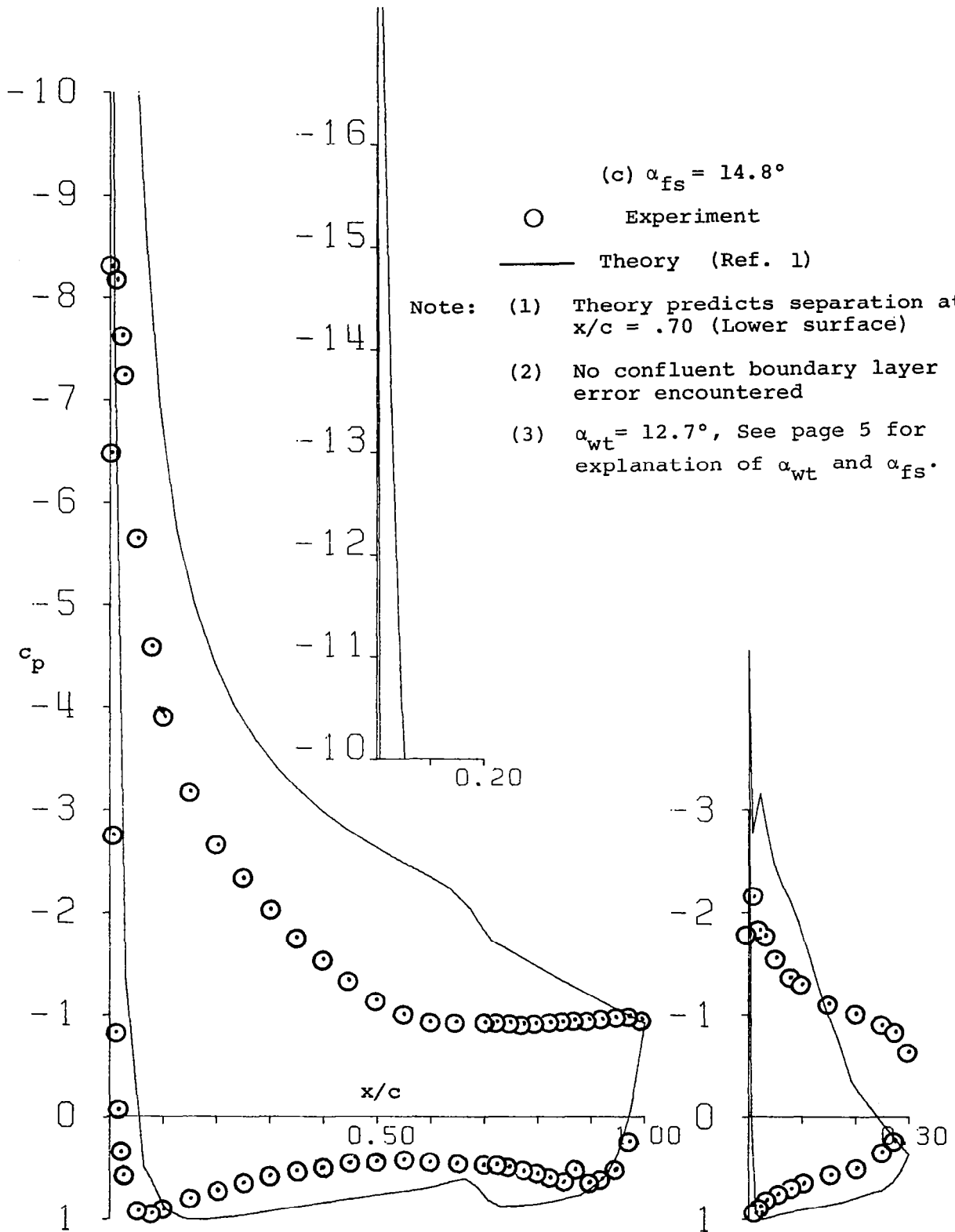


Figure 45 - Concluded.

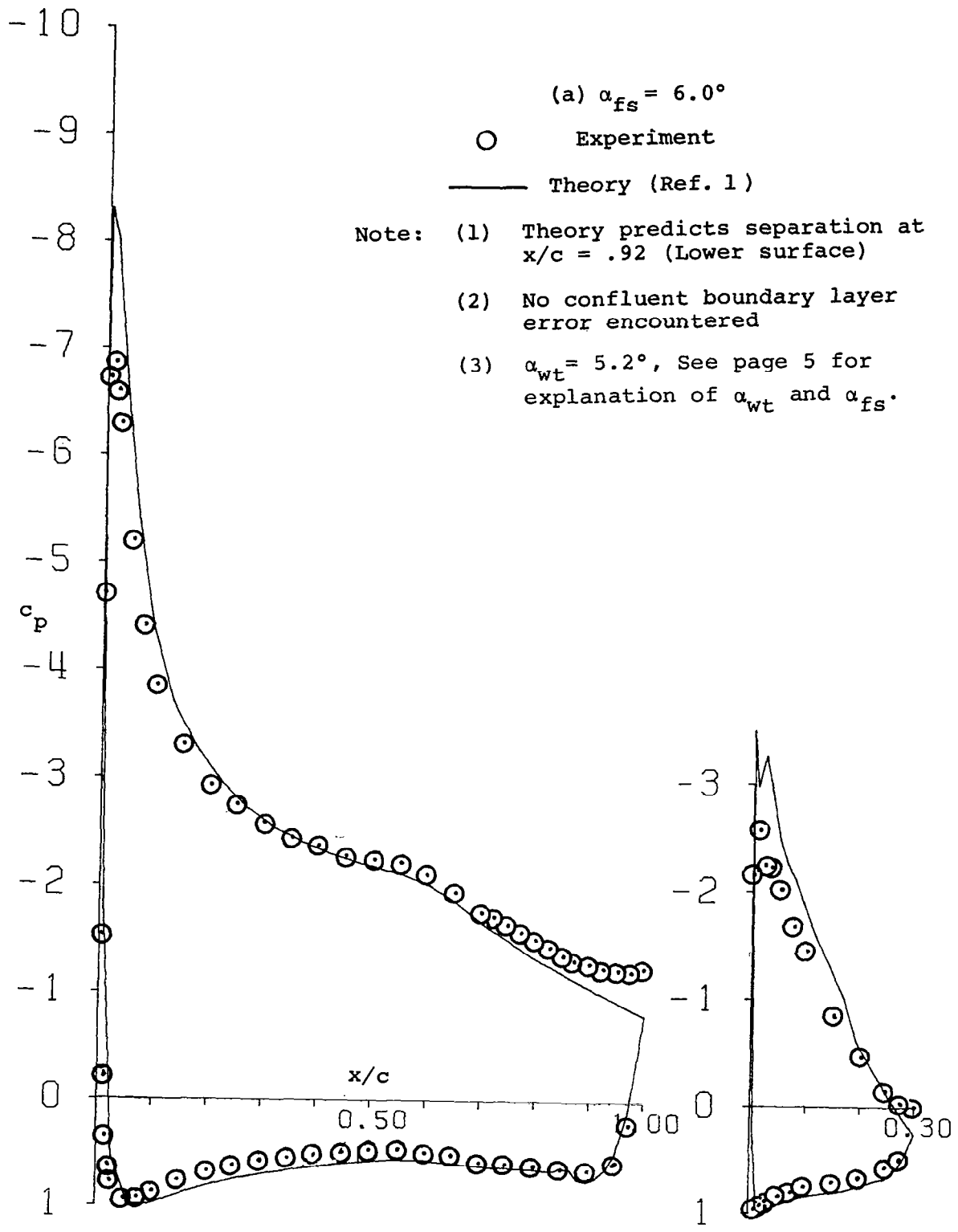


Figure 46 - Theoretical and Experimental Pressures, Blended Cove.

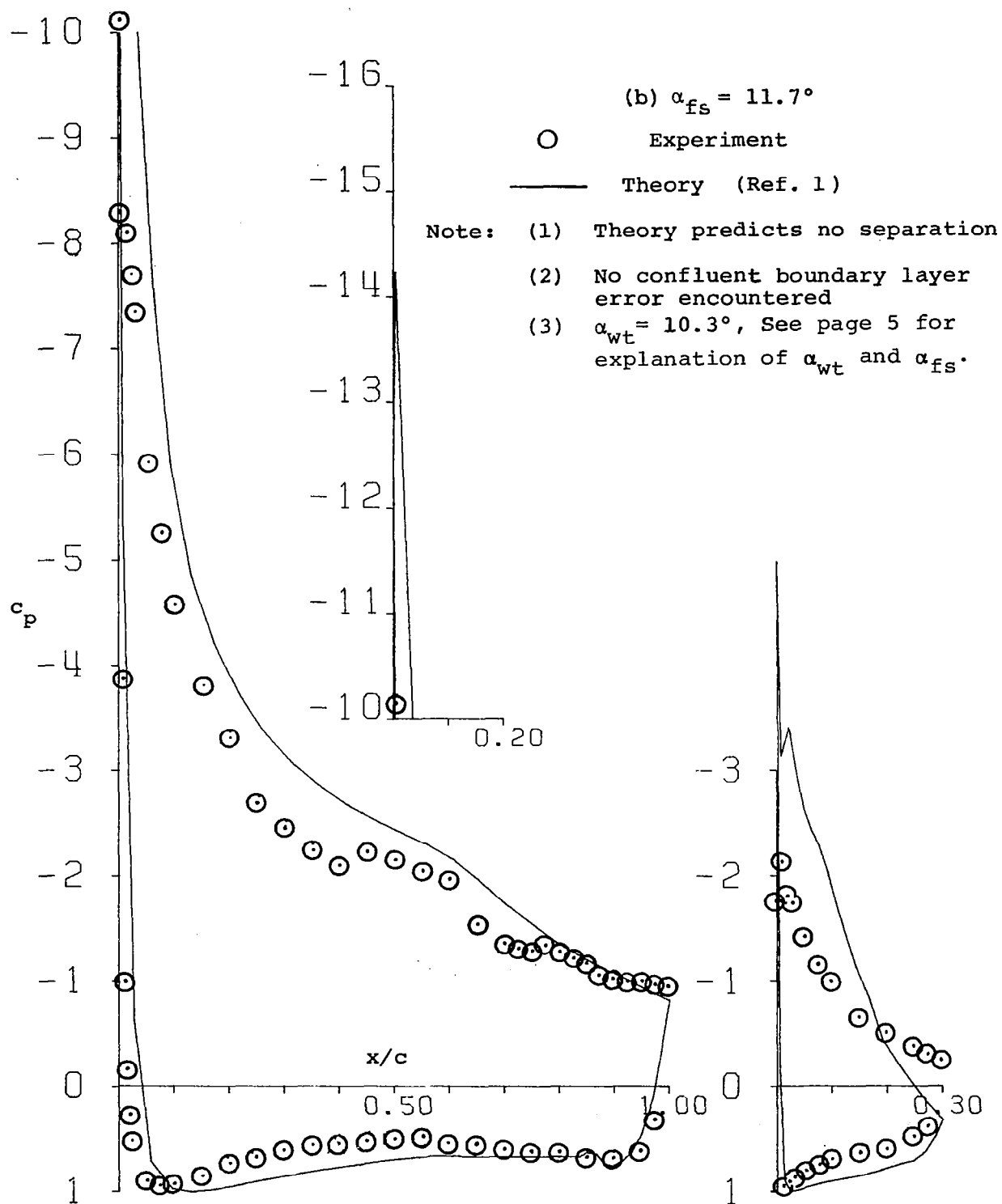


Figure 46 - Continued.

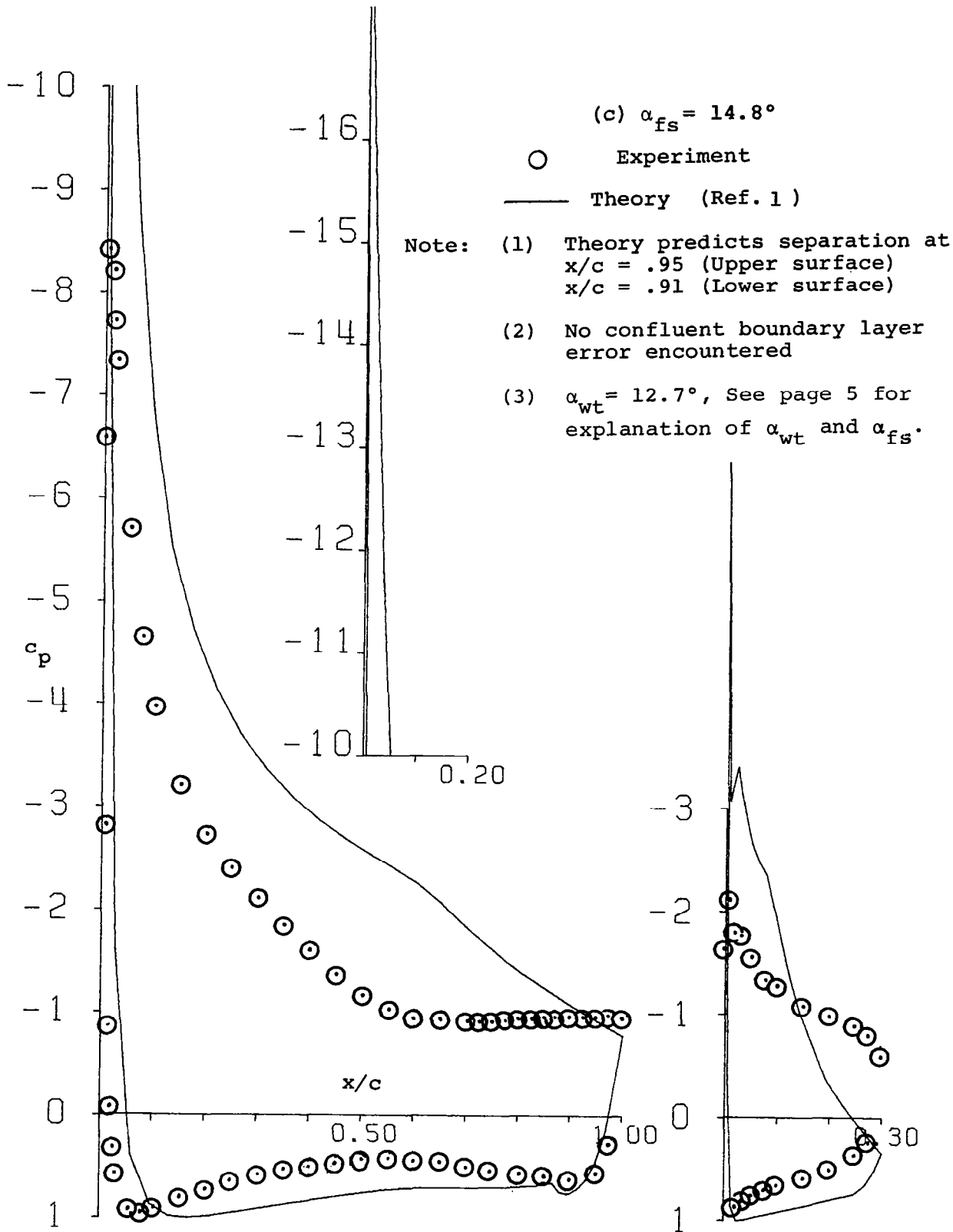
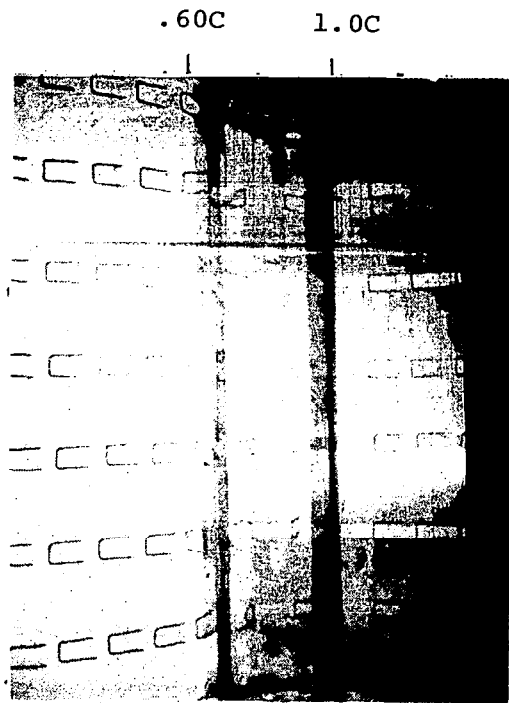


Figure 46 - Concluded.



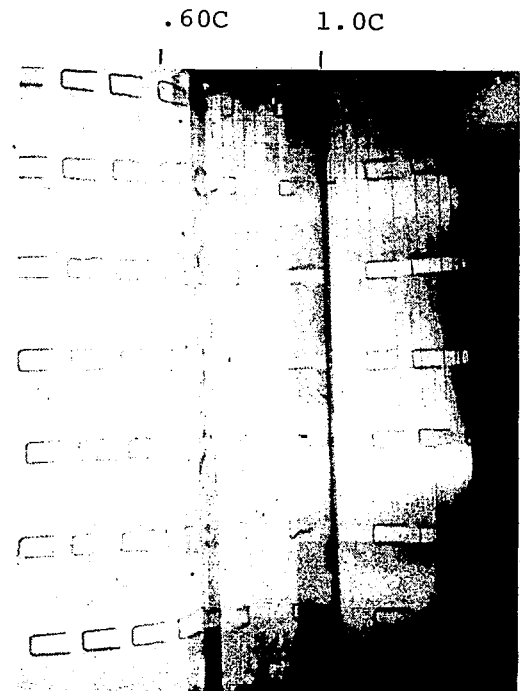
$\alpha = 0^\circ$



$\alpha = 5^\circ$



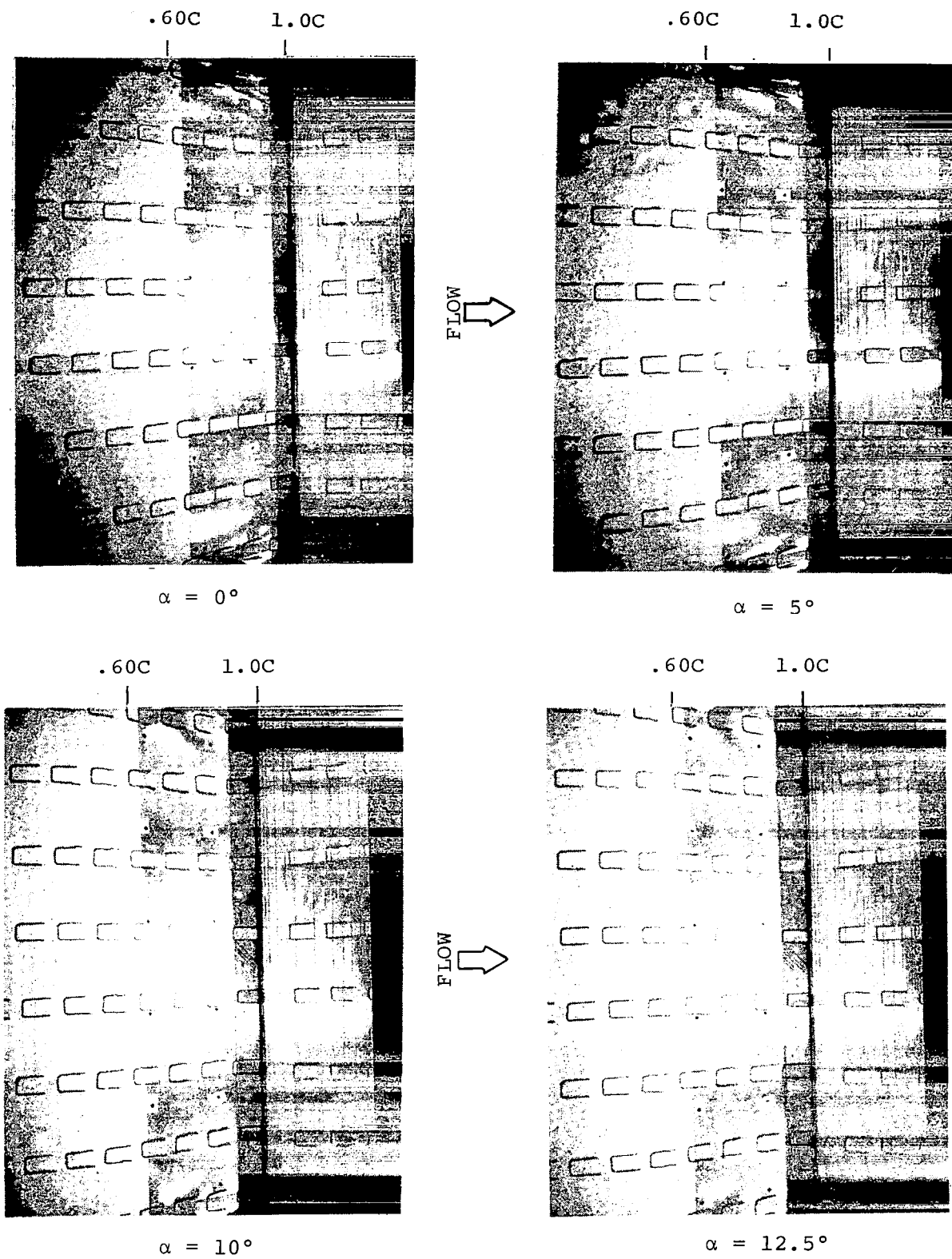
$\alpha = 10^\circ$



$\alpha = 12.5^\circ$

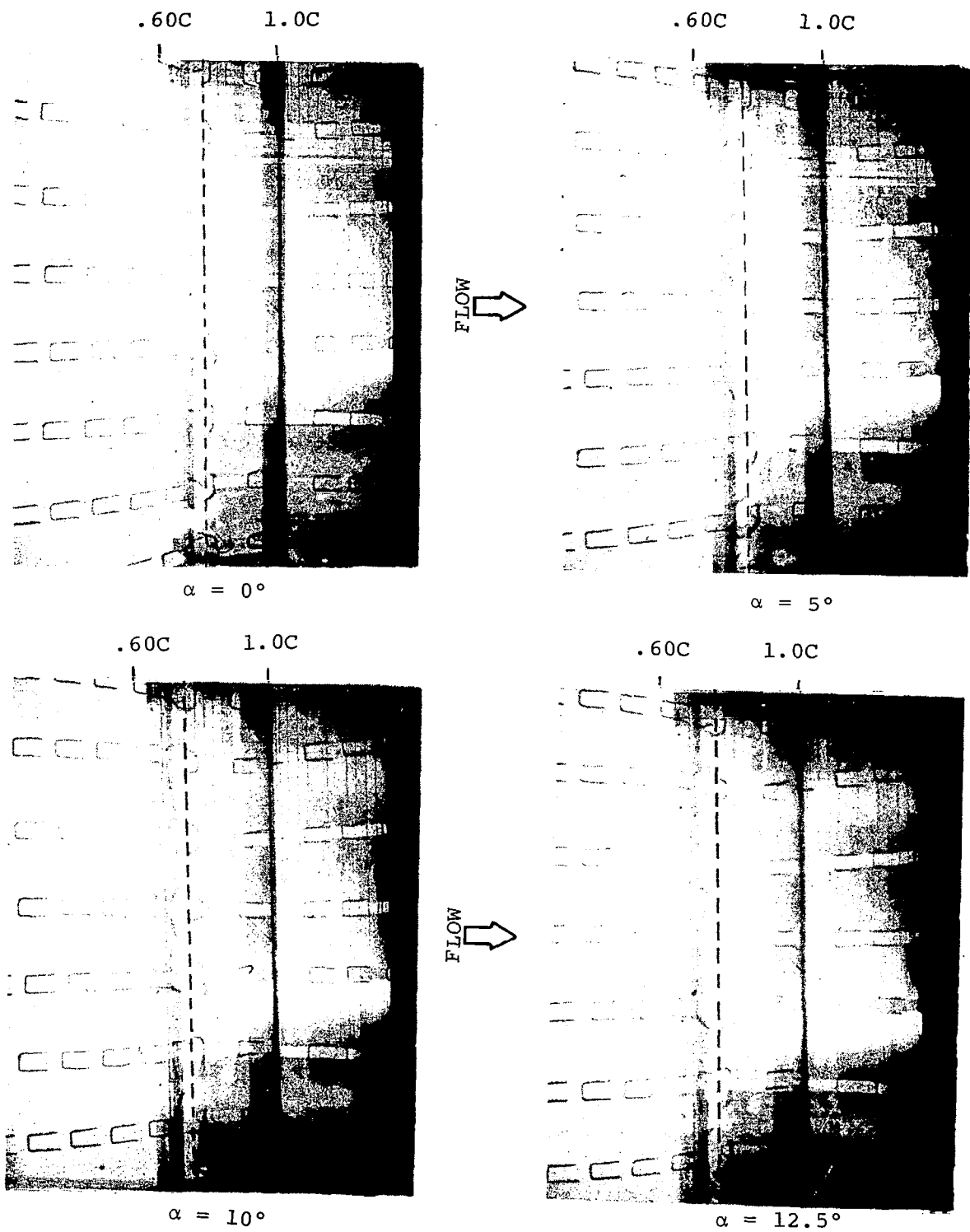
(a) STANDARD COVE

Figure 47- Lower Surface Tuft Patterns.

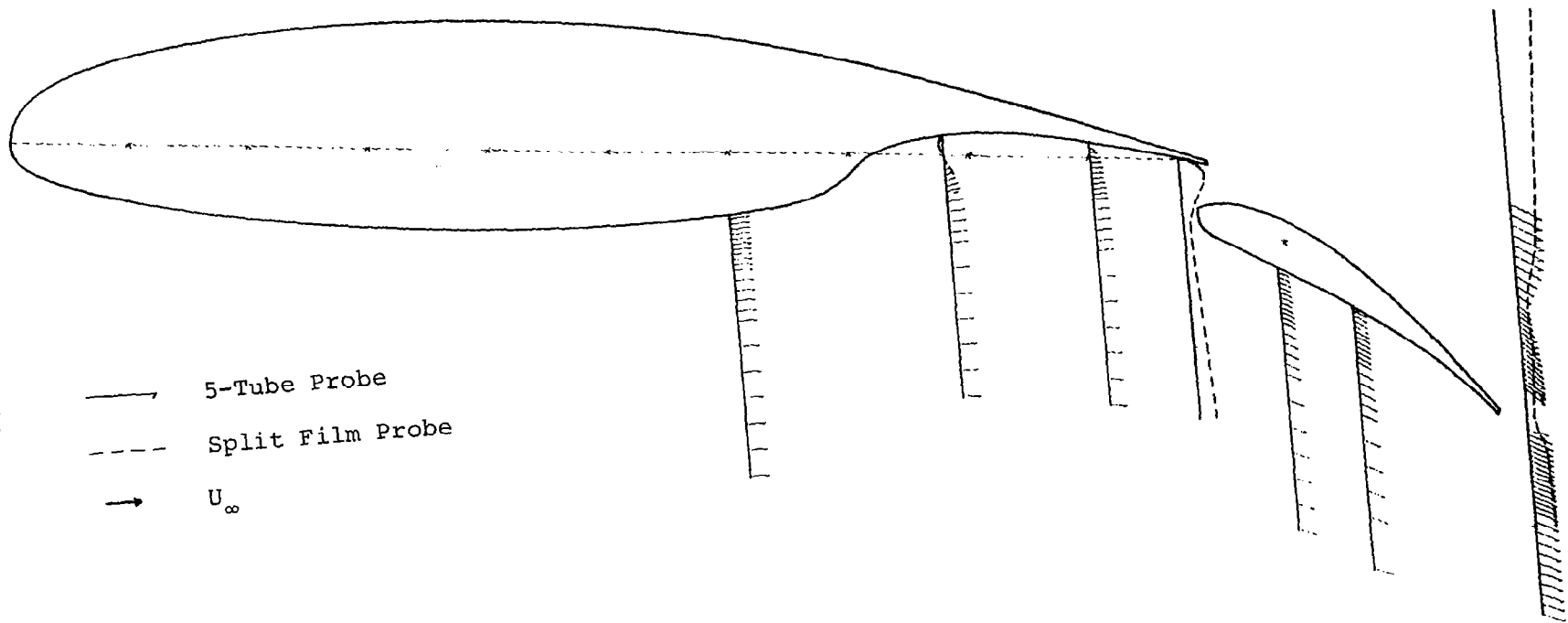


(b) BLENDED COVE

Figure 47- Continued.



(c) SHARP LIP COVE
 Figure 47- Concluded.

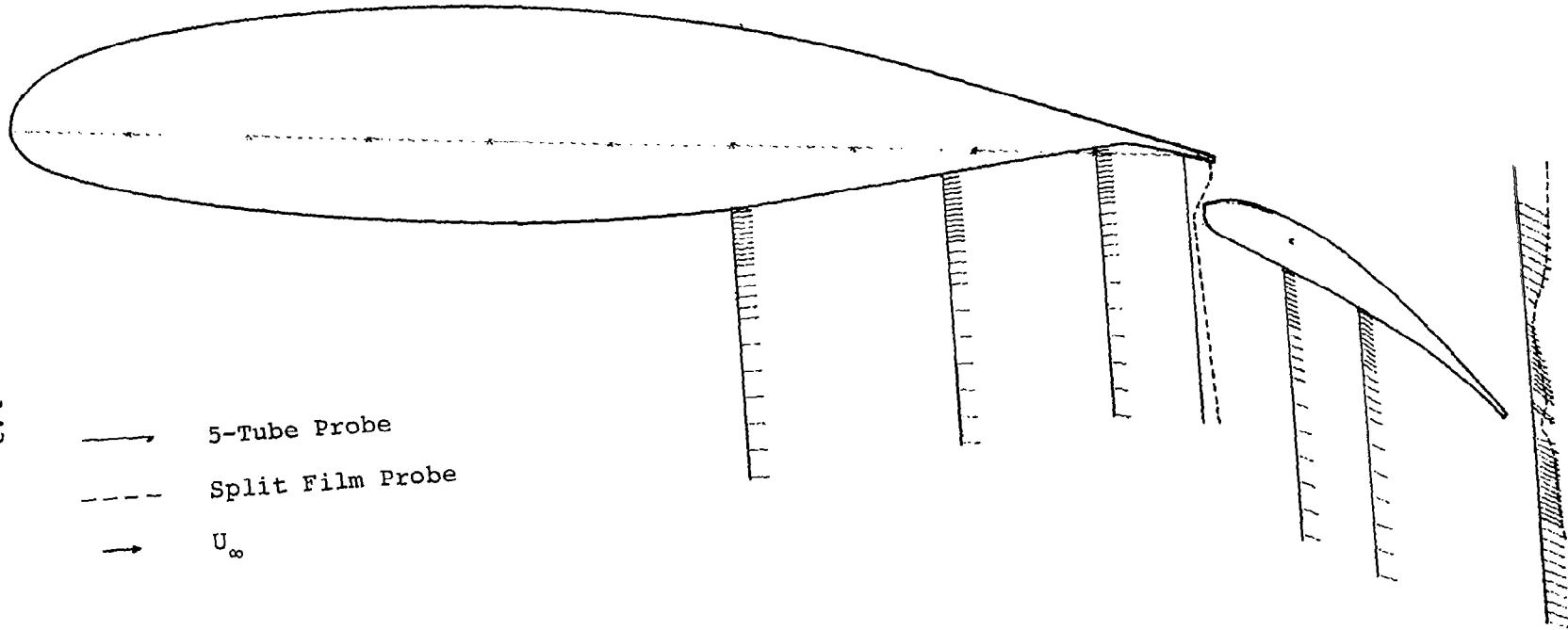


(a) STANDARD COVE

Figure 48 - Experimental Velocity Profiles, $\alpha = 5.2^\circ$.

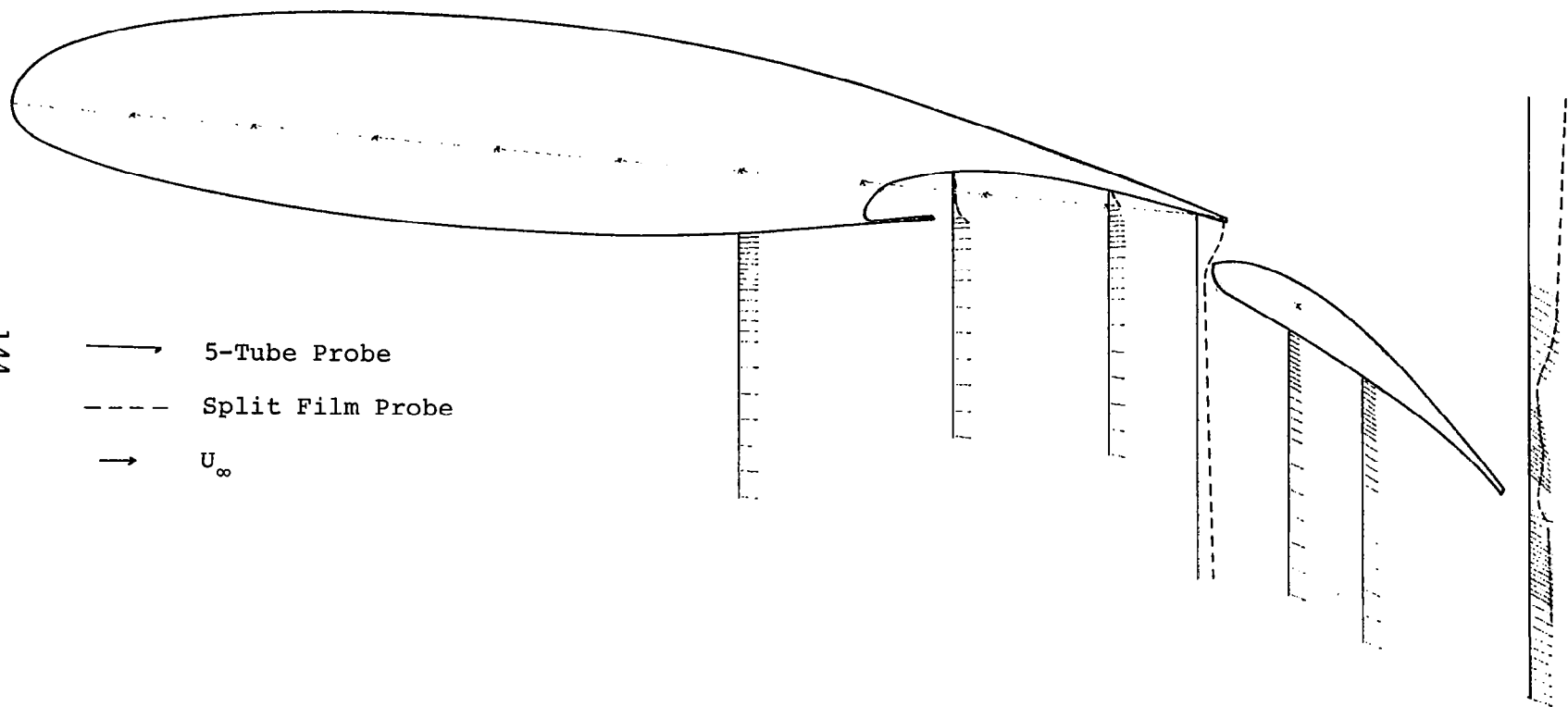
143

- 5-Tube Probe
- - - Split Film Probe
- U_{∞}



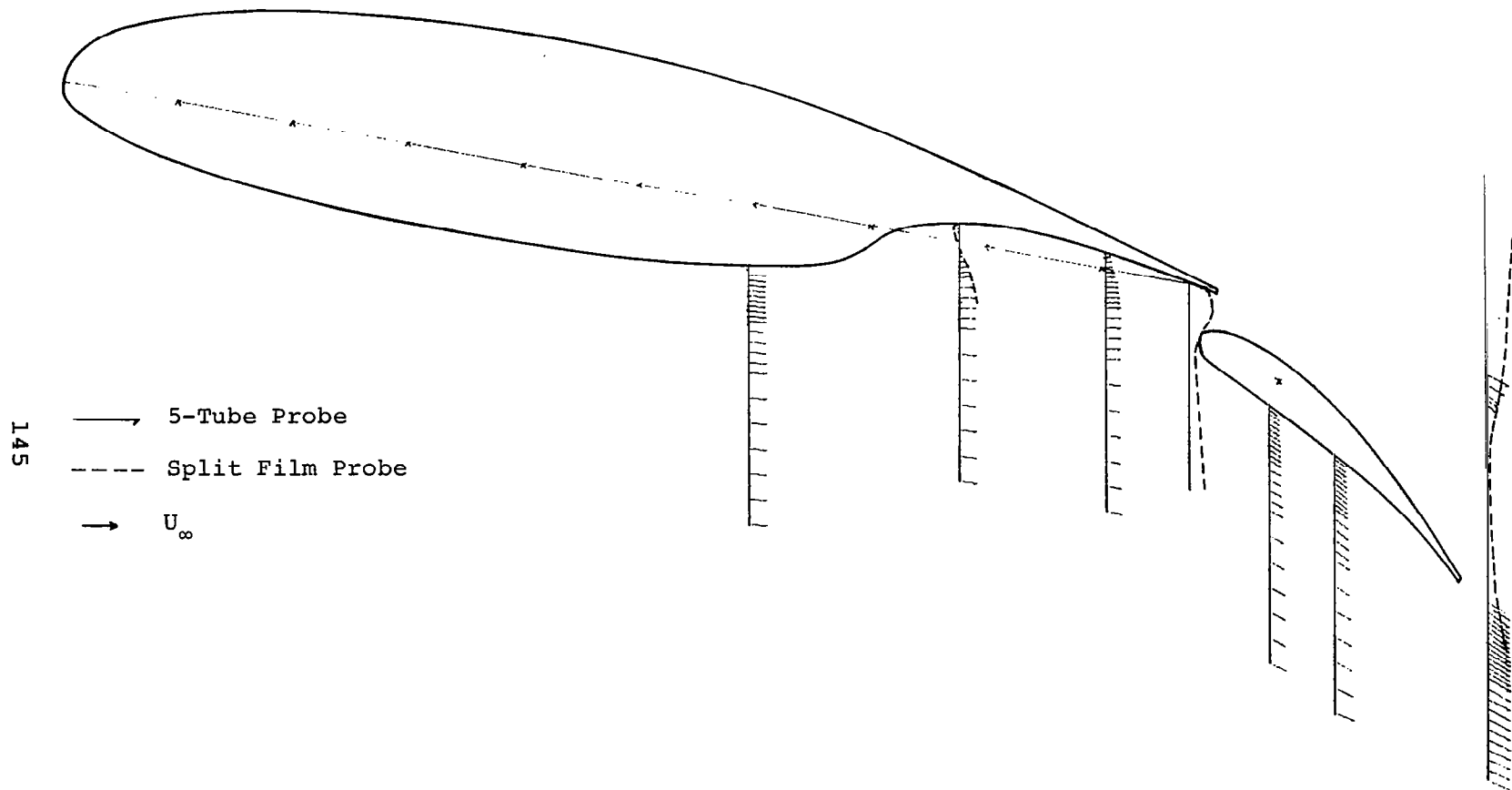
(b) BLENDED COVE

Figure 48 - Continued.



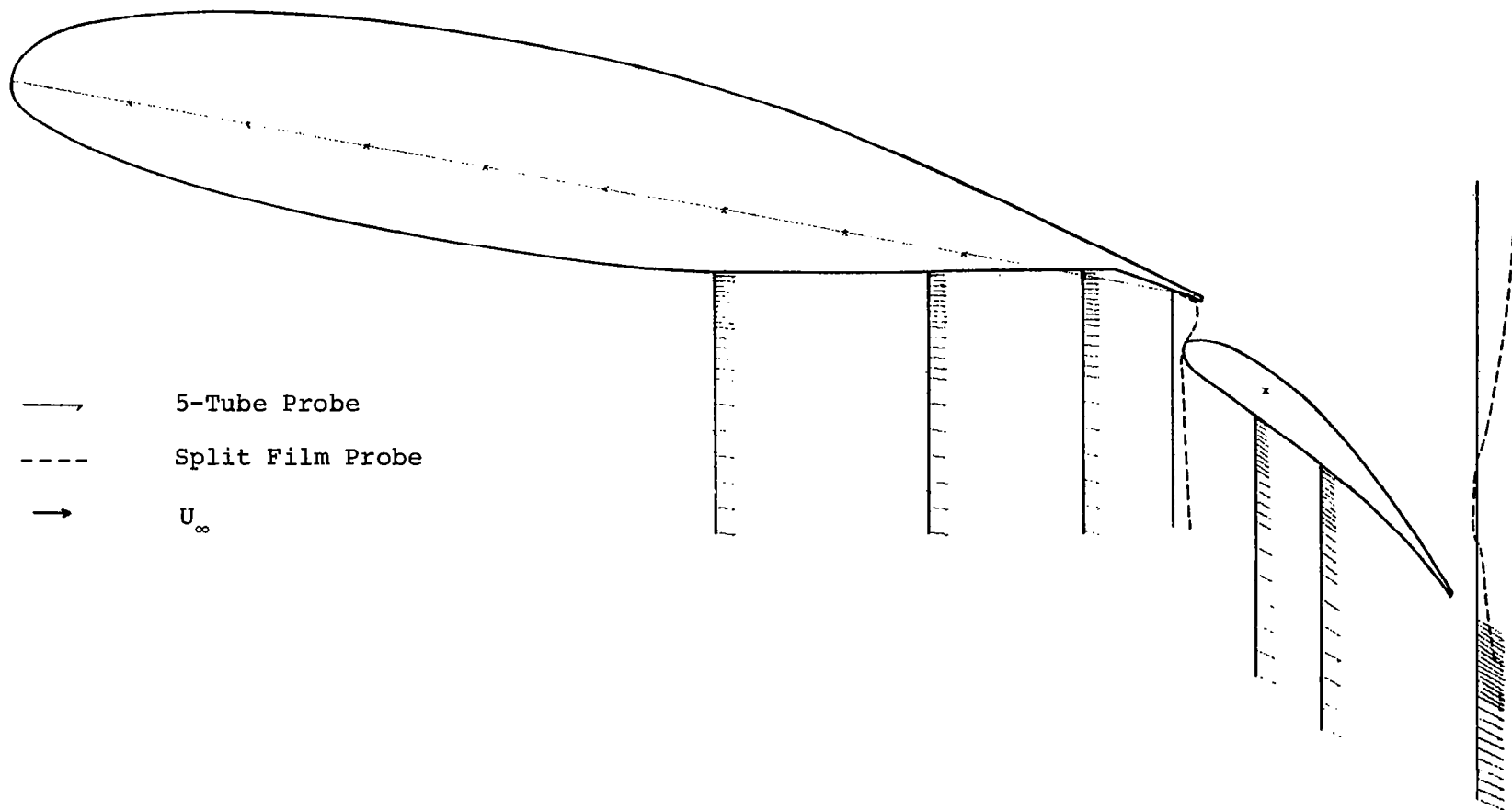
(c) SHARP LIP COVE

Figure 48- Concluded.



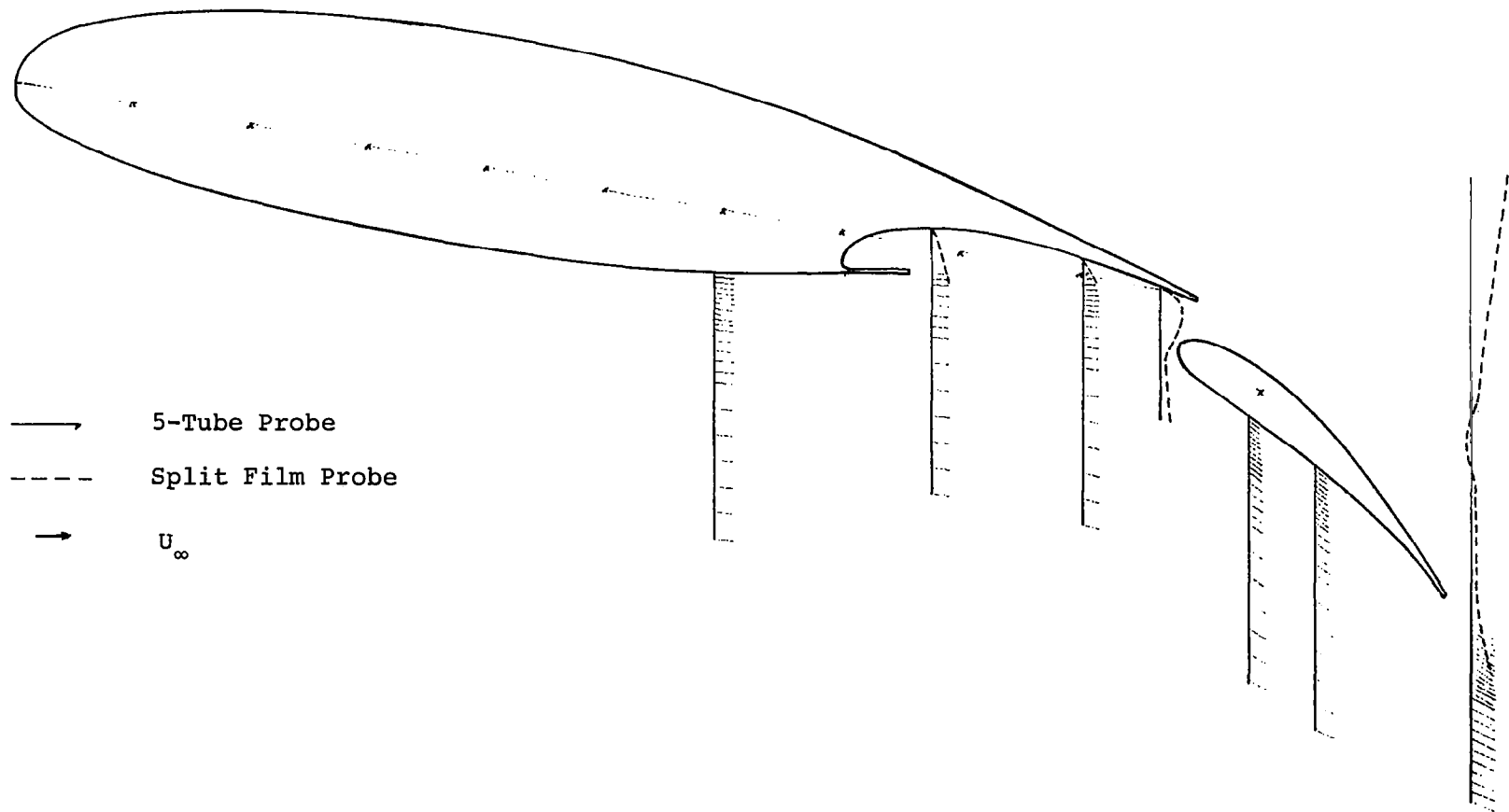
(a) STANDARD COVE

Figure 49 - Experimental Velocity Profiles, $\alpha = 10.3^\circ$



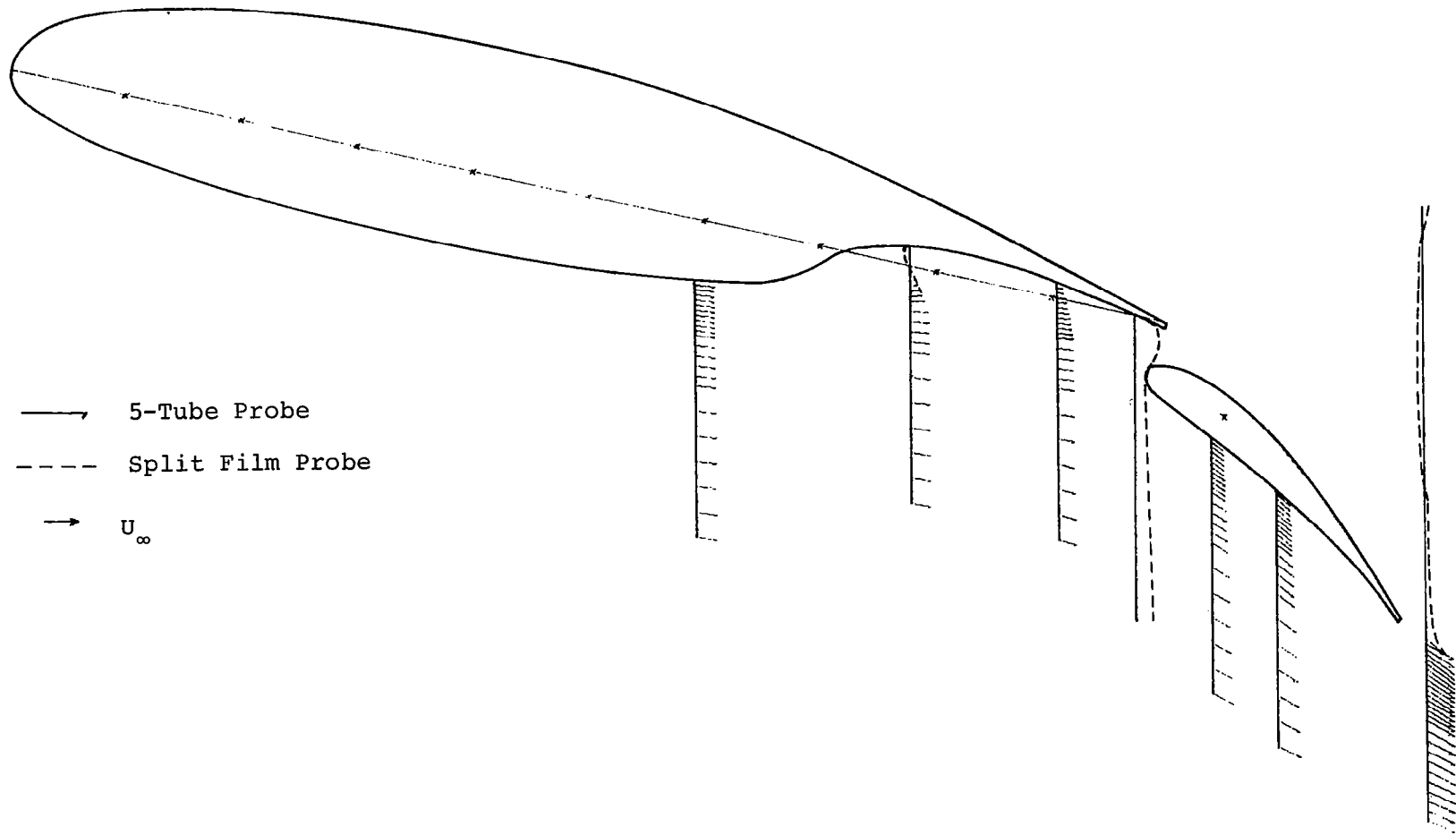
(b) BLENDED COVE

Figure 49 - Continued.



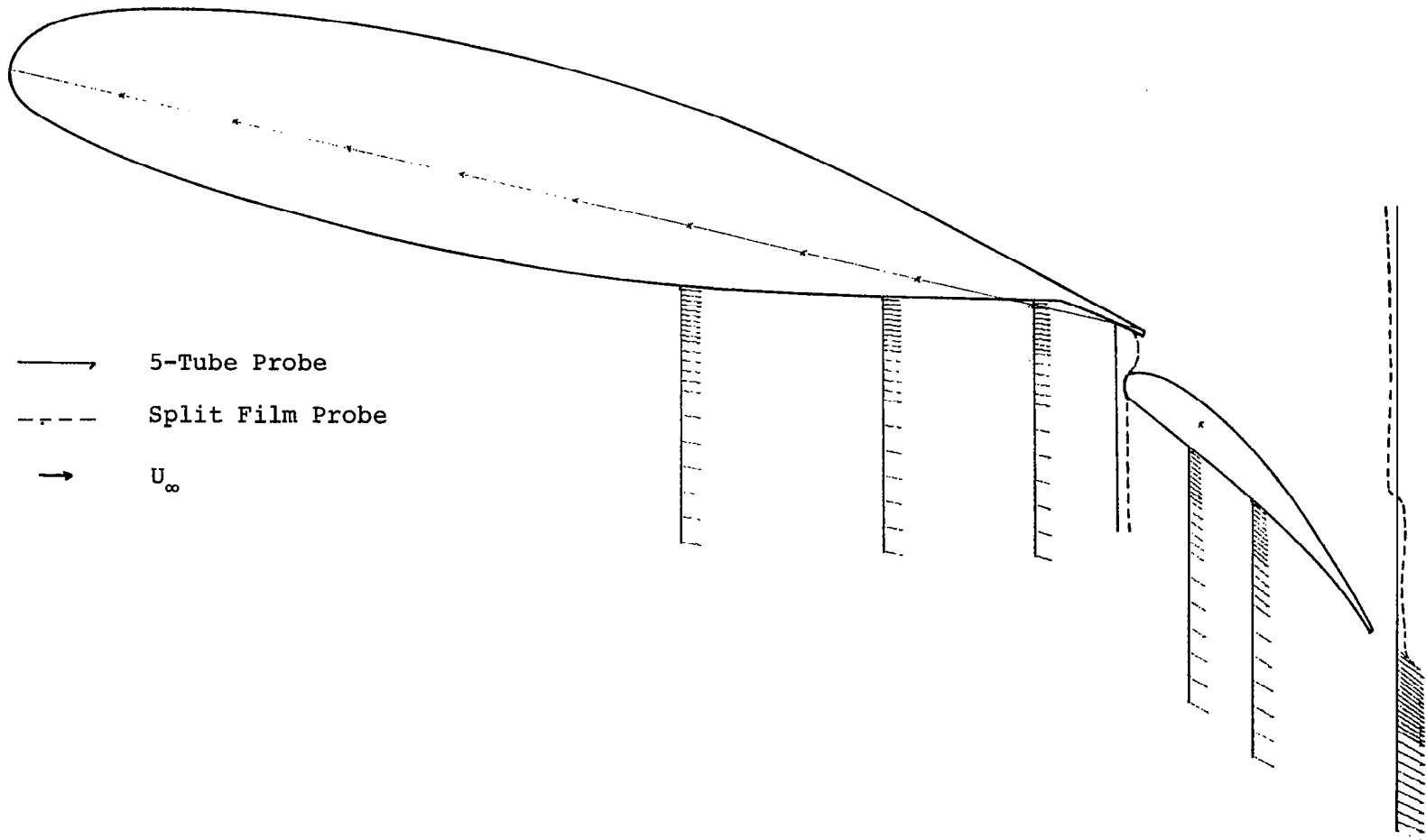
(c) SHARP LIP COVE

Figure 49- Continued.



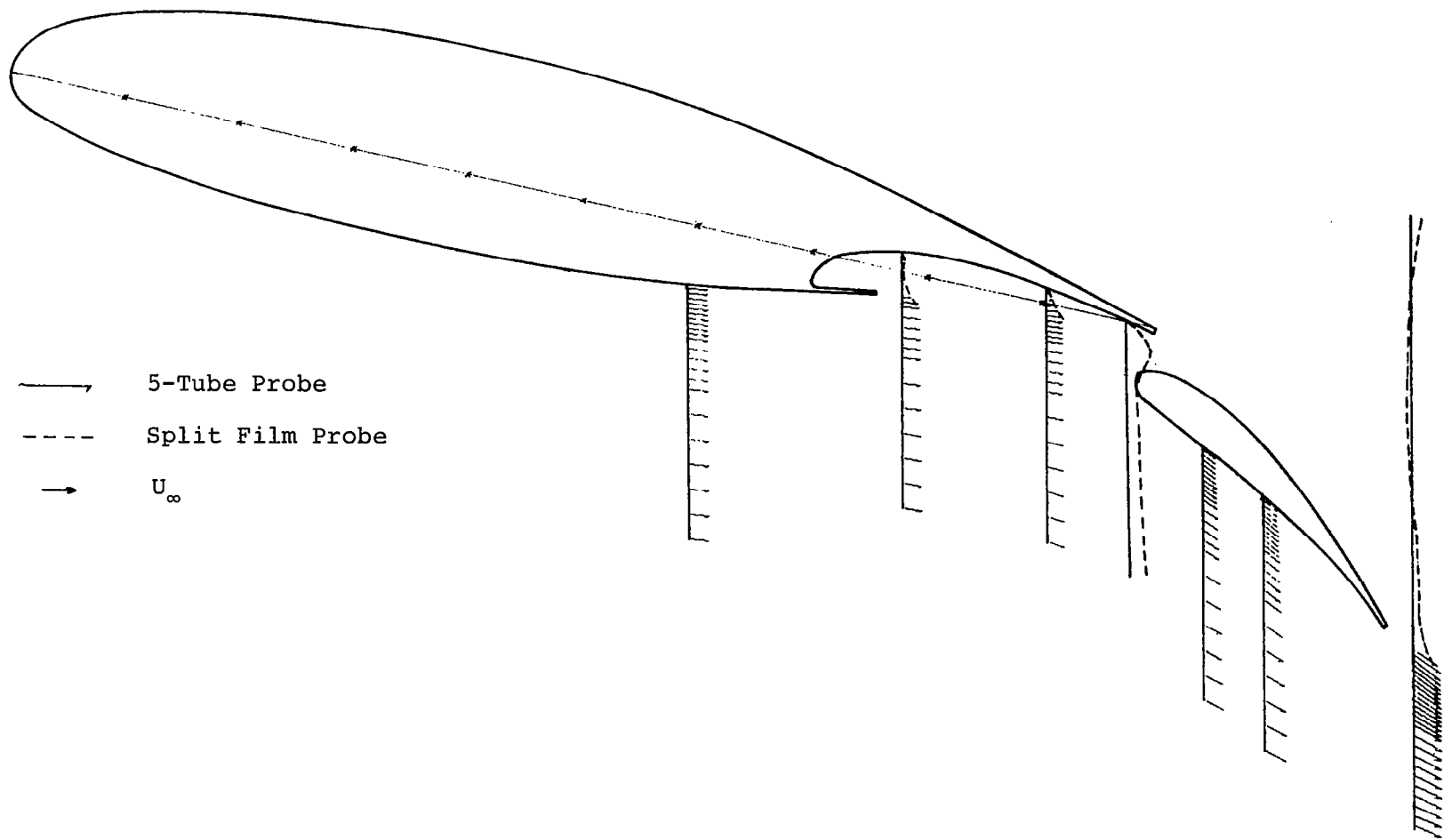
(a) STANDARD COVE

Figure 50 - Experimental Velocity Profiles, $\alpha = 12.7^\circ$



(b) BLENDED COVE

Figure 50 - Continued.



(c) SHARP LIP COVE

Figure 50 - Concluded.

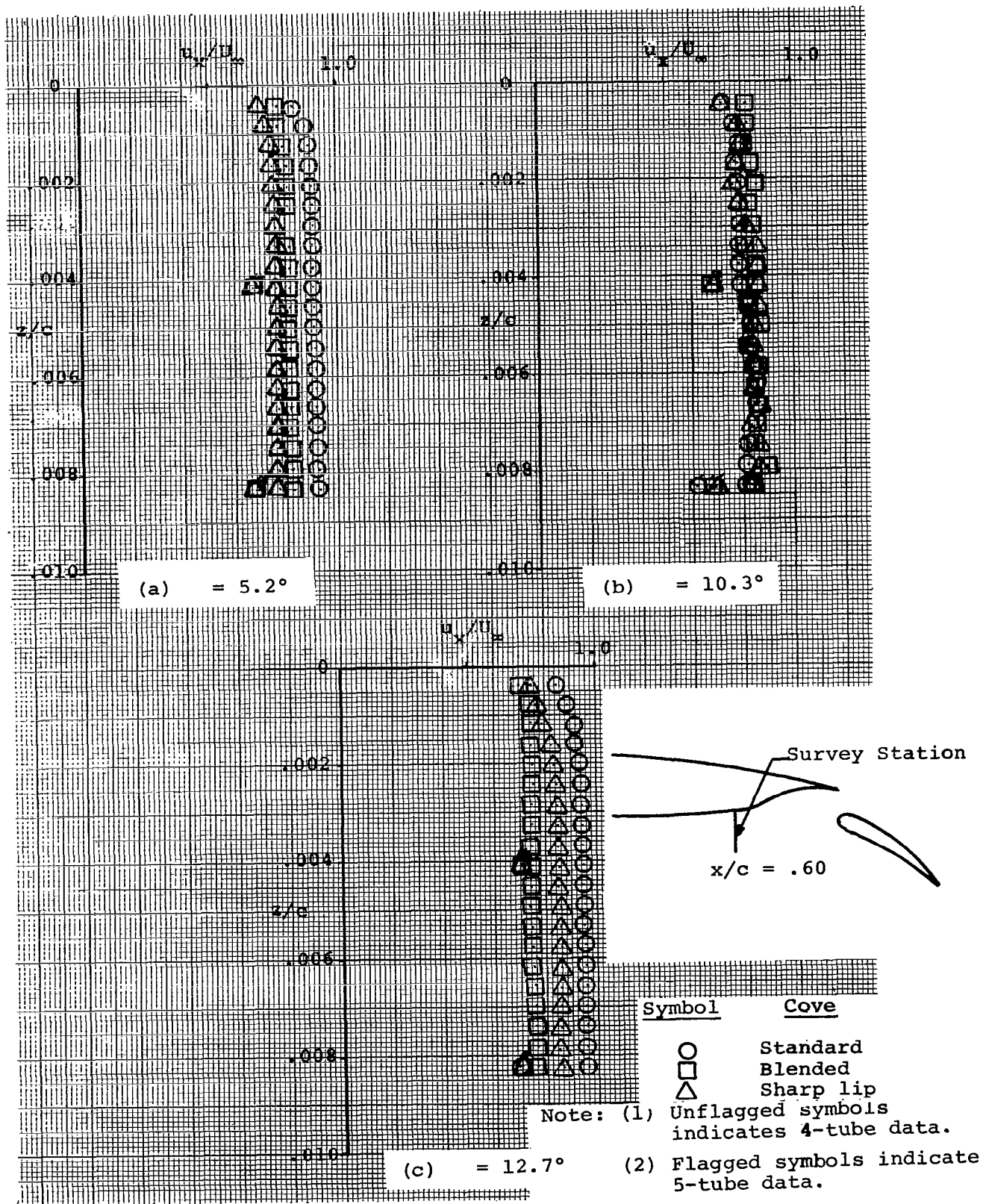
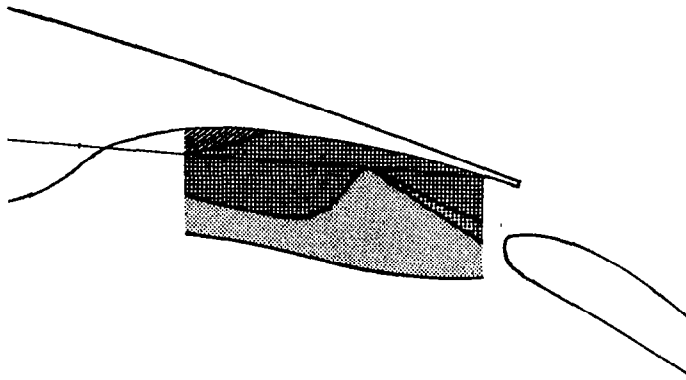
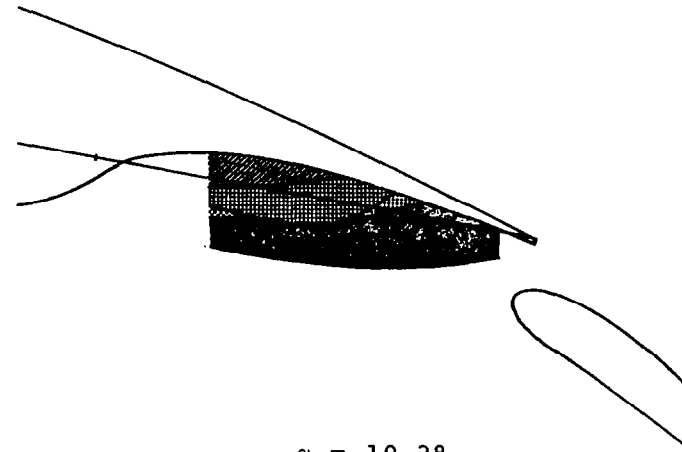
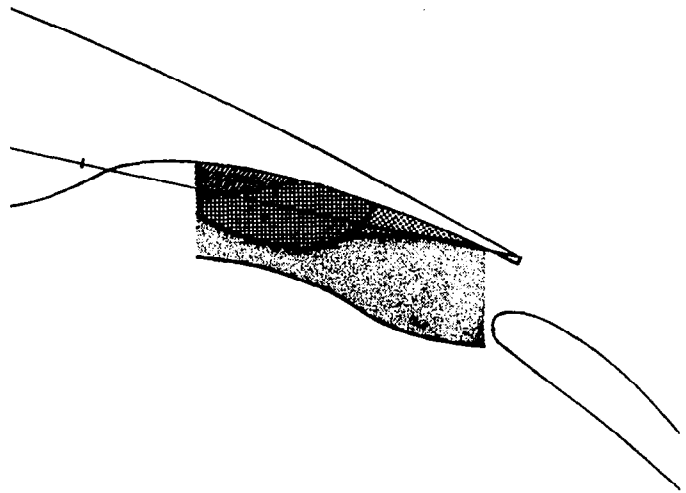


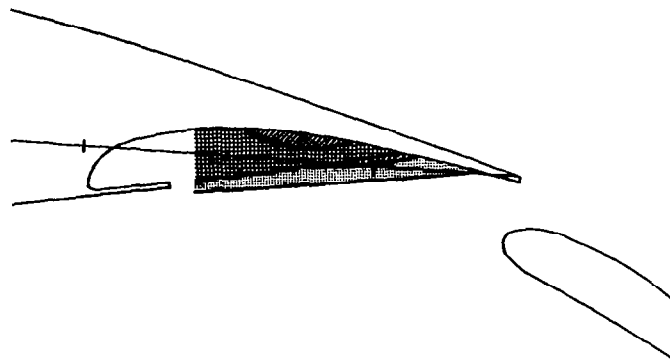
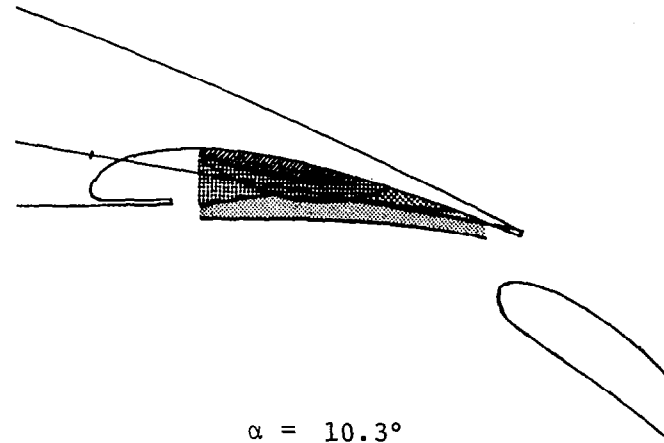
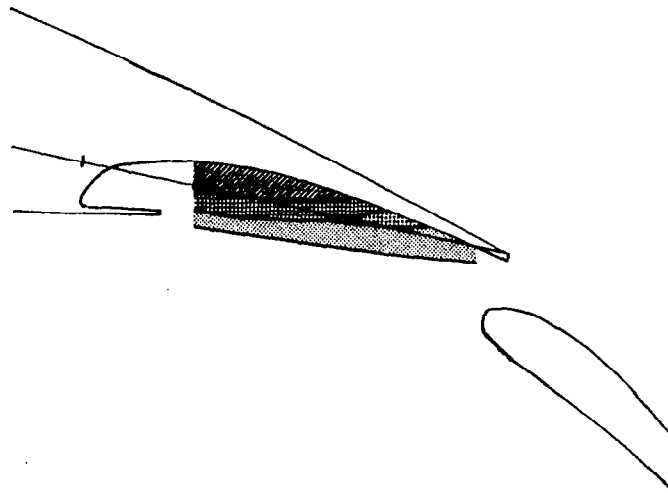
Figure 51 - Near Wall Velocity Profiles, $x/c = 0.60$.


 $\alpha = 5.2^\circ$

 $\alpha = 10.3^\circ$

 $\alpha = 12.7^\circ$

- Heavy Turbulence - Reversed > 50% Time
- Heavy Turbulence - 1% Time < Reversed < 50% Time
- Heavy Turbulence
- Moderate Turbulence
- Smooth

 $RN = 2.2 \times 10^6$
 $Mach\ No. = 0.13$

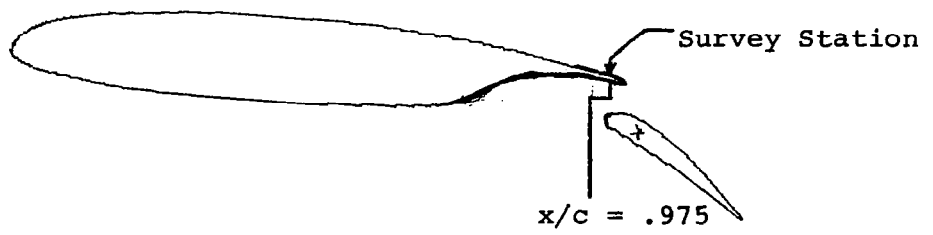
Figure 52 - Split Film Turbulence Surveys, Standard Cove.


 $\alpha = 5.2^\circ$

 $\alpha = 10.3^\circ$

 $\alpha = 12.7^\circ$

-  Heavy Turbulence - Reversed > 50% Time
-  Heavy Turbulence - 1% Time < Reversed < 50% Time
-  Heavy Turbulence
-  Moderate Turbulence
-  Smooth

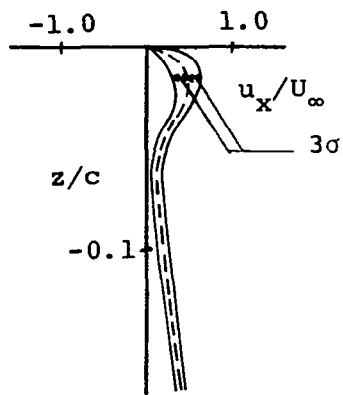
 $RN = 2.2 \times 10^6$
 $Mach\ No. = 0.13$

Figure 53 - Split Film Turbulence Surveys, Sharp Lip Cove.

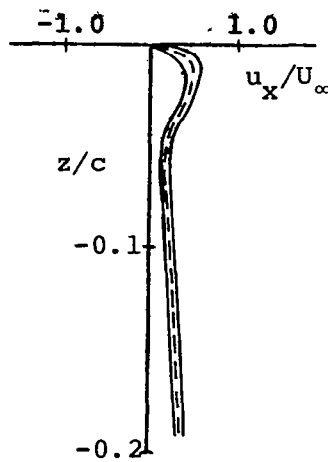


σ = Standard Deviation

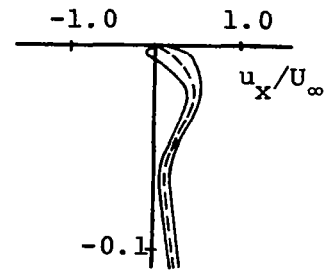
- - - Mean Value



(a) Standard Cove

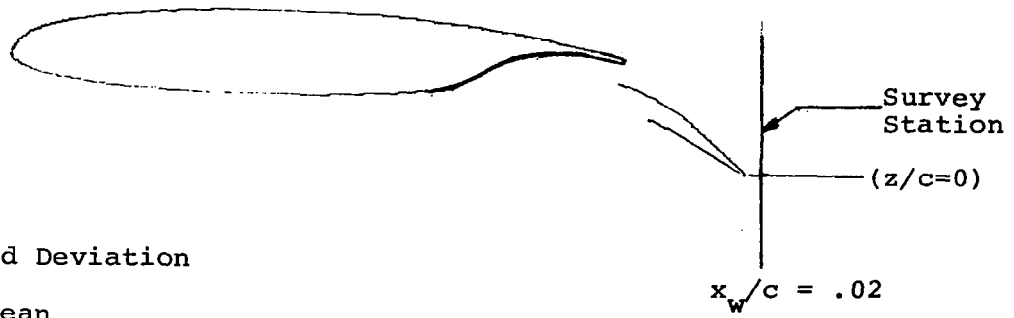


(b) Blended Cove



(c) Sharp Lip Cove

Figure 54- Flap Velocity Profiles, $x/c = .975, \alpha = 10.3^\circ$.



σ = Standard Deviation

- - - - - Mean

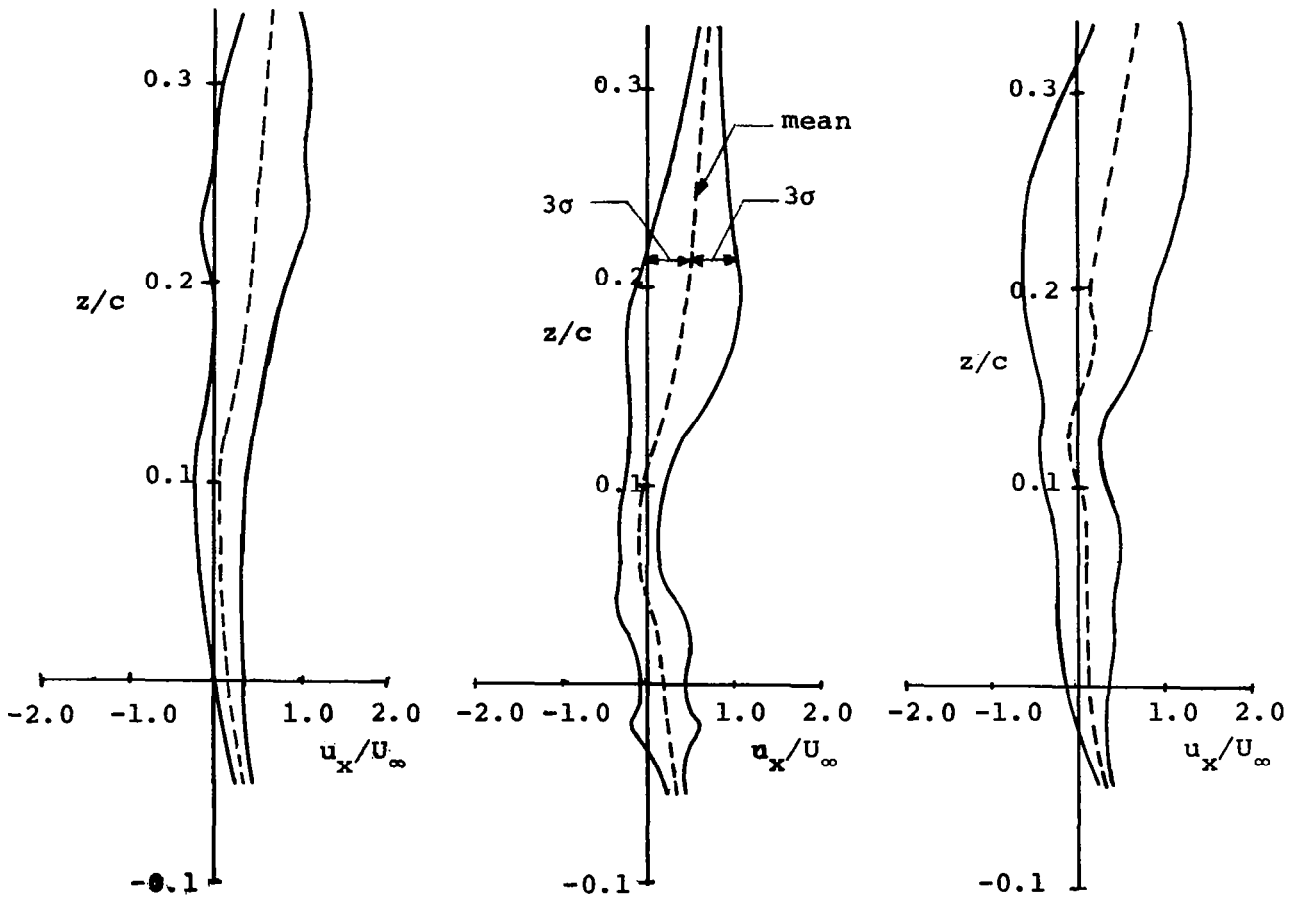
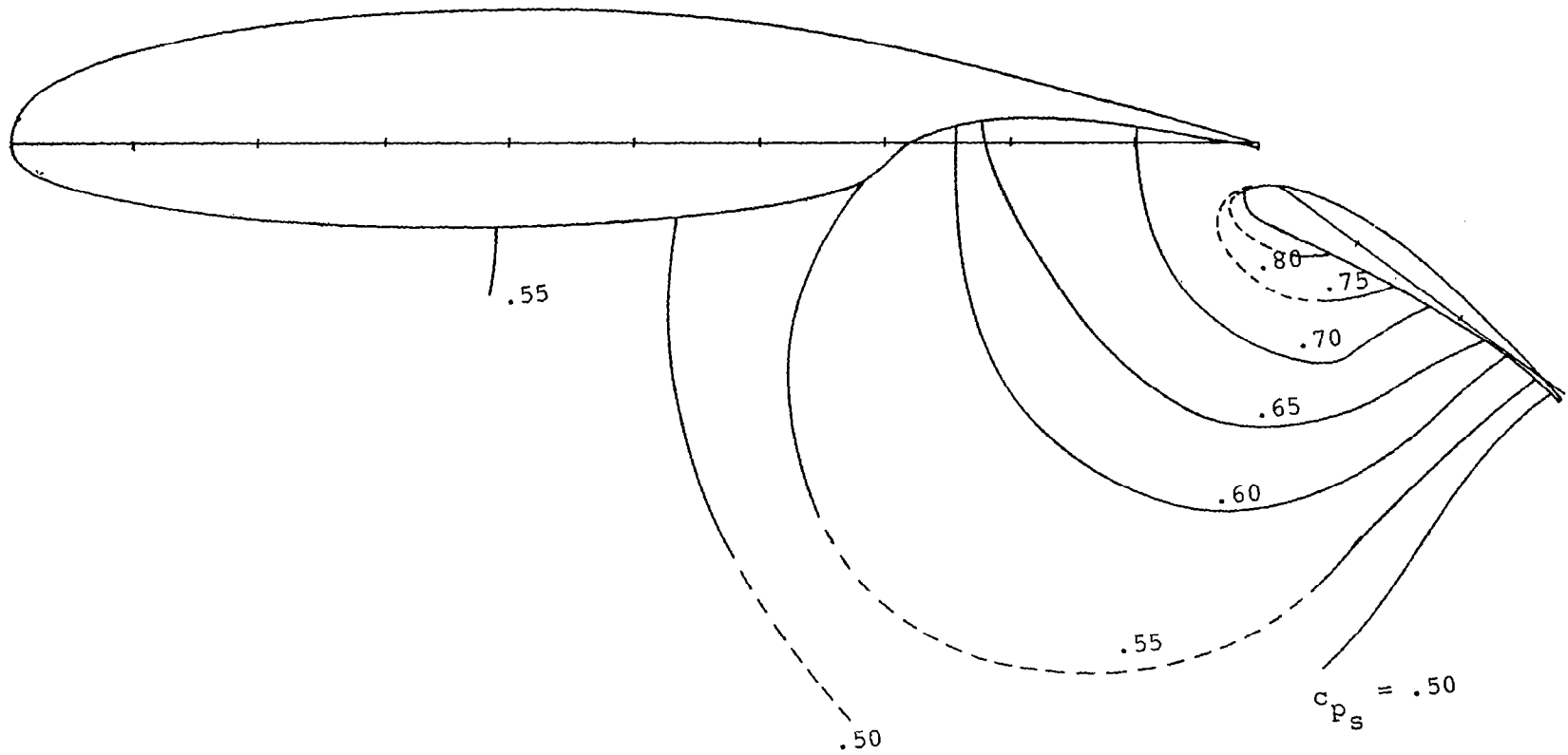
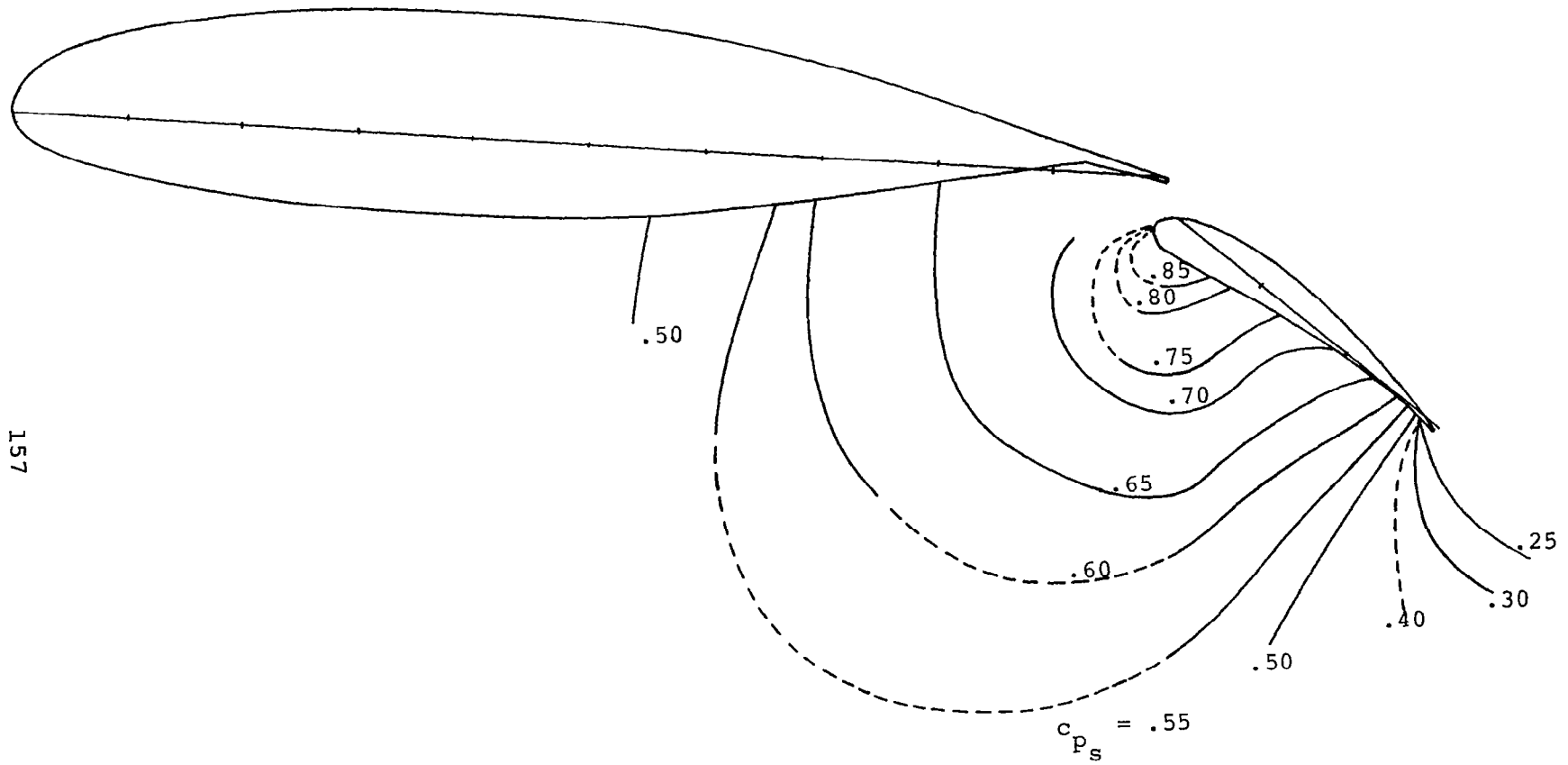


Figure 55 - Wake Velocity Profile from Split Film Probe, $x_w/c = .02$, $\alpha = 10.3^\circ$.



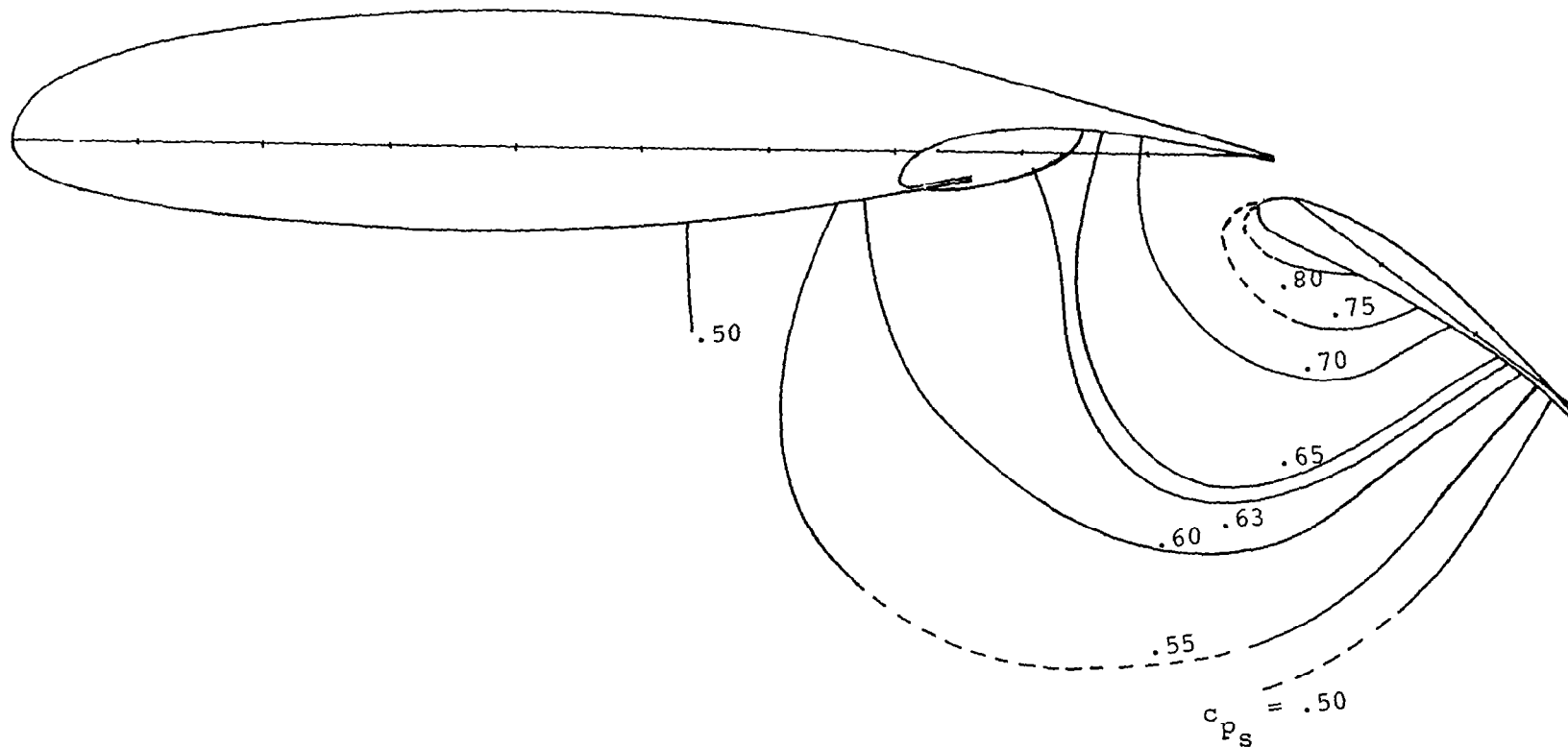
(a) STANDARD COVE

Figure 56- Static Pressure Contours, $\alpha = 5.2^\circ$.

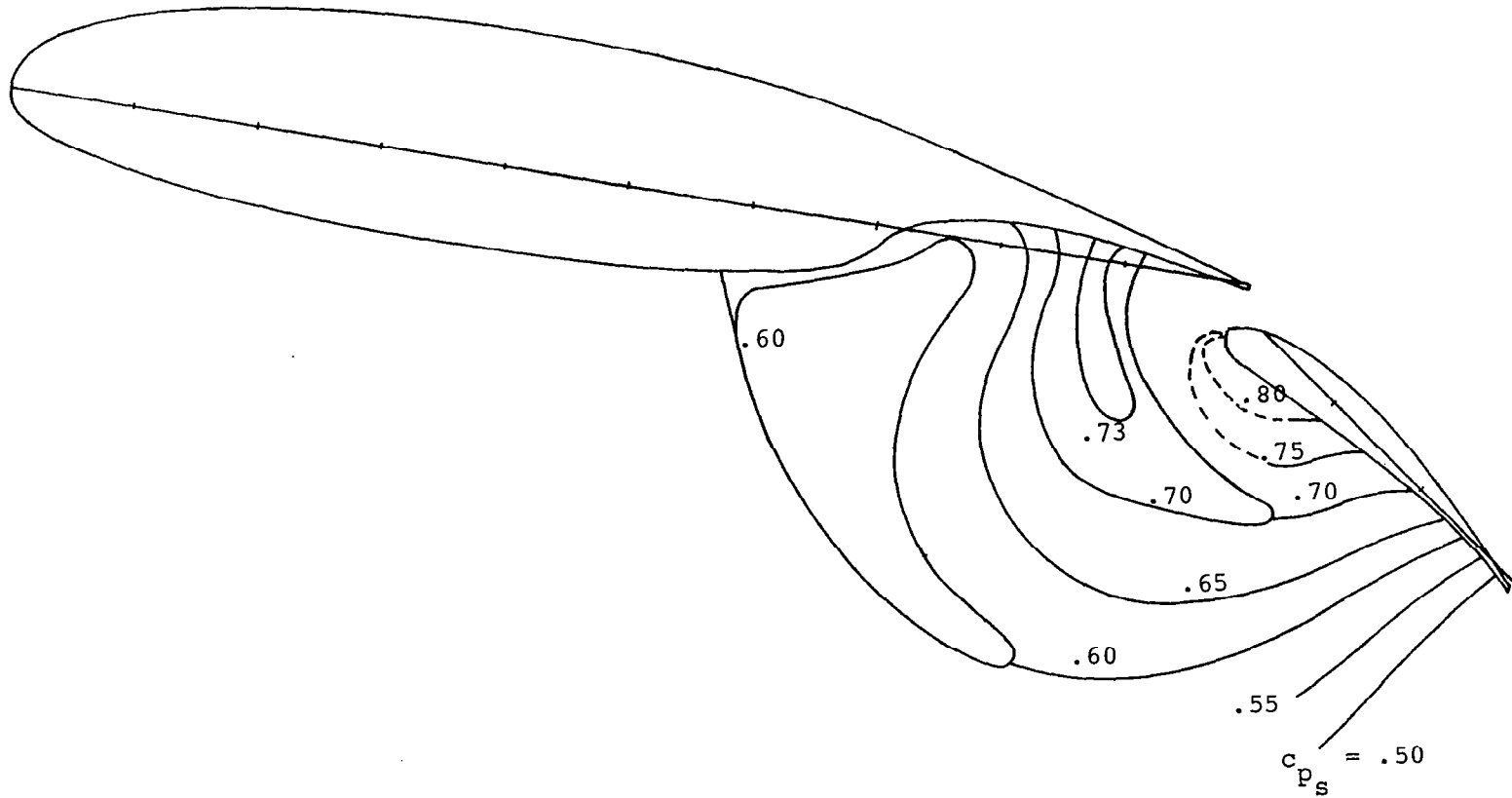


(b) BLENDED COVE

Figure 56 - Continued.

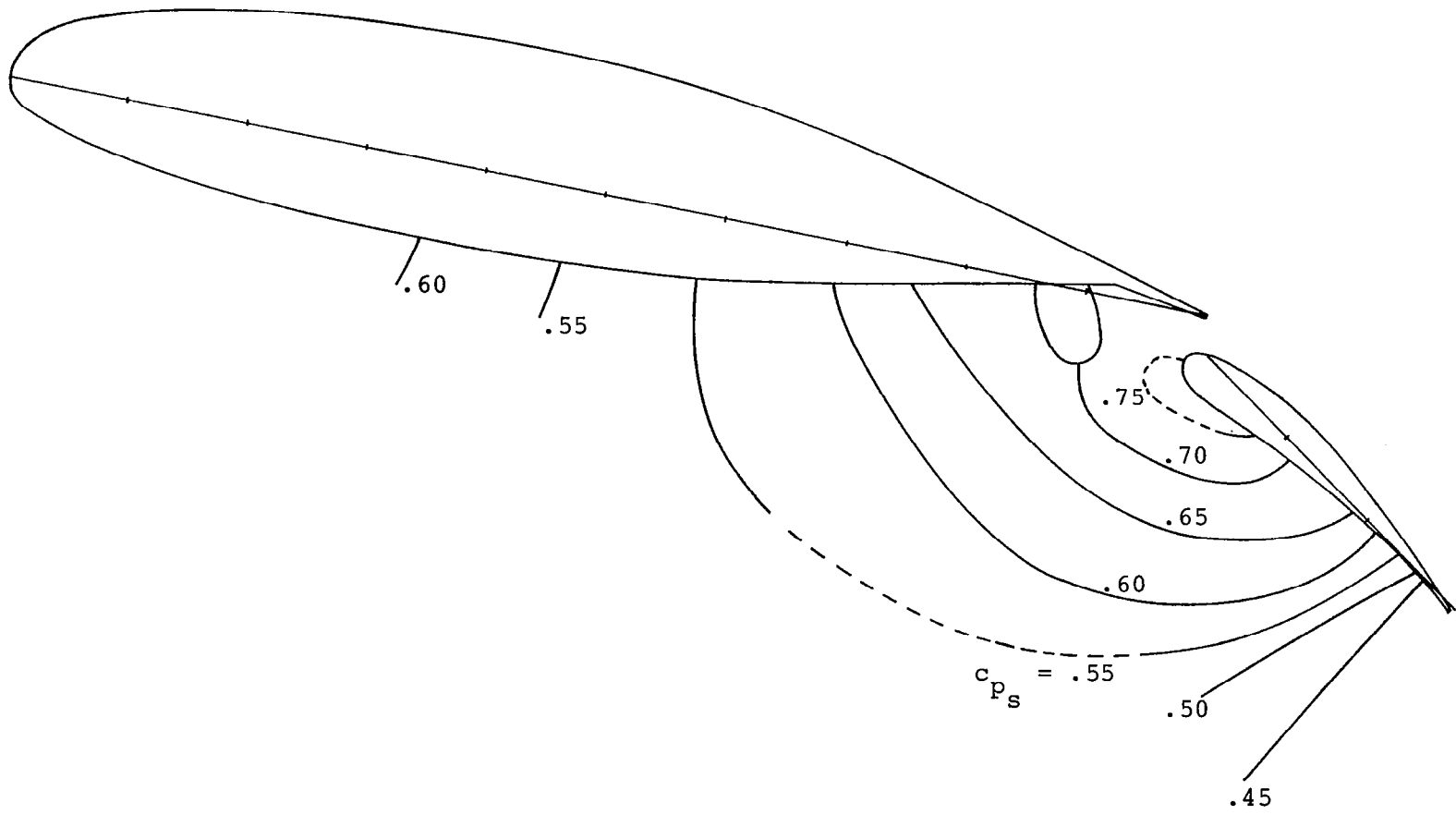


(c) SHARP LIP COVE
Figure 56 - Concluded.



(a) STANDARD COVE

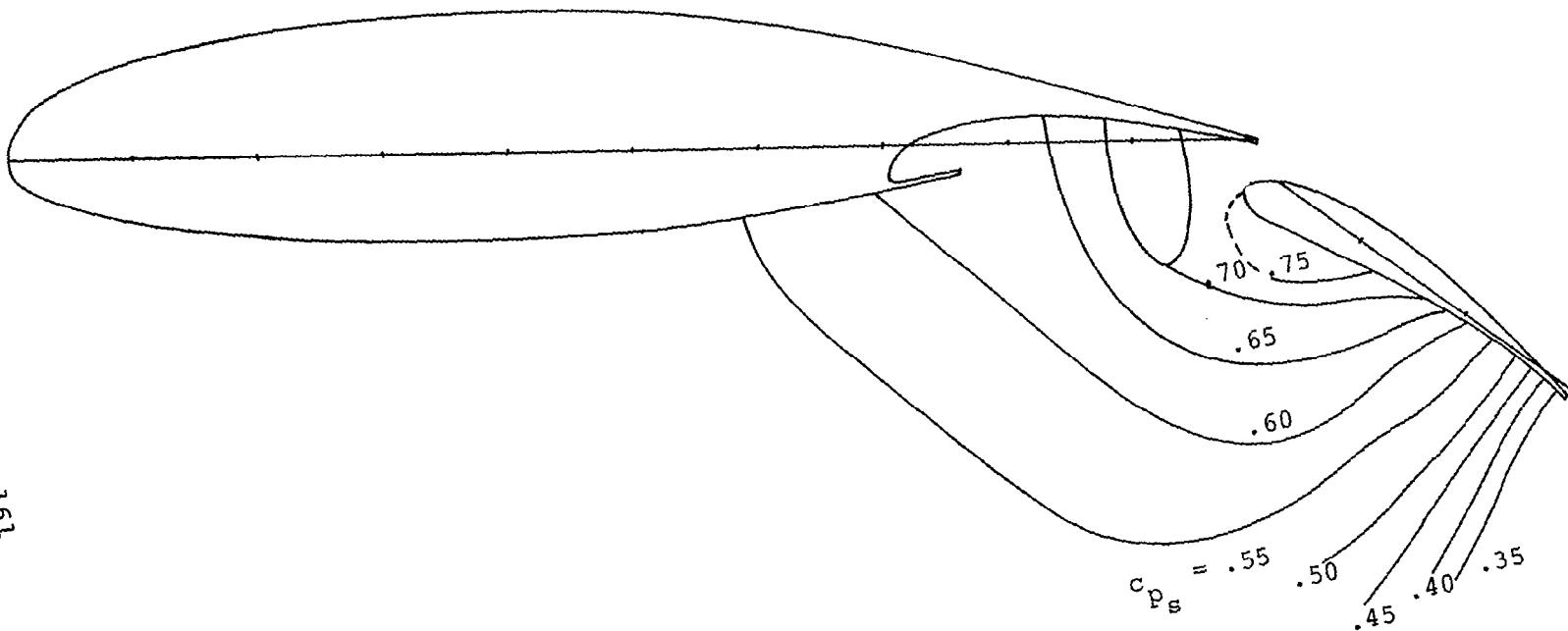
Figure 57- Static Pressure Contours, $\alpha = 10.3^\circ$.



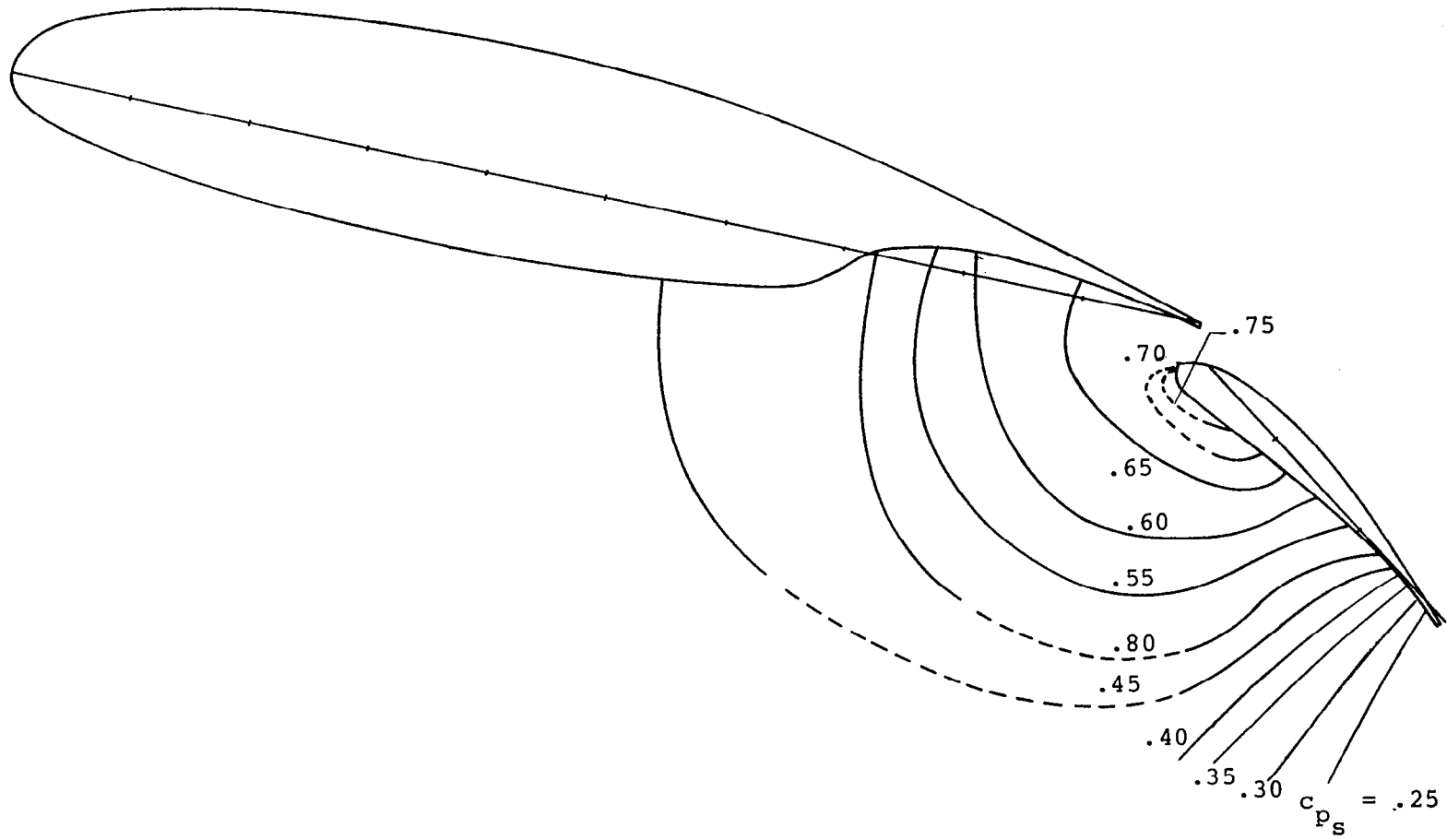
(b) BLENDED COVE

Figure 57- Continued.

161

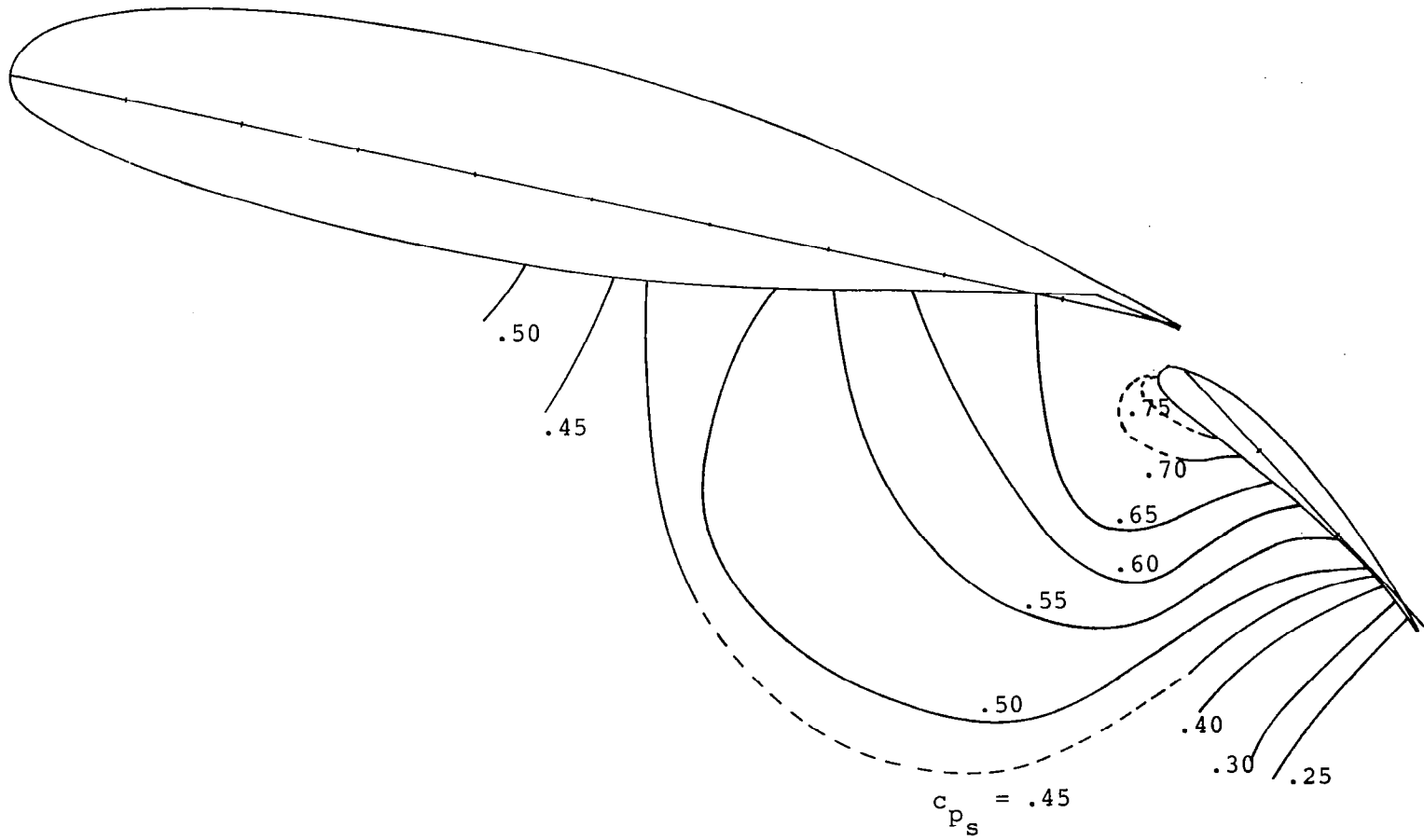


IN T.T.P. COVE



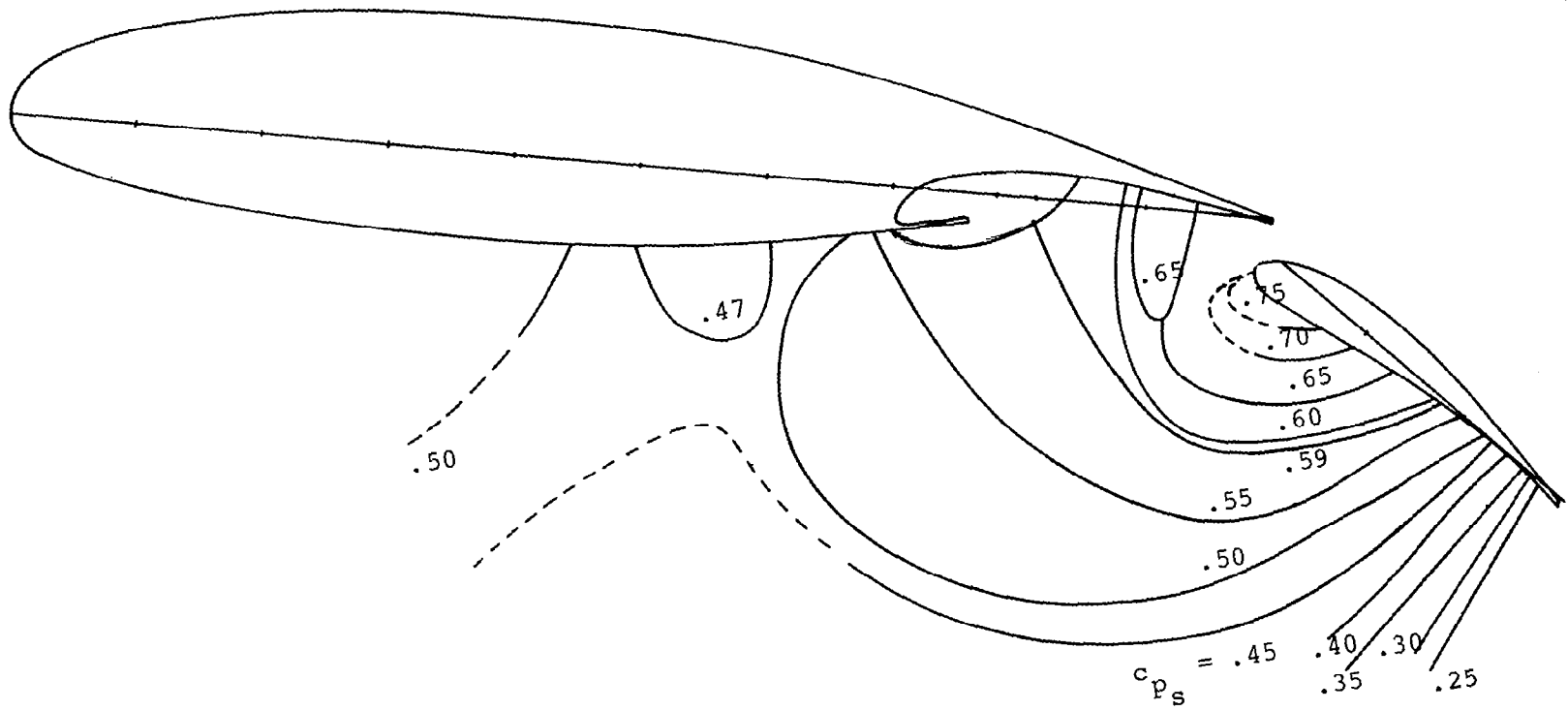
(a) STANDARD COVE

Figure 58- Static Pressure Contours, $\alpha = 12.7^\circ$.



(b) BLENDED COVE

Figure 58 - Continued.



(c) SHARP LIP COVE
58- Concluded.

1. Report No. NASA CR-3687		2. Government Accession No.		3. Recipient's Catalog No.	
4. Title and Subtitle ADDITIONAL FLOW FIELD STUDIES OF THE GA(W)-1 AIRFOIL WITH 30-PERCENT CHORD FOWLER FLAP INCLUDING SLOT-GAP VARIATIONS AND COVE SHAPE MODIFICATIONS				5. Report Date May 1983	
				6. Performing Organization Code	
7. Author(s) W. H. Wentz, Jr., and C. Ostowari				8. Performing Organization Report No. AR 79-3	
9. Performing Organization Name and Address Wichita State University Wichita, Kansas 67208				10. Work Unit No.	
				11. Contract or Grant No. NGR 17-003-021	
12. Sponsoring Agency Name and Address National Aeronautics and Space Administration Washington, DC 20546				13. Type of Report and Period Covered Contractor Report	
				14. Sponsoring Agency Code	
15. Supplementary Notes Langley Technical Monitor: Kevin W. Noonan					
16. Abstract Experimental measurements have been made to determine the effects of slot gap opening and flap cove shape on flap and airfoil flow fields. Test model was the GA(W)-1 airfoil with 0.30c Fowler flap deflected 35 degrees. Tests were conducted with optimum, wide and narrow gaps, and with three cove shapes. Three test angles were selected, corresponding to pre-stall, $c_{l_{max}}$ and post-stall conditions. Reynolds number was 2.2×10^6 and Mach number was 0.13. Force, surface pressure, total pressure, and split-film turbulence measurements were made. Results were compared with theory for those parameters for which theoretical values were available.					
17. Key Words (Suggested by Author(s)) General aviation airfoils Separated flow fields GA(W)-1 airfoil High lift systems			18. Distribution Statement FEDD Distribution Subject Category 02		
19. Security Classif. (of this report) Unclassified		20. Security Classif. (of this page) Unclassified		21. No. of Pages 170	22. Price

Available: NASA's Industrial Applications Centers